ADVANCED STEEL CONSTRUCTION

An International Journal

Volume 21 Number 3

June 2025

CONTENTS

Technical Papers

The Hong Kong Institute of Steel Construction
Website: *http://www.hkisc.org*
ISSN 1816-112X
Science Citation Index Expanded, Materials Science Citation Index and ISI Alerting
Cover: Greater Bay Area Cultural and Sports Center， China. Photo@ Li Hua-Bo

---

ADVANCED STEEL CONSTRUCTION

VOL.21, NO.3 (2025)

ADVANCED STEEL CONSTRUCTION

an International Journal

ISSN 1816-112X

Volume 21 Number 3

June 2025

Advanced Steel Construction

an international journal

ISSN 1816-112X

Science Citation Index Expanded, Materials Science Citation Index and ISI Alerting

EDITORS-IN-CHIEF

Asian Pacific, African and organizing Editor
S.L. Chan
South China University of Technology, China

American Editor
W.F. Chen
Univ. of Hawaii at Manoa, USA

European Editor
R. Zandonini
Trento Univ., Italy

ASSOCIATE EDITORS

Y.P. Liu
South China University of Technology, China

S.W. Liu
The Hong Kong Polyt. Univ., Hong Kong, China

INTERNATIONAL EDITORIAL BOARD

F.G. Albermani
Central Queensland Univ., Australia

I. Burgess
Univ. of Sheffield, UK

F.S.K. Bijlaard
Delft Univ. of Technology, The Netherlands

M.A. Bradford
The Univ. of New South Wales, Australia

D. Camotim
Technical Univ. of Lisbon, Portugal

C.M. Chan
Hong Kong Univ. of Science & Technology, Hong Kong, China

T.H.T. Chan
Queensland Univ. of Technology, Australia

T.M. Chan
The Univ. of Hong Kong, Hong Kong, China

Z.H. Chen
Tianjin Univ., China

S.P. Chiew
Nanyang Technological Univ., Singapore

G.G. Deierlein
Stanford Univ., California, USA

L. Dezi
Univ. of Ancona, Italy

D. Dubina
The Politehnica Univ. of Timosoara, Romania

R. Greiner
Technical Univ. of Graz, Austria

L. Gardner
Imperial College of Science, Technology and Medicine, UK

Y. Goto
Nagoya Institute of Technology, Japan

L.H. Han
Tsinghua Univ. China

S. Herion
University of Karlsruhe, Germany

G.W.M. Ho
Ove Arup & Partners Hong Kong Ltd., Hong Kong, China

Todd A. Helwig
University of Texas at Austin, USA

B.A. Izzuddin
Imperial College of Science, Technology and Medicine, UK

J.P. Jaspart
Univ. of Liege, Belgium

S. A. Jayachandran
IIT Madras, Chennai, India

S.E. Kim
Sejong Univ., South Korea

S. Kitipornchai
The Univ., of Queensland, Australia

D. Lam
Univ. of Bradford, UK

H.F. Lam
City Univ. of Hong Kong, Hong Kong, China

G.C Li
Shenyang Jianzhu Univ., China

G.Q. Li
Tongji Univ., China

J.Y.R. Liew
National Univ. of Singapore, Singapore

E.M. Lui
Syracuse Univ., USA

Y.L. Mo
Univ. of Houston, USA

J.P. Muzeau
CUST, Clermont Ferrand, France

D.A. Nethercot
Imperial College of Science, Technology and Medicine, UK

Y.Q. Ni
The Hong Kong Polyt. Univ., Hong Kong, China

D.J. Oehlers
The Univ. of Adelaide, Australia

J.L. Peng
Yunlin Uni. of Science & Technology, Taiwan, China

K. Rasmussen
The Univ. of Sydney, Australia

J.M. Rotter
The Univ. of Edinburgh, UK

C. Scawthorn
Scawthorn Porter Associates, USA

P. Schaumann
Univ. of Hannover, Germany

Y.J. Shi
Tsinghua Univ., China

G.P. Shu
Southeast Univ. China

L. Simões da Silva
Department of Civil Engineering, University of Coimbra, Portugal

G. Shi
Tsinghua Univ., China

J.G. Teng
The Hong Kong Polyt. Univ., Hong Kong, China

G.S. Tong
Zhejiang Univ., China

K.C. Tsai
National Taiwan Univ., Taiwan, China

C.M. Uang
Univ. of California, USA

B. Uy
University of Western Sydney, Australia

M. Veljkovic
Univ. of Lulea, Sweden

F. Wald
Czech Technical Univ. in Prague, Czech

Y.C. Wang
The Univ. of Manchester, UK

B. Wu
South China University of Technology, China

Y.B. Wang
Tongji Univ., China

D. White
Georgia Institute of Technology, USA

Y.L. Xu
Southwest Jiaotong University, China

E. Yamaguchi
Kyushu Institute of Technology, Japan

Y.B. Yang
National Taiwan Univ., Taiwan, China

Y.Y. Yang
China Academy of Building Research, Beijing, China

B. Young
The Hong Kong Polyt. Univ., Hong Kong, China

X.L. Zhao
The Hong Kong Polyt. Univ., Hong Kong, China

X.H. Zhou
Chongqing University, China

S.Y. Zhu
The Hong Kong Polyt. Univ., Hong Kong, China

R.D. Ziemian
Bucknell Univ., USA

J.X. Zhao
South China University of Technology, China

Cover: Greater Bay Area Cultural and Sports Center, China. Photo@ Li Hua-Bo

e-copy of IJASC is free to download at "www.ascjournal.com" in internet and mobile apps.

General Information
Advanced Steel Construction, an international journal

Aims and scope

The International Journal of Advanced Steel Construction provides a platform for the publication and rapid dissemination of original and up-to-date research and technological developments in steel construction, design and analysis. Scope of research papers published in this journal includes but is not limited to theoretical and experimental research on elements, assemblages, systems, material, design philosophy and codification, standards, fabrication, projects of innovative nature and computer techniques. The journal is specifically tailored to channel the exchange of technological know-how between researchers and practitioners. Contributions from all aspects related to the recent developments of advanced steel construction are welcome.

Subscription inquiries and change of address. Address all subscription inquiries and correspondence to Member Records, IJASC. Notify an address change as soon as possible. All communications should include both old and new addresses with zip codes and be accompanied by a mailing label from a recent issue. Allow six weeks for all changes to become effective.
The Hong Kong Institute of Steel Construction
HKISC
c/o Prof. SL Chan,
Unit 209B, Photonics Centre, No. 2 Science Park East Avenue,
Hong Kong Science Park, Shatin, N.T., Hong Kong, China.
Tel: 852- 3595 6150 Fax: 852- 3619 7238
Email: ceslchan@connect.polyu.hk Website: *http://www.hkisc.org/*
ISSN 1816-112X
Science Citation Index Expanded, Materials Science Citation Index and ISI Alerting

ISSN 1816-112X

Science Citation Index Expanded, Materials Science Citation Index and ISI Alerting

Advanced Steel Construction
an international journal

VOLUME 21 NUMBER 3 June 2025

Technical Papers

Advanced Steel Construction – Vol. 21 No. 3 (2025) 182–193
DOI:10.18057/IJASC.2025.21.3.1

STRUCTURAL PROPERTIES OF COLD-FORMED THIN-WALLED RECTANGULAR HIGH-STRENGTH STAINLESS-STEEL SPLICED TUBULAR COLUMNS UNDER AXIAL COMPRESSION AND COMPRESSION-BENDING

Jun Zhao [1], Yang Peng [2], Hao-Xuan Li [3], Xin-Xin Zhang [4] and Jun Dong [2, *]

[1] School of Civil Engineering and Architecture, Changzhou Institute of Technology,
Changzhou 213032, China
[2] College of Civil Engineering, Nanjing Tech University, Nanjing 211816, China
[3] Jiangsu Open University, Nanjing 214257, China
[4] Zhejiang Changneng Planning and Design Co., Ltd., Zhejiang 310030, China
** (Corresponding author: E-mail: dongjun@njtech.edu.cn)*

ABSTRACT

Stainless-steel had the advantages of high strength, high corrosion resistance and easy welding, it was suitable for cold-formed thin-walled components in marine engineering. However, most cold-formed thin-walled steel components were single-limb, it had the defect of insufficient stiffness in the weak axis direction. To solve this problem, two stainless-steel lipped channels were spliced into a rectangular tube through plug welds, and an efficient cold-formed thin-walled rectangular stainless-steel spliced tubular columns was proposed. By means of splicing, the singly-symmetric cross-sections such as lipped channel sections could be transformed into doubly-symmetric cross-sections, significantly improving the axial compression performance and bending performance of the members. Three series of axial compression short column tests were carried out. The results showed that both the V-shaped stiffeners and the straight ribs played a full stiffening role in the axial compression test. Compared with the RHS-1 series components, the capacity of the RHS-2 series increased by 46.15%, the capacity of the RHS-3 series components increased by 55.38%. The finite element parameter analysis of axial compression short columns, compression-bending short columns and median long columns was carried out. The results showed that for axial compression short columns, V-shaped stiffeners and the width-thickness ratio had a great influence on failure modes. When the depth of the V-shaped stiffener was 32 mm and the angle was 90°, the section performance was optimal. When the slenderness ratio was in the range of 33.55-147.56, the overall buckling failure occurred. For compression-bending short columns and median long columns, the eccentricity ratio and the slenderness ratio had a great influence on failure modes. When the eccentricity ratio increased from 0.1 to 2.0, the ultimate compression-bending capacity decreased by 72.14% and 69.01% respectively. When the slenderness ratio was in the range of 14.81-98.73, the compression-bending stability capacity decreased significantly with the increase of the slenderness ratio. A modified calculation formula for the compression-bending capacity was proposed, with high accuracy.

ARTICLE HISTORY

Received:	15 November 2024
Revised:	31 December 2024
Accepted:	1 January 2025

KEYWORDS

High-strength stainless-steel;
Spliced rectangular tubular column;
Axial compression short column test;
Compression-bending;
Finite element analysis

1. Introduction

With the rapid development of marine steel structures, the corrosion problem became the greatest weakness in marine engineering [1-3]. Compared with austenitic stainless-steel, the high-strength stainless-steel not only had high strength, but also had low manufacturing costs [4-6]. Cold-formed thin-walled components could effectively improve the stability performance and capacity [7-11]. However, the cold-formed thin-walled high-strength stainless-steel columns had few research.

With the development of cold-formed thin-walled technology, the research on cold-formed thin-walled steel columns began to be widely carried out [12-16]. Generally, there were three buckling modes for cold-formed thin-walled steel axial compression columns, including local buckling failure, distortional buckling failure and overall buckling failure [17-19]. D.A. Padilla-Llano [20] analyzed the overall buckling, distortional buckling and local buckling behaviors of single-limb C-shaped steel components under cyclic loading. The results showed that under the two different loading conditions, the initial stiffness of the components had little difference. When the load was greater than the peak load, the stiffness decreased significant under the cyclic load. Y. Lu [21] conducted axial compression tests on 18 single-limb cold-formed thin-walled C-shaped steel components, providing theoretical basis for the subsequent axial compression test. H.X. Niu [22] carried out axial compression numerical simulation of components with four stiffening methods. The results showed that under the same steel consumption, the axial compression ultimate capacity of the components with V-shaped stiffeners increased most significantly. B. Young [23] conducted axial compression performance test on the "bow" shaped high-strength cold-formed thin-walled steel double-limb column. The results showed that using the direct strength method to calculate the axial compression ultimate load of the column had certain safety. Reyes [24] studied the box-section axial compression components of welded double-limb C-shaped cold-formed thin-walled steel. The results showed that when calculating its capacity using the specification AISI S100-2007, the slenderness ratio of the components needed to be corrected compared with median long columns. I. Georgieva [25] conducted compression-bending test on double-limb Z-shaped section columns. The results showed that when the slenderness ratio was large, out-of-plane instability would occur, and the overall initial defects had a great influence on the ultimate capacity. J. Zhang [26] conducted axial compression test on I-shaped section columns formed by two web-stiffened C-shaped steel, and proposed four models for solving and calculating the critical buckling load of the section. F. Liao [27] conducted axial compression test on short columns composed of C-shaped steel and U-shaped steel through self-tapping bolts. The results showed that the short columns all suffered from local buckling and distortional buckling failure. In the current research, most of the cold-formed thin-walled components were formed by connecting two or more single-limb components through bolts or welding, while no experts conducted research on welded high-strength stainless-steel columns.

This paper proposed a cold-formed thin-walled rectangular high-strength stainless-steel spliced tubular columns. Experiments of axial compression short columns, finite element analysis of axial compression of short columns, compression-bending short and median long columns were carried out. Key parameters that affect the structural performance was studied, and the calculation formula for the ultimate capacity of compression-bending columns was proposed.

2. Axial compression test of short columns

2.1. Design and fabrication of specimens

The duplex stainless-steel had higher yield strength, lower strain strengthening coefficient and stronger corrosion resistance than austenitic stainless-steel, and the material properties were as shown in reference [28]. The axial compression short column specimens in the experiment were shown in Fig.1.

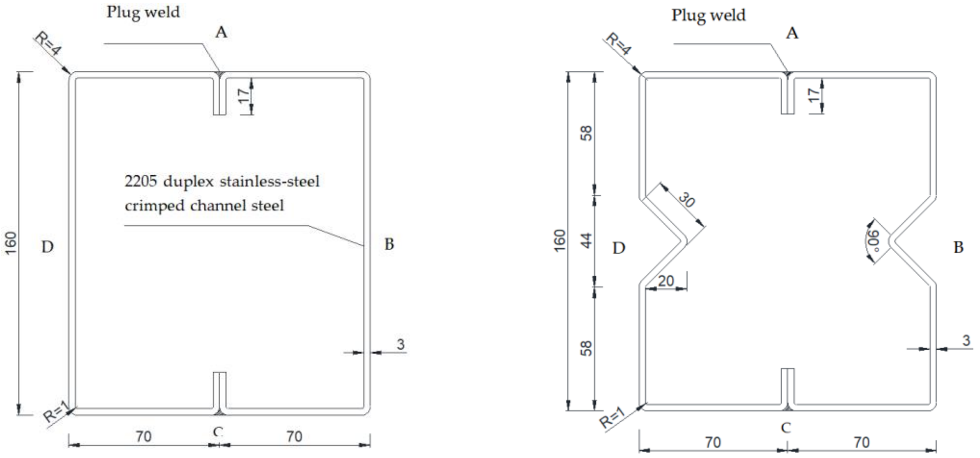

(a) RHS-1 Series (b) RHS-2 Series

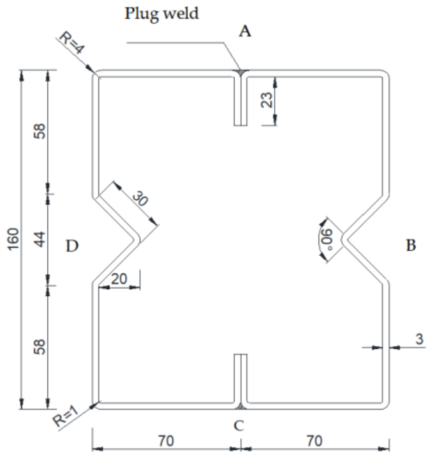

(c) RHS-3 Series

Fig. 1 Detailed dimensions of components

Fig. 2 Axial compression short columns

The specimens could be divided into three groups, namely RHS-1, RHS-2, and RHS-3. The thickness of the plate was 3mm, and the length of the short column was 3 times the length of the web of the lipped channel steel, that is, 480mm. The lipped length of the RHS-3 series was 26mm. The same metal and the same technological equipment were used to manufacture a total of 9 components. The fabricated components were shown in Fig.2.

Due to the limitations of the manufacturing process, there were differences between the actual components and the design dimensions. The actual dimensions were shown in Table 1. To accurately obtain the specific detailed dimensions of the test components, the average value of the three measurement results were taken as the actual dimension of the component to avoid accidental errors during the measurement process. Through defect measurement, it was found that the initial geometric defects of the component along the length direction were much smaller than those caused by the protrusions on the weld edges, and the defect amplitude did not exceed 1 mm. Therefore, the initial geometric defects along the length direction did not affect the axial compression performance of the component.

Table 1
Measured dimensions of the components

Specimen number	H(mm)	B(mm)	a(mm)	t(mm)	Length of the V-shaped stiffeners (mm)	L (mm)
RHS-1-1	162.0	139.0	20	2.97	-	479.5
RHS-1-2	162.5	139.0	20	3.02	-	479.0
RHS-1-3	162.0	139.0	20	3.00	-	479.0
RHS-2-1	164.0	142.0	20	3.04	30	479.0
RHS-2-2	164.0	141.5	20	3.00	30	479.5
RHS-2-3	164.5	142.0	20	3.02	30	479.0
RHS-3-1	163.5	143.0	26	2.95	30	479.0
RHS-3-2	162.0	143.0	26	2.98	30	479.0
RHS-3-3	164.0	142.5	26	2.98	30	479.5

2.2. Test equipment and loading test scheme

2.2.1. Test preparation

The specimen was divided into square meshes at intervals of 30mm along the length direction to facilitate the observation and measurement of the deformation of the plate during the test process. For axial compression short columns, the most likely position for its local buckling was in the middle of the component. Displacement meters were set in the direction perpendicular to the plate at the middle section. A total of 3 displacement meters were set at the middle section of the RHS-1 series component, of which one displacement meter was arranged in the middle of the long side, and one displacement meter was arranged in the middle of the two sub-plates on the short side respectively. The RHS-2 and RHS-3 series were similar, and the displacement meters were all arranged in the middle of the sub-plates on the long side and the short side. The RHS-1 series components pasted 3 strain gauges at the middle section and the sections at B/2 from the ends at the upper and lower parts, and a total of 9 strain gauges were pasted on the entire component. The RHS-2 series components pasted 4 strain gauges at the middle section and the sections 80mm from the ends at the upper and lower parts, and a total of 12 strain gauges were pasted on the entire component. The RHS-3 series components pasted 4 strain gauges at the middle section and the sections at B/2 from the ends at the upper and lower parts, and a total of 12 strain gauges were pasted on the entire component.

2.2.2. Loading equipment and loading system

The loading equipment was a 1000T microcomputer-controlled electro-hydraulic servo pressure-shear testing machine, and the test device is shown in Fig.3. The short column components were arranged in the center of the loading platform through the end plates welded at both ends, and the load was transmitted through the end plates. The minimum displacement control speed was 0.5mm/min. The test process was displacement-controlled loading, and the loading process was continuous. The loading process could be divided into three stages. The first stage: The test system was debugged through preloading. The loading speed was 0.05mm/s (3mm/min) to 5kN to make the end plate and the test platform closely connected, and then the load was reduced to 0kN, that is, the load and displacement data were cleared, and then the readings of the strain gauge and the displacement meter were cleared. The second stage: The formal loading stage, the testing machine was controlled to move downward at a speed of 0.01mm/s (0.6mm/min), until the capacity of the component reached the peak. The third stage: The post-loading stage, when the load reached 80% of the estimated load, the moving speed was changed, and the loading was carried out at a speed of 0.05mm/s (3mm/min) to make the capacity of the component reach the ultimate capacity, and the component was damaged. Until the axial compression capacity dropped to about 80% of the peak load, the loading was stopped and the test ended.

Fig. 3 Loading equipment

2.3. Test results and analysis

2.3.1. Test process and main phenomena

As the load increased, the intervals of the "click-click" sounded emitted by the components gradually became longer, and gradually accompanied by small concave-convex local buckling of the components. When local buckling first occurred, the buckling shape was symmetrically distributed. As the load increased, the buckling half-wave gradually increased. When the ultimate load was reached, the buckling deformation of the plates expanded faster and the deformation degree was more obvious. The typical failure states of different series of components were shown in Fig.8. It could be seen no damage occurred at the weld position and the end of the component, the strength of the plug weld was sufficient, and the end restraint was sufficient. One half-wave buckling occurred on the long side of the RHS-1 component, and one half-wave buckling occurred on the short side. One half-wave buckling occurred in each of the two sub-plates on the long side of the RHS-2 component, and one half-wave buckling occurred in the middle of the short side. One half-wave buckling occurred in each of the two sub-plates on the long side of the RHS-3 component, and two half-waves buckling occurred on the upper part of the short side.

The failure modes were in line with the main objectives of component design. By comparing the members of the RHS-1 series with those of the RHS-2 series, it was found that the V-shaped stiffeners with a side length of 20 mm had sufficient stiffness to divide the lipped channel web members into two sub-plates. These two sub-plates buckled similarly to stiffened plates respectively. When comparing the members of the RHS-2 series with those of the RHS-3 series, by increasing the length of the lips, the height of the straight ribs on the short side of cold-formed thin-walled members formed by the lips was increased, so that the stiffness of the straight lips met the minimum stiffness requirement for intermediate stiffeners. However, since the straight ribs on the short side were connected by one-side plug welds through the lips, although the stiffness of the straight ribs formed by the two lips met the requirements, the width-thickness ratio exceeded the minimum width-thickness ratio limit for plates without local buckling. But because there was a certain margin in the code's limitation on the width-thickness ratio, the width-thickness ratio of the 26-mm lips in this paper only slightly exceeded the limit, and the lips did not buckle preferentially during the actual test process.

2.3.2. Test data and analysis

The comparison of the axial displacement-load curves of 9 components was shown in Fig.4. As the load gradually increased, the gap between the component section and the indenter gradually disappeared, and the component gradually transformed into full-section compression. The elastic modulus of the component gradually increased and stabilized, which was manifested in the curve as a linear increase in load with displacement. As the load increased further, the component undergone concave and convex deformation, the slope of the curve decreased and became negative, and the load began to decrease after reaching its peak load.

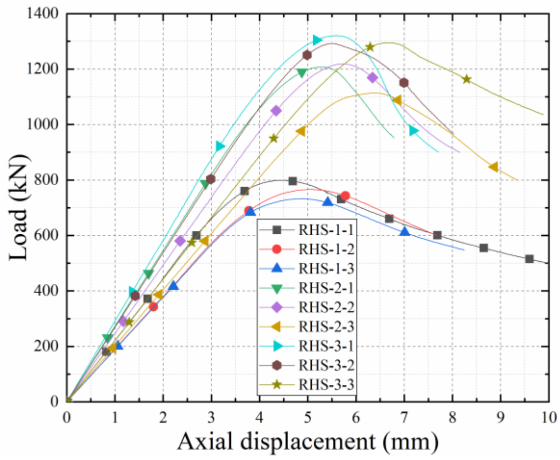

Fig. 4 Comparison of axial displacement-load curves

A displacement meter was installed in the middle of the component to record the variation of the lateral displacement at the measuring point in the middle of the component with the load during the axial compression process. The curves of lateral displacement-load of three series components were shown in Fig.5. It could be found that for the series of RHS-1 components, a relatively obvious lateral displacement occurred on surface B at around 300 kN, and local buckling occurred. The local buckling on surface B occurred earlier than that on surface C. For the series of RHS-2 components, a relatively obvious lateral displacement occurred on surface C at around 900 kN, indicating local buckling. The local buckling on surface C happened earlier than that on surface B. For the series of RHS-3 components, a relatively obvious lateral displacement occurred on surface C at around 1150 kN, meaning local buckling occurred. The local buckling on surface C occurred earlier than that on surface B. This thus proved that the installation of V-shaped stiffeners improved the local stability performance of the long sides of the spliced tubular columns, causing the location of local buckling to shift from the long sides to the short sides. The optimization of the flange length further enhanced the local stability performance of the short sides of the built-up members.

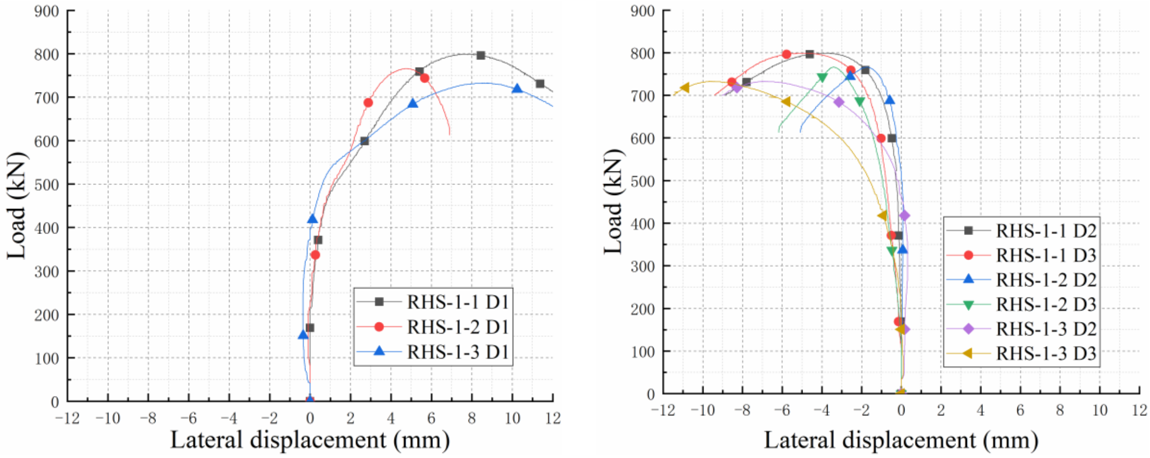

(a) Surface B of RHS-1 series components (b) Surface C of RHS-1 series components

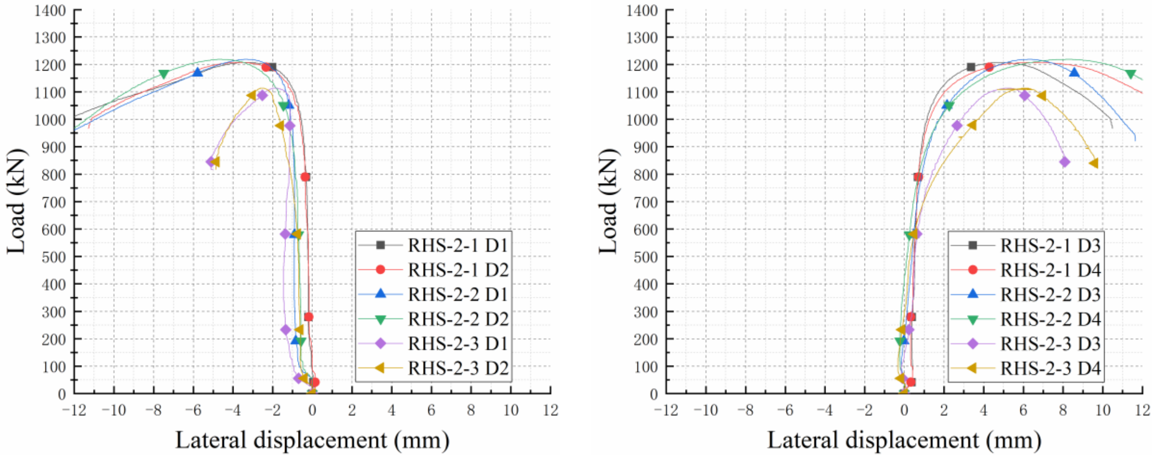

(c) Surface B of RHS-2 series components (d) Surface C of RHS-2 series components

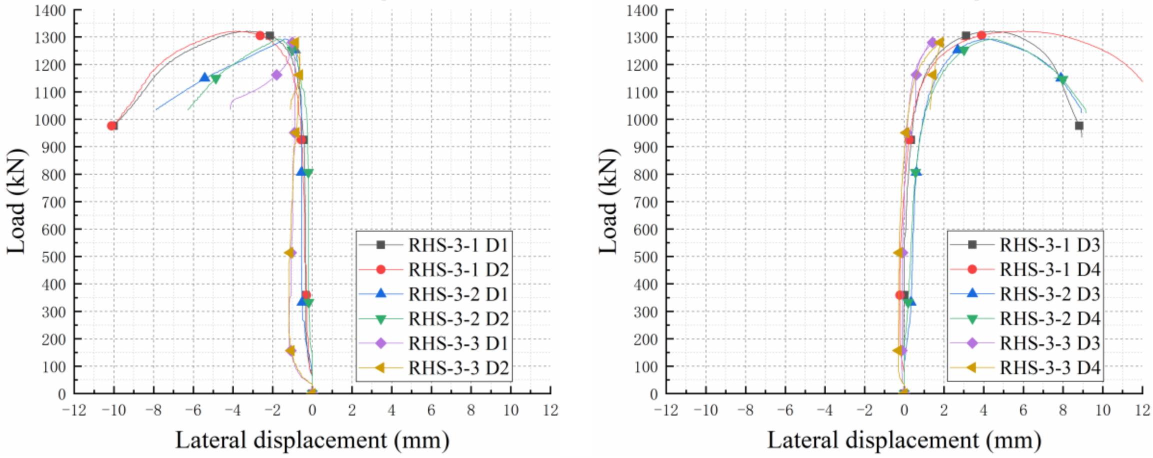

(e) Surface B of RHS-3 series components (f) Surface C of RHS-3 series components

Fig. 5 Load-lateral displacement curve of different series of components

Table 2
Mechanical properties of axial compression specimens

Specimens	Section form	Section area (mm^2)	Ultimate capacity (kN)	Extreme displacement（mm）	Ultimate strength (MPa)	$\frac{N_u}{A\sigma_{0.2}}$	Failure mode
RHS-1-1	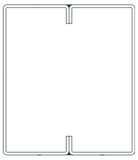	1955.98	799	4.34	408.49	0.68	Local buckling; A half-wave on the long side; A half-wave on the short side
RHS-1-2			765	4.98	391.11	0.65	
RHS-1-3			734	4.84	374.26	0.62	
	Average value		766	4.72	391.62	0.65	

RHS-2-1	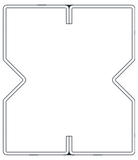	2057.67	1207	5.22	586.59	0.97	Local buckling; Two half-waves on the long side; A half-wave on the short side
RHS-2-2			1219	5.72	592.42	0.98	
RHS-2-3			1113	6.28	540.90	0.90	
	Average value		1180	5.74	573.30	0.95	
RHS-3-1	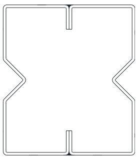	2129.65	1321	5.55	620.29	1.03	Local buckling; Two half-waves on the long side; Two half-waves on the short side
RHS-3-2			1292	5.48	606.67	1.00	
RHS-3-3			1295	6.62	608.08	1.01	
	Average value		1303	5.88	611.68	1.01	

2.3.3. Results of the test

Analyzed the axial displacement-load curve, the mechanical properties such as the initial elastic modulus and ultimate capacity of the components were obtained, as shown in Table 2.

For the RHS-1 series components, the capacity was about 766 kN. The capacity of the RHS-2 series components reached 1180 kN. The capacity of the RHS-3 series components was about 1303 kN. The bearing performance of the RHS-2 series components was improved by about 46.15% compared with the RHS-1 series components, and the capacity of the RHS-3 series components was improved by about 55.38% compared with the RHS-1 series components. The method of setting V-shaped stiffeners at the web of the stainless-steel lipped channel and extending the length of the lipped part could effectively improve the bearing performance.

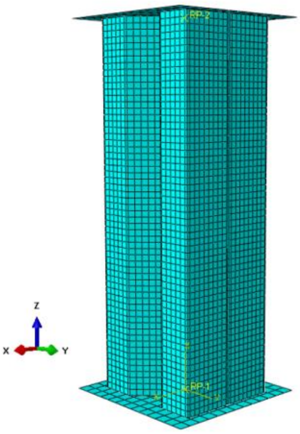

Fig. 6 Model grid division diagram

3. Finite element modeling and validation

3.1. Establishment of the FEM

For the short column, the mesh size was selected as 10mm×10mm, while for the median-long column, since its model was simple and regular, its mesh size was also selected as 10mm×10mm. For the welded end plates, the mesh size was selected as 20mm×20mm. The mesh division schematic diagram of short columns was shown in Fig.6. For the contact area at the lipped joint, the normal behavior adopted the surface-to-surface hard contact. The tangential behavior adopted the isotropic friction analysis, in which the anti-slip coefficient was taken as 0.25. As for the welding at the splicing of the components, the binding (Tie) was used to constrain all degrees of freedom. Boundary conditions and loading diagram was shown in Fig.7.

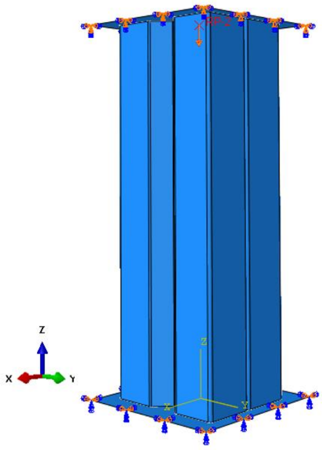

Fig. 7 Boundary conditions and loading diagram

3.2. Verification of the FEM

The final failure modes of the three series of RHS-1, RHS-2 and RHS-3 short columns were all local buckling. The finite element simulation results were in good agreement with the test results, and the comparison results were shown in Fig.8.

The load-axial displacement curves of the three series of short columns were shown in Fig.9. The load-displacement curves of the short columns obtained by FEM were in good agreement with the test results.

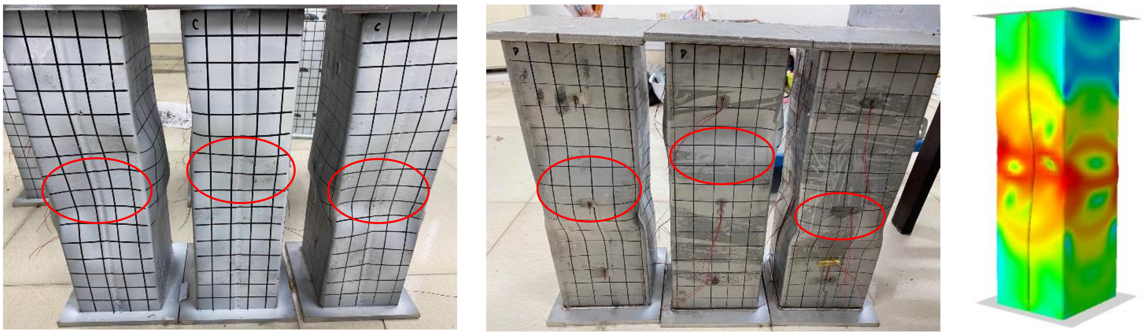

(a) RHS-1 series

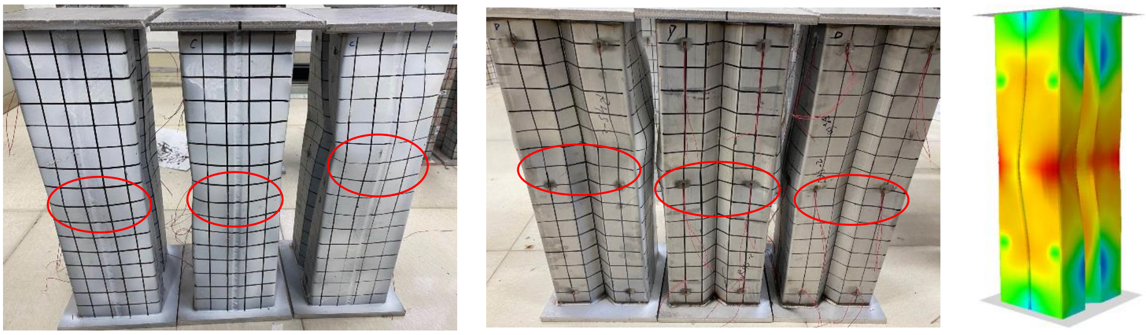

(b) RHS-2 series

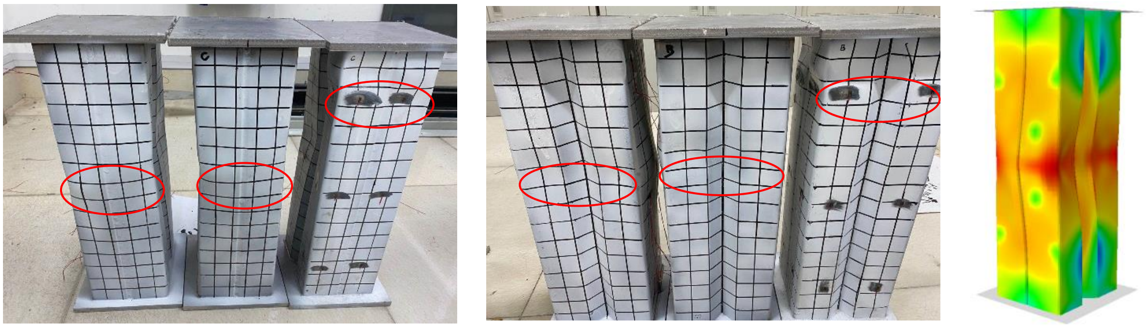

(c) RHS-3 series

Fig. 8 Comparison of failure modes of axial compression short columns

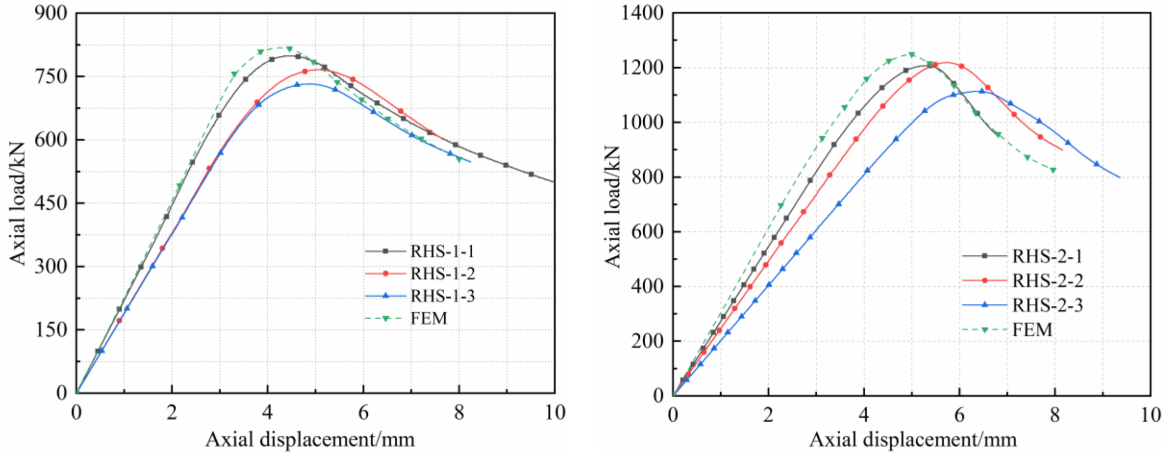

(a) RHS-1 series

(b) RHS-2 series

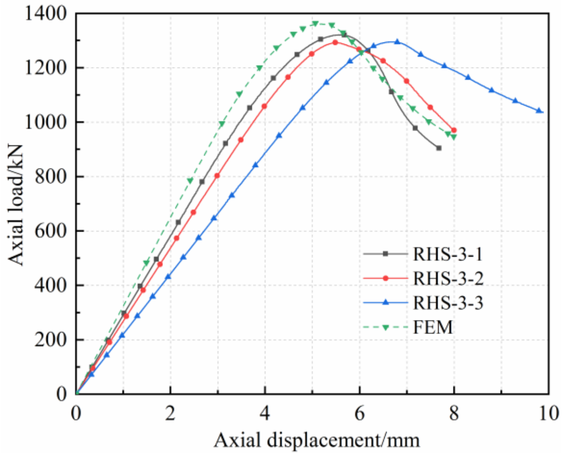

(c) RHS-3 series

Fig. 9 Comparison of axial displacement-load curves

4. Numerical analysis of structural performance and compression-bending capacity calculation

4.1. Analysis of the influence of main parameters of short columns

4.1.1. The influence of the size of V-shaped stiffeners

Ensuring the parameters such as the length of the component being 480mm, the section thickness being 3mm, and the lipped width being 26mm remained unchanged, the depths of the V-shaped stiffeners were 20mm, 23mm, 26mm, 29mm, 32mm, and 35mm respectively, and the angles were 30°, 45°, 60°, 75°, 90°, 105°, and 120° respectively, with a total of 42 components. The ultimate axial compression capacity of all components was obtained through ABAQUS, and the relationship curves between the depth and angle of the V-shaped stiffeners and the ultimate axial compression capacity were plotted, as shown in Fig.10.

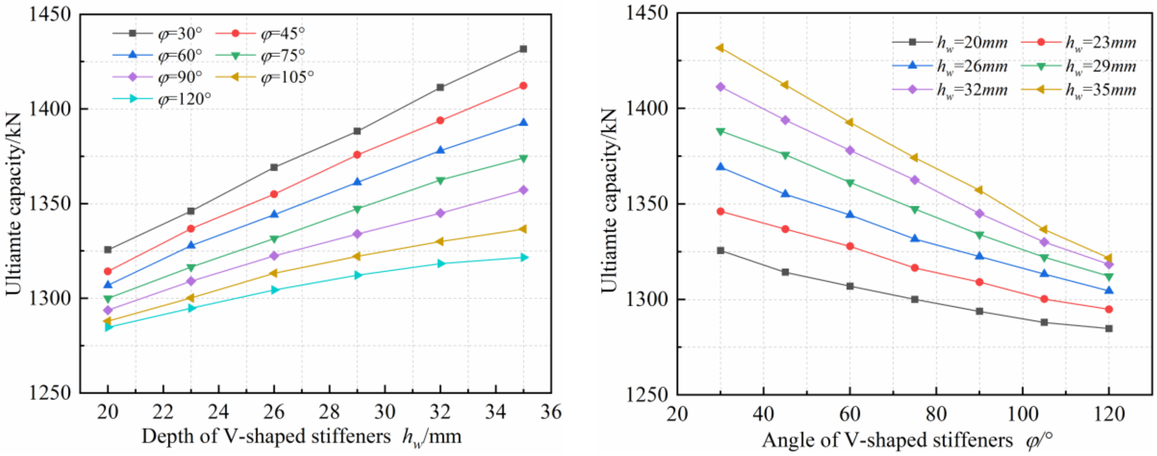

(a) Relationship curve between ultimate capacity and depth of V-shaped stiffeners

(b) Relationship curve between ultimate capacity and angle of V-shaped stiffeners

Fig. 10 Influence of V-shaped stiffeners on ultimate capacity of axial compression columns

It could be seen from Fig.10, the axial compression ultimate bearing capacity of the spliced tubular columns increased linearly with the increase of the depth of the V-shaped stiffeners. When the depth of the V-shaped stiffeners increased from 20 mm to 35 mm, the axial compression ultimate bearing capacity was enhanced by approximately 2.79%-7.41%. On the other hand, the axial compression ultimate bearing capacity decreased linearly with the increase of the angle of the V-shaped stiffeners. Moreover, the smaller the depth of the V-shaped stiffeners was, the gentler the decreasing trend was. For different depths of the V-shaped stiffeners, when the angle of the V-shaped stiffeners increased from 30° to 120°, the axial compression ultimate bearing capacity was reduced by approximately 3.08%-7.79%.

The capacity performance index $N_u/A\sigma_{0.2}$ of the short column was calculated, and the scatter diagram between it and the width-thickness ratio of the V-shaped stiffeners was plotted to further analyze the influence of the V-shaped stiffeners on the axial compression performance of short columns, as shown in Fig.11.

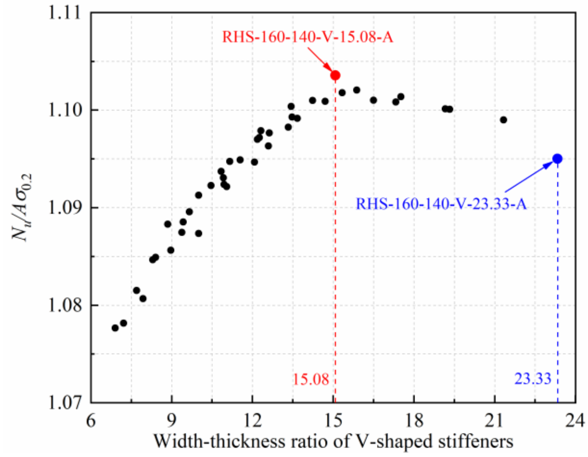

Fig. 11 The scatter diagram of the capacity performance index and the width-thickness ratio

When the width-thickness ratio of the V-shaped stiffeners plate was less than 15.08, the capacity performance index $N_u/A\sigma_{0.2}$ increased with the increase of the width-thickness ratio, and the growth trend gradually slowed down. When the width-thickness ratio was greater than 15.08, the capacity performance index $N_u/A\sigma_{0.2}$ fluctuated slightly with the increase of the width-thickness ratio. When the width-thickness ratio was greater than 19.33, the capacity performance index $N_u/A\sigma_{0.2}$ decreased significantly. The reason was that the width-thickness ratio of the V-shaped stiffener plates was relatively large and exceeded the width-thickness ratios of the web sub-plates and the flange plates. This caused the V-shaped stiffeners to experience local buckling prior to the web and the flange, further leading to a significant reduction in the capacity performance index $N_u/A\sigma_{0.2}$ of the load-bearing capacity. When designing the V-shaped stiffeners, it was recommended that the width-thickness ratio be controlled between 14 and 18, and should not exceed 19.33.

When the width-thickness ratio was 15.08, the capacity performance index $N_u/A\sigma_{0.2}$ reached the maximum, that is, the utilization efficiency of the section and the material reached the highest. Therefore, the width-thickness ratio of all components in the subsequent parameter analysis was controlled to be 15.08, that is, the depth of the V-shaped stiffeners was 32mm and the angle was 90°.

4.1.2. The influence of the height-thickness ratio

According to the regulations on the lipped width in CECS 410: 2015 [29], the optimized setting range of the lipped width was 20-36mm, with a total of 9 components. The ultimate axial compression capacity was obtained through ABAQUS, and the relationship curve between the lipped width and the ultimate axial compression capacity was plotted, as shown in Fig.12.

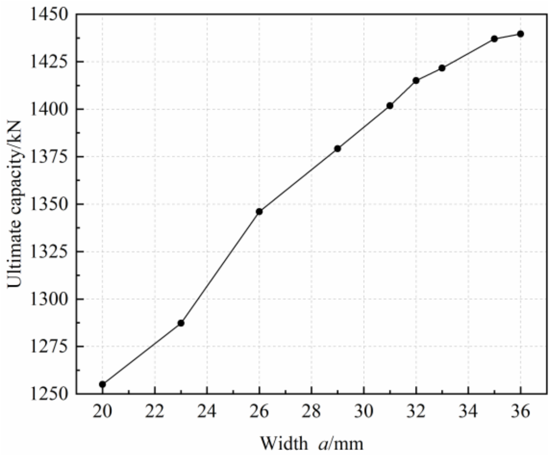

Fig. 12 Effect of lipped width on ultimate capacity of axial compression columns

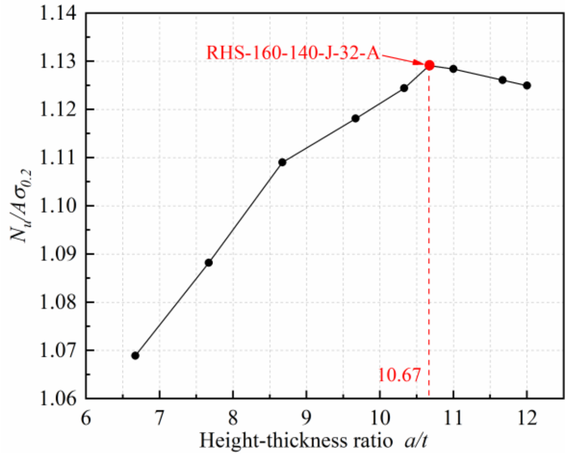

Fig. 13 Point-line diagram of the capacity performance index and height-thickness ratio

The ultimate axial compression capacity increased with the increase of the lipped width, and as the lipped width increased, the growth trend gradually flattened. When the lipped width increased from 20mm to 23mm, 26mm, 29mm, 31mm, 32mm, 33mm, 35mm, and 36mm respectively, the ultimate axial compression capacity of short columns increased by 2.57%, 7.25%, 9.89%, 11.69%, 12.76%, 13.28%, 14.51%, and 14.71% respectively. The capacity performance index $N_u/A\sigma_{0.2}$ was calculated, and the dot-line graph between it and the height-thickness ratio was plotted to further analyze the influence of the lipped part on the axial compression performance, as shown in Fig.13.

When the lipped width was less than 32mm, that is, height-thickness ratio was less than 10.67, the capacity performance index $N_u/A\sigma_{0.2}$ increased with the increase of the height-thickness ratio. When the lipped width was greater than 32mm, that is, the height-thickness ratio was greater than 10.67, as the height-thickness ratio continued to increase, the capacity performance index $N_u/A\sigma_{0.2}$ gradually decreased. When the lipped width was 32mm, that is, the height-thickness ratio was 10.67, the capacity performance index $N_u/A\sigma_{0.2}$ reached the maximum, that is, the utilization efficiency of the section and the material reached the highest.

4.1.3. The influence of the width-thickness ratio

In this section, finite element modeling and calculation were carried out respectively for two short columns of the same height-width ratio but different sizes. The section forms were shown in Fig.14. According to the actual engineering application, the selection range of the section thickness was 1.0mm to 4.0mm, and the corresponding range of the maximum width-thickness ratio (flange width-thickness ratio) was 10.0 to 87.5, with a total of 60 columns.

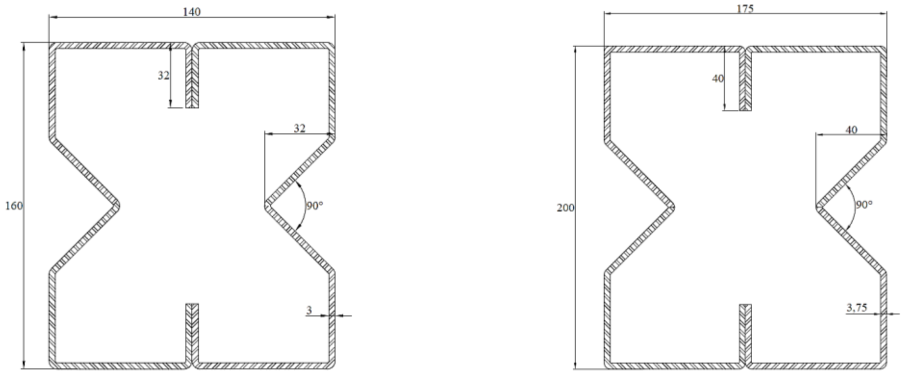

（a）RHS-160-140-A　　（b）RHS-200-175-A

Fig. 14 Section schematics for plate width-thickness ratio parameter analysis

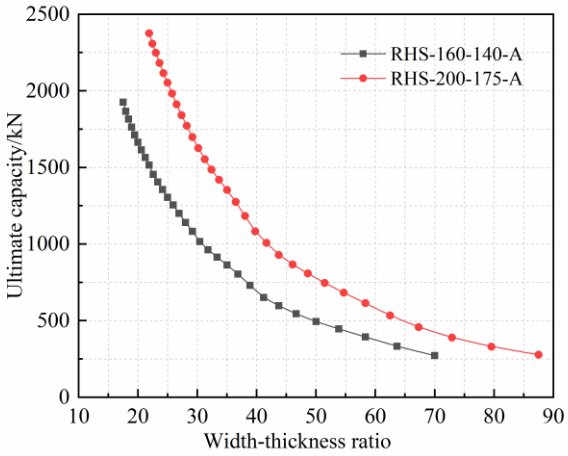

Fig. 15 Relationship curve between ultimate capacity and width-thickness ratio of plates

The ultimate axial compression capacity was obtained through ABAQUS, and the relationship curve between the maximum width-thickness ratio of the plate (flange width-thickness ratio) of the cold-formed thin-walled rectangular tubular column and the ultimate axial compression capacity was plotted, as shown in Fig.15.

When the width-thickness ratio increased, the ultimate axial compression capacity of all short columns gradually decreased, and the decreasing trend gradually flattened with the increase of the width-thickness ratio. When the maximum width-thickness ratio increased from 17.5 to 70, the ultimate axial compression capacity of the RHS-160-140-A series short columns decreased by about 85.9%. When the maximum width-thickness ratio increased from 21.9 to 87.5, the ultimate axial compression capacity of the RHS-200-175-A series short columns decreased by about 88.3%. The scatter diagram N_u/Af_y with the width-thickness ratio according to the most unfavorable plate in the section was drawn, as shown in Fig.16.

For the critical width-thickness ratio limits of stiffened and unstiffened plates, the stipulated values in the Chinese code CECS 410: 2015 were rather conservative and had large differences. In order to make full use of the characteristics of the stainless-steel material and achieve a more economical and reasonable design purpose, take the value of 1 on the ordinate of the fitting curve as the width-to-thickness ratio limit of the compression plate element, and round it to an integer. It was recommended that the critical width-thickness ratio of the stiffened plates be 34, and that of the unstiffened plates be 15.

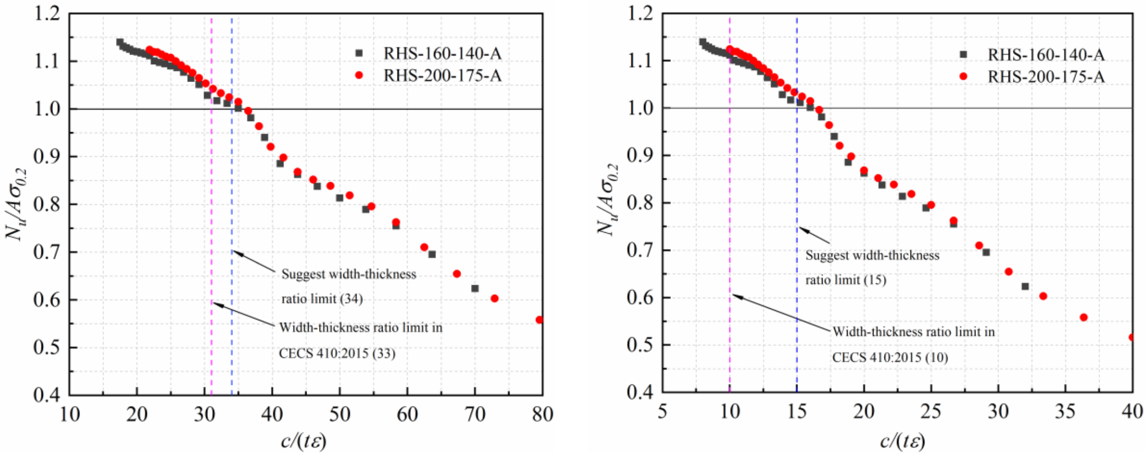

(a) Ribbed components　　(b) Non-ribbed components

Fig. 16 Recommended critical width-thickness ratio of compressed plates

4.1.4. The influence of the slenderness ratio

At present, the Chinese code stipulated that the allowable slenderness ratio of the axial compression component was 150. Therefore, the length was selected to vary from 480mm to 7200mm, and the variation range of the slenderness ratio was 9.82-147.56, with a total of 33 components. The ultimate axial compression capacity of all components was calculated. The relationship curves between the slenderness ratio and the ultimate axial compression capacity, the relationship curves between the slenderness ratio and the capacity performance index $N_u/A\sigma_{0.2}$ were plotted, as shown in Fig.17 and Fig.18.

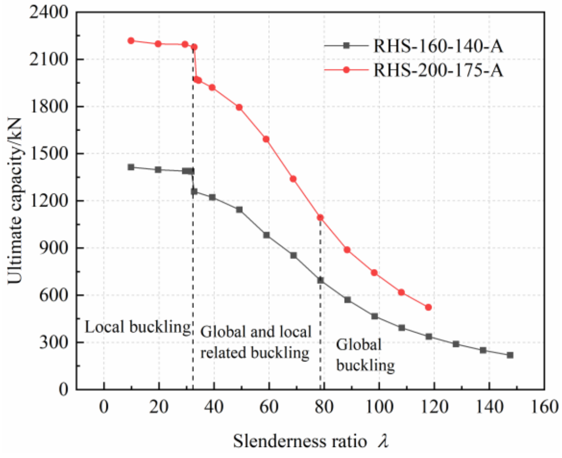

Fig. 17 Relationship curve between ultimate capacity and slenderness ratio

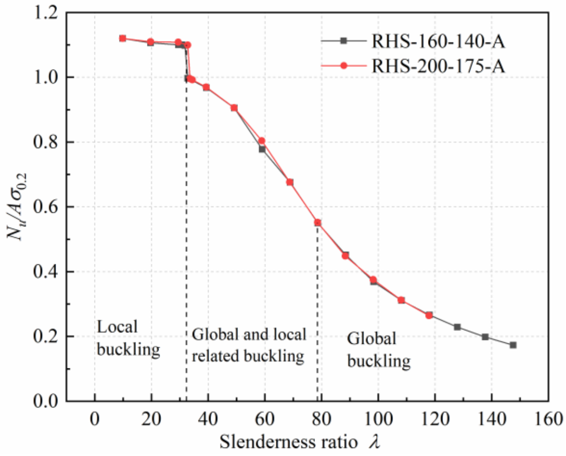

Fig. 18 Relationship curve between the capacity performance index and slenderness ratio

When the slenderness ratio $\lambda \leq 32.74$, the ultimate axial compression capacities were similar, indicating that within this slenderness ratio range, the slenderness ratio had a small influence on the ultimate axial compression capacity, the failure mode was still local buckling. When the slenderness ratio increased from 32.791 to 147.56, the ultimate axial compression capacity of the RHS-160-140-A series components decreased from 1258.31 kN to 218.348 kN, with a reduction of 80.26%. When the slenderness ratio increased from 33.55 to 117.85, the ultimate axial compression capacity of the RHS-200-175-A series components decreased from 1971.34 kN to 522.495 kN, with a reduction of 73.49%. The relationship curves of the ultimate axial compression capacity of different series of components all had inflection points. The slenderness ratio had a significant influence on the ultimate axial compression capacity of the short columns, the failure mode was the overall instability. When the slenderness ratio $\lambda \leq 32.74$, because the failure mode was local buckling, the capacity performance index $N_u/A\sigma_{0.2}$ was close. When the slenderness ratio $\lambda > 33.55$, because the failure mode was overall buckling, the capacity performance index $N_u/A\sigma_{0.2}$ gradually decreased as the slenderness ratio increased, and as the slenderness ratio increased, the decreasing trend gradually flattened.

4.2. Analysis of the influence of main parameters of compression-bending short columns and median long columns

4.2.1. The influence of the relative eccentricity of the load

In practical engineering applications, the compression-bending members were mostly in the state of eccentric compression around the strong axis. Therefore, in this section, only the finite element parametric analysis of spliced tubular columns under eccentric compression around the strong axis would be carried out. And the analysis will be conducted with two commonly used member lengths (900 mm and 3000 mm) in practical engineering. Ensuring that the section thickness was 3mm, the width-thickness ratio of the V-shaped stiffeners plate was 15.08, and the height-thickness ratio was 10.67 remained unchanged, only by changing the eccentricity of the load, the influence of the relative eccentricity of the load on the compression-bending performance of the cold-formed thin-walled rectangular high-strength stainless-steel spliced tubular columns was studied. The load eccentricities were respectively set to 8mm, 16mm, 32mm, 64mm, 96mm, 128mm, and 160mm, and the corresponding relative eccentricities of the load were respectively 0.1, 0.2, 0.4, 0.8, 1.2, 1.6, and 2.0. And two commonly used component lengths (900mm, 3000mm) in actual engineering were selected, with a total of 14 components. The ultimate compression-bending stability capacity under different relative eccentricities of the load was obtained, and the relationship curve was plotted, as shown in Fig.19.

When the slenderness ratio $\lambda_x = 14.81$ and $\lambda_x = 48.79$, as the relative eccentricity of the load increased, the ultimate compression-bending capacity gradually decreased, and as the relative eccentricity of the load increased, the decreasing trend of the ultimate capacity gradually flattened. When the relative eccentricity of the load increased from 0.1 to 2.0, the ultimate compression-bending capacity eccentrically compressed around the strong axis decreased by 72.14% and 69.01% respectively, indicating that the relative eccentricity of the load had a significant influence on the ultimate capacity of the compression-bending column.

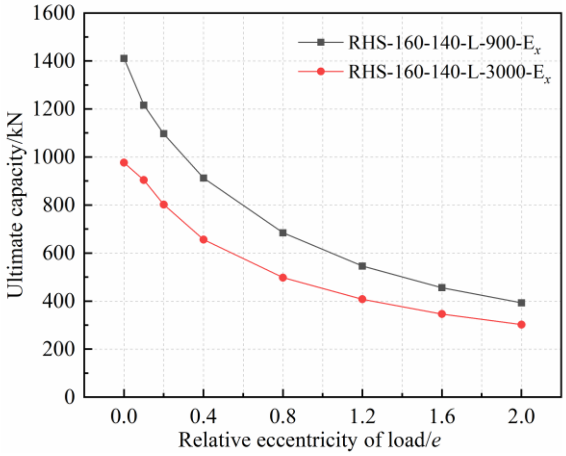

Fig. 19 Relationship curve between relative eccentricity of load and ultimate capacity

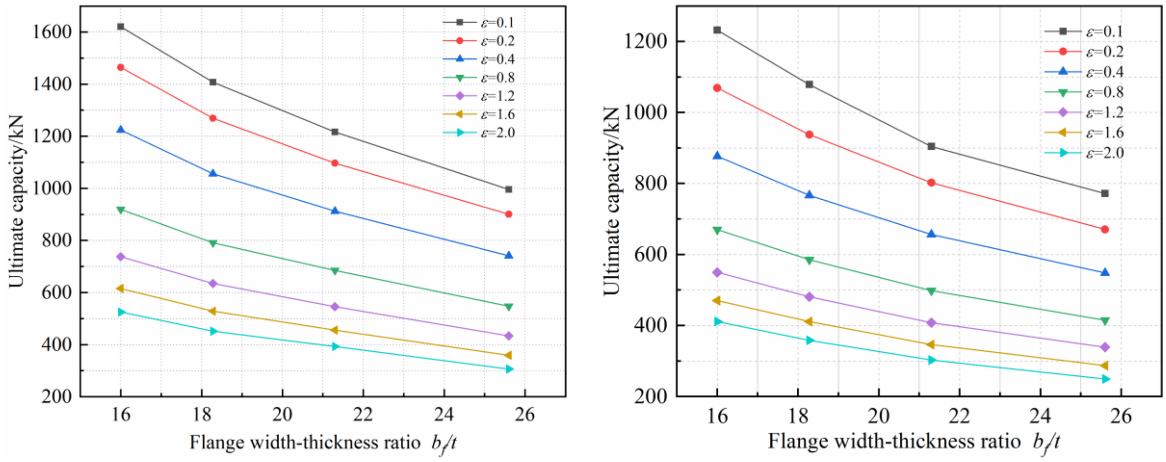

(a) 900mm eccentric compression component around the strong axis (a) 3000mm eccentric compression component around the strong axis

Fig. 20 Relationship curve between width-thickness ratio and ultimate compression-bending capacity

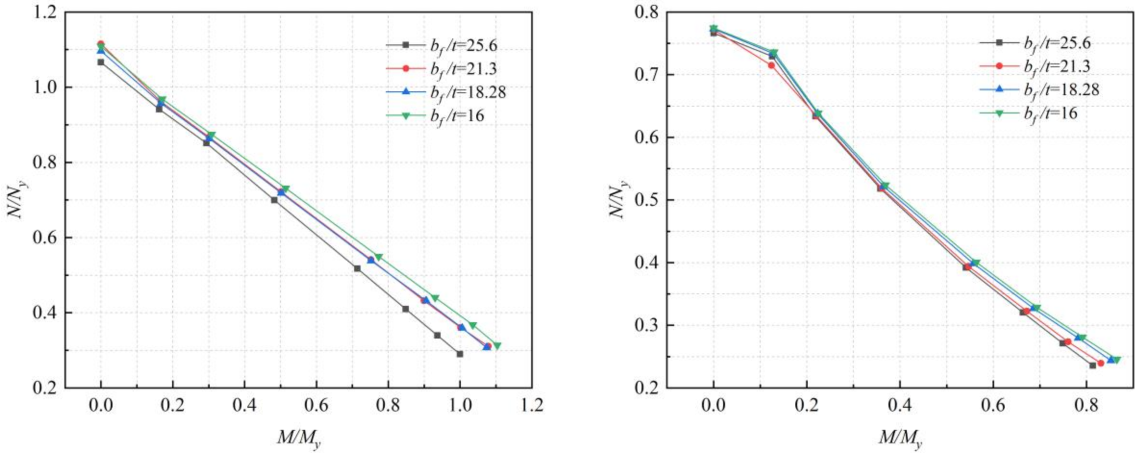

(a) RHS-160-140-L-900-Ex series (b) RHS-160-140-L-3000-Ex series

Fig. 21 Stable capacity N-M correlation curve of spliced components

4.2.2. The influence of the width-thickness ratio

The section thicknesses were 2.5mm, 3mm, 3.5mm, and 4.0mm, that is, the maximum width-thickness ratio of the plate (flange width-thickness ratio) was 25.6, 21.3, 18.28, and 16. The analysis was carried out with two commonly used component lengths (900mm, 3000mm), with a total of 56 components. The ultimate compression-bending stability capacity of the cold-formed thin-walled components with different section thicknesses was obtained, as shown in Fig.20. Considering that the section thickness had a direct influence on the cross-sectional area, in order to eliminate the influence of the cross-sectional area, the finite element calculation results were sorted and plotted into the axial force-bending moment correlation curve, as shown in Fig.21. As the bending moment M increased, the spacing of the N-M curve under the same abscissa gradually increased, indicating that as the relative eccentricity of the load increased, the influence of the width-thickness ratio on the ultimate compression-bending stability capacity gradually strengthened. In other words, as the width-thickness ratio of the flange increased, the downward trend of the N-M curve gradually became gentler, also represented the influence of the width-thickness ratio on the ultimate compression-bending stability capacity gradually strengthened.

4.2.3. The influence of slenderness ratio

Ensuring that the section thickness was 3mm, the width-thickness ratio of the V-shaped stiffeners plate was 15.08, and the height-thickness ratio was 10.67 remained unchanged, only by changing the component length, the influence of the slenderness ratio on the compression-bending performance of the cold-formed thin-walled high-strength stainless-steel spliced was studied. The component length varied from 900mm to 6000mm, and the corresponding variation range of the slenderness ratio was 14.81 to 98.73, with a total of 35 components. The compression-bending stability capacity with different slenderness ratios was obtained, and the relationship curve between the slenderness ratio and the compression-bending stability capacity was plotted, as shown in Fig.22.

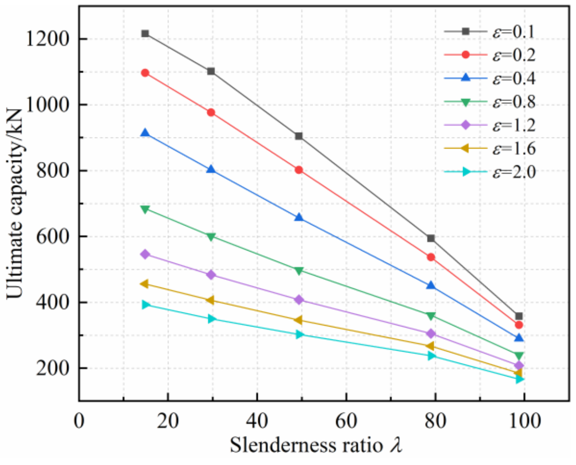

Fig. 22 Relationship curve between ultimate capacity and slenderness ratio

With the slenderness ratio increased, the compression-bending stability capacity decreased significantly, and as the relative eccentricity of the load increased, the decreasing trend flattened. Longitudinally comparing the compression-bending stability capacities of components with different relative eccentricities of the load, it could be found that as the slenderness ratio increased, the influence of the relative eccentricity of the load on the compression-bending stability capacity gradually decreased. The reason was that as the slenderness ratio increased, the overall stiffness significantly attenuated, and the final failure mode was mainly overall buckling.

4.3. Recommendation of compression-bending capacity calculation formula

According to the calculation formulas for the compression-bending bearing capacity in the Chinese code CECS 410:2015 [29] and the American code AISI S100-16 [30], the ultimate compression-bending stability bearing capacity of the spliced tubular columns was calculated respectively, as shown in Fig.23. Then, a comparative analysis was carried out between the calculation results of the codes and those of the finite element simulation. The average value of the ratio N_{FEA}/N_u between the finite element simulation result N_{FEA} and the calculation result N_u of the Chinese code was 1.127, with a standard deviation of 0.151 and a coefficient of variation of 0.134. The average value of the ratio N_{FEA}/N_d between the finite element simulation result N_{FEA} and the calculation result N_d of the American code was 1.133, with a standard deviation of 0.115 and a coefficient of variation of 0.102. Overall, the calculation results of the American code, which adopted the load and restraint factor design method, were more accurate than those of the Chinese code, which adopted the effective width method. However, compared with the finite element simulation results, the calculation results of both the Chinese and American codes had relatively large differences, a high degree of dispersion, and the calculation results of some spliced tubular columns tended to be unsafe.

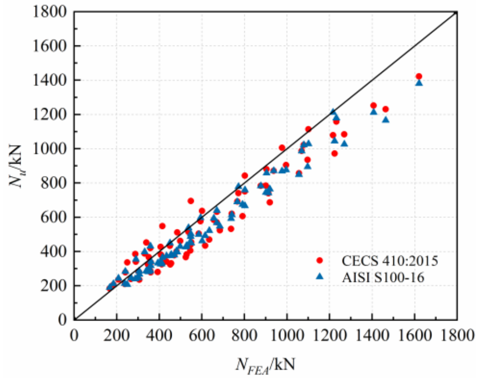

Fig. 23 Scatter diagram of compression-bending capacity of spliced tubular columns calculated by Chinese and American codes

Made appropriate modifications to the calculation formula for the ultimate bending-compression stability bearing capacity proposed in the Chinese code, so that it could be applicable to the new high-strength stainless-steel spliced tubular compression-bending columns proposed in this paper. The Chinese code CECS410: 2015 stipulated that for the strength of compression-bending components, it could be calculated according to the Eq.(1):

$$\sigma = \frac{N}{A_{en}} \pm \frac{M_x}{W_{enx}} \pm \frac{M_y}{W_{eny}} \le f \tag{1}$$

Where： N -Axis compressive pressure;

A_{en} -Effective cross-section area of the component;

M_x, M_y -The bending moment around the main axes x-axis and y-axis;

W_{enx}, W_{eny} -The effective net section modulus for the main axes x-axis and y-axis.

When calculating the stability of compression-bending components, when within the plane of the bending moment action, it can be calculated according to the Eq.(2) and Eq.(3):

$$\frac{N}{\varphi_x A_e}+\frac{\beta_m M}{\left(1-\varphi_x \frac{N}{N_E'}\right)W_e}\le f \tag{2}$$

$$N_E'=\frac{\pi^2 E_0 A}{1.165\lambda^2} \tag{3}$$

Where, β_m -Equivalent bending moment coefficient, $\beta_m = 1.0$;

M -Calculating the bending moment;

N_E' -Euler critical load;

W_e -The effective section modulus of the maximum compression edge in the bending plane.

When the bending moment is outside the plane of action, the stability of the compression-bending component can be calculated according to the Eq.(4):

$$\frac{N}{\varphi_y A_e}+\frac{\eta M}{\varphi_{bx} W_{ex}}\le f \tag{4}$$

Where, φ_y -Overall stability coefficient of the bending component out of bending moment;

η -Cross section influence coefficient, for the rectangular section column, $\eta = 0.7$;

φ_{bx} -Overall stability coefficient of the bending component, for the rectangular section, because of its large torsional stiffness, $\varphi_{bx} = 1.0$.

Referring to the form of the calculation formula of the in-plane compression-bending capacity of ordinary steel, the calculation formula of the compression-bending capacity in the Chinese code was modified. According to the finite element simulation results, the least square method was used for multiple linear regression fitting, and the modified formula was obtained as Eq. (5) and Eq. (6):

$$\frac{N}{\varphi_x A_e}+\frac{\beta_m M}{\gamma\left(1-\varphi_x \frac{N}{N_E'}\right)W_e}\le f \tag{5}$$

$$\gamma = 1.245 + 1.97\times 10^{-4}\varepsilon^{13.7} \tag{6}$$

As for the calculation formula of the compression-bending capacity outside the plane of the bending moment action, since the rectangular tubular column proposed was not a completely rectangular section, and according to the finite element simulation results, the section influence coefficient was adjusted and taken as $\eta = 0.85$. According to the modified calculation formula of the compression-bending capacity in the Chinese code, the calculation of the cold-formed thin-walled rectangular compression-bending column was carried out. The results were compared with the finite element simulation results, as shown in Fig.24, where N_u' was the calculated result after the modification of the Chinese code.

It could be concluded that the average value of the ratio N_{FEA}/N_u' was 1.034, the standard deviation was 0.022, the coefficient of variation was 0.021, and the maximum difference was only 8.5%. This indicated that the calculated results of the modified compression-bending capacity were very close to the finite element simulation results and were feasible for calculating the ultimate compression-bending stability capacity of the cold-formed thin-walled rectangular tubular column.

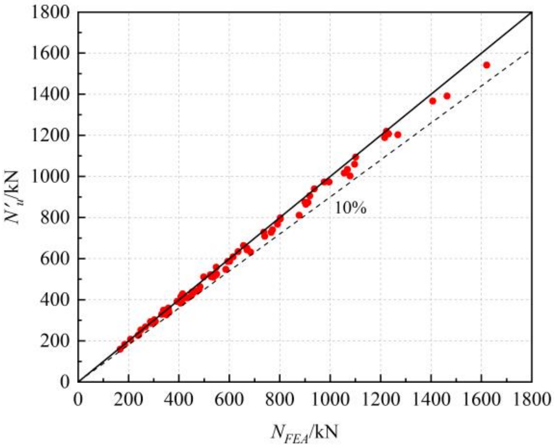

Fig. 24 Compression-bending capacity calculated by the Chinese code after revision

5. Conclusions

This paper designed a cold-formed thin-walled rectangular high-strength stainless-steel spliced tubular columns to meet the requirements of the marine steel structure. Experiment of axial compression short columns, finite element analysis of axial compression short columns, compression-bending short columns and median long columns was carried out. The main conclusions were as follows:

(1) Two stainless-steel lipped channels spliced into rectangle columns effectively enhanced the stable capacity of short columns. Compared with the RHS-1 series short columns, the capacity of the RHS-2 series increased by 46.15%, the capacity of the RHS-3 series increased by 55.38%. The V-shaped stiffeners and the straight ribs played a full stiffening role in the axial compression test, improving the final buckling mode of the short columns and reflecting the efficiency of the spliced section.

(2) The main failure mode of the axial compression short columns was the local buckling failure. The V-shaped stiffeners changed the position where local buckling occurred from the long side to the short side, and the two sub-plates on the long side buckled respectively. Optimizing the length of the straight ribs formed by the lipped edge changed the buckling half-wave of the short side from one buckling half-wave to two buckling half-waves.

(3) For rectangular spliced axial compression short columns, the V-shaped stiffeners and the slenderness ratio had a great influence on failure modes. When the depth of the V-shaped stiffener was 32 mm and the angle was 90°, the section performance was optimal. When the slenderness ratio was in the range of 33.55-147.56, the overall buckling failure occurred.

(4) For rectangular spliced compression-bending short columns and median long columns, the eccentricity ratio and the slenderness ratio had a great influence on failure modes. When the eccentricity ratio increased from 0.1 to 2.0, the ultimate compression-bending capacity decreased by 72.14% and 69.01% respectively. When the slenderness ratio was in the range of 14.81-98.73, the compression-bending stability capacity decreased significantly with the increase of the slenderness ratio.

(5) A modified calculation formula for the ultimate capacity of compression-bending columns was proposed, it can be used to expand the application scope of Chinese code and American code, with high accuracy.

In the future, experimental research on median long spliced tubular columns is recommended. Moreover, only V-shaped stiffeners are installed in the middle of the web to improve the axial compression bearing capacity, more composite section forms can be explored to promote the application of stainless-steel in load-bearing members in offshore steel structures.

Reference

[1] M. Ahmed, R.I. Shahin, S.A. Yehia, M. Emara, V.I. Patel, Q.Q. Liang, Nonlinear analysis of square steel-reinforced concrete-filled steel tubular short columns considering local buckling, Struct. Concr. (2023) 69-84.

[2] Y.F. Yang, M. Liu, F. Fu, Experimental and numerical investigation on the performance of three-legged CFST latticed columns under lateral cyclic loadings, Thin-Walled Struct. 132 (2018) 176-194.

[3] M. Ahmed, S.A. Yehia, R.I. Shahin, M. Emara, V.I. Patel, Q.Q. Liang, Numerical simulation and design of circular steel-reinforced concrete-filled steel tubular short columns under axial loading, Mag. Concr. Res. (2023) 1-44.

[4] Q.X. Wu, Z.K. Xu, H.H. Yuan, Z.Q. Qin, Experimental study of axial compressive performance of UHPC-encased CFST composite stub columns, J. Build. Struct. 44 (12) (2023) 183-193.

[5] J. Cai, J. Pan, X. Li, Behavior of ECC-encased CFST columns under axial compression, Eng. Struct. 171 (2018) 1-9.

[6] M.F. Hassanein, V.I. Patel, M. Elchalakani, H.T. Thai, Finite element analysis of large diameter high strength octagonal CFST short columns, Thin-Walled Struct. 123 (2018) 467-482.

[7] P. Ayough, N.H.R. Sulong, Z. Ibrahim, Analysis and review of concrete-filled double skin steel tubes under compression, Thin-Walled Struct. 148 (2020) 106495.

[8] Z.W. Shao, X.X. Zha, C.Y. Wan, Design method of fire-resistance capacity of reinforced-concrete-filled steel tube column under axial compression, Fire Saf. J. 129 (2022) 103572.

[9] K.U. Ukanwa, G.C. Clifton, J.B. Lim, S.J. Hicks, U. Sharma, A. Abu, Simple design procedure for concrete filled steel tubular columns in fire, Eng. Struct. 155 (2018) 144-156.

[10] A.P.C. Duarte, B.A. Silva, N. Silvestre, J. de Brito, E. Julio, J.M. Castro, Tests and design of short steel tubes filled with rubberised concrete, Eng. Struct. 112 (2016) 274-286.

[11] Q.H. Tan, L. Gardner, L.H. Han, T.Y. Song, Fire performance of steel reinforced concrete-filled stainless steel tubular (CFSST) columns with square cross-sections, Thin-Walled Struct. 143 (2019) 106197.

[12] E. Ellobody, Nonlinear behavior of concrete-filled stainless steel stiffened slender tube columns, Thin-Walled Struct. 45(2007) 259-273.

[13] Z.M. Lai, A.H. Varma, Noncompact and slender circular CFT members: Experimental database, analysis, and design, J. Constr. Steel Res. 101 (2014) 455-468.

[14] F. Aslani, B. Uy, Z. Tao, Predicting the axial load capacity of high-strength concrete filled steel tubular columns, Steel Compos. Struct. 19 (2015) 967-993.

[15] W.F. Zhang, L. Gardner, M.A. Wadee, On the uniform torsional rigidity of square concrete-filled steel tubular (CFST) sections, Struct. 43 (2022) 249-2521.

[16] Z. Tao, B. Uy, Analysis and design of concrete-filled stiffened thin-walled steel tubular columns under axial compression, Thin-Walled Struct. 47 (2009) 1544-1556.

[17] J.G. Wei, X. Luo, Z.C. Lai, B.C. Chen, Experimental study on axial compressive behavior of circular UHPC filled high-strength steel tube short columns, J. Struct. Eng. 41 (2020) 16-28.

[18] S. Chen, R. Zhang, L.J. Jia, J.Y. Wang, P. Gu, Structural behavior of UHPC filled steel tube columns under axial loading, Thin-Walled Struct. 130 (2018) 550-563.

[19] Z. Xu, Study on the flexion capacity of reinforced cold-bent thin-walled C-shaped steel axial compression component , Huazhong University of Science and Technology, 2019. (in Chinese)

[20] D.A. Padilla-Llano, C.D. Moen, M.R. Eatherton, Cyclic axial response and energy dissipation of cold-formed steel framing components, Thin-Walled Struct. (2014) 95-107.

[21] Y. Lu, T. Zhou, W. Li, et al, Experimental investigation and a novel direct strength method for cold-formed built-up I-section columns, Thin-Walled Struct. 112 (2017) 125-139.

[22] H.X. Niu, A.H. Han, Y.J. Hou, Numerical analysis of cold-formed thin-walled C-shaped steel columns in different stiffening forms, Low temperature building technology, 44 (2022) 85-88. (in Chinese)

[23] B. Young, J. Chen, Design of cold-formed steel built-up closed sections with intermediate stiffeners, J. Struct. Eng. 134 (2008) 727-737.

[24] W. Reyes, A. Guzmán, Evaluation of the slenderness ratio in built-up cold-formed box sections, J. Constr. Steel Res. 67 (2011) 929-935.

[25] I. Georgieva, L. Schueremans, L. Vandewalle, et al. Numerical study of built-up double-Z components in bending and compression, Thin-Walled Struct. 60 (2012) 85-97.

[26] J. Zhang, B. Young, Compression tests of cold-formed steel I-shaped open sections with edge and web stiffeners, Thin-Walled Struct. 52 (2012) 1-11.

[27] F. Liao, H. Wu, R. Wang, et al. Compression test and analysis of multi-limbs built-up cold-formed steel stub columns, J. Constr. Steel Res. 128 (2017) 405-415.

[28] H.X. Li, Experimental study on cold-formed thin-walled rectangular tubular stub columns of assembled stainless-steel under axial compression, Nanjing Tech University, 2020. (in Chinese)

[29] Technical specification for stainless-steel structures: CECS410: 2015, China Planning Press, Beijing, 2015 (in Chinese).

[30] AISI-S100-2016, North American cold-formed steel specification, American Iron and Steel Institute, 2016.

Advanced Steel Construction – Vol. 21 No. 3 (2025) 194–203
DOI:10.18057/IJASC.2025.21.3.2

STUDY ON SHEAR BEHAVIOR OF T-SHAPED SHEAR CONNECTORS IN PREFABRICATED CONCRETE COMPOSITE FLOOR SLAB

Zeng-Mei Qiu *, Wen-Zhuang Pei, Guo-Chang Li and Zhi-Jian Yang

School of Civil Engineering, Shenyang Jianzhu University, Shenyang 110168, China
** (Corresponding author: E-mail: qzmfighting@126.com)*

ABSTRACT

This study proposed to apply T-shaped shear connectors to join prefabricated concrete slabs with H-beams and thereby ensure the overall working performance of building floor systems. The push-out tests on T-shaped connector specimens with different flange and web thicknesses were conducted aiming to investigate the shear behavior of this connector. Then the finite element software ABAQUS was used to establish test models, and the accuracy of the established models were verified according to the comparative experimental results to analyze the stress development process and key parameters influencing connector shear behavior. The results showed that the T-shaped connector with high initial stiffness and shear capacity, and its characteristic displacement complied with the lower limit value of permissible slip specified for the flexible shear connector in Eurocode 4, confirming its excellent ductility. The connector web thickness had the greatest effect on shear capacity, the second was the steel yield strength, whereas the connector width had the least influence. Finally, the recommended cross-sectional dimensions for the T-shaped connector were given, as well as the shear bearing capacity equation for this connector was derived, which could provide theoretical basis and design suggestions for its application in prefabricated concrete composite floor structure.

ARTICLE HISTORY

Received:	28 November 2024
Revised:	27 December 2024
Accepted:	1 January 2025

KEYWORDS

Prefabricated concrete composite floor slabs;
Push-out test;
T-shaped shear connector;
Shear behavior;
Finite element simulation

1. Introduction

The prefabricated steel structure–composite slab system offers advantages such as rapid constructability, controllable quality, and structural stability [1]. The prefabricated concrete floor slab of this system has been widely applied as it provides excellent integrity, suitable crack resistance, and high stiffness while realizing a large net interior space. As a result, prefabricated slabs have become one of the widely used floor forms in composite steel structures [2]. However, the bond between the prefabricated floor slab and steel beam is insufficient to bear the longitudinal shear force generated under large load. Therefore, shear connectors must be set between them to ensure the integrated working performance of composite system [3].

The primary function of a shear connector is to resist the longitudinal shear and horizontal uplifting force between the prefabricated floor slab and supporting section steel [4]. Studs are the traditional form of shear connector and are widely used in practical engineering applications [5-6]. However, with the rapid development of composite structures, scholars from all over the world have successively proposed different forms of shear connectors and applied them to various building structures, including perforated Perfobond Leisten (PBL) shear connector as well as truss shear connector, channel steel, and angle steel. Notably, the angle steel connector can be provided in more configurations, realizes more convenient construction, uses less material, exhibits superior shear behavior compared to the channel steel connector, and the mechanical performances of its connection can be guaranteed by fixing the steel plate on to the flange of steel beam using a fillet weld applied by conventional welding equipment; as a result, the angle steel connector is widely applied in structures with high shear capacity requirements [7].

At present, numerous researchers have studied various aspects of angle shear connectors. For example, Viest et al. [8] firstly performed the push-out and bending tests of channel steel connectors in the 1950s, providing a valuable reference for the subsequent research of assorted section steel connectors. Based on the results of monotonic push-out and cyclic loading tests, Shariat et al. [9] observed that the shear capacity of angle steel were lower than that of channel steel, but the shorter angle connectors and longer channel connectors exhibited superior ductility. Furthermore, Haroon et al. [10]、Arévalo et al. [11] and Hajime et al. [12] respectively analyzed the section size, arrangement angle steel connectors and arrangement spacing of angle connectors, and put forward some corresponding design suggestions. Zhou et al. [13] conducted push-out tests of angle steel and determined that the equation provided by American Code for calculating the bearing capacity was too conservative; they proposed an empirical equation for shear bearing capacity that is suitable for concrete strengths greater than 20 MPa and connector thicknesses greater than 6 mm. Notably, Cui et al. [14] conducted beam tests indicating that angle steel connectors can replace slab reinforcement; concrete slabs welded with angle connectors exhibited excellent overall performance with higher stiffness and lower cost than traditional prefabricated slabs. Tang et al. [15] experimentally and theoretically determined that the connection position of the upper flange of steel beam and angle steel connector in a tunnel structure was prone to concrete void formation，and this phenomenon will seriously affect the shear stiffness and bearing capacity of the angle steel, but improved its deformation capacity. In addition, a few scholars have studied other forms of connection. Soty et al. [16] found that the thickness to height ratio of shear connectors and orientation angle of L-shaped connectors would affect the final failure form and shear resistance mechanism of L-shaped connectors, considered the effect on material strength, connector size, and orientation angle on its shear capacity. Wang et al. [17] analyzed the mechanical performances of angle steel, channel steel and T-shaped PBL connectors under repeated loading, and found that the stiffness of them decreased continuously; the PBL connector exhibited particularly obvious shear stiffness degradation.

Unlike prior studies on angle or channel steel connectors, this study focuses on T-shaped shear connectors, which offer advantages in ductility, stiffness, and ease of construction, as well as provide a long welding length and large contact area with the H-beam that result in strong shear and uplift resistance (see Fig. 1). Various T-shaped shear connector configurations with different web and flange thicknesses were accordingly subjected to push-out tests to determine their failure modes, whole loading process and load–slip curves. These results were subsequently applied to verify finite element simulation and further analyze the influence of the component sizes of T-shaped connector and material strength on the shear behaviors of the connectors. Finally, the shear bearing capacity calculation formula of the T-shaped connector was put for word according to the simulation results, providing a reference for the application of this connector in future buildings.

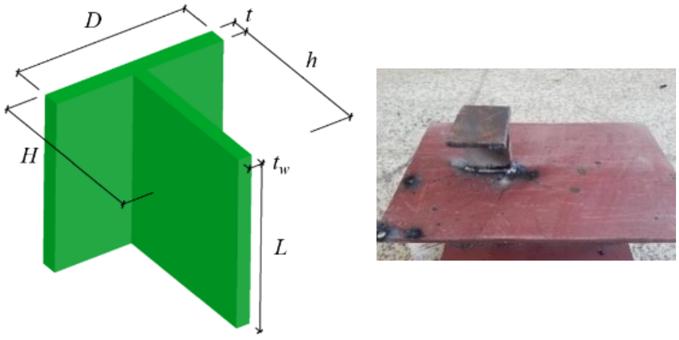

Fig. 1 T-shaped shear connector

2. Experiment materials and methods

2.1. Specimen design

According to EN 1994-1-1(EC 4) [18], the design of test specimens was shown in Fig. 2. Each specimen comprised a 300 mm × 300 mm × 10 mm × 15 mm H-beam, 500 mm × 150 mm × 400 mm concrete slab (cast-in-place and prefabricated), and 700 mm × 350 mm × 100 mm cast-in-place concrete base. An end plate is welded at the loading position of H-beam to make that the components are stressed uniformly in the loading project, and the size is 350 mm × 35 0mm × 20 mm. In this test, the thickness of the shear connector flange and web plate were the influencing factors, resulting in eight specimens in the four groups detailed in Table 1.

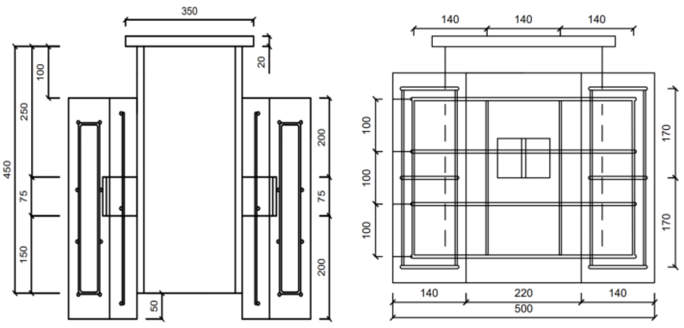

(a) Front view (b) Lateral view

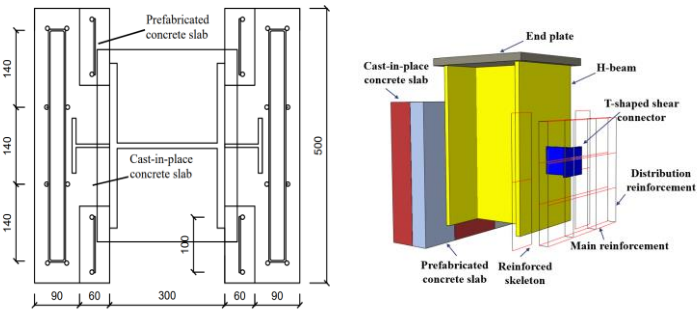

(c) Top view (d) Model diagram

Fig. 2 Test specimen dimensions and structural diagram

Table 1
Parameters of tested T-shaped shear connectors

Specimen	H	D	L	t_w	t	l_w
number	(mm)	(mm)	(mm)	(mm)	(mm)	(mm)
TG-1	100	100	75	6	8	75
TG-2	100	100	75	6	8	75
TG-3	100	100	75	8	8	75
TG-4	100	100	75	8	8	75
TG-5	100	100	75	6	10	75
TG-6	100	100	75	6	10	75
TG-7	100	100	75	8	10	75
TG-8	100	100	75	8	10	75

Note: H, D and L are the height, width and length of the T-shaped connector, respectively; t_w is the web thickness; t is the flange thickness; l_w is the weld length.

2.2. Material properties

Table 2 lists the material parameters of the steel components: the T-shaped shear connectors, H-beams, and end plates were all made of Q235B grade steel. The slab reinforcement was made of HPB300 grade steel with ϕ8 threaded bars in the stressed direction and ϕ6 threaded bars in the distributed direction. The prefabricated slab was made of C30 concrete, and the cast-in-place slab and base were made of C45 concrete; According to compressive strength test of concrete cube (150mm). The average compressive strength of C30 concrete was 30.0 MPa and its elastic modulus was 3.00×10^4 MPa; the average compressive strength of C45 concrete was 45.3 MPa and its elastic modulus was 3.35×10^4 MPa.

Table 2
Material properties of steel

Thickness of steel plate(mm)	Type	f_y(MPa)	f_u(MPa)	E_s(GPa)
6	Q235B	413.3	480.0	206
8	Q235B	425.6	483.7	204

Note: f_y, f_u and E_s are the yield strength, tensile strength and elastic modulus of steel, respectively.

2.3. Loading device and scheme

A 100t jack was selected for force loading in the test as shown in Fig. 3. The loading scheme comprised a monotonic concentrated-load static test with preloading and formal loading stages. This scheme was consistent with that used in [19].

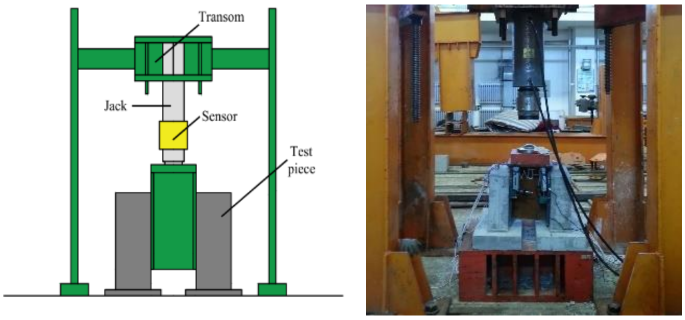

(a) Schematic presentation of test setup (b) Test device

Fig. 3 Test setup

2.4. Measurement system

The response of each specimen to the applied load was determined by measuring its strain and deformation. Fig. 4 (a) depicts the arrangement of the connector strain gauges. Strain rosette T1 was located on the web of T-shaped connector, near the weld at the flange of H-beam, rosette T2 was located in the middle of the web, and rosettes T3–T5 were located on both sides and at the middle of the flange. The equivalent strain values for the rosettes were calculated from the strain values in three directions [19]. Fig. 4 (b) depicts the displacement meter arrangement. In order to obtain the relative slip value between H-beam and T-shaped connector as well as the vertical displacement of H-beam relative to composite slab, two displacement meters were placed in the middle of the H-beam, one parallel and one perpendicular to the weld between the connector and H-beam.

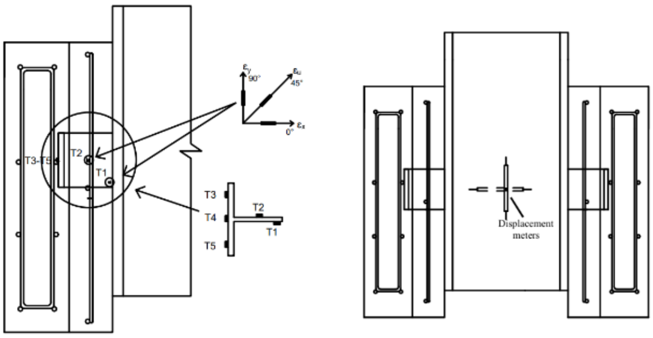

(a) Strain gauges (b) Displacement meters

Fig. 4 Measurement layout

3. Experiment results

3.1. Test phenomena and failure modes

The failure modes of the specimens with different parameters were similar, exhibiting an obvious slip between the prefabricated concrete floor slab and H-beam. Failure occurred at the weld between the H-beam and T-shaped shear connector, accompanied by wide cracks in the nearby concrete slab.

The observed test phenomena are described in this section considering TG-8 as a typical specimen. The specimen showed no obvious change in the initial loading stage. The first crack appeared on the CR-1 plane when the load reached 75% of the peak value (see Fig. 5(a)). The length and width of this crack gradually extended with further increase in load, followed by the appearance of a second crack on the C-1 plane (see Fig. 5(b)). The specimen suddenly exhibited a large displacement when the peak load was achieved, at which time a third crack appeared on the C-2 plane and multiple microcracks appeared near the second and third cracks (see Fig. 5(c)). As the contact surface between the concrete slab and H-beam was completely disconnected at this time, the loading was stopped. The observed crack pattern of the specimen presented local spalling of the concrete slab on plane C-2 (see Fig. 5(d)). The maximum crack widths of 1.5 and 0.9 mm on planes CR-1 and C-1, respectively, a number of 0.12–0.35 mm wide microcracks between the concrete slab and T-shaped connector on the C-2 surface, and a fourth crack on the concrete base that was only 0.15 mm wide.

(a) CR-1 plane fracture

(b)C-1 plane fracture

(c) C-2 plane fracture

(d) The concrete block on side C-2 falls off

Fig. 5 Specimen failure mode

3.2. Load-slip curves

Fig. 6 shows the comparison of load-slip (P–δ) curves of specimens. Each group of specimens reached yield at 70–75% of their peak load. Different degrees of fracture appeared between the prefabricated floor slab and H-beam at peak load, the loading was stopped, and the slip value increased slowly with the subsequent decrease in applied load. The characteristic slip values for the specimens were within 15.67–30.56 mm, exceeding the lower limit for flexible connectors in Eurocode 4 (> 6 mm) [18]. When the connector web thickness was 6 mm, a thicker flange increased the yield and peak loads; the yield and peak loads of TG-5 were 11.6% and 24.4% higher, respectively, than those of TG-2. When the web thickness was 8 mm, the change of flange thickness had little effect on its yield load, but its peak load increased by 15.4%. When the flange thickness was 8 mm, the yield and peak loads increased by 30.6% and 21.4% with the increase of web thickness, respectively, and when it was 10 mm, by 22.7% and 13.5%.

The ultimate shear capacity versus ductility coefficient (D_c) curves shown in Fig. 7 [20]. The D_c values of each specimen were 39.2, 21.8, 94.5, and 61.3. After reaching the yield load, each P–δ curve exhibits a long plateau, indicating excellent ductility. Changing the flange thickness had a great effect on the D_c: when the web thickness was 6 mm and 8 mm, an increase in flange thickness from 8 mm to 10 mm increased the D_c value by 2.4 times and 2.8 times, respectively. Compared with traditional bolted connectors [21], its D_c values were within 1.97-2.07, while the D_c values of T-shaped shear connectors were within 21.8-94.5, indicating that T-shaped shear connectors have better ductility.

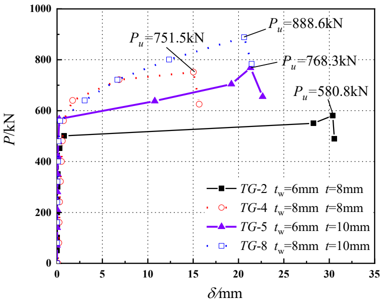

Fig. 6 Load–slip curves

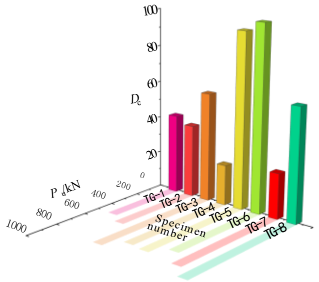

Fig. 7 Ultimate shear capacity–ductility coefficient curves

3.3. Load-strain curves

Fig. 8 compares the load-strain curves of the evaluated specimens, and the strain value was negative under compression and positive under tension. The curves for rosettes T1 and T2 exhibit the same trends in each group, and the strain in the connector flange of each group exhibited no obvious change during the entire loading process, indicating that no yield phenomenon occurred within. The connector webs were consistently in tension, and the bottom of the web connecting with the H-beam was the first to yield. The yield strain was attained at the center of the connector webs in specimens TG-2 and TG-5, but not at those in specimens TG-4 and TG-8. This phenomenon indicates that an increase in web thickness can effectively delay the yield of the shear connector, whereas an increase in flange thickness has little influence.

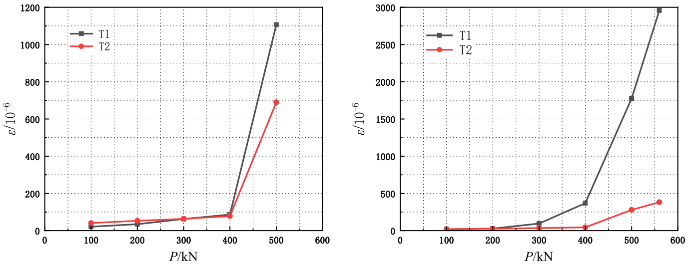

(a)TG-2

(b)TG-4

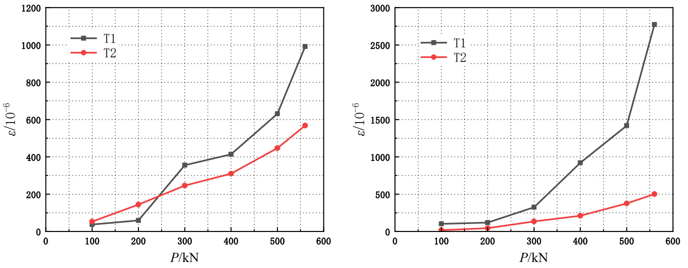

(c)TG-5

(d)TG-8

Fig. 8 Load–strain curves

4. Finite element analysis

4.1. Model establishment and verification

The finite element analysis (FEA) software ABAQUS was used to perform refined and expanded numerical simulations evaluating the shear behavior of T-shaped connector specimens subjected to push-out loading.

4.1.1. Material constitutive models

For concrete, the concrete plastic damage model provided in ABAQUS was selected for analysis. As shown in Fig. 9 (a), the inelastic stage was defined using the stress–strain curve provided in the Code for design of concrete structures [22]. The double-fold elastic–plastic constitutive model was defined for the steel material [23] as shown in Fig. 9 (b).

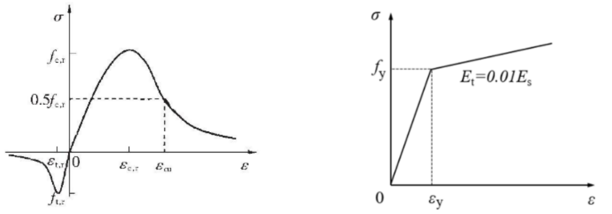

(a) Stress-strain curve of concrete (b) Stress-strain curve of steel

Fig. 9 Material constitutive models

4.1.2. Finite element type and component mesh division

The FEA model established in this study comprised a prefabricated concrete slab, cast-in-place concrete slab, H-beam, T-shaped shear connector, and steel reinforcement; the geometric size of each component was consistent with those of the push-out specimen evaluated in Section 3. The concrete slabs, H-beam, and T-shaped shear connector components were modeled using the C3D8R reduced integral eight-node solid element; the reinforcement bars were modeled using the T3D2 truss element [24]. The general mesh division in the model was 20 mm with a refined mesh of 10 mm at locations where the stress was concentrated, such as the T-shaped connector and the opening of cast-in-place concrete slab, to accurately simulate the stress development process while limiting the computational burden and facilitating model convergence. The complete mesh is shown in Fig. 10.

4.1.3. Boundary conditions and loading methods

Binding constraint was applied between the prefabricated concrete slab and cast-in-place concrete slab and between the H-beam and T-shaped shear connector. Hard contact was applied between the prefabricated floor slab and H-beam. Surface-to-surface contact was applied between the cast-in-place concrete slab and H-beam and between the cast-in-place concrete slab and T-shaped shear connector with penalty friction [25-26] coefficients of 0.2 and 0.4, respectively, in the tangential direction. Embedded constrain was applied to the reinforcement. The bottoms of the cast-in-place and prefabricated concrete slab were completely fixed, and the upper surface of H-beam was coupled to simulate the applied displacement loading. The completed FEA model is shown in Fig. 10.

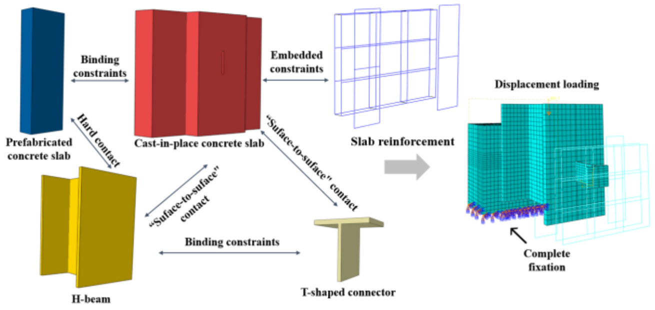

Fig. 10 FEA model boundary conditions and mesh division

4.1.4. Model validation

The test and FEA-obtained P–δ curves are compared in Fig. 11 and the detailed results are provided in Table 3. The P–δ curves obtained by the FEA simulation were basically consistent with those determined by testing, showing relative errors of less than 10% between peak loads, confirming the accuracy of the FEA modeling approach.

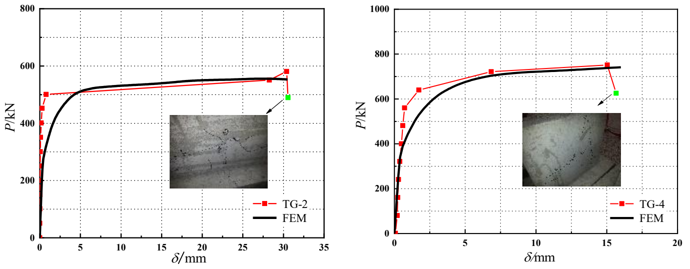

(a) TG-2 (b) TG-4

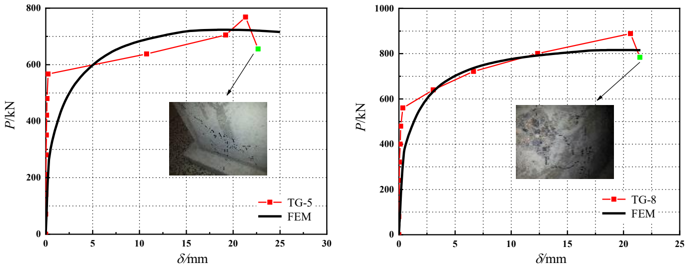

(c) TG-5 (d) TG-8

Fig. 11 Comparison of test and FEA-obtained P–δ curves

Table 3

Comparison of test and FEA-obtained results

Specimen number	Test Results $P_{u,t}$(kN)	Mean value	Simulation results $P_{u,s}$(kN)	$P_{u,s}/P_{u,t}$
TG-1	511.4	546.1	555.61	1.02
TG-2	580.8			
TG-3	848.1	799.8	747	0.93
TG-4	751.5			
TG-5	768.3	725.4	726.99	1.0
TG-6	682.5			
TG-7	797.8	843.2	820.36	0.97
TG-8	888.6			

Note: $P_{u,t}$ and $P_{u,s}$ are the shear bearing capacity obtained by test and numerical simulation, respectively.

4.2. Analysis of the stress development process

The numerical analysis model of specimen TG-2 is used as an example in this discussion of the stress development process. As shown in Fig. 12, the FEA-obtained P–δ curve can be divided into three stages between points O, A, B, and C: the elastic working stage in segment OA, elastic–plastic working stage in segment AB, and strengthening stage in segment BC. Point O denotes the beginning of loading, point A denotes when the T-shaped connector reaches the yield load, point B denotes as the entire section at the bottom of the web reaches the tensile limit (i.e., strain rosettes T1 and T2 fail), and point C denotes when the shear connector reaches its peak load ($P_{u,t}$) and loading is stopped. The stress and strain nephograms of each component at these characteristic points are shown in Figs. 13–15.

In segment OA, the connector is within the elastic working range, and the initial stiffness of the specimen was large. When the curve reached point A, considerable stress was present at the weld between the H-beam and connector (see Fig. 13(b)) and extrusion contact occurred between the side of the web of connector close to H-beam and the cast-in-place concrete slab, which slab experienced large local strain, while the prefabricated concrete slab experienced almost no strain (see Fig. 13(c)). The shear connector began to yield locally from the lower part at the position of the welding surface between the web and H-beam (see Fig. 13(d)) when the load was 0.49 $P_{u,t}$ and the displacement was 0.42 mm.

Next, the specimen entered the elastic–plastic working stage in segment AB. At point B, the stress at the weld between the bottom of the shear connector and H-beam was close to the yield value (see Fig. 14(b)), corresponding to the considerable compressive strain in the concrete slab at the shear connector web, which locally exceeded the ultimate compressive strain by 0.0033, indicating concrete slab cracking (see Fig. 14(c)). Furthermore, the entire bottom section of the connector web reached the ultimate tensile stress (480 MPa). At this time, obvious shear deformation appeared at the weld joint, and the shear force was transmitted to the flange plate from the web plate, and the stress began to occur at the connection position between the flange and the web (Figure 14d).

Finally, the specimen entered the strengthening stage in segment BC. At point C, the stress in the middle-lower part of the weld between T-shaped connector and H-beam reached yield (Fig. 15(b)), and the concrete slab below the connector web reached the ultimate compressive strain. At this time, the concrete slab was crushed, which coincided to the observed experimental phenomenon (Fig. 15(c)), the top of the joint between T-shaped connector flange and web yielded locally, also the web completely reached the ultimate tensile stress from the side near the H-beam to the middle. Eventually the connection lost its shear capacity (see Fig. 15(d)).

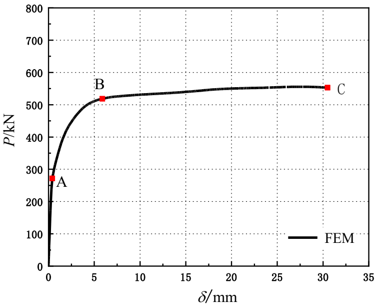

Fig. 12 TG-2 load–slip curve

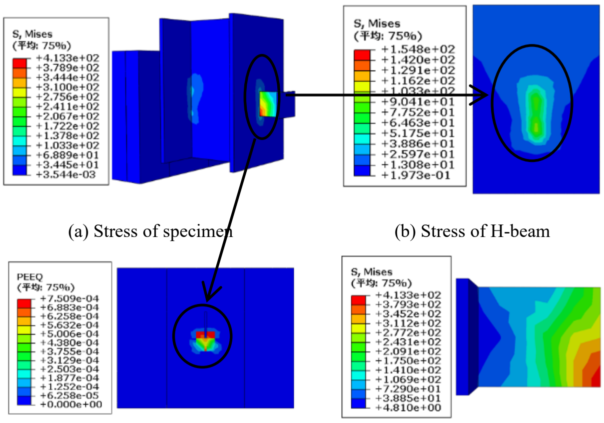

(a) Stress of specimen (b) Stress of H-beam

(c) Strain of concrete slab (d) Stress of connector

Fig. 13 Stress and strain in each part of TG-2 at point A

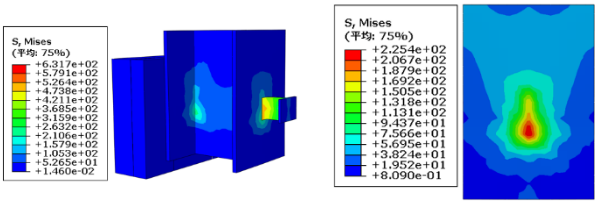

(a) Stress of specimen (b) Stress of H-beam

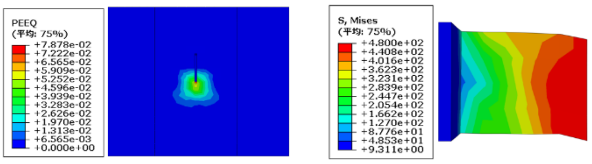

(c) Strain of concrete slab (d) Stress of connector

Fig. 14 Stress and strain in each part of TG-2 at point B

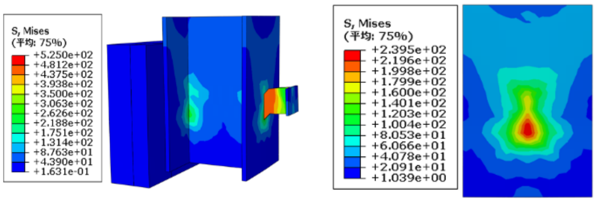

(a) Stress of specimen (b) Stress of H-beam

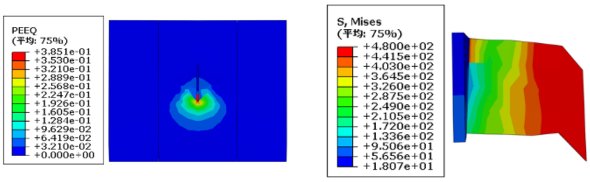

(c) Strain of concrete slab (d) Stress of connector

Fig. 15 Stress and strain in each part of TG-2 at point C

4.3. Extended parameter analysis

The influence law of different parameters on shear behavior of the T-shaped shear connector was further investigated using 48 numerical models with web thicknesses t_w of 6–14 mm, flange thicknesses t of 6–14 mm, connector lengths L of 65–95 mm, web heights h of 42–92 mm, connector widths D of 80–110 mm, prefabricated concrete compressive strength f_{cu}' of 30–70 MPa, cast-in-place concrete compressive strength f_{cu} of 30–70 MPa, and steel yield strengths f_y of 235–460 MPa, as detailed in Table 4.

4.3.1. Effect of web thickness

The bearing capacity of T-shaped connector increased slightly as t_w was increased from 6 to 7 mm, then increased in an approximately linear fashion at an average rate of 6.5% when t_w was increased from 7 to 13 mm, and finally decreased when t_w was increased from 13 to 14 mm (see Fig. 16(a)). Therefore, increasing the web thickness within a specified scope can effectively enhance the shear capacity of this connector, but it should not exceed 13 mm.

4.3.2. Effect of flange thickness

The bearing capacity of T-shaped connector continuously improved as t was increased from 6 to 11 mm, then decreased at higher thicknesses (see Fig. 16(b)). The primary reason for this change was that the increase in load began to transmit the shear force through the web to flange. Once the web completely yielded from the bottom near the H-beam, the load could not be effectively transmitted to the flange, causing the impact of changing t on the bearing capacity of the connector to gradually reduce. These results suggest that the flange thickness should not exceed 11 mm.

4.3.3. Effect of connector length

The bearing capacity of T-shaped connector improved as L was increased from 65 to 95 mm, and its most significant improvement of 10.2% occurred with the increase in L from 85 to 95 mm (see Fig. 16(c)). The primary reason for this result was that a longer connector increased the weld area, effectively improving the shear capacity of the connection.

4.3.4. Effect of web height

The bearing capacity of T-shaped connector increased by 9.9% and 14.1% when h was increased from 42 to 52 mm and 62 mm, respectively, above which further increase in h had no significant effect (see Fig. 16(d)). Therefore, it indicates that increasing the web height in a certain range has almost no impact on the bearing capacity, and it is recommended that the web height need not exceed 62 mm.

4.3.5. Effect of connector width

The bearing capacity of T-shaped connector only increased by 0.2% when D was increased from 80 to 90 mm, and improved only slightly more when it was increased to 100 mm (see Fig. 16(e)). Therefore, the connector width has little influence on its shear capacity, and can be set as required to satisfy the structural design requirements, particularly regarding the required lifting resistance.

4.3.6. Effect of prefabricated concrete compressive strength

When f_{cu}' was between 30 MPa and 70 MPa, its shear capacity enhanced negligibly, and only when f_{cu}' was increased from 30 to 40 MPa, its shear capacity enhanced by 2.1% (see Fig. 16(f)). Therefore, considering the effects on bearing capacity as well as economy, the strength of the prefabricated concrete should be 40 MPa.

4.3.7. Effect of cast-in-place concrete compressive strength

Increasing f_{cu} effectively improved the bearing capacity of T-shaped connector. The improvement effect of bearing capacity gradually decreased with increasing f_{cu} from 30 to 60 MPa, but remained generally consistent thereafter (see Fig. 16(g)). Therefore, the strength of the cast-in-place concrete need not exceed 60 MPa.

4.3.8. Effect of steel yield strength

The shear capacity of T-shaped connector increased by varying degrees with increasing f_y. Each subsequent increase in f_y from 235 to 275, 355, 390, 420, and 460 MPa increased the shear capacity by 4.9%, 6.4%, 2.4%, 2.6%, and 2.2%, respectively. (see Fig. 16(h)). Therefore, the optimal shear capacity can be realized using a connector steel strength of 355 MPa.

4.4. Design recommendations for T-shaped shear connectors

The results of parameter analysis obtained in Section 4.3 demonstrate that the web thickness, flange thickness, connector length, web height and material strength, all significantly influence the shear behavior of T-shaped connector. These results suggest that T-shaped connector designs should consider a web thickness less than 13 mm, flange thickness less than 11 mm, and web height less than 62 mm and should provide a connector width and length meeting the structural requirements of the Specifications for hot rolled section steel [27] and the Code for design of concrete structures [22]. Considering both economic and structural design requirements, the proposed size selection of a T-shaped shear connector is shown in Table 5.

Table 5
Size selection of T-shaped shear connector

Influencing parameter	Selection range	Optimum value
t_w(mm)	$6 \leqslant t_w \leqslant 13$	13
t(mm)	$6 \leqslant t \leqslant 11$	10
L(mm)	design requirements	75
h(mm)	$42 \leqslant h \leqslant 62$	62
D(mm)	design requirements	80

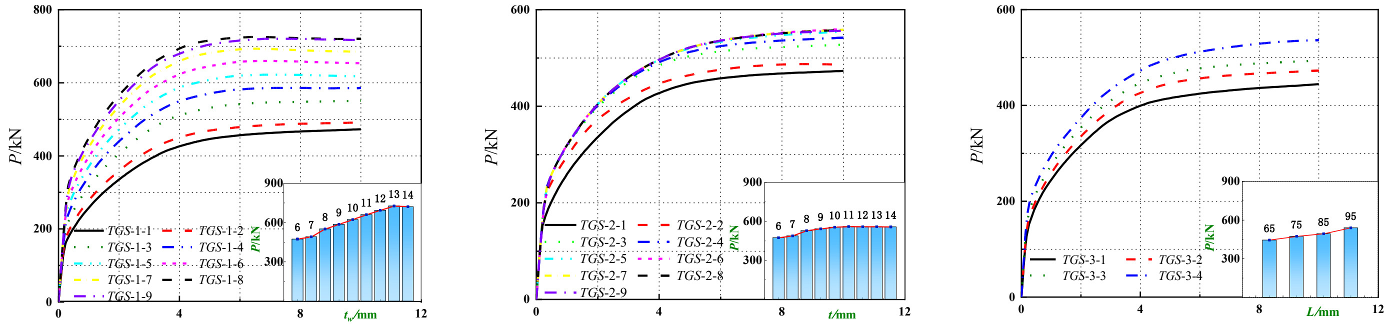

(a) Web thickness (b) Flange thickness (c) Connector length

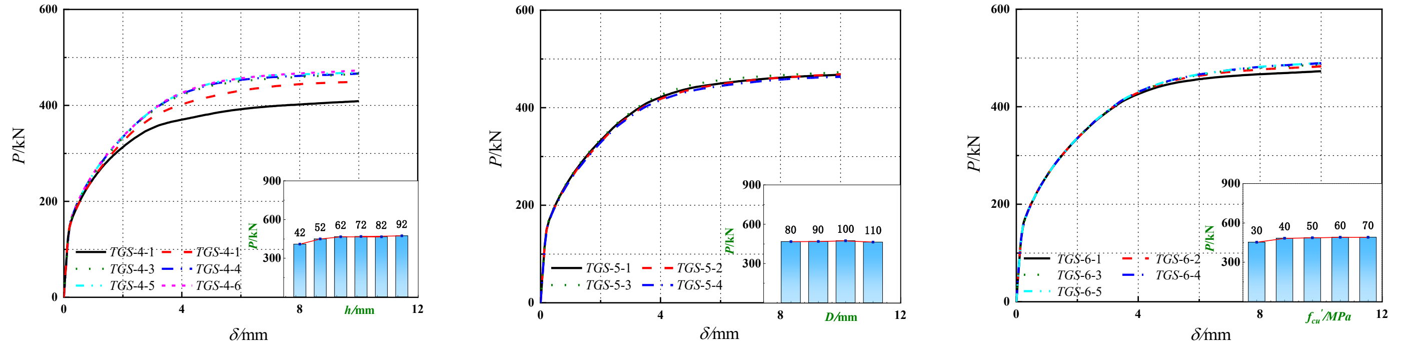

(d) Web height (e) Connector width (f) Prefabricated concrete compressive strength

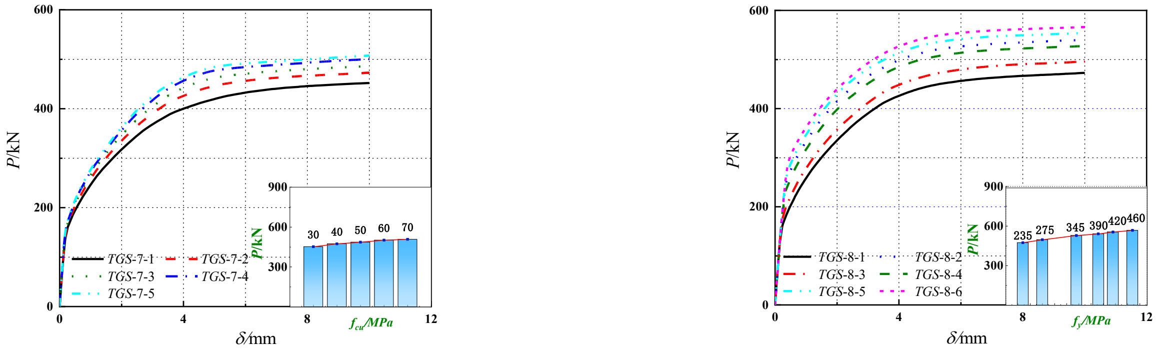

(g) Cast-in-place concrete compressive strength (h) Steel yield strength

Fig. 16 Load-slip curves with different parameters

Table 4
Specimen details for FEA evaluation

Numerical model number	$H\times D\times L$(mm)	t_{w}(mm)	t(mm)	f_{cu}'(MPa)	f_{cu}(MPa)	f_{y}(MPa)	h(mm)	$P_{\mathrm{u,s}}$(kN)
TGS-1-1	100×100×75	6	8	30	40	235	92	472.8
TGS-1-2	100×100×75	7	8	30	40	235	92	491.4
TGS-1-3	100×100×75	8	8	30	40	235	92	550.9
TGS-1-4	100×100×75	9	8	30	40	235	92	585.6
TGS-1-5	100×100×75	10	8	30	40	235	92	622.2
TGS-1-6	100×100×75	11	8	30	40	235	92	659.6
TGS-1-7	100×100×75	12	8	30	40	235	92	693.1
TGS-1-8	100×100×75	13	8	30	40	235	92	725.5
TGS-1-9	100×100×75	14	8	30	40	235	92	720.5
TGS-2-1	98×100×75	6	6	30	40	355	92	473.2
TGS-2-2	99×100×75	6	7	30	40	355	92	487.2
TGS-2-3	100×100×75	6	8	30	40	355	92	527.4
TGS-2-4	101×100×75	6	9	30	40	355	92	542.1
TGS-2-5	102×100×75	6	10	30	40	355	92	554.5
TGS-2-6	103×100×75	6	11	30	40	355	92	559.4
TGS-2-7	104×100×75	6	12	30	40	355	92	558.1
TGS-2-8	105×100×75	6	13	30	40	355	92	557.5
TGS-2-9	106×100×75	6	14	30	40	355	92	556.6
TGS-3-1	100×100×65	6	8	30	40	235	92	444.4
TGS-3-3	100×100×85	6	8	30	40	235	92	493.8
TGS-3-4	100×100×95	6	8	30	40	235	92	539.1
TGS-4-1	50×100×75	6	8	30	40	235	42	408.8
TGS-4-2	60×100×75	6	8	30	40	235	52	449.4
TGS-4-3	70×100×75	6	8	30	40	235	62	466.3
TGS-4-4	80×100×75	6	8	30	40	235	72	466.4
TGS-4-5	90×100×75	6	8	30	40	235	82	468.7
TGS-5-1	100×80×75	6	8	30	40	235	92	467.3
TGS-5-2	100×90×75	6	8	30	40	235	92	468.5
TGS-5-4	100×110×75	6	8	30	40	235	92	463.5
TGS-6-2	100×100×75	6	8	40	40	235	92	482.8
TGS-6-3	100×100×75	6	8	50	40	235	92	486.5
TGS-6-4	100×100×75	6	8	60	40	235	92	489.2
TGS-6-5	100×100×75	6	8	70	40	235	92	489.6
TGS-7-1	100×100×75	6	8	30	30	235	92	452.1
TGS-7-3	100×100×75	6	8	30	50	235	92	486.2
TGS-7-4	100×100×75	6	8	30	60	235	92	500.6
TGS-7-5	100×100×75	6	8	30	70	235	92	507.6
TGS-8-2	100×100×75	6	8	30	40	275	92	495.9
TGS-8-3	100×100×75	6	8	30	40	355	92	527.4
TGS-8-4	100×100×75	6	8	30	40	390	92	540.0
TGS-8-5	100×100×75	6	8	30	40	420	92	553.9
TGS-8-6	100×100×75	6	8	30	40	460	92	566.2

Note: TGS-1-1 is regarded as a standard part, which is the same parameter as TGS-3-2, TGS-4-6, TGS-5-3, TGS-6-1, TGS-7-2 and TGS-8-1, so only one set of data is listed.

5. Calculation of shear bearing capacity

5.1. Calculating methods of shear bearing capacity

Nie et al. [28] analyzed the mechanical behaviors of 49 channel steel connectors and proposed an equation:

$$P_u = (0.6df_y + (6t + 0.15b)f_c)L \tag{1}$$

where d and t are the web and flange thickness, b is the flange width, L is the channel steel length, f_y and f_c are the steel yield strength and concrete compressive strength, P_u is the shear bearing capacity.

The Code for design of steel and concrete composite bridges [29] provided an equation to calculate the bearing capacity of a channel steel that considers the simultaneous shear forces on the channel web and flange as follows:

$$P_u = 0.26(t + 0.5t_w)L\sqrt{E_c f_c} \tag{2}$$

where t and t_w are the flange average thickness and web thickness, L is the channel steel length, f_c and E_c are the concrete compressive strength and elastic modulus.

The shear bearing capacity calculation equation given in AISC/ANSI 360-10 [30] takes into account the impact of the flange thickness of angle steel connector on its shear strength as follows:

$$P_u = 0.3(t_f + 0.5t_w)L\sqrt{E_c f_c} \tag{3}$$

where t_f, t_w and L are the average thickness flange, web thickness and angle steel length.

Notably, the equation given in Eurocode 4 [18] for obtaining the bearing capacity of angle steel does not consider the interaction between the connector and concrete, only considers the influence of the weld strength as follows:

$$P_u = \min(Q_{u1} = \frac{Af_c}{1.5}, Q_{u2} = aL\frac{f_y}{\sqrt{3}}) \tag{4}$$

where A is the angle steel area and a is the theoretical thickness of weld.

Comparing the T-shaped connector shear bearing capacity calculated using the national codes with the test and FEA results in Table 6, the results obtained using Eqs. (1)–(3) are clearly too conservative, Eqs. (2) and (3) do not consider the impact of the steel strength of connector on bearing capacity. Furthermore, the values obtained by Eq. (4) are higher than those determined by the FEA with considerable errors and dispersions. This occurred because the shape and size of T-shaped connector have different effects than those of the angle steel connector on shear capacity.

5.2. Calculation formula of shear bearing capacity

The equation for the shear bearing capacity of channel steel proposed by Nie [28] was modified by using the multiple linear regression analysis based on the FEA results given in Section 4 to obtain the following shear bearing capacity equation for the T-shaped connector:

$$P_u = (0.75t_w f_y + (0.52t + 0.96L)f_c)h \tag{5}$$

Table 6 compares the values calculated using Eq. (5) with those obtained by the experiment and FEA, indication suitable agreement with an average error less than 10% and a standard deviation of 0.23. Therefore, the calculation formula established in this paper can be used for predicting the shear capacity of the T-shaped shear connector.

Table 6
Comparison results of shear bearing capacity

Number	$P_{u,t}$(kN)	Mean value	μ_1	μ_2	μ_3	μ_4	μ
TGS-1-1	236.4		0.65	0.71	0.82	1.76	0.97
TGS-1-2	245.7		0.67	0.72	0.83	1.70	1.00
TGS-1-3	275.5		0.63	0.67	0.77	1.53	0.95
TGS-1-4	292.8		0.63	0.66	0.76	1.45	0.95
TGS-1-5	311.1		0.63	0.64	0.74	1.37	0.95
TGS-1-6	329.8		0.63	0.63	0.73	1.30	0.94
TGS-1-7	346.6		0.63	0.62	0.72	1.24	0.94
TGS-1-8	362.8		0.63	0.61	0.71	1.19	0.95
TGS-1-9	360.3		0.66	0.64	0.74	1.21	1.00
TGS-2-1	236.6		0.71	0.58	0.67	1.74	1.18
TGS-2-2	243.6		0.73	0.63	0.73	1.70	1.15
TGS-2-3	263.7		0.71	0.64	0.74	1.58	1.06
TGS-2-4	271.1		0.72	0.68	0.78	1.55	1.04
TGS-2-5	277.3		0.73	0.72	0.83	1.52	1.02
TGS-2-6	279.7		0.76	0.77	0.89	1.51	1.01
TGS-2-7	279.1		0.79	0.83	0.95	1.53	1.02
TGS-2-8	278.8		0.82	0.88	1.02	1.54	1.02
TGS-2-9	278.3		0.85	0.94	1.08	1.55	1.03
TGS-3-1	222.2		0.60	0.66	0.76	1.64	0.96
TGS-3-3	246.9		0.71	0.78	0.90	1.89	1.00
TGS-3-4	269.6		0.72	0.79	0.92	1.92	0.98
TGS-4-1	204.4		0.75	0.83	0.95	2.04	0.51
TGS-4-2	224.7		0.68	0.75	0.87	1.85	0.58
TGS-4-3	233.2		0.66	0.72	0.84	1.79	0.67
TGS-4-4	233.2		0.66	0.72	0.84	1.79	0.77

TGS-4-5	234.4		0.66	0.72	0.83	1.78	0.88
TGS-5-1	233.7		0.64	0.72	0.83	1.78	0.99
TGS-5-2	234.3		0.65	0.72	0.83	1.78	0.98
TGS-5-4	231.8		0.67	0.73	0.84	1.80	0.99
TGS-6-2	241.4		0.64	0.70	0.81	1.73	0.95
TGS-6-3	243.3		0.63	0.69	0.80	1.71	0.95
TGS-6-4	244.6		0.63	0.69	0.80	1.70	0.94
TGS-6-5	244.8		0.63	0.69	0.80	1.70	0.94
TGS-7-1	226.1		0.58	0.62	0.72	1.38	0.87
TGS-7-3	243.1		0.71	0.79	0.91	2.07	1.06
TGS-7-4	250.3		0.77	0.85	0.98	2.40	1.16
TGS-7-5	253.8		0.84	0.92	1.06	2.73	1.26
TGS-8-2	248.0		0.66	0.68	0.79	1.68	1.00
TGS-8-3	263.7		0.71	0.64	0.74	1.58	1.06
TGS-8-4	270.0		0.72	0.63	0.72	1.54	1.09
TGS-8-5	277.0		0.74	0.61	0.70	1.50	1.11
TGS-8-6	283.1		0.76	0.60	0.69	1.47	1.14
AVE			0.69	0.71	0.82	1.68	0.97
STE			0.07	0.09	0.10	0.29	0.14
TG-1	255.7	273.05	0.77	0.66	0.76	1.93	1.39
TG-2	290.4						
TG-3	424.1	399.9	0.63	0.49	0.57	1.33	1.11
TG-4	375.8						
TG-5	384.2	362.7	0.64	0.59	0.68	1.47	0.83
TG-6	341.3						
TG-7	398.9	421.6	0.67	0.54	0.63	1.27	1.03
TG-8	444.3						
AVE			0.67	0.57	0.66	1.50	1.09
STE			0.06	0.06	0.07	0.26	0.23

Note: μ_1 to μ are the ratio of the calculated value obtained by Eq. (1) to Eq. (5) to $P_{u,t}$, respectively; AVE is the average value, STE is the standard deviation.

6. Conclusion

This study completed eight push-out tests and established larges of accurate numerical models on the T-shaped shear connectors in prefabricated concrete composite floor slabs to determine the effect of different parameters on their shear behavior, and put for word a design equation of shear bearing capacity. The following conclusions were obtained:

1) The T-shaped shear connector had a large initial stiffness and excellent ductility during the service stage. The characteristic slip values of the evaluated specimens were between 15.67 and 30.56 mm, meeting the requirements of Eurocode 4 for flexible connectors (> 6 mm).

2) The failure mode of each specimen exhibited shear failure at the connection between T-shaped shear connector and H-beam, obvious fracture between the H-beam and composite slab, and multiple cracks in the prefabricated concrete slab with a maximum width of 1.5 mm.

3) The section dimension of T-shaped connector and material strength had different degrees of impact on its shear capacity: the web thickness had the greatest influence whereas the connector width and prefabricated concrete compressive strength had almost no influence. On the premise of considering shear behavior, economy and structural requirements, some suggestions on the optimal selection of cross-section size of T-shaped connectors are given.

4) The results of extensive FEA simulations were analyzed using the multiple linear regression method to propose a formula for the shear bearing capacity of a T-shaped connector, which are expected to provide theoretical basis for the application of this shear connectors in prefabricated concrete composite floor system so as to improve the overall performance and economy of structures.

Acknowledgments

The investigation was supported by the National Key Research and Development Program of China (Grant No. 2017YFC0703407) and Shenyang Science and Technology Program of China (Grant No. 23503609).

References

[1] Yu S, Liu Y and Wang D. "Review of thermal and environmental performance of prefabricated buildings: Implications to emission reductions in China". Renewable and Sustainable Energy Reviews, 137:110472, 2021.

[2] Li X, Xie W and Yang T. "Carbon emission evaluation of prefabricated concrete composite plates during the building materialization stage". Building and Environment, 232, 110045, 2023.

[3] LI G, CAO K and YANG Z. "Finite Element Analysis of Steel Reinforced Concrete Stub Columns with New Shear Connectors under Axial Compression". Journal of Shenyang Jianzhu University (Natural Science), 38(2):202-210, 2022. (in Chinese)

[4] Yossef M, Chen A and Elsayad M. "Deconstructable variable stiffness shear connectors in FRP deck resting on multigirder bridge system: Analytical model". Engineering Structures, 307:117932, 2024.

[5] Jakovljević I, Spremić M and Marković Z. "Shear behaviour of demountable connections with bolts and headed studs". Advanced Steel Construction (Accepted for Publication on 16th May 2023), 2023.

[6] Xu Q, Sebastian W and Lu K. "Development and Performance of Innovative Steel Wedge Block–Crossed Inclined Stud–UHPC Connections for Composite Bridge". Journal of Structural Engineering, 148(9):04022128, 2022.

[7] Shariati A T A. "Monotonic behavior of C and L shaped angle shear connectors within steel-concrete composite beams: an experimental investigation". Steel & Composite Structures: An International Journal, 35(2):237-247, 2020.

[8] Viest I M. "Full-scale tests of channel shear connectors and composite t-beams". University of Illinois at Urbana-Champaign, 1951.

[9] Shariati M, Sulong N H R and Suhatril M. "Comparison of behaviour between channel and angle shear connectors under monotonic and fully reversed cyclic loading". Construction and Building Materials, 38(38):582-593, 2013.

[10] Haroon M, Lee H D and Shin K J. Performance of angle shear connectors for U-shaped steel concrete infilled composite beams. Heliyon, 10(3): e25119, 2024.

[11] Arévalo D, Hernández L and Gómez C. "Structural performance of steel angle shear connectors with different orientation". Case Studies in Construction Materials, 14: e00523, 2021.

[12] Hajime O, Yoshio K. "JSCE Research Subcommittee on Steel-Concrete Sandwich Structures". Design code for steel-concrete sandwich structures–Draft, 20:1-21, 1992.

[13] ZHOU W, BAI J and LEI Y. "Experimental study on the lattice type of angle steel connectors——the fourth of the series of studies on steel-concrete composite truss". Journal

of Hefei University of Technology (Natural Science Edition), (02):126-130, 1994. (in Chinese)

[14] CUI J, ZHANG X. “The Study of Composite Beam Flexural Test and Shear Strength of Angle Connectors. Journal of Anhui Jianzhu University, 31(01):1-9, 2023. (in Chinese)

[15] TANG L, FAN J and NIE J. “Experimental study on the mechanical performance of angle shear connectors with and without concrete gaps”. Engineering Mechanics, 37(10): 45-55+115, 2020. (in Chinese)

[16] Soty R, Shima H. “Formulation for shear force–relative displacement relationship of L-shape shear connector in steel–concrete composite structures”. Engineering Structures, 46:581-592, 2013.

[17] WANG X, DENG W and ZHANG J. “Mechanical characteristics of shear connectors under repeated loads”. Journal of Jiangsu University of Technology (Natural Science Edition), 39(06):708-713, 2018. (in Chinese)

[18] EN1994-1-1, “Eurocode 4: Design of composite steel and concrete structures. Part 1-1: General rules and rules for buildings”. Brussels: CEN; 2004.

[19] QIU Z. “Development and Performance Study of New Connection between Prefabricated Concrete Laminated Floor Slab and Steel Beam”. Shenyang: Shenyang Jianzhu University, 2014. (in Chinese)

[20] YAN Y, DENG P and HOU H. “Experimental study on shear resistance of bolt connector in steel-concrete composite beam”. Journal of Shandong University of Science and Technology (Natural Science), 40(02): 51-59, 2021. (in Chinese)

[21] YANG Y, ZHANG S and CHEN X. “Experimental study on the shear behavior of a bolt connector in a steel-concrete composite beam”. Journal of Harbin Engineering University. 45(06):1076-1084, 2024. (in Chinese)

[22] GB 50010—2010, “Code for design of concrete structures”. China Architecture & Building Press, Beijing, 2010. (in Chinese)

[23] LI G, WANG Z and YANG Z. “Experimental study on shear behavior of π-type crestbond shear connectors”. Journal of Building Structures, 43(06):75-86, 2022. (in Chinese)

[24] Luo Y B, Sun S K and Yan J B. “Shear behavior of novel demountable bolted shear connector for prefabricated composite beam”. Advanced Steel Construction, 18(4):745-752, 2022.

[25] REN C, YUAN Y, CHEN Y. “Finite Element Analysis on Shear Performance Large-Diameter Short Stud Connectors in Prefabricated Steel-Thin UHPC Composite Beams”. Industrial Construction, 53(11):180-187, 2023. (in Chinese)

[26] Yan J B, Zhang W. “Numerical analysis on steel-concrete-steel sandwich plates by damage plasticity model: From materials to structures”. Construction and Building Materials, 149: 801-815, 2017.

[27] GB/T 706-2016, “Hot rolled section steel. Standards Press of China”, Beijing, 2016. (in Chinese)

[28] NIE J, SUN G. “Study on steel channel shear connector of steel-concrete composite beams”. Industrial Construction, (10):8-13+57, 1990. (in Chinese)

[29] GB 50917-2013, “Code for design of steel and concrete composite bridges”. China Planning Press, Beijing, 2013. (in Chinese)

[30] ANSI/AISC 360-10, “AISC. Specification for structural steel buildings”, American Institute of Steel Construction, Chicago, Illinois, 2010.

Advanced Steel Construction – Vol. 21 No. 3 (2025) 204–217
DOI:10.18057/IJASC.2025.21.3.3

NUMERICAL STUDY AND EVALUATION OF THE SHEAR CAPACITY OF SCREW DOUBLE-SHEAR CONNECTIONS

Wen-Hao Liu [1, 2], Lu Deng [2, 3], Yu-Long He [2, *], Tao Wang [1, 2] and Huan Liu [2]

[1] Key Laboratory of Concrete and Prestressed Concrete Structures of Ministry of Education, Southeast University, Nanjing 210096, China
[2] College of Civil Engineering, Hunan University, Changsha 410082, Hunan, China
[3] Key Laboratory for Damage Diagnosis for Engineering Structures of Hunan Province, Hunan University, Changsha 410082, Hunan, China
** (Corresponding author: E-mail: heyl@hnu.edu.cn)*

ABSTRACT

Previous studies have primarily focused on the performance of screw single-shear connections (SSCs) and rarely investigated the performance and calculation methods of screw double-shear connections (DSCs). The first study examines the effect of various parameters on the shear capacity of single-screw DSCs. The results indicate that the steel strength, steel plate thickness, screw diameter, and connection method have significant effects on the shear capacity of thin steel screw DSCs. Specifically, when the steel strength increases from 235 MPa to 550 MPa, the maximum increase in the shear capacity is 81.2%. An increase in steel plate thickness from 0.8 mm to 3.0 mm results in a minimum increase of 34.6% in shear capacity. Similarly, increasing the screw diameter from 3.5 mm to 6.3 mm leads to at least a 35.2% increase in shear capacity. Moreover, changing from the SSC to DSC can result in a maximum increase of 95.4% in shear capacity. Next, the shear performance of screw group DSCs is analyzed parametrically. It is found that when the steel plate thickness is 3.0 mm and the number of screws increases to 3, the failure mode transitions from a coupled bearing and shear failure to bearing failure. Additionally, when the number of screws increases from 2 to 5, the shear capacity of screw group DSCs increases by at least 9.6%. The effect of screw spacing on shear capacity decreases as the number of screws increases, while variations in screw arrangement have minimal impact on shear capacity. Furthermore, increasing the steel plate thickness from 0.8 mm to 1.2 mm results in a minimum 51.1% increase in shear capacity, and increasing the thickness from 1.2 mm to 3.0 mm leads to at least an 88.0% increase in shear capacity. Finally, the results of the parametric analyses are used to evaluate the applicability of design equations for screw DSCs. The findings indicate that the AISC specification provides accurate predictions for single screw DSCs, regardless of whether bearing or shear failure occurs. In contrast, for screw group DSCs, the AISC predictions tend to be conservative when the specimen experiences coupled bearing and shear failure, and unsafe when bearing failure occurs.

ARTICLE HISTORY

Received:	18 March 2024
Revised:	6 January 2025
Accepted:	8 January 2025

KEYWORDS

Double-shear connections (DSCs);
Screw group connection;
Shear capacity;
Failure modes;
Design formula

1. Introduction

Cold-formed steel (CFS) structures are widely used in low-rise buildings around the world [1]. However, key challenges in the development of mid- and high-rise CFS buildings include the low shear capacity and inadequate lateral stiffness of combined shear walls [2]. The lateral resistance of these walls is directly influenced by the diaphragm effect of the sheathings, and reliable screw connections between the sheathings and light-gauge steel studs are crucial to ensuring the diaphragm effect functions properly, thereby guaranteeing the structural load-carrying capacity [1]. As a critical shear connection element, the shear performance of screw connections significantly impacts the load-carrying capacity of the entire connected system. Therefore, examining the shear performance of screw connections is essential.

Considerable efforts and contributions have been made by numerous scholars in investigating the shear performance of screw connections. Pekoz [3] summarized the results of over 3500 tests on screw connections and developed design provisions. Rogers et al. [4] found that the predicted values from AS/NZS4600, CSA-S136, and AISI codes were unsafe when fastening two steel plates with different thicknesses. Laboube and Sokol [5-7] revealed a significant “screw group effect” in screw connections. Experimental research by Roy et al. [8] and Huynh et al. [9] demonstrated that screw arrangement affects the strength of the connection. Moreover, Huynh et al.[10] proposed a modified design formula for screw connections. Vy et al. [11] concluded that the tilting and bearing capacity design methodologies for screw connections in current standards are reliable at ambient temperatures. For elevated temperature, the shear capacity must be multiplied by a reduction factor accounting for the temperature effect. Lu et al. [12] presented modified equations for determining the shear capacity of screw connections at both ambient and elevated temperatures. Chen et al. [13] experimentally examined the single-shear behavior of screw connections between CFSs at different temperatures and explored the influence of screw diameter, steel type, and plate thickness on shear capacity. Guan et al. [14] developed a detailed FE model to investigate the effect of various parameters on the shear behavior of screw connections. Chen et al. [15] conducted experimental studies on the shear capacity and failure modes of screw connections between steel-timber composite structures. Feng et al. [16] concluded that the screw diameter and plate thickness greatly affect the shear capacity of screw connections. Lu et al. [17] identified limitations in the design equations of existing codes for predicting the shear capacity of screw groups.

Through literature research, the authors have found that screw DSCs are primarily used in midply shear wall (MSW) structures [2, 18-25], as illustrated in Fig. 1. In MSWs, the sheathing is placed in the center of the wall, sandwiched between the two side studs and the upper and lower tracks. Notably, the studs in MSWs are rotated by 90° relative to those in traditional shear walls, with screws passing through the studs, sheathing, and studs in sequence. This change results in a shift from single-shear to double-shear force mechanisms, significantly enhancing the shear capacity and lateral stiffness of MSWs [18-21]. Experimental studies by Varoglu et al. [18-19] revealed that the shear capacity and lateral stiffness of wood MSW are 2 to 3 times greater than those of traditional wood shear walls. Zhou et al. [22] and Brière et al. [23] investigated the seismic performance of CFS-MSWs and concluded that their shear capacity and lateral stiffness are 2 to 4 times higher than those of traditional CFS shear walls. Based on the theoretical design equations proposed by Yanagi et al. [26] for determining the shear capacity of steel plate shear walls, it can be concluded that using design equations for screw SSCs to estimate the shear capacity of MSWs is conservative.

However, existing studies have predominantly focused on the shear performance of screw SSCs, with limited attention given to screw DSCs. Zhou et al. [27] conducted monotonic and cyclic loading tests on the shear performance of nail SSCs and DSCs, demonstrating that the shear capacity and stiffness of nail DSCs are significantly higher than those of nail SSCs. Liu [28] performed an experimental study on single-screw DSCs for thicker steel plates and derived corresponding design equations. However, the influence of various parameters on the shear capacity of single-screw DSCs remains unclear. Despite the aforementioned research efforts, there is a lack of studies addressing the shear performance of screw group DSCs, and the existing shear capacity design equations are applicable only to screw SSCs. Further verification is required to assess whether these equations are suitable for predicting the shear resistance of screw DSCs.

Based on the problems mentioned above, this study aims to adopt the verified FE model to investigate the shear performance of both single screw and screw group DSCs. The study explores the influence of various parameters, including sheet strength and thickness, screw diameter, screw connection type, number of screws, screw spacing, and screw arrangement, on the failure modes and shear capacity of single screw and screw group DSCs. Finally, the results of the parametric analyses are used to evaluate the applicability and feasibility of the design formulas for single screw or screw group DSCs, as proposed by AISI S100-2016 [29], GB 50018-2002 [30], EN 1993-1-3:2006 [31], and AISC 360-16 [32].

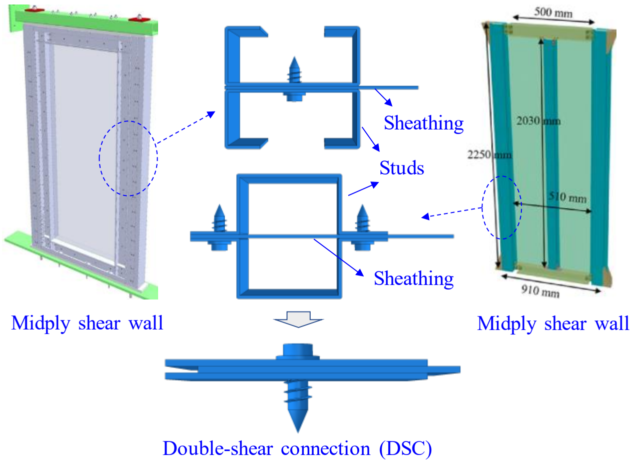

Fig. 1 Application of screw DSCs

2. Modeling and validation

2.1. *FE model*

The FE models of screw DSC and SSC were established based on the test specimen geometry in the literature [28]. The dimensions of the steel plate were 220 mm × 50 mm, with sheet thickness (T) ranging from 3.0 mm to 6.0 mm. The steel plate was made of Q235 steel, and the mechanical properties were obtained from tensile coupon tests [28]. It is noted that the overlap length between steel plates was 60 mm, and three different screw diameters (D) were used: 4.8 mm, 5.5 mm, and 6.3 mm. To prevent tearing failure at the ends and edges of the plates, the screw end and edge distances were 30 mm and 25 mm, respectively. Notably, the distance from the center of the screw hole to the end of the plate satisfies the general code requirement of being greater than $3D$.

The FE model of screw DSC and SSC is shown in Fig. 2. Due to the complex structure of the screw, modeling and meshing become challenging. Additionally, the intricate contact between the threads and the steel plate may cause convergence issues in the calculation, leading to significantly higher computational costs. To address these challenges, simplifications were made to the screw solid model, based on the screw modeling methods outlined in the literature [8,33]. The simplifications include: (1) treating the screw and washer as a single solid unit; (2) simplifying the screw head and threaded shank into a cylinder shape; (3) neglecting any damage to the steel plate or the screw during the drilling process; and (4) disregarding the preload force generated in the steel plate by the screw.

Comment 3: The manuscript mentions several simplifications in the FE model (e.g., ignoring the preload force, thread interactions, and damage to the steel plates during drilling). While these are justified for computational efficiency, the potential impact of these assumptions on the accuracy of results should be discussed more explicitly.

During modeling, C3D8R elements are used for all model components. The steel constitutive model adopts an ideal elastic-plastic model, considering material hardening effects. The elastic modulus (E) was set at 206 GPa, the second modulus was $0.01E$, and Poisson's ratio (v) was 0.3. Since self-drilling screws are primarily made of carbon steel, which exhibits brittle fracture when the ultimate strength is reached, the ductile damage criterion is adopted for the screws. The fracture strain and stress triaxiality values were referenced from the literature [8, 34]. After repeated trial calculations and calibration, the fracture strain and stress triaxiality values in this study were 0.762 and 0.207, respectively. Moreover, the elastic modulus and ultimate strength of the screws were 206 GPa and 1250 MPa, respectively [1]. Considering the stress concentration caused by the screw threads, the stress concentration factor was set at 1.79 [35], and the effective ultimate strength was taken as 700 MPa. Contact pairs are defined between steel plates and between steel plates and self-drilling screws. The contact properties include hard contact in the normal direction and tangential behavior governed by the penalty method, with a friction coefficient of 0.3. In the screw DSC model (see Fig. 2(a)), the right ends of the upper and lower steel plates are fully fixed, and a displacement load was applied in the U1 direction at the coupling point RP-1 on the left end of the middle plate. The boundary constraints and applied loads for the screw SSC model (see Fig. 2(b)) are identical to those for the screw DSC model. The maximum displacement, based on the load-displacement curves derived from the tests, was applied to the FE model. For consistency, the displacement load at RP-1 is set to 6 mm. It should be noted that the mesh was refined at the locations where the stresses are concentrated, and coarser mesh elements were used in areas of lower stress. To capture the stress concentration area effectively, the area had a side length of 30 mm, as shown in Fig. 2. To avoid convergence issues due to complex interactions between the screws and the holes in the steel plate, an explicit dynamic solver was employed.

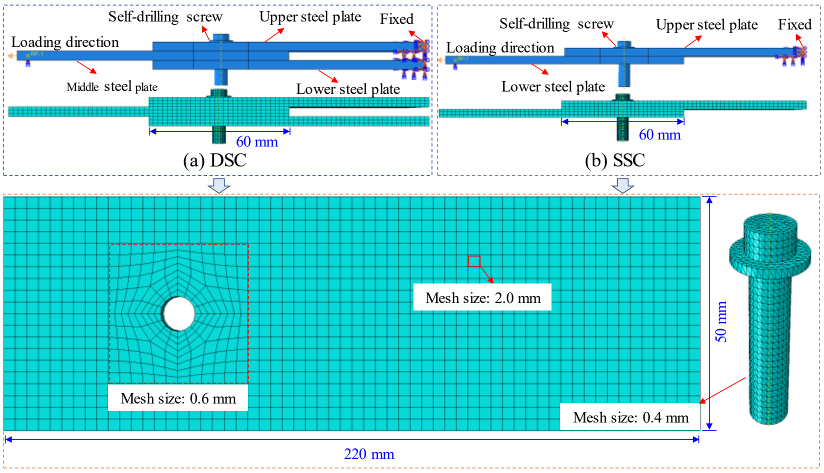

(a) DSC (b) SSC

Fig. 2 FE model

2.2. *Model validation*

To further validate the accuracy of the established FE model, the numerical results were compared with the experimental results.

2.2.1. *Failure modes*

Experimental studies [28] have shown that the failure modes of single screw DSCs can be classified into three types: bearing failure, coupled bearing and shear failure, and shear failure. When bearing failure occurred in screw DSCs (see Fig. 3(a)), the middle steel plate near the screw hole experienced significant plastic deformation along the thickness direction, while the screw shank produced notable bending without shearing. This failure mode exhibits clear warning signs before the specimen fails, indicating ductile damage. When coupled bearing and shear failure occurred in screw DSCs, self-drilling screw shear fracture was accompanied by noticeable deformation near the hole wall of the middle steel plate, the shear failure surface formed at the junction of the steel plates, as depicted in Fig. 3(b). When shear failure occurred in screw DSCs, the screw shank developed two shear failure surfaces, and these failure surfaces are smooth. The failure surfaces occurred in the junction of the steel plates. In addition, as demonstrated in Fig. 3(c), when shear failure occurred, the screw head remained perpendicular to the steel plate, while the screw bottom tilted slightly. There is no significant deformation of the screw holes, and no clear warning signs precede the failure, indicating a brittle failure.

In addition, experimental studies have shown that the failure modes of single-screw SSCs can be classified into two types: shear failure and screw tilting accompanied by steel plate warping, as illustrated in Fig. 4. It is found that there is no noticeable deformation near the screw hole before screw shear failure, and no warning signs are evident, indicating brittle failure. When screw tilting and steel plate warping occurred, the screw shank produced significant plastic deformation, with the screw shank tilting in the direction of the applied force.

Compared to the failure modes of screw SSCs, screw DSCs exhibit a key difference: during bearing failure, the middle steel plate near the screw holes undergoes significant plastic deformation along the thickness direction. As shown in the stress distribution diagram, the screw-bearing region in DSCs is approximately rectangular, whereas the screw-bearing region in SSCs is triangular. For screw DSCs, the specimen typically experiences coupled bearing and shear failure, the phenomenon not observed in single-screw SSCs. In the case of shear failure, DSCs have two smooth shear failure surfaces, while SSCs only have one.

Comparing the failure modes concluded from the tests and simulations, it is found that the failure modes of the two are in good agreement.

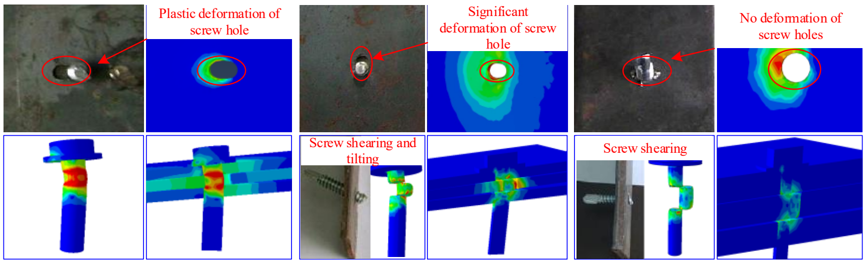

(a) Bearing failure (b) Combined bearing and shear failure (c) Shear failure

Fig. 3 Failure modes validation for DSCs

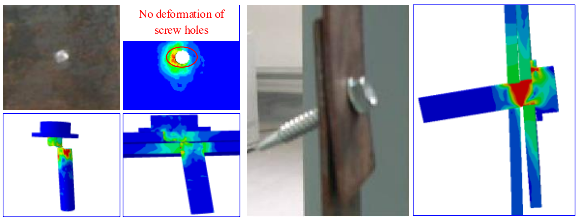

(a) Shear failure (b) Screw tilting and steel plate warping

Fig. 4 Failure modes validation for SSCs

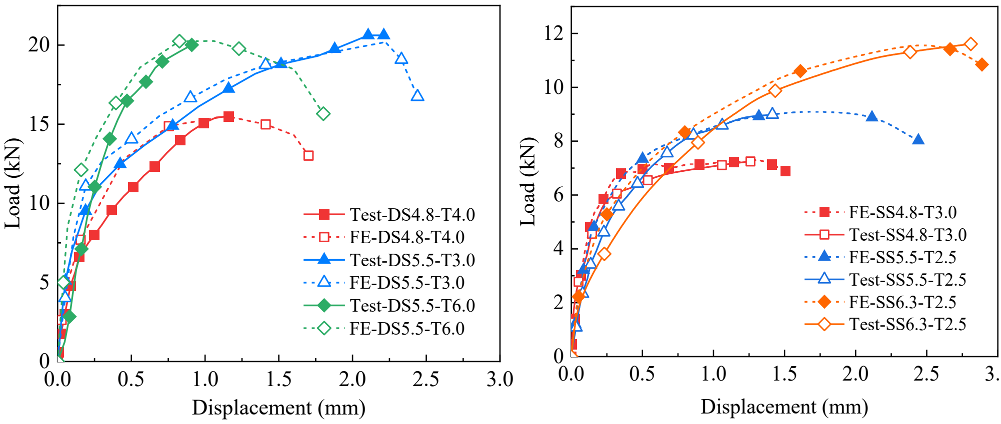

(a) DSCs (b) SSCs

Fig. 5 Comparison of load versus displacement curves

2.2.2. Load versus displacement curves

Fig. 5 compares the load versus displacement curves obtained from tests and simulations. It can be observed that the load-displacement curves for screw DSCs or SSCs can be classified into three phases. Initially, during the loading phase, the screw connections behave elastically. As loading continues, the stiffness of screw connections gradually decreases, plastic deformation increases, and the load grows nonlinearly with the displacement, which corresponds to the plastic phase. Finally, when the shear capacity of screw DSCs reaches its peak value, displacement and deformation continue to increase, but the shear capacity suddenly decreases, and the stiffness becomes negative, signaling the failure stage. These findings are generally consistent with the analyses presented in the literature [28]. Due to the inevitable damage during specimen fabrication, the simulation results tend to be higher than the test results. Overall, the load-displacement curves for both screw DSCs and SSCs are well simulated using the FE method.

2.2.3. Shear capacity

Fig. 6 compares the shear capacity of single screw DSCs and SSCs obtained from both tests and simulations. It is seen that the test and FE values for both screw DSCs and SSCs are in good agreement. Statistical analysis indicates that the average value of $P_{\mathrm{Test}}/P_{\mathrm{FE}}$ of screw DSCs is 1.01, with a coefficient of variation of 2.67%, and the absolute value of the error does not exceed 5%. The average value of $P_{\mathrm{Test}}/P_{\mathrm{FE}}$ of screw SSCs is 1.00, with a coefficient of variation of 0.93%, and an absolute value of error does not exceed 2%. These results demonstrate that the FE model can simulate the shear capacity of screw DSCs and SSCs with high accuracy.

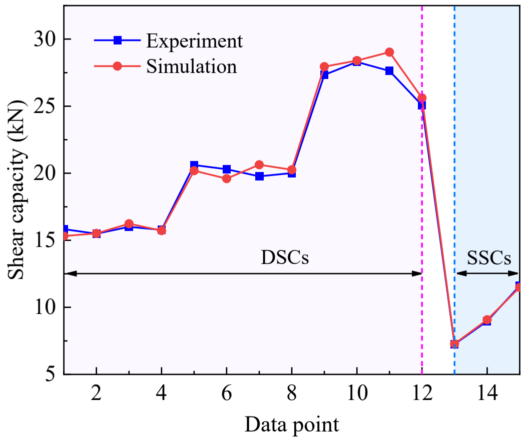

Fig. 6 Comparison of test values with FE values

2.2.4. Summary

Based on the analysis in subsections 2.2.1 to 2.2.3, the results demonstrate that the FE model accurately replicates the shear performance of screw DSCs and SSCs, making it suitable for subsequent parametric studies.

3. Shear capacity analysis for single screw DSCs

This section discusses the influences of steel strength, sheet thickness, screw diameter, and screw connection types on the shear capacity of specimens, based on validated FE models. The steel strengths considered are Q235, Q345, Q460, and Q550, with corresponding material properties provided in Table 1. Four different sheet thicknesses are used: 0.8 mm, 1.2 mm, 3.0 mm, and 6.0 mm. The screw diameters considered are 3.5 mm, 4.8 mm, 5.5 mm, and 6.3 mm. The screw connection types include single-shear and double-shear configurations.

Table 1
Material properties of steel [36-37]

Steel strength	f_y (MPa)	f_u (MPa)	E (GPa)	ε_y	ε_u
Q235	235	305	206	0.0011	0.0351
Q345	345	448	206	0.0017	0.0517
Q460	460	550	206	0.0022	0.0459
Q550	550	670	206	0.0027	0.0609

3.1. The influence of steel strength

The relationship curves of the shear resistance of screw DSCs with the change of steel strength are plotted in Fig. 7. It is observed that for *T* not exceeding 3.0 mm, the shear capacity of screw DSCs increases with steel strength. This is primarily due to bearing failure being the dominant mode of failure for smaller values of *T*, where the shear capacity is mainly controlled by the plate strength. A minimum of 7.9% increase in shear capacity is achieved when the steel strength is increased from 235 MPa to 550 MPa. In addition, as *D* increases, the influence of steel strength on the shear resistance becomes more pronounced. The maximum increase in shear capacity from 235 MPa to 550 MPa was 81.2% when *D* was increased to 6.3 mm. However, when *T* exceeds 3.0 mm, shear failure becomes more prevalent, and the shear capacity is primarily determined by the screw strength. In this case, the effect of steel strength on the shear capacity of single screw DSCs is minimal, with a change in shear capacity of less than 5%.

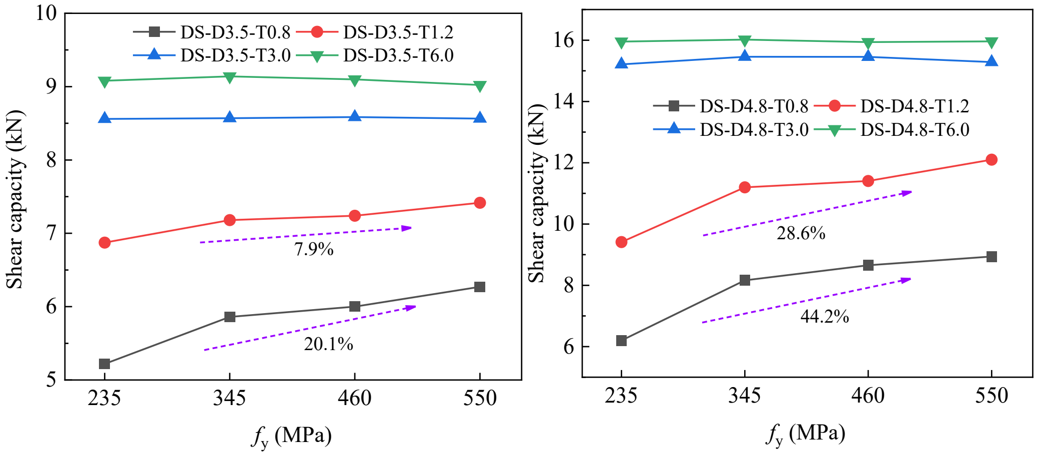

(a) *D*=3.5 mm (b) *D*=4.8 mm

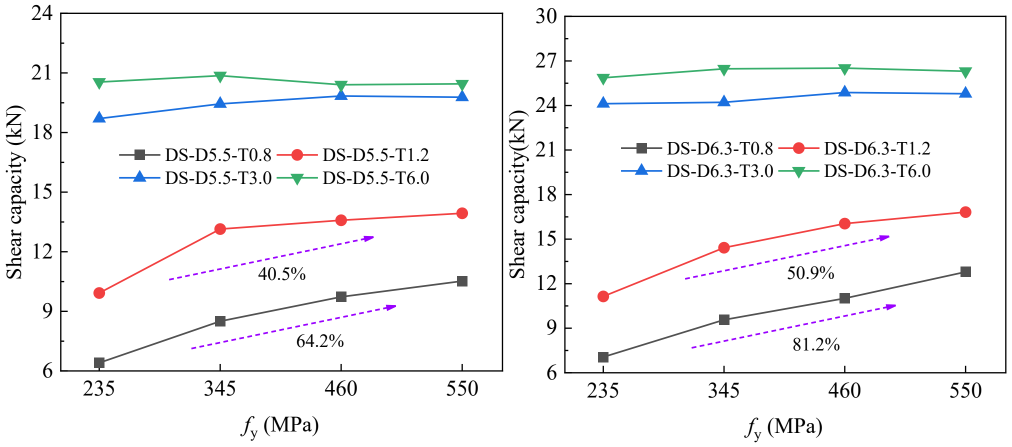

(c) *D*=5.5 mm (d) *D*=6.3 mm

Fig. 7 The influence of steel strength

3.2. The influence of sheet thickness

Fig. 8 gives the relationship curves of the shear capacity of single screw DSC specimens with sheet thicknesses (*T*). It is found that the shear capacity rises with the increase of *T* and eventually stays almost unchanged. Specifically, the shear capacity of screw DSCs increases by at least 34.6% and up to 241.8% as *T* grows from 0.8 mm to 3.0 mm. This increase is attributed to the larger bearing area provided by the thicker plate, which significantly enhances the shear capacity. However, as *T* exceeds 3.0 mm, the influence of further increases in *T* on shear capacity becomes negligible. This is because, beyond this threshold, shear failure becomes the dominant failure mode, and the shear capacity is controlled by the screw strength. Specifically, when *T* increases from 3.0 mm to 6.0 mm, the maximum increment in shear capacity is only 9.8%.

3.3. The influence of screw diameter

The relationship curves between shear capacity and screw diameter (*D*) are presented in Fig. 9. It is seen that the shear capacity of screw DSCs rises almost linearly with an increase in *D*. From Fig. 9(a)-(b), it is noticed that when *D* increases from 3.5 mm to 6.3 mm, the shear capacity increases by at least 35.2% and 62.2%, respectively. This is due to the increased bearing area resulting from the larger screw diameter, which in turn enhances the shear capacity. The influence of increasing *D* on shear capacity is more pronounced as the steel strength increases, as the shear capacity under bearing failure is positively correlated with both the steel strength and bearing area. As shown in Fig. 9(c)-(d), when *T* exceeds 3.0 mm, the shear capacity curves of different steel strengths almost overlap, indicating that the influence of increasing *D* on shear capacity becomes similar across different steel strengths. This is mainly because, for *T* exceeding 3.0 mm, the screw shank is exposed to shear failure.

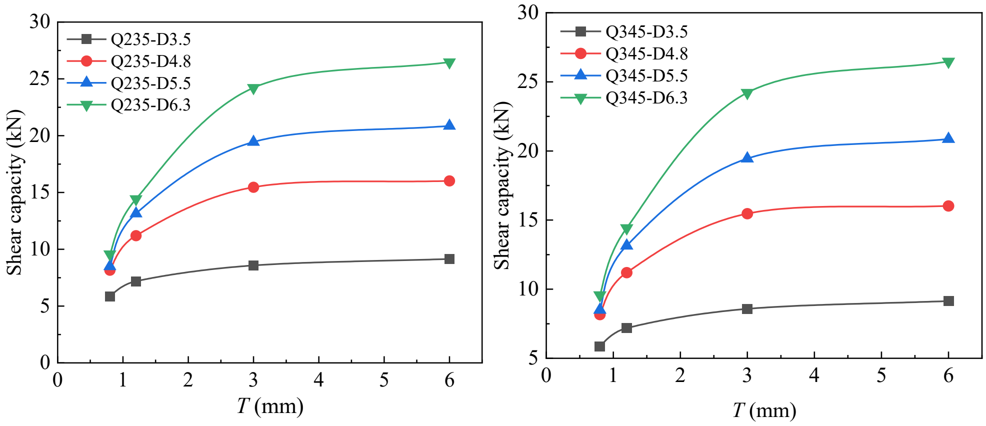

(a) f_y=235 MPa (b) f_y=345 Mpa

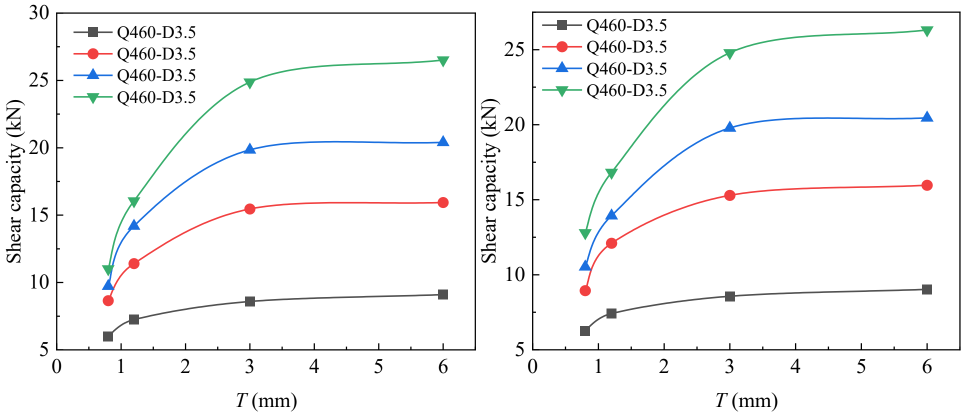

(c) f_y=460 MPa (b) f_y=550 MPa

Fig. 8 The effect of *T*

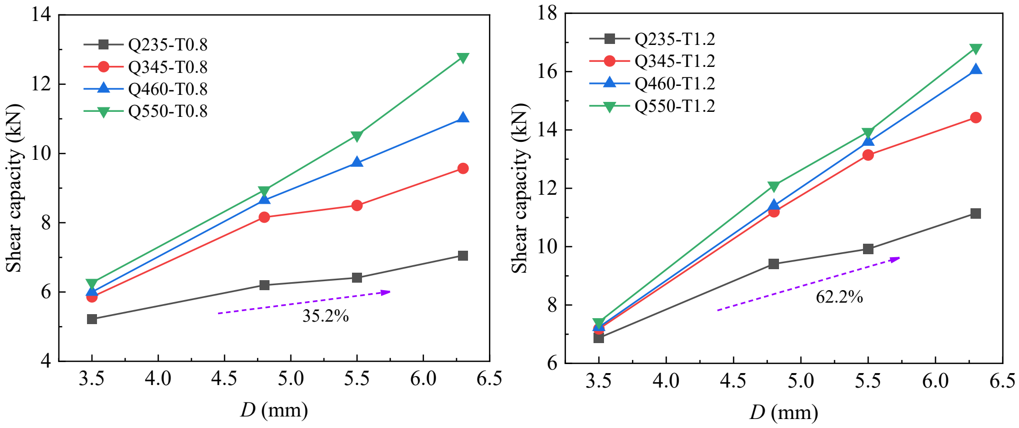

(a) *T*=0.8 mm (a) *T*=1.2 mm

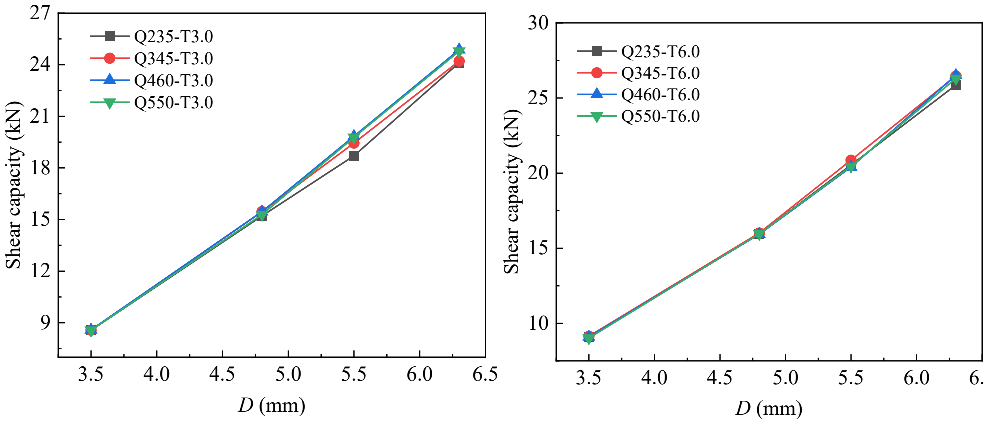

(c) *T*=3.0 mm (d) *T*=6.0 mm

Fig. 9 The effect of *D*

3.4. The influence of screw connection type

To investigate the influence of screw connection type on the shear behavior, 54 specimens were prepared for comparative analysis in this subsection. The steel strengths used were Q235, Q345, and Q420, the sheet thicknesses were 0.8 mm, 1.2 mm, and 2.0 mm, and the screw diameters included three types: 4.8 mm, 5.5 mm, and 6.3 mm. The screw connection types considered were single-shear and double-shear configurations. Figs. 10-12 illustrate the impact of different screw connection types on shear capacity for various parameters. These figures show that the shear capacities of single-screw DSCs are significantly higher than those of single-screw SSCs. In addition, Table 2 lists the FE values of shear capacity for 54 sets of specimens. It is observed that when the screw connection type changes from single-shear to double-shear, the shear capacity increases by at least 30.9%, with a maximum increase of 95.4%. During bearing failure, the middle steel plate of DSCs is constrained by the upper and lower steel plates, allowing for a more efficient utilization of the steel strength. In the case of shear failure, DSCs have two shear surfaces, while SSCs only have one, resulting in a significantly higher shear capacity for DSCs compared to SSCs. Notably, the screw connection type also changes the failure mode of specimens. Specifically, when *T* increases to 2.0 mm, screw SSCs experience coupled bearing and shear failure, while screw DSCs mainly undergo bearing failure.

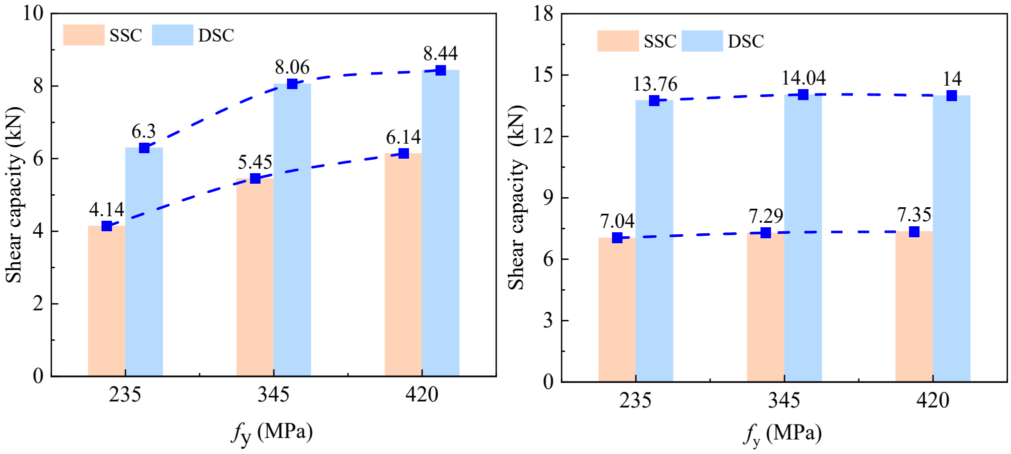

(a) *D*=4.8 mm, *T*=0.8 mm (b) *D*=4.8 mm, *T*=2.0 mm

Fig. 10 The influence of steel strength

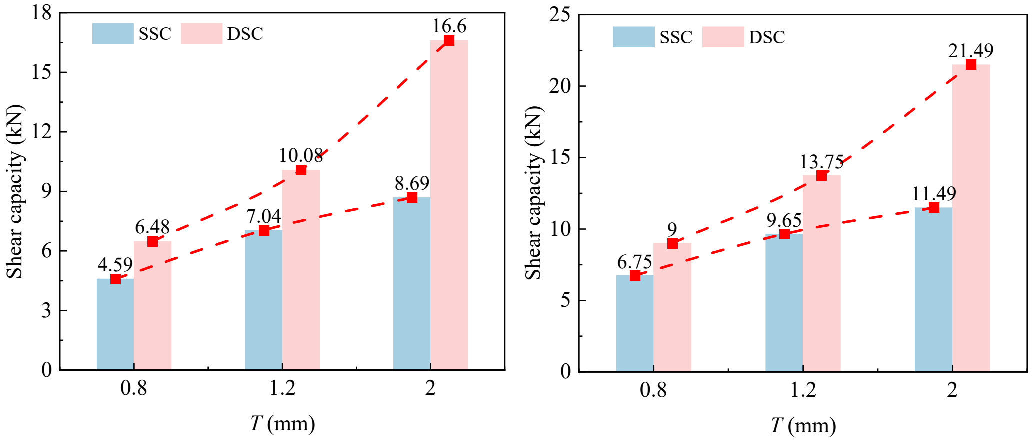

(a) f_y =235MPa, *D*=5.5mm (b) f_y =345MPa, *D*=6.3mm

Fig. 11 The influence of *T*

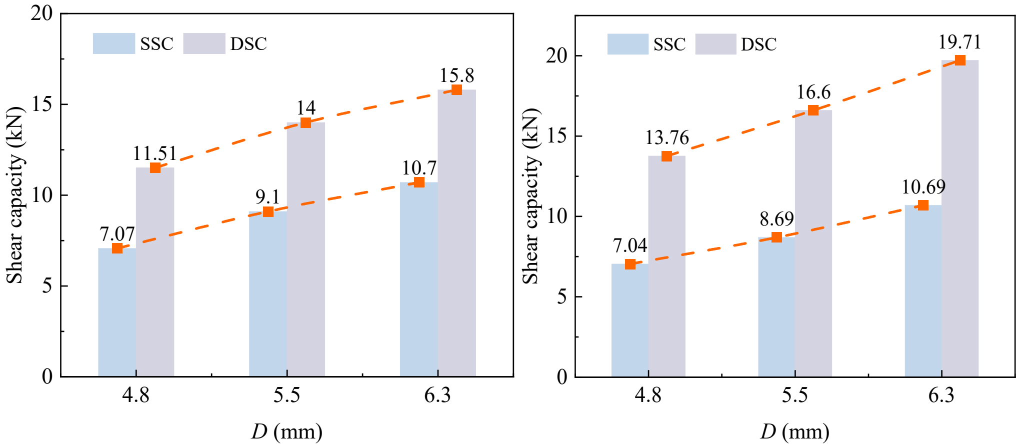

a) f_y = 420 MPa, T=1.2mm b) f_y =235MPa, T=2.0mm

Fig. 12 The influence of *D*

Table 2
The effect of screw connection type on shear capacity and failure modes

No.	Specimen name	P_u (kN)		Failure mode		$\frac{P_{u-DSC} - P_{u-SSC}}{P_{u-SSC}} \times 100\%$
		DSC	SSC	DSC	SSC	
1	Q235-D4.8-T0.8	6.30	4.14	B	B	52.2%
2	Q235-D4.8-T1.2	9.39	6.13	B	B	53.2
3	Q235-D4.8-T2.0	13.76	7.04	B	B+S	95.5%
4	Q235-D5.5-T0.8	6.48	4.59	B	B	41.2%
5	Q235-D5.5-T1.2	10.08	7.04	B	B	43.2%
6	Q235-D5.5-T2.0	16.60	8.69	B	B+S	91.0%
7	Q235-D6.3-T0.8	6.65	5.08	B	B	30.9%
8	Q235-D6.3-T1.2	10.68	7.38	B	B	44.8%
9	Q235-D6.3-T2.0	19.71	10.69	B	B+S	84.4%
10	Q345-D4.8-T0.8	8.06	5.45	B	B	48.0%
11	Q345-D4.8-T1.2	11.32	7.02	B	B	61.3%
12	Q345-D4.8-T2.0	14.04	7.29	B	B+S	92.4%
13	Q345-D5.5-T0.8	8.68	6.06	B	B	43.3%
14	Q345-D5.5-T1.2	13.17	8.66	B	B	52.1%
15	Q345-D5.5-T2.0	17.34	9.17	B	B+S	89.1%
16	Q345-D6.3-T0.8	9.00	6.75	B	B	33.4%
17	Q345-D6.3-T1.2	13.75	9.64	B	B	42.6%
18	Q345-D6.3-T2.0	21.49	11.49	B	B+S	87.1%
19	Q420-D4.8-T0.8	8.44	6.14	B	B	37.6%
20	Q420-D4.8-T1.2	11.51	7.07	B	B	62.9%
21	Q420-D4.8-T2.0	14.00	7.35	B	B+S	90.4%
22	Q420-D5.5-T0.8	9.64	6.83	B	B	41.3%
23	Q420-D5.5-T1.2	14.00	9.10	B	B	53.8%
24	Q420-D5.5-T1.2	17.53	9.30	B	B+S	88.4%
25	Q420-D6.3-T0.8	10.39	7.70	B	B	35.0%
26	Q420-D6.3-T1.2	15.80	10.70	B	B	47.7%
27	Q420-D6.3-T2.0	21.56	11.67	B	B+S	84.7%

Notes: "B" represents bearing failure; "S" denotes shear failure. $P_{u\text{-DSC}}$ and $P_{u\text{-SSC}}$ denote the shear capacity of screw DSCs and SSCs, respectively.

4. Shear capacity analysis for screw group connections

Although Section 3 provided a parametric analysis of the shear capacity of single-screw DSCs, in practical engineering, components are typically connected using two or more screws. Previous research has demonstrated a remarkable group effect on the shear capacity of screw group SSC specimens [5-7]. To gain a deeper understanding of the shear performance of screw group DSCs, this section discusses the effects of various parameters on shear capacity and failure modes.

4.1. Model parameters

In this study, four parameters are considered: the number of screws, screw spacing and arrangement, and steel plate thickness. The number of screws (n) is 2, 3, 4, and 5. The screw spacing (s) is defined as 2D, 3D, and 4D, where D adopts 4.8 mm. The screw arrangement is divided into two types, A and B, as indicated in Fig. 13. The steel plate thicknesses (T) are 0.8 mm, 1.2 mm, and 3.0 mm, respectively, with Q235 steel strength. As an example, S2-A-3D-T3.0 indicates a configuration where S2 denotes 2 screws with arrangement A, 3D represents a screw spacing of 3 times the screw diameter, and T3.0 denotes a steel plate thickness of 3.0 mm. It is noted that when n is increased to 5 and s is raised to 4D, the screw connection no longer satisfies the specification requirements. Therefore, when n reaches 5, only s of 2D and 3D are considered. In total, 42 specimens were prepared to investigate the shear performance of screw group DSCs with different parameters.

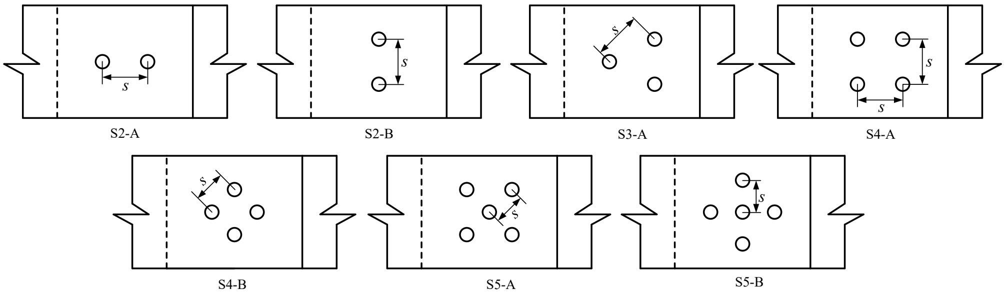

Fig. 13 Number and arrangement of screws

4.2. Failure modes

Based on the FE results, the failure modes of screw group DSCs can be classified into two categories: bearing failure and coupled bearing and shear failure. Fig. 14 exhibits typical failure modes for 14 specimens. When T is less than 3.0 mm or n exceeds 2, the specimen primarily experiences bearing failure.

When T reaches 3.0 mm and n is 2, the specimen mainly undergoes coupled bearing and shear failure. As indicated in Fig. 14(a), when $n = 2$, the screw arrangement is A, and $T = 0.8$ mm, the specimen is primarily subjected to bearing failure. In this case, the deformation of screw holes in the middle plate, near the forced end, is larger than that of the screw holes farther from the forced end, and there is no significant deformation of the screw shank. However, when the screw arrangement is changed to B, the deformation of the two screw holes in the middle steel plate remains almost identical, with no noticeable deformation of the screw shank, as illustrated in Fig. 14 (b). When T increases to 3.0 mm, the specimen undergoes coupled bearing and shear failure, as displayed in Fig. 14 (c)-(d). In this failure mode, the screw holes in the middle steel plate experience significant plastic deformation, the screws exhibit a shear failure surface, and the failure surface occurs at the junction of the upper and the middle steel plates. In addition, a significant shear deformation in the screw shank is observed at the junction of the lower and the middle steel plates. When n exceeds 2, the specimens primarily experience bearing failure, as shown in Fig. 14(e)-(n). In this case, the screw holes in the middle steel plate near the forced end undergo obvious plastic deformation, while those farther from the forced end deform less. The screw holes in the upper and lower plates show no visible deformation. As T increases (see Fig. 14(f), (h), (j), (l), and (n)), the screw shank produces significant bending deformation. However, as n increases, the bending deformation of the screw shank decreases.

It is concluded that both n and T significantly influence the failure mode of screw group DSCs. However, when the number of screws exceeds 2, further increases in the number of screws do not affect the failure mode. Within the specified range of screw spacing, neither the spacing nor the arrangement has a significant impact on the failure mode. However, it is noted that the screw arrangement affects the degree of plastic deformation in the screw holes.

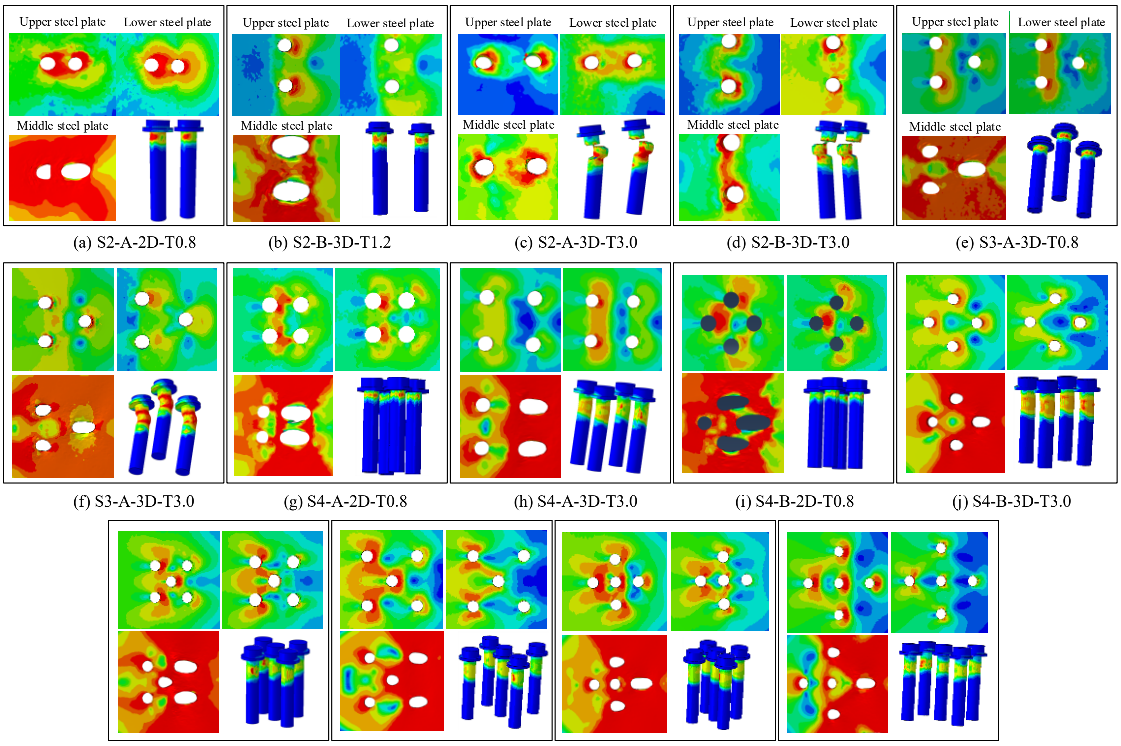

(a) S2-A-2D-T0.8 (b) S2-B-3D-T1.2 (c) S2-A-3D-T3.0 (d) S2-B-3D-T3.0 (e) S3-A-3D-T0.8

(f) S3-A-3D-T3.0 (g) S4-A-2D-T0.8 (h) S4-A-3D-T3.0 (i) S4-B-2D-T0.8 (j) S4-B-3D-T3.0

(k) S5-A-2D-T3.0 (l) S5-A-3D-T3.0 (m) S5-B-2D-T3.0 (n) S5-B-3D-T3.0

Fig. 14 Failure mode of screw group DSCs

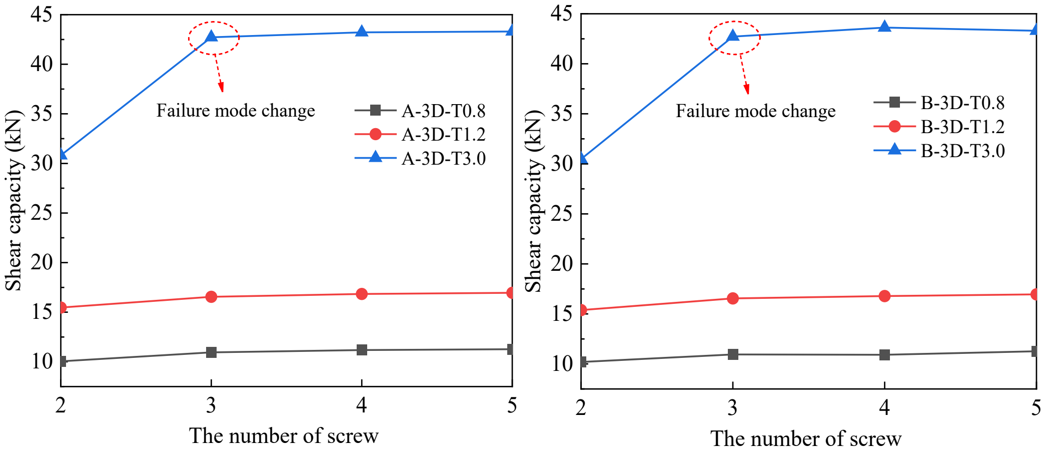

(a) Arrangement A (b) Arrangement B

Fig. 15 Effect of n on shear capacity

4.3. Parametric analysis

4.3.1. The influence of the number of screws

Fig. 15 presents the relationship curves for the variation of shear capacity of screw group DSCs with n. It is observed that the shear capacity increases as n increases. When T is 0.8 mm or 1.2 mm, the effect of increasing n on the shear capacity is minimal. Specifically, when n increases from 2 to 5, the shear capacity increases by 12.1% and 9.6% for screw arrangement A, and by 10.5% and 10.2% for screw arrangement B, respectively. This indicates that for smaller values of T, the specimens primarily experience bearing failure, and the screw strength is not fully utilized, so increasing n has a limited effect on the shear capacity. However, when T increases to 3.0 mm and n rises from 2 to 3, the shear capacity increases by 38.7% and 40.2% for screw arrangements A and B, respectively. When the number of screws increases further from 3 to 5, the shear capacity remains largely unchanged. This suggests that at $T = 3.0$ mm, specimens connected with 2 screws experience coupled bearing and shear failure, and the shear capacity is mainly governed by the screw strength. However, when *n* increases to 3, the failure mode changes from coupled bearing and shear failure to bearing failure, which is mainly controlled by the strength of the steel plate. Therefore, the increase in shear capacity is notably influenced when *n* rises from 2 to 3, but further increases in *n* (from 3 to 5) have little impact, as the failure mode remains bearing failure.

4.3.2. The influence of screw spacing

Fig. 16 presents the relationship curves showing the variation in the shear capacity of screw group DSC specimens to screw spacing. From Fig. 16(a)-(b), it is observed that when *n* is 2 and *T* is 0.8 mm or 1.2 mm, the shear capacity of screw group DSCs increases as *s* increases. Specifically, when *s* increases from 2*D* to 4*D*, the shear capacity increases by up to 15.2%, with a minimum increase of 12.1%. When *T* is increased to 3.0 mm, the effect of *s* on shear capacity becomes negligible, with the maximum change in shear capacity being only 2.0%. From Fig. 16(c)-(d), it is seen that when *n* is increased to 4, the effect of *s* on shear capacity diminishes, with the maximum amplitude change being only 7.4%. Similarly, from Fig. 16 (e)-(f), when *n* is raised to 5 and *s* is increased from 2*D* to 3*D*, the maximum increase in shear capacity for screw group DSCs with different plate thicknesses is 7.1%, 9.6%, and 1.5%, respectively. Overall, it can be concluded that the effect of screw spacing on the shear capacity of screw group DSCs decreases as the number of screws increases.

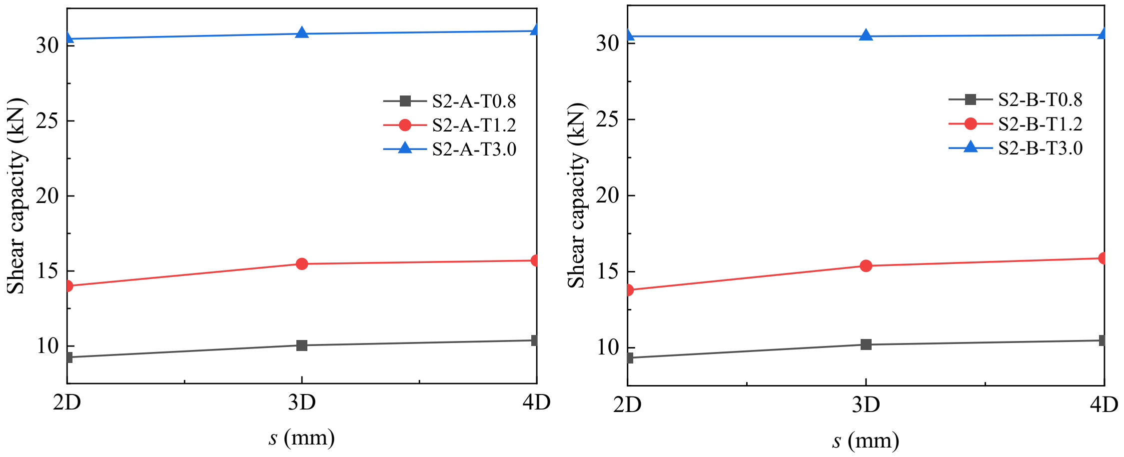

(a) S2-A
(b) S2-B

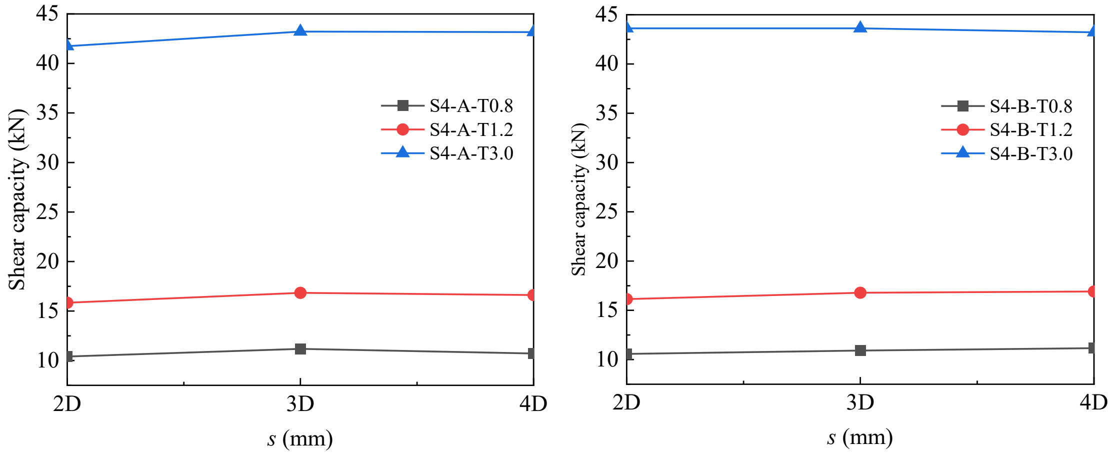

(c) S4-A
(d) S4-B

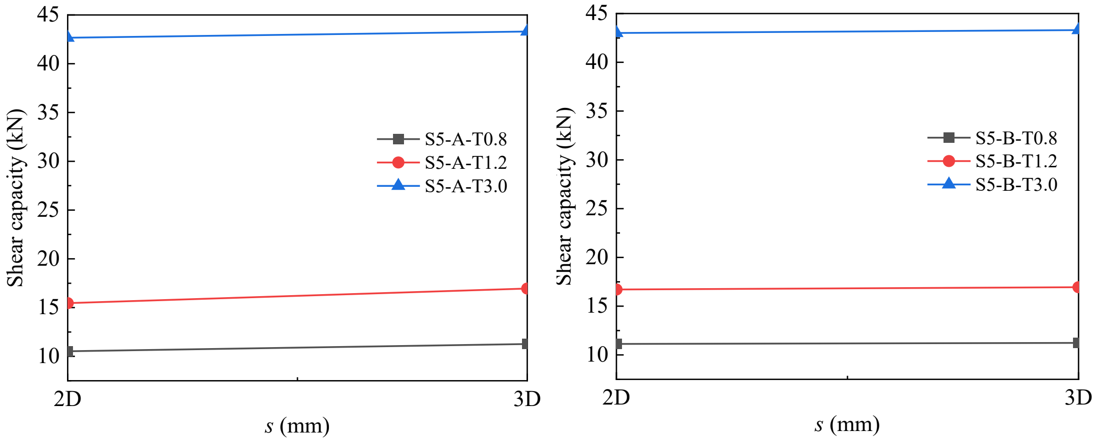

(e) S5-A
(f) S5-B

Fig. 16 Effect of *s* on shear capacity

4.3.3. The influence of the screw arrangement

Table 3 presents the influence of screw arrangement on the shear capacity and peak displacement of the screw group DSCs. It can be observed from the table that, when *s* and *T* are held constant, changing the screw arrangement has negligible impact on the shear capacity but a noticeable effect on the peak displacement. When *n* is 2, the peak displacement in arrangement A is generally greater than in arrangement B. However, as *n* increases to 4 or 5, the peak displacement in arrangement B becomes greater than in arrangement A. This can be attributed to the fact that when *n* is 2 and the screw arrangement is B, the displacements of the two screw holes are independent of each other, with each screw sharing half of the external load, resulting in nearly identical displacements for the screw holes. In contrast, when the screw arrangement is A, the displacements between the two screw holes are interdependent. The displacement in the screw holes near the tensile side is larger, while the displacement in the hole away from the tensile side is suppressed. Moreover, when multiple screws are used for the connection, a shear lag effect occurs, causing the screw holes near the tensile side to experience larger shear forces and greater deformation. As a result, for *n* = 4 or 5, the peak displacement in arrangement B generally exceeds that in arrangement A.

Table 3
Effect of screw arrangement on shear capacity and peak displacement

Specimen name	P_A/kN	Δ_A/mm	P_B/kN	Δ_B/mm	$\frac{\lvert P_B - P_A \rvert}{P_A}\times 100\%$
S2-2D-T0.8	9.25	6.41	9.33	4.92	0.9%
S2-3D-T0.8	10.05	6.50	10.20	6.11	1.5%
S2-4D-T0.8	10.38	7.04	10.48	6.35	1.0%
S2-2D-T1.2	14.00	5.84	13.79	6.12	1.5%
S2-3D-T1.2	15.47	6.78	15.38	6.12	0.6%
S2-4D-T1.2	15.70	6.49	15.88	6.33	1.2%
S2-2D-T3.0	30.47	2.87	30.47	2.37	0.0%
S2-3D-T3.0	30.81	2.30	30.47	2.04	1.1%
S2-4D-T3.0	30.99	2.32	29.86	2.05	3.7%
S4-2D-T0.8	10.41	4.39	10.58	5.75	1.6%
S4-3D-T0.8	11.18	5.06	10.92	5.34	2.3%
S4-4D-T0.8	10.71	4.65	11.16	5.60	4.2%
S4-2D-T1.2	15.84	5.25	16.14	6.15	1.9%
S4-3D-T1.2	16.84	5.53	16.78	5.43	0.4%
S4-4D-T1.2	16.61	5.30	16.91	5.84	1.8%
S4-2D-T3.0	41.74	6.33	43.62	6.89	4.5%
S4-3D-T3.0	43.22	6.53	43.62	6.89	0.9%
S4-4D-T3.0	43.16	6.33	43.22	6.47	0.1%
S5-2D-T0.8	10.52	4.18	11.13	5.36	5.8%
S5-3D-T0.8	11.27	5.36	11.23	5.38	0.4%
S5-2D-T1.2	15.46	6.49	16.71	5.34	8.1%
S5-3D-T1.2	16.95	5.49	16.94	5.68	0.1%
S5-2D-T3.0	42.67	6.04	43.01	6.40	0.8%
S5-3D-T3.0	43.30	6.16	43.30	6.19	0.0%

4.3.4. The influence of sheet thickness

Fig. 17 displays the relationship curves between shear capacity and sheet thickness (*T*). It is observed that the shear capacity increases almost linearly with *T*. Specifically, the shear capacity of screw group DSCs increases by at least 51.1% when *T* rises from 0.8 mm to 1.2 mm. When T increases from 1.2 mm to 3.0 mm, the shear capacity increases by a maximum of 176.0% and a minimum of 88.0%. These results demonstrate that the sheet thickness has a remarkable impact on the shear capacity of screw group DSCs.

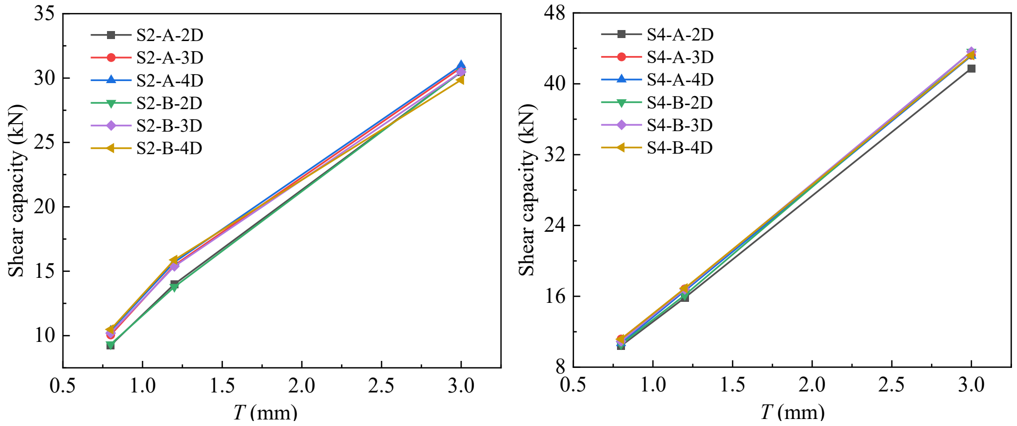

(a) S2 (b) S4

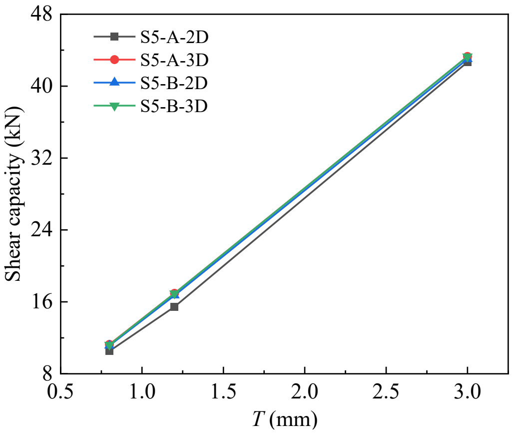

(c) S5

Fig. 17 Effect of T on shear capacity

5. Evaluation of design formulas

5.1. Design formulas for single screw SSCs

Currently, design formulas for predicting the shear capacity of single screw SSCs are available in AISI S100-2016 [29], GB 50018-2002 [30], EN 1993-1-3:2006 [31], and AISC 360-16 [32]. The specific forms of these formulas are as follows.

5.1.1. Screw shear failure

AISI S100-2016, GB 50018-2002, and EN 1993-1-3:2006 specify the shear capacity of single screw SSCs as shown in Eq. (1):

$$P_n = A_n F_n \tag{1}$$

where A_n indicates the screw cross-sectional area, F_n is the screw shear capacity, taken as 225MPa [28].

AISC 360-16 [32] specifies that the design shear capacity of the connections as:

$$P_n = \varphi A_n F_{nv} \tag{2}$$

Where F_{nv}=0.45F_u, φ=0.75.

5.1.2. Screw tilting accompanied by bearing failure

AISI S100-2016 defines the shear capacity as follows:

(1) When $t_2/t_1 \le 1.0$, the shear capacity of single screw SSCs takes the minimum value of Eqs. (3)~(5).

$$P_n = 4.2\sqrt{t_2^3 d} F_{u2} \tag{3}$$

$$P_n = 2.7 t_1 d F_{u1} \tag{4}$$

$$P_n = 2.7 t_2 d F_{u1} \tag{5}$$

where d denotes the nominal screw diameter, t_1 and t_2 represent the sheet thickness in contact with and away from the screw head, respectively, and F_{u1} and F_{u2} denote the sheet strength in contact with and away from the screw head, respectively.

(2) When $t_2/t_1 \ge 2.5$, the shear capacity of single screw SSCs takes the minimum value of Eqs. (6)~(7).

$$P_n = 2.7 t_1 d F_{u1} \tag{6}$$

$$P_n = 2.7 t_2 d F_{u1} \tag{7}$$

(3) When $1.0 < t_2/t_1 < 2.5$, the shear capacity of single screw SSCs is a linear interpolation of the two aforementioned scenarios.

GB 50018-2002 states:

(1) When $t_1/t = 1.0$, the shear capacity of single screw SSCs is calculated by Eq. (8).

$$P_n = 3.7\sqrt{t^3 d} f \quad \text{and} \quad P_n \le 2.4tdf \tag{8}$$

where t represents the thinner plate thickness, respectively, t_1 denotes the thicker plate thickness; f indicates the design tensile strength of the steel plate being connected.

(2) When $t_1/t \ge 2.5$, the shear capacity of single screw SSCs is derived by Eq. (9).

$$P_n \le 2.4tdf \tag{9}$$

(3) When $1.0 < t_1/t < 2.5$, the shear capacity of single screw SSCs is a linear interpolation of the two aforementioned scenarios.

EN 1993-1-3:2006 provides for the shear capacity for screw SSC specimens as determined by Eq. (10).

$$P_n = \alpha F_u dt \tag{10}$$

Where

$$\begin{aligned}
&\alpha = 3.2\sqrt{t_1/d} \le 2.1,\ \ t_2/t_1 = 1.0;\\
&\alpha = 3.2\sqrt{t_1/d} \le 2.1,\ \ t_2/t_1 \ge 2.5,\ \ t_1 < 1.0\text{mm};\\
&\alpha = 2.1,\ \ t_2/t_1 \ge 2.5,\ \ t_1 \ge 1.0\text{mm};
\end{aligned}$$

When $1.0 < t_2/t_1 < 2.5$, α is determined by linear interpolation.

AISC 360-16 specifies that the shear capacity of single screw SSCs is calculated by Eq (11).

$$P_n = 2.4\varphi F_u dt \tag{11}$$

where φ = 0.75, F_u denotes the sheet strength.

5.2. Design formulas for screw group SSCs

The shear capacity and reduction coefficient for the screw group SSC specimens can be derived from Eq. (12) and Eq. (13), respectively.

$$P = nP_1R_L \tag{12}$$

$$R_L = \left(0.535 + \frac{0.467}{\sqrt{n}}\right) \le 1.0 \tag{13}$$

where P_1 stands for the shear capacity of single screw SSCs; P represents the shear capacity of screw group SSCs; n denotes the number of screws; R_L represents the group effect reduction coefficient.

5.3. Comparison of FE values with predicted results

5.3.1. Comparison of shear capacity of single screw DSCs

Since the shear capacity formulas of the current specifications are only applicable to screw SSCs, the shear capacity of single screw DSCs can be calculated by adapting the formulas for screw SSCs and DSCs. Specifically, the shear capacity of screw DSCs is obtained by multiplying the SSCs shear capacity formulas by a coefficient n_v, where $n_v = 2$, indicating the presence of two shear surfaces. In addition, it is noticed that when shear failure or coupled bearing and shear failure occurs, the difference in the shear capacity between the specimens is not significant, so the same calculation formula is applied to both failure modes.

Table 4 provides a statistical analysis of the FE and theoretical shear capacity of screw DSCs, where P_u and P_n denote the FE and theoretical values, respectively. Table 4 shows that the design formulas of the GB, EN, and AISC specifications tend to be conservative when specimens undergo bearing failure. Specifically, the shear capacity of screw DSCs is underestimated by 19%, 38%, and 13%, respectively, with the average predicted shear capacity from the AISC specification being closest to the FE values. In addition, as shown in Fig. 18(a), when specimens experience bearing failure, the errors between the FE and theoretical values can reach up to 20%. Although the Chinese, American, and European specifications tend to be more conservative, some predicted values are biased towards being unsafe. Overall, the AISC specification provides a better agreement with the FE values. In cases of shear failure, the AISI, GB, and EN specifications are excessively conservative, with the shear capacity being underestimated by 86%. As seen in Fig. 18(b), the predicted values from the AISC specification align well with the FE values, with errors between the two being less than 20%. In conclusion, the AISC specification is more suitable for evaluating the shear capacity of single screw DSCs, regardless of whether bearing or shear failure occurs.

Table 4
Statistical characteristics on P_u/P_n for single screw DSCs

Failure modes	Number of specimens		P_u/P_n			
			AISI	GB	EN	AISC
Bearing failure	47	Mean	1.05	1.19	1.38	1.13
		COV/%	26.4%	26.5%	26.5%	18.5%
Shear/Coupled bearing and shear failure	16	Mean	1.86	1.86	1.86	0.99
		COV%	4.8%	4.8%	4.8%	4.8%

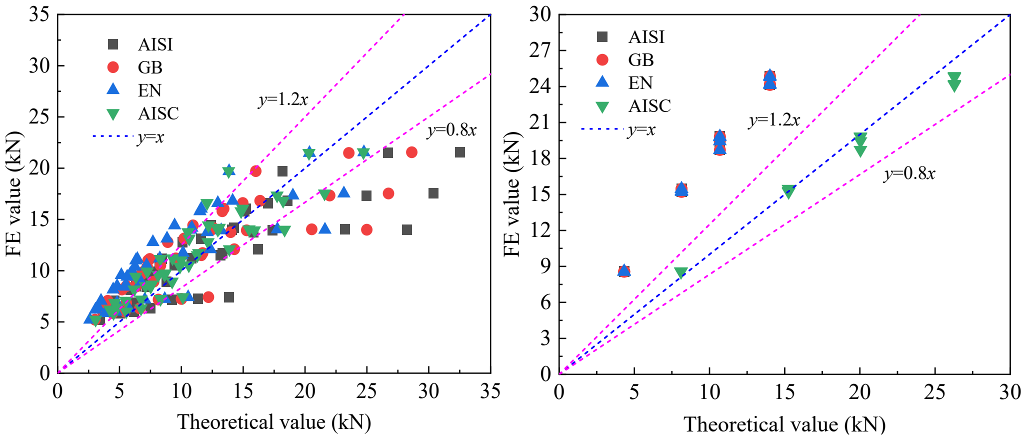

(a) Bearing failure (b) Shear or coupled bearing and shear failure

Fig. 18 Comparison of FE values with theoretical values for single screw DSCs

5.3.2. Comparison of shear capacity of screw group DSCs

Table 5 provides the statistical results of the FE versus predicted values of screw group DSCs. In addition, Fig. 19 shows the comparison of FE values with predicted values. Combined with Table 5 and Fig. 19, it is observed that when the specimen experiences bearing failure, the predicted shear capacity is insecure, with the average shear capacity being overestimated by 26% and the coefficient of variation reaching 27.11%. When the specimen undergoes coupled bearing and shear failure, the predicted shear capacity is more conservative, with the mean capacity underestimated by 16% and the coefficient of variation reduced to 1.16%. Therefore, the prediction equations can be employed to evaluate the shear capacity of specimens under coupled bearing and shear failure. However, for specimens undergoing bearing failure, the errors between most predicted and FE values exceed 20%, indicating that the existing prediction formulas are not suitable for assessing the shear capacity of screw group DSCs.

Table 5
Statistics on the ratio of FE values to predicted values for screw group DSCs

Failure mode	Number of specimens		P_u/P_n	P_u/P_c
Bearing failure	36	Mean	0.74	1.25
		COV/%	27.11	29.62
Coupled bearing and shear failure	6	Mean	1.16	/
		COV%	1.16	/

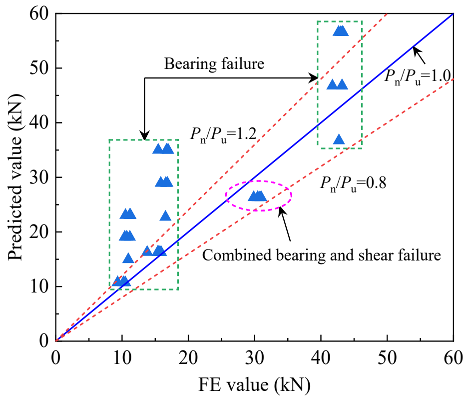

Fig. 19 Comparison of FE values with predicted values for screw group DSCs

5.4. Design formula modification

From the analyses in subsection 5.3.3, it is found that when the specimen undergoes bearing failure, the calculated shear capacity of screw group DSCs tends to be unsafe. Therefore, the existing equations for calculating the shear capacity of screw group DSCs have been modified, as shown in Eqs. (14)-(15). The comparison between the calculated values from the modified formula and the FE values is presented in Fig. 20. It can be observed that when the specimen experiences bearing failure, the calculated values from the modified formula are conservative.

$$P_c = \alpha n P_1' R_m \tag{14}$$

$$R_{\mathrm{m}}=\left(0.535+\frac{0.467}{\sqrt{2n}}\right)\leq 1.0 \tag{15}$$

where $P_1{}'$ represents the shear capacity of single screw DSCs, and α indicates the shear capacity modification factor. When $T = 3.0$ mm and $n > 2$, the specimen primarily experiences bearing failure, with the screw shank undergoing significant shear deformation, in which case $\alpha = 0.9$. For all other cases, $\alpha = 0.6$. P_{c} denotes the modified shear capacity of screw group DSCs, where n is the number of screws, and $2n$ indicates the number of screw shear surfaces. R_{m} is the modified group effect reduction factor.

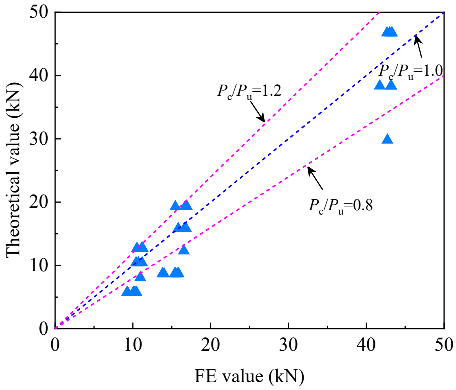

Fig. 20 Comparison of FE values and modified shear capacity of screw group DSCs

6. Conclusion

This study investigated the shear performance of screw DSCs using a validated FE model. The effects of steel strength, sheet thickness, screw diameter, screw connection types, number of screws, screw spacing, and screw arrangement on the failure modes and shear capacity of screw DSCs were discussed. Finally, the results of the parametric analyses were used to evaluate the applicability and feasibility of existing design formulas for predicting the shear capacity of single screw and screw group DSCs. The main conclusions are as follows:

(1) The parametric analysis results show that the shear capacity increases with steel strength when the sheet thickness is less than 3.0 mm. The shear capacity initially increases with sheet thickness and eventually stabilizes. Additionally, the shear capacity increases almost linearly with screw diameter. Notably, the shear capacity of screw DSCs is significantly higher than that of screw SSCs, although the relationship is not a simple twofold correlation.

(2) The failure modes of screw group DSCs can be classified into two types: bearing failure and coupled bearing and shear failure. Both the number of screws and the steel plate thickness significantly influence the failure mode of screw group DSCs. However, when the number of screws exceeds 2, further increases in the number of screws do not affect the failure mode. Screw spacing and screw arrangement have a minimal effect on the failure mode.

(3) The shear capacity of screw group DSCs increases with the number of screws. When the sheet thickness reaches 3.0 mm and the number of screws increases to 3, the failure mode changes from coupled bearing and shear failure to bearing failure. Beyond this point, further increases in the number of screws have minimal impact on the shear capacity. The effect of screw spacing on the shear capacity diminishes as the number of screws increases. While the screw arrangement has little effect on the shear capacity, it significantly impacts the peak displacement. Additionally, the shear capacity of screw group DSCs increases almost linearly with an increase in plate thickness.

(4) The evaluation results show that the predictions from the AISC specification formulas agree well with the FE values, regardless of whether bearing or shear failure occurs in single-screw DSCs. Therefore, the AISC specification is more suitable for evaluating the shear capacity of single-screw DSCs. In addition, the current specifications tend to be more conservative when evaluating the shear capacity of single-screw SSCs.

(5) When evaluating the shear capacity of screw group DSCs, it is found that the predicted shear capacity is not conservative in cases of bearing failure. However, the modified shear capacity for screw group DSCs is conservative, ensuring compliance with the requirements for a biased safe design. In cases of coupled bearing and shear failure, the predicted shear capacity remains on the conservative side.

Declaration of competing interests

The authors declare that they have no known competing financial interests or personal relationships that could have appeared to influence the work reported in this paper.

Acknowledgments

The authors gratefully acknowledge the financial support provided by the Science and Technology Innovation Plan Project of Hunan Province (Grant 2018NK2053) and Changsha Excellent Innovative Youth Training Program (Project No. kq1802001).

Reference

[1] W.H. Liu, L. Deng, W.J. Zhong, Y.L. Yang, Parametric study on the pull-out performance of screw connections in cold-formed thin-walled steel structures, Eng. Struct. 274 (2023): 115007, https://doi.org/10.1016/j.engstruct.2022.115007.

[2] Y.H. Xing, O. Zhao, W.Y. Wang, Testing, modelling and analysis of full-scale cold-formed steel center-sheathed shear walls in fire, Eng. Struct. 284 (2023): 115970, https://doi.org/10.1016/j.engstruct.2023.115970.

[3] T. Pekoz. Design of cold-formed steel screw connections, International Specialty Conference on Cold-formed Steel Structures, 1990.

[4] C.A. Rogers, G.J. Hancock, Screwed connection tests of thin G550 and G300 sheet steels, J. Struct. Eng. 125 (2) (1999): 128-136, https://doi.org/10.1061/(ASCE)0733-9445(1999)125:2(128).

[5] R.A. Laboube, M.A. Sokol, Behavior of screw connections in residential construction, J. Struct. Eng. 128 (1) (2002): 115-118, https://doi.org/10.1061/(ASCE)0733-9445(2002)128:1(115).

[6] S. Seleim, R.A. Laboube, Behavior of low ductility steels in cold-formed steel connections, Thin-Walled Struct. 25 (2) (1996): 135-151, https://doi.org/10.1016/0263-8231(95)00039-9.

[7] M.A. Sokol, R.A. Laboube, W. Yu, Determination of the tensile and shear strengths of screws and the effect of screw patterns on cold-formed steel connections, Center for Cold Formed Steel Structures Library, 1998, 1-172.

[8] K. Roy, H.H. Lau, T.C.H. Ting, R. Masood, A. Kumar, J.B.P. Lim, Experiments and finite element modelling of screw pattern of self-drilling screw connections for high strength cold-formed steel, Thin-Walled Struct. 145 (2019): 106393, https://doi.org/10.1016/j.tws.2019.106393.

[9] M.T. Huynh, C.H. Pham, G.J. Hancock, Experimental behaviour and modelling of screwed connections of high strength sheet steels in shear, Thin-Walled Struct, 146 (1) (2020): 106357, https://doi.org/10.1016/j.tws.2019.106357.

[10] M.T. Huynh, C.H. Pham, G.J. Hancock, Design of screwed connections in cold-formed steels in shear, Thin-Walled Struct.154 (5) (2020): 106817, https://doi.org/10.1016/j.tws.2020.106817.

[11] W. Lu, M. Pentti, J. Outinen, Z.C. Ma, Design of screwed steel sheeting connection at ambient and elevated temperatures, Thin-Walled Struct. 49 (12) (2011): 1526-1533, https://doi.org/10.1016/j.tws.2011.07.014.

[12] S.T. Vy, M. Mahendran, Screwed connections in built-up cold-formed steel members at ambient and elevated temperatures, J. Constr. Steel Res. 192 (2022): 107218, https://doi.org/10.1016/j.jcsr.2022.107218.

[13] W. Chen, J.H Ye, M.Y. Zhao, Steady-and transient-state response of cold-formed steel-to-steel screwed connections at elevated temperatures, J. Constr. Steel Res. 144 (2018): 13–20, https://doi.org/10.1016/j.jcsr.2018.01.016.

[14] G. Quan, J. Ye, W.C. Li, Computational modelling of cold-formed steel lap joints with screw fasteners, Structures. 33 (2021): 230-245, https://doi.org/10.1016/j.istruc.2021.04.062.

[15] Z.H. Chen, X.Y. Niu, J.D. Liu,K. Khan, Experimental study of thin-walled steel-timber single-shear connection with a self-tapping screw, Structures. 34 (2021): 4389-4405. https://doi.org/10.1016/j.istruc.2021.10.028.

[16] R.Q. Feng, Q. Cai, Y. Ma, G.R. Yan, Shear analysis of self-drilling screw connections of CFS walls with steel sheathing, J. Constr. Steel Res. 167 (2020): 105842, https://doi.org/10.1016/j.jcsr.2019.105842.

[17] L.F. Lu, D. Wang, W. Wang, H.H. Wu, K. Ding, K.K. Darkwah, H.W. Yan, Shear bearing capacity of self-drilling screw group connections of CFS sheets, Structures. 35 (2021): 160-171, https://doi.org/10.1016/j.istruc.2021.10.096.

[18] E. Varoglu, E. Karacabeyli, S. Stiemer, C. Ni, Midply wood shear wall system: Concept and performance in static and cyclic testing, J. Struct. Eng. 132 (9) (2006):1417-1425, https://doi.org/10.1061/(ASCE)0733-9445(2006)132:9(1417).

[19] E. Varoglu, E. Karacabeyli, S. Stiemer, C. Ni, M. Buitelaar, D. Lungu, Midply wood shear wall system: performance in dynamic testing, J. Struct. Eng. 133 (7) (2007): 1035-1042, https://doi.org/10.1061/(ASCE)0733-9445(2007)133:7(1035).

[20] W. Zheng, W.D. Lu, W.Q. Liu, Y. Li, Lateral loading behavior of glulam frame-midply hybrid lateral systems, Constr. Build. Mater. 220 (2019): 53-63, https://doi.org/10.1016/j.conbuildmat.2019.05.182.

[21] W. Zheng, W.D. Lu, W.Q. Liu, L. Wang, Z.B. Ling, Experimental investigation of laterally loaded double-shear-nail connections used in midply wood shear walls, Constr. Build. Mater. 101 (2015): 761-771, https://doi.org/10.1016/j.conbuildmat.2015.10.100.

[22] X.H. Zhou, Y.X. Zou, L. Xu, X.M. Yao, Y. Shi, Y. Guan, Seismic behavior of cold-formed thin-walled steel plate shear wall, J. Build. Struct. 5 (2020): 65-75.

[23] V. Brière, V. Santos, C.A. Rogers, Cold-formed steel centre-sheathed (mid-ply) shear walls, Soil Dyn. Earthq. Eng. 114 (11) (2018): 253-266, https://doi.org/10.1016/j.soildyn.2018.07.008.

[24] R. Deng, L. Ye, Y. Gao, Y. Shi, Y.H. Wang, Behaviour of cold-formed steel framed shear walls with slitted sheathing under lateral loading, Thin-Walled Struct. 192 (2023): 111108, https://doi.org/10.1016/j.tws.2023.111108.

[25] J.C. Wu, C.A. Rogers, Cold-formed steel centre-sheathed (mid-ply) shear walls of intermediate resistance, Thin-Walled Struct, 188 (2023): 110834, https://doi.org/10.1016/j.tws.2023.110834.

[26] N. Yanagi, C. Yu, Effective strip method for the design of cold-formed steel framed shear wall

with steel sheathing, J. Struct. Eng. 140 (4) (2013): 04013101, https://doi.org/10.1061/(ASCE)ST.1943-541X.0000870.

[27] L.N. Zhou, Y.H. Chui, C. Ni, Influence of middle member thickness on properties of double-shear nail joints, J. Struct. Eng. 144 (8) (2018): 04018109, https://doi.org/10.1061/(ASCE)ST.1943-541X.0002126.

[28] N. Liu, Research on shear behavior and design method of self-tapping screw connecting, Heilongjiang: Harbin Institute of Technology, 2007.

[29] AISI S100-2016, North American Specification for the Design of Cold-Formed Steel Structural Members. Washington D.C.: American Iron and Steel Institute, 2016.

[30] GB 50018−2002, Technical code of cold-formed thin-walled steel structures. Beijing: China Planning Press, 2002.

[31] EN 1993-1-3:2006, Eurocode 3, Design of Steel Structures - Part 1-3 General Rules - Supplementary Rules for Cold-formed Members and Sheeting. Brussels: The European Committee for Standardization, 2006.

[32] ANSI/AISC 360-16, Specification for structural steel buildings, American Institute of Steel Construction, 2016.

[33] L.F. Lu, Y.P. Zhang, W.Q. Fang, D.H. Yang, Experimental investigation and numerical analysis on shear-bearing capacity for self-drilling screw connections of cold-formed thin-walled steel II: Numerical analysis, J. Cent. South Univ. (Science and Technology). 44 (8) (2013): 3493-3502.

[34] J. Choung, C.S. Shim, H.C. Song, Estimation of failure strain of EH36 high strength marine structural steel using average stress triaxiality, Mar. Struct. 29 (1) (2012): 1-21, https://doi.org/10.1016/j.marstruc.2012.08.001.

[35] X.L. Zhang, Y.C. Zhang, Finite element analysis for shearing resistance of screw connections in crest-fixed profiled steel sheeting, Progress in Steel Building Structures. 12 (2) (2010): 23-29.

[36] Y. Shi, X.H. Zhou, Y. Guan, X.M. Yao, Study on mechanical behavior and effective length of cold-formed thin-walled steel roof truss, J. Build. Struct. 40 (11) (2019): 65−75.

[37] G. Shi, X. Zhu, Study on constitutive model of high-strength structural steel under monotonic loading, Eng. Mech. 34 (2) (2017): 50−59.

Advanced Steel Construction – Vol. 21 No. 3 (2025) 218–230
DOI:10.18057/IJASC.2025.21.3.4

LOCAL BUCKLING MECHANISM OF COLD-FORMED STEEL BUILT-UP COLUMNS: EXPERIMENTAL AND NUMERICAL INVESTIGATION

Yan-Chun Li [1], Yan Lu [2], Ai-Hong Han [1], Wei-Hua Li [1], Xin-Wei Wang [1] and Zong-Liang Wu [1, *]

[1] School of Civil Engineering And Communication, North China University of Water Resources and Electric Power, Zhengzhou 450045, China
[2] School of Civil Engineering Inner Mongolia University of Technology, Hohhot, Inner Mongolia, P.R.China
** (Corresponding author: E-mail: 13523442144@163.com)*

ABSTRACT

This study aims to providing in-depth insights into the local buckling mechanisms of cold-formed steel built-up box section (CFSBBS) columns. The CFSBBS is constructed from C- and U-section components that are connected using self-drilling screws at the flanges. The investigation encompasses both experimental and numerical analyses of buckling behaviors, failure characteristics, the interaction of plates, and the ultimate bearing capacity of the columns. The dimensions of the specimens were meticulously designed to facilitate the examination of pure local buckling modes, utilizing finite strip software CUFSM and the direct strength method. A finite element model was established to perform parametric studies aimed at elucidating the impact of the built-up flange plates on the buckling performance of CFSBBS columns. Three cross-sectional types were developed to assess the effect of screw spacing on the failure modes and ultimate bearing capacities of the CFSBBS columns. The results indicate that the in-plane deformation of the C-section flanges is partially constrained by the U-section flanges. The shape of the local buckling half-wave of the C-section may change due to the interaction of buckling between the C- and U-section component. Nevertheless, the influence on the ultimate bearing capacity is relatively small, within 10%. The findings of this research will serve as a foundational basis for future investigations.

ARTICLE HISTORY

Received:	25 March 2024
Revised:	3 January 2025
Accepted:	8 January 2025

KEYWORDS

Cold-formed steel built-up box section columns;
Local buckling;
Screw spacing;
Experiment;
Numerical simulation;
Plate group effect

1. Introduction

Local buckling represents a common challenge that differentiates cold-formed steel (CFS) from hot-rolled steel sections. Notably, CFS members retain their load-bearing capacity even after experiencing local buckling, attributable to the membrane effect inherent in CFS materials. Research on local buckling has its origins in the analysis of individual thin plates, with a primary focus on assessing their stability performance at the point of branch buckling. Numerous scholars have investigated the buckling modes of CFS built-up columns [1-6]. The ultimate bearing capacity of the CFS built-up columns was studied through experiment, numerical simulation, and theory [7-9]. The influence of the mutual effect between the plates and components in the CFS built-up members was not ignored [10,11]. However, few scholars analyze this key factor from the instability mechanism.

The majority of research concerning local buckling has primarily concentrated on individual thin plates, with analyses focusing on stability at the bifurcation point. Timoshenko [12] conducted a comprehensive investigation into the critical buckling load (CBL) of plates subjected to various boundary conditions and loading scenarios. Nonetheless, it is important to note that the plates within an actual cross-section are not independent entities. The plates constituting compression members exert a mutual constraint during local buckling, a phenomenon referred to as the "plate group effect" [13]. This effect serves to restrict the initial buckling of certain plates, ultimately leading to simultaneous buckling across all plates. To account for this interaction, a theoretical formula was proposed for calculating the local CBL of compressed members, incorporating the "plate group effect" [14]. Szymczak and Kujawa [14] further explored the theoretical aspects of the local CBL in simply supported channel steel, emphasizing the significance of the "plate group effect" [15,16]. CFS built-up box-section columns, which are comprised of multiple plates, also experience this mutual constraint, thereby influencing their buckling modes and ultimate strength. The buckling modes and the ultimate strength of CFS built-up columns will be affected by this factor. Consequently, it is imperative to consider the stability of the individual panels when designing such columns. However, there exists a paucity of research addressing the "plate group effect" specifically in the context of CFS built-up columns.

Several studies have examined the behavior of CFS built-up columns, primarily emphasizing the effects of geometric dimensions, screw spacing, screw arrangement, and cross-sectional types on the load-bearing capacity of these columns [17-20]. Fratamico [21] conducted experimental investigations into the buckling and failure behavior of composite columns, quantifying the ultimate strength, built-up actions, buckling interactions, and collapse behaviors of CFS built-up members. Kherbouche [5] performed both experimental and numerical analyses to assess the ultimate strength, deformation patterns, and lateral displacements of CFS closed-section columns, while also evaluating the impact of the thickness of the built-up components on bearing capacity and proposing a calculation method based on the direct strength approach. Chen [22] explored CFS back-to-back built-up columns with varying cross-sectional types, analyzing how the form of stiffening and the dimensions of web openings affect the bearing capacity of the CFS built-up columns. The majority of research concerning screw spacing has concentrated on the bearing capacity and failure modes of CFS built-up members [19-23]. Comprehensive investigations into the influence of screw spacing on the interaction between assembled plates are limited. Existing research indicates that the assembly effect does not enhance the ultimate capacity of CFS built-up box sections or built-up I-section members that are subjected to local buckling. Members characterized by partially built-up sections are prone to distortional buckling in the open component and local buckling in the closed component. Consequently, the relationship between various buckling modes and the ultimate capacity of built-up members is intricate [24-28]. Most studies yield only qualitative findings, which lack consistency. Both experimental and theoretical analyses have been performed to assess the mechanical performance and load-bearing capacity of CFS columns across different built-up configurations [29-33]. Lu [34] conducted a theoretical examination of the bearing capacity of CFS C-section columns subjected to local buckling and subsequently proposed a method for calculating this capacity. However, a systematic approach to adequately account for the "plate group effect" within the effective width method (EWM) remains unresolved.

This study presents an experimental and numerical investigation into the local buckling mechanisms and ultimate load-bearing capacity of CFSBBS columns. The research examines the effects of various factors on the buckling mode and overall bearing capacity of the built-up columns. A precise finite element model was developed and validated against experimental data to facilitate subsequent finite element parameter analyses. The findings of this research offer valuable insights for the design of cross-sectional dimensions of CFSBBS columns and establish a foundational basis for future investigations.

2. Experiment

2.1. Material properties

The experimental specimen utilized in this study was composed of the CFS galvanized steel plate, specifically of steel grade S280, sourced from the web of a CFS column from the same production batch, with a thickness of 1.2 mm. All tensile testing of the steel was performed based on the standard (GB/T228.1-2010) for tensile testing of materials. The apparatus employed for material property testing is illustrated in Fig. 1. The experimental setup incorporates a displacement-controlled loading system, operating at a loading rate of 1.5 mm/min. The testing machine autonomously manages the loading procedure and systematically records pertinent data throughout the duration of the test. A strain gauge, as depicted in Fig. 1(a), is affixed to both the front and back sides of the specimen at the midpoint of the original gauge length. Data collection is facilitated by the DH3820 high-speed static strain testing and analysis system. The outcomes of the material properties assessment are listed in Table 1.

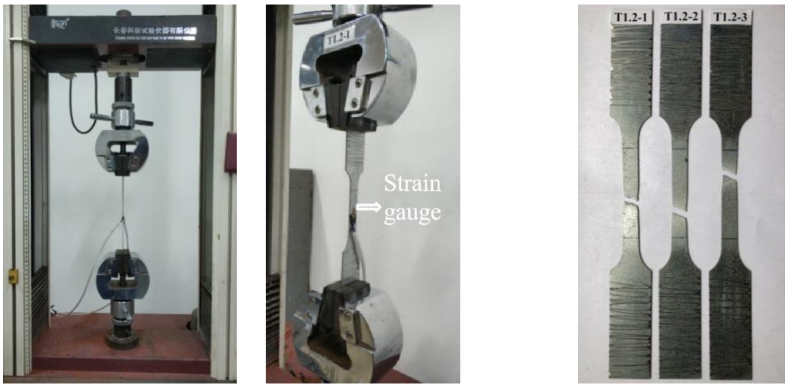

(a) Tensile testing device

(b) Testing specimen

Fig. 1 Material properties test

Table 1
Results of the material properties test

Specimens	Yield stress(N/mm^2)		Ultimate stress(N/mm^2)		Elastic modulus(10^{5}N/mm^2)		Elongation(%)	
	f_y	Mean	f_u	Mean	E	Mean	δ	Mean
T1.2-1	295.53		344.53		1.959		45	
T1.2-2	293.28	292.95	348.02	345.53	1.915	1.939	44	45.33
T1.2-3	290.04		344.05		1.943		47	

2.2. Experimental specimens

2.2.1. Section design of specimens

Three distinct types of cross-sectional members were subjected to testing, specifically C-section, U-section, and built-up box-section, as illustrated in Fig. 2(a). The local CBL (P_{crL}) and the distortional CBL (P_{crD}) for each specimen were calculated utilizing the CUFSM software [35], ensuring that the columns experienced buckling and failure in a purely local mode. The dimensions of the cross-section must satisfy the conditions $P_{\mathrm{crL}}<0.5P_{\mathrm{crD}}$ and $P_{\mathrm{uL}}<P_{\mathrm{crD}}$, where P_{uL} represents the ultimate capacity of local buckling determined through the DSM [36]. To further confirm that the designed specimens would undergo pure local buckling, finite element analysis was conducted using ABAQUS software. The nomenclature for the specimens is detailed in Fig. 2(b). For example, in B120-45-A1, The letter B represents built-up; the number 120 indicates the height of the web; the second number 45 refers to the screw spacing; the letter A represents axial compression; the last number 1 represents the number of repeated specimens.

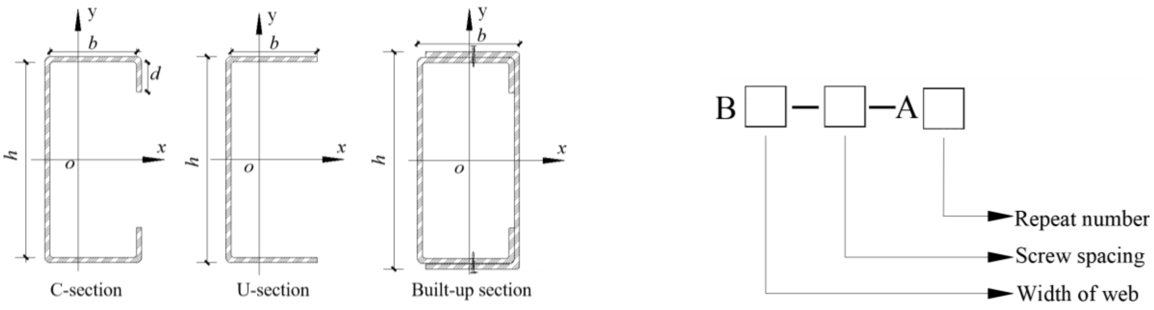

(a) Section type of test specimens

(b) Naming of test pieces

Fig. 2 Overview of test piece

The CFSBBS column was assembled using ST4.8 self-drilling screws, which were strategically positioned at the center of the flanges. The half-wavelength of the specimen obtained by the software CUFSM was used as the design basis for the length of specimens and the screw spacing. According to the height of the web, two types specimens of 120 series and 140 series were studied in this paper. The local buckling half-wavelengths of 120 series and 140 series specimens obtained from CUFSM were 89.9mm and 104.2mm, respectively. The specimen is subjected to fixed-end boundary conditions at both extremities. The specimen's length was approximately three times greater than the height of the web as advised by the Structural Stability Research Council (SSRC) [37]. Consequently, the lengths of the test specimens are 360 mm and 420 mm, respectively. Furthermore, the arrangement of the screws was established based on the buckling half-wavelengths, which include measurements of 45 mm, 90 mm, 150 mm, as well as 50 mm, 100 mm, and 150 mm, respectively, as illustrated in Fig. 3.

In Fig. 2(a), the variables h, b, and d denote the height of web, the width of flange, and the length of lip, respectively. The variable t signifies the thickness of the plate, while R indicates the outer radius of the bending angle. The actual cross-sectional dimensions of all specimens, as detailed in Table 2, have been measured to accurately reflect the real conditions.

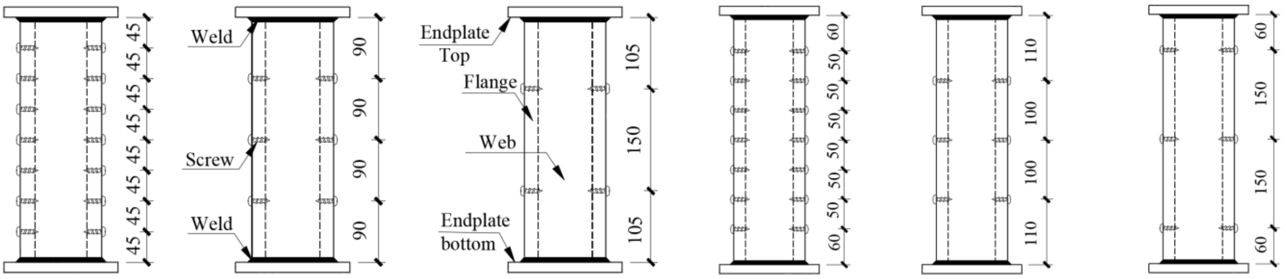

(a) B120 series column (L=360mm) (b) B140 series column (L=420mm)

Fig. 3 Layout of self-drilling screw spacing (unit: mm)

Table 2
Measured dimensions of the CFS built-up box-section column (unit: mm)

Specimens	Part	L	h	b_1	b_2	d_1	d_2	t	R	P_t/kN	P_{FE}/kN	P_{FE}/P_t
B120-45-A1	a	361	113.0	45.5	46.0	12.5	15.0	1.16	4.0	92.05	100.93	1.096
	b		117.0	49.0	48.0	\	\	1.17	3.5			
B120-45-A2	a	364	114.5	46.0	45.0	13.0	16.5	1.17	3.8	91.04	97.70	1.073
	b		116.0	47.5	50.0	\	\	1.16	3.5			
B120-45-A3	a	365	116.5	47.0	46.0	12.0	13.5	1.16	2.8	86.93	94.95	1.092
	b		118.0	49.0	47.0	\	\	1.14	3.0			
B120-90-A1	a	350	115.0	45.0	47.0	11.5	12.5	1.18	3.5	92.02	100.25	1.089
	b		116.0	48.0	51.0	\	\	1.17	3.5			
B120-90-A2	a	360	115.0	46.5	44.5	12.5	14.0	1.16	3.5	89.85	98.24	1.093
	b		118.0	50.0	47.0	\	\	1.16	3.0			
B120-90-A3	a	365	115.0	47.5	46.5	13.5	12.0	1.18	4.0	94.84	100.10	1.055
	b		118.0	46.5	50.0	\	\	1.17	2.8			
B120-150-A1	a	362	115.5	45.5	45.0	13.0	12.5	1.16	3.8	97.18	99.35	1.022
	b		118.0	47.5	50.5	\	\	1.14	3.5			
B120-150-A2	a	363	115.5	46.0	46.0	16.5	13.0	1.14	3.3	86.61	95.29	1.100
	b		118.0	47.5	49.0	\	\	1.16	3.0			
B120-150-A3	a	362	114.5	46.0	46.5	14.5	12.5	1.17	3.3	89.03	97.37	1.094
	b		113.0	45.5	46.0	12.5	15.0	1.16	4.0			
B140-50-A1	a	420	136.5	45.0	46.0	21.0	17.5	1.17	2.8	95.63	98.85	1.034
	b		137.0	47.0	47.0	/	/	1.16	4.0			
B140-50-A2	a	421	138.0	46.5	47.0	21.0	17.0	1.17	3.8	93.74	98.70	1.053
	b		139.0	45.5	47.0	/	/	1.16	3.5			
B140-50-A3	a	422	135.0	47.0	45.5	20.5	17.5	1.17	3.0	86.61	88.66	1.024
	b		138.0	46.5	47.0	/	/	1.14	3.5			
B140-100-A1	a	421	135.0	45.5	45.5	16.5	20.0	1.15	3.5	88.28	95.47	1.081
	b		136.0	46.5	48.0	/	/	1.16	4.5			
B140-100-A2	a	420	135.0	41.0	46.5	21.0	17.0	1.21	3.5	93.09	102.26	1.099
	b		138.0	46.5	47.0	/	/	1.18	3.5			
B140-100-A3	a	420	135.0	44.5	45.0	17.0	20.0	1.17	3.8	95.77	104.84	1.095
	b		137.5	47.5	47.5	/	/	1.15	3.8			
B140-150-A1	a	420	136.0	44.0	45.0	21.5	16.5	1.17	3.0	91.98	98.74	1.073
	b		137.0	45.5	50.0	/	/	1.16	4.0			
B140-150-A2	a	415	134.5	45.0	44.5	17.0	18.5	1.15	3.5	95.82	101.17	1.056
	b		138.0	45.0	47.0	/	/	1.15	3.8			
B140-150-A3	a	420	135.0	45.5	46.0	17.0	20.5	1.17	3.5	103.40	105.61	1.021
	b		137.5	47.5	46.0	/	/	1.17	3.8			
Mean												1.069
SD												0.028

2.2.2. Initial geometrical imperfection

The buckling mode and load-bearing capacity of CFS members are influenced by initial geometric imperfections. Consequently, it is essential to assess the initial geometric imperfections of the specimen prior to applying any load. The procedure commenced with the placement of the specimen on a measuring platform, followed by the positioning of a rigid rod on a designated plate. A measurement was then obtained using a dial gauge (refer to Fig. 4(a)), after which the rigid rod was removed to facilitate the measurement of an additional value. The dial gauge utilized has a measurement range of 50 mm and an accuracy of 0.01 mm. The difference between the two recorded values represents the unflatness of the plate. The symbols denoting the measured locations and imperfection parameters are depicted in Fig. 4(b). The results of the measurements are presented in Table 3. $\delta_{w,L1}/t$, $\delta_{w,L2}/t$, $\delta_{f,L1}/t$, $\delta_{f,L2}/t$ represent the ratio of local initial imperfection to the thickness of the specimen. The maximum values of $\delta_{w,L1}/t$, $\delta_{w,L2}/t$, $\delta_{f,L1}/t$, $\delta_{f,L2}/t$ are 0.417, 0.500, 0.500, 0.333, respectively, as shown in Table 3. The data indicate that the initial geometric imperfections for these specimens are minimal, thereby satisfying the quality standards for steel structure construction.

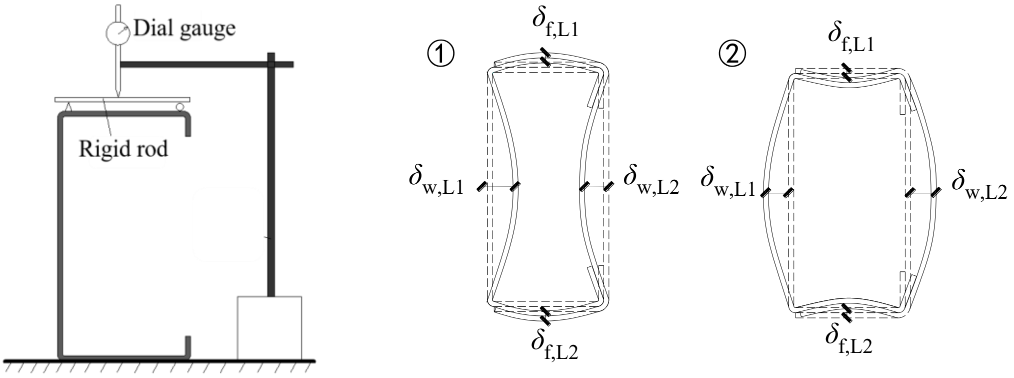

(a) Initial imperfection device (b) Imperfection parameter symbols

Fig. 4 Initial imperfection measurement

Table 3
Initial imperfection of the CFS built-up box-section column

Specimens	t/mm	Bending/mm（Concave+，convex-）				$\delta_{w,L1}/t$	$\delta_{w,L2}/t$	$\delta_{f,L1}/t$	$\delta_{f,L2}/t$
		Web of C-section($\delta_{w,L1}$)	Web of U-section($\delta_{w,L2}$)	Left flange($\delta_{f,L1}$)	Right flange($\delta_{f,L2}$)				
B120-45-A1	1.2	0.5	0.4	0.2	0.3	0.417	0.333	0.167	0.250
B120-45-A2	1.2	0.3	0.6	0.2	0.2	0.250	0.500	0.167	0.167
B120-45-A3	1.2	0.2	0.3	0.1	0.3	0.167	0.250	0.083	0.250
B120-90-A1	1.2	0.2	0.3	0	0.3	0.167	0.250	0.000	0.250
B120-90-A2	1.2	-0.1	-0.6	-0.4	-0.3	-0.083	-0.500	-0.333	-0.250
B120-90-A3	1.2	0.3	0.4	0.5	0.2	0.250	0.333	0.417	0.167
B120-150-A1	1.2	0.5	0.3	0.3	0.3	0.417	0.250	0.250	0.250
B120-150-A2	1.2	0.5	0.4	0.6	0.3	0.417	0.333	0.500	0.250
B120-150-A3	1.2	0.5	0.4	0.2	0.3	0.417	0.333	0.167	0.250
B140-50-A1	1.2	0.3	0.4	0.5	0.3	0.250	0.333	0.417	0.250
B140-50-A2	1.2	0.4	0.2	0.2	0.4	0.333	0.167	0.167	0.333
B140-50-A3	1.2	0.2	0.5	0.2	0.4	0.167	0.417	0.167	0.333
B140-100-A1	1.2	0.3	0.5	0.2	0.3	0.250	0.417	0.167	0.250
B140-100-A2	1.2	0.5	0.4	0.3	0.4	0.417	0.333	0.250	0.333
B140-100-A3	1.2	0.3	0.5	0.6	0.3	0.250	0.417	0.500	0.250
B140-150-A1	1.2	0.3	0.6	0.6	0.3	0.250	0.500	0.500	0.250
B120-90-A3	1.2	0.3	0.4	0.5	0.2	0.250	0.333	0.417	0.167
B120-150-A1	1.2	0.5	0.3	0.3	0.3	0.417	0.250	0.250	0.250
B120-150-A2	1.2	0.5	0.4	0.6	0.3	0.417	0.333	0.500	0.250
B120-150-A3	1.2	0.5	0.4	0.2	0.3	0.417	0.333	0.167	0.250
B140-50-A1	1.2	0.3	0.4	0.5	0.3	0.250	0.333	0.417	0.250
B140-50-A2	1.2	0.4	0.2	0.2	0.4	0.333	0.167	0.167	0.333
B140-50-A3	1.2	0.2	0.5	0.2	0.4	0.167	0.417	0.167	0.333
B140-100-A1	1.2	0.3	0.5	0.3	0.3	0.250	0.417	0.250	0.250
B140-100-A2	1.2	0.4	0.4	0.3	0.4	0.333	0.333	0.250	0.333
B140-100-A3	1.2	0.3	0.5	0.6	0.3	0.250	0.417	0.500	0.250
B140-150-A1	1.2	0.3	0.6	0.6	0.3	0.250	0.500	0.500	0.250
B140-150-A2	1.2	0.3	0.3	0.4	0.1	0.250	0.250	0.333	0.083
B140-150-A3	1.2	0.2	0.3	0.2	0.2	0.167	0.250	0.167	0.167
MAX						0.417	0.500	0.500	0.333

2.3. Loading preparation

The specimen undergoes axial compressive loading via a testing apparatus, as illustrated in Fig. 5. The CFSBBS column was constructed with an end plate measuring 360 mm × 280 mm × 16 mm, which was secured using fillet welds. Subsequently, the assembly was positioned on the apparatus depicted in Fig. 5 to establish the boundary conditions necessary for a fixed joint at both ends of the column.

In this study, strain gauges and Linear Variable Differential Transformers (LVDTs) were strategically positioned on all test specimens to facilitate precise measurements of strain and displacement variations during the loading process. Furthermore, strain gauges were installed at corresponding locations both internally and externally at the same cross-sectional position to assess the CBL of the specimens, as depicted in Fig. 6. Specifically, strain gauges were placed at one-quarter, mid-point, and three-quarters along the length of the column to effectively capture the peaks and troughs of the buckling wave. Initially, a vertical alignment instrument was employed to ensure geometric alignment of the specimen post-installation. Following this, a preload of 1 kN was applied to monitor strain value changes at the symmetrical measurement points of the specimen, thereby achieving physical alignment. Upon completion of both geometric and physical alignment, formal loading commenced, with an initial loading amplitude set at 5% of the estimated ultimate load for each loading increment. Once 80% of the estimated ultimate load was attained, the loading amplitude for subsequent increments was adjusted to 2% of the estimated ultimate load.

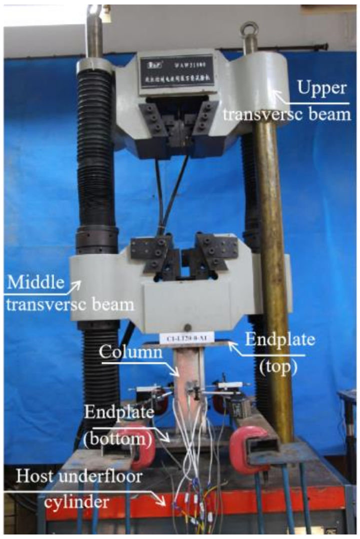

Fig. 5 Test loading device

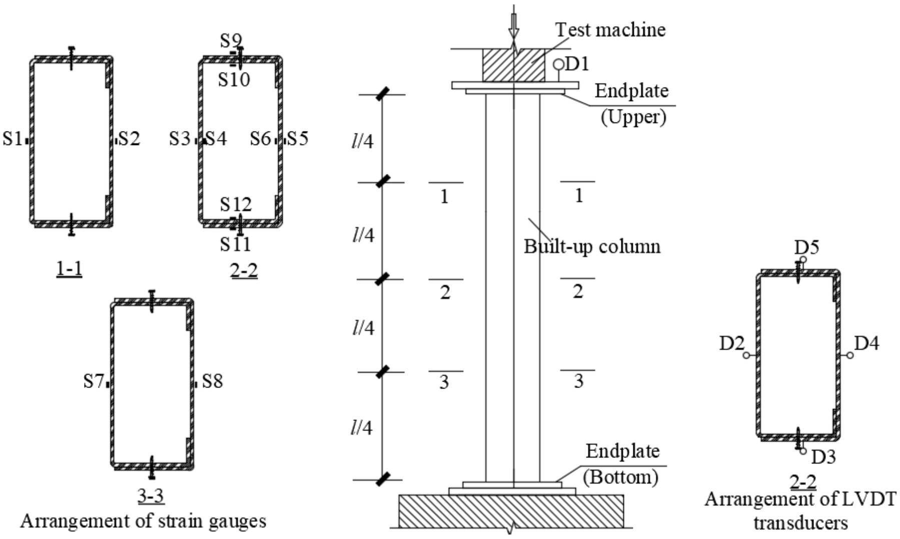

Fig. 6 Arrangement of strain gauges and LVDT transducers

2.4. Experimental results and discussion

2.4.1. Buckling behaviors of test members

Figs 7~8 show the buckling behaviors of B120 and B140 series built-up columns. The local buckling occurred first in Figs 7~8(Buckling) as the compression load increased, regardless of the specimen section types. As the idea of designing the specimen, there are three local buckling half waves in the experimental phenomenon. It can be observed that the specimens with screw spacing of 45 mm and 50 mm appear convex-concave-convex waves from the top to the bottom of the column. While the phenomena of the concave-convex-concave waves appear on the specimens with 90 mm, 100 mm, and 150 mm screw spacing.

As can be seen in Figs 7~8(Buckling), the U-section part buckled locally with the flange outwards, while the corresponding C-section part buckled locally with peaks and valleys from top to bottom on its web. It should be pointed out that the inward deformation of the U-section part can not be overserved for all the investigated members. The reason for such a phenomenon can be ascribed to the built-up interaction effect, i.e., the existing C-section part constrains the corresponding U-section part's flange inwards deformation while its flange can deform outwards freely. Additionally, for the specimens whose failure positions are close to the end plate, it is mainly caused by artificial welding errors or initial defects, but the load-bearing capacity of the three specimens is basically the same.

Nonetheless, given that the constructed members exhibit a consistent reserve of strength following local buckling, the column remains capable of supporting the additional compressive load. As the load continues to escalate, the out-of-plane deformation resulting from local buckling becomes markedly pronounced, as illustrated in Fig. 7~8(Peak). Ultimately, it was observed that columns failed in the local buckling mode Figs. 7~8(Failure). Similarly with the buckling occurring stage in Figs 7~8(Buckling), all the investigated members in the failed stage with their web buckled inwards and flange buckled outwards, i.e., the built-up interaction effect also exists in the post-local-buckling bearing stage. As a result, the existence of a built-up interaction effect makes the local buckling deformation mechanism of such built-up members different from that of the single limb member.

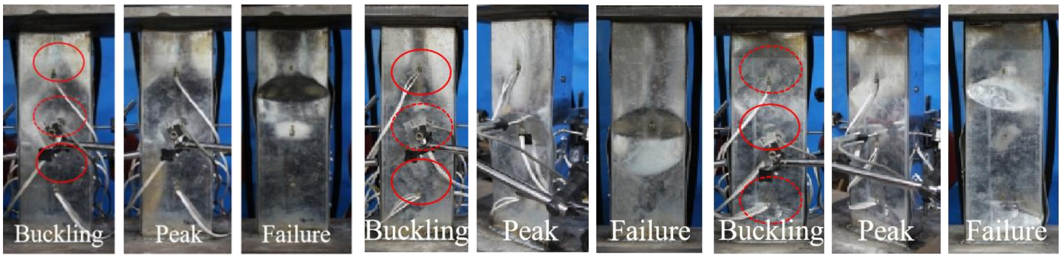

(a) B120-45 (b) B120-90 (c) B120-150

Fig. 7 Buckling mode and failure characteristic of B120 series specimens

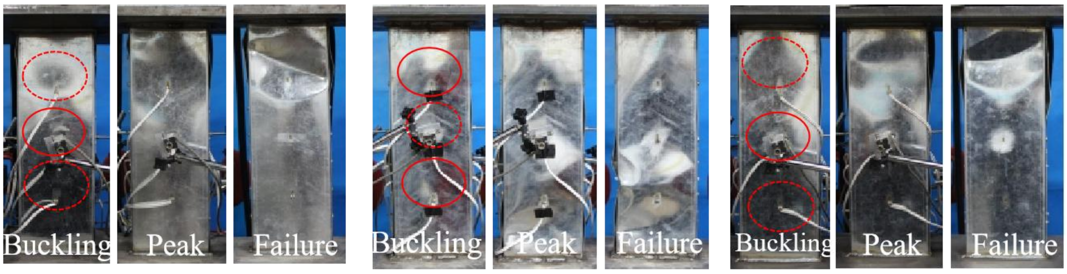

(a) B140-50 (b) B140-100 (c) B140-150

Fig. 8 Buckling mode and failure characteristic of B140 specimens

2.4.2. lateral deflection

The lateral deflection of the specimen provides a more precise representation of the specimen's buckling throughout the loading process. The lateral deflection & load-bearing capacity curves of the webs and flanges were illustrated in Fig. 9. The displacement gauges D3 and D5, positioned on the flanges of specimens B120-45-A1 and B120-90-A1, yield positive values, while gauge D2 on the web of the U-section and gauge D4 on the web of the C-section produce negative values. This indicates that the flanges of the U-section at the mid-span location are experiencing outward buckling, whereas the webs are undergoing inward buckling, which aligns with the observed experimental phenomena. Conversely, for specimens C4-L120-150-A1 and C4-L140-150-A1, the displacement gauges D3 and D5 register negative values, while D2 and D4 yield positive values. This suggests that the flanges of the U-section at the mid-span location are buckling inward, while the webs are buckling outward, a pattern that is similarly observed in the C-section. This behavior is consistent with the experimental findings. Notably, for specimen B140-50-A1, the flanges exhibit outward buckling during the initial buckling phase; however, upon reaching the load-bearing capacity, the flanges ultimately attempt to buckle inward. This behavior may be attributed to the post-buckling strength inherent in the specimen, which contributes to re-stability. Fig. 9(e) indicates that the displacement recorded by gauge D3 is 0, which may be attributed to a failure of the displacement gauge D3.

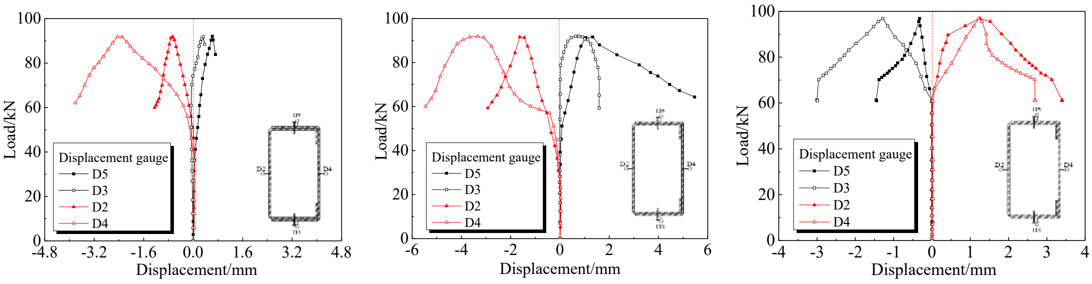

(a) B120-45-A1 (b) B120-90-A1 (c) B120-150-A1

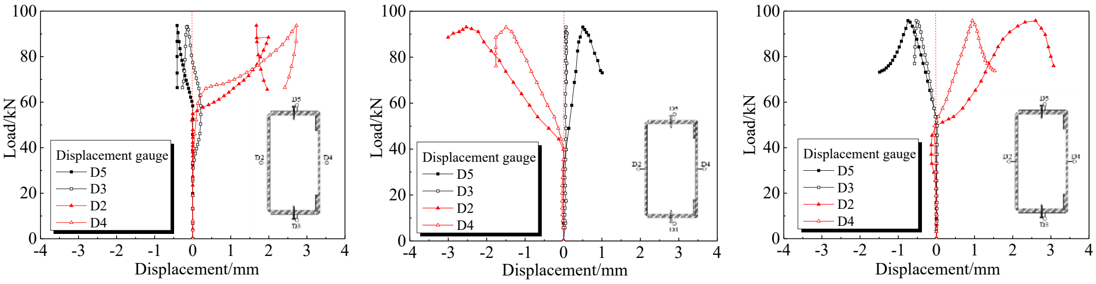

(d) B140-50-A1 (e) B140-100-A1 (f) B140-150-A1

Fig. 9 Load-deflection curve of the built-up columns

2.4.3. Buckling pattern

The possible local buckling modes of CFS built-up box section columns under axial pressure can be predicted from the experimental phenomena. Generally, webs and flanges buckle inward and buckle outward for single-limb members (see Fig.10(a)-10(b)). The two flanges must be symmetrically outward to ensure the 90-degree angle corner if the web buckles inward, as presented in Fig.10(a) and Fig.10(b). However, such local buckling phenomena will not be uniform for CFS built-up specimens, especially for CFS built-up columns with different screw spacing. The possible local buckling modes of the CFSBBS columns by the experimental investigation are presented in Fig.10(c-f). (i) Two types of local buckling modes in the flanges between the screws are defined: ① web buckling outward and the flanges will buckle inward (see Fig.10(c)); ② web buckling inward and the flanges will buckle outward (see Fig.10(d)). It is worth noting that the deformation of the built-up flanges is coordinated buckling (the degree and direction of the out-of-plane deflection of the two single plates are basically the same) whether it is buckling inward or buckling outward. The results indicate that the C-section has a coordinated and supportive effect on the deformation of the U-section. (ii) Fig.10(e) presents the buckling modes of the built-up section close to the screw position. The two flanges of the C-section buckle outward and the web tries to buckle inward. The two flanges of the U-section buckle outward and the web is slightly buckling inward, due to the coordination effects. It is worth mentioning that the two flanges are attached together that the distance from the screw to the intersection line between the flange and the web of the U-section (see Fig.10(e)). It indicates that the constraint effect of screws. (iii) The local buckling modes of the built-up section away from the screw position are shown in Fig.10(f). The two flanges of the C-section buckle inward and the web try to buckle inward. The two flanges of the U-section buckle inward and the web is slightly buckling outward, due to the coordination effects. (iv) Someone may feel that the C-section and U-section flanges in the CFS built-up box section will be tightly bonded together at the screw position. However, the experimental phenomena show that this is not the case (see Fig.10(g)). There is only one type of local buckling mode for the two flanges of the C-section, that is, webs buckling inward and flanges try to buckle outward. This is due to the effect of the screw thread on its drawing, so that the buckling modes of webs buckling outward and flanges buckling inward cannot appear. It should be noted that the test showed that the screw would tilt, but it was not pulled out and cut. This also shows that the shear slip occurs in the built-up flange plates. From the mechanical point of view, the axial pressure will produce a lateral force when the column is buckling. Due to the screw tilting, it is impossible to effectively resist this part of the new lateral force, which makes the local force of the member nonuniform, and may produce stress concentration in some parts. It accelerates the material to enter the yield stage and reduces the load-bearing capacity of the column.

It can be seen that the buckling mode of the U-section is affected and determined by that of the C-section. The mechanism of local buckling instability of the CFSBBS column is revealed, which further shows that the cooperative working performance of the built-up members is better and is conducive to the stability of the structure.

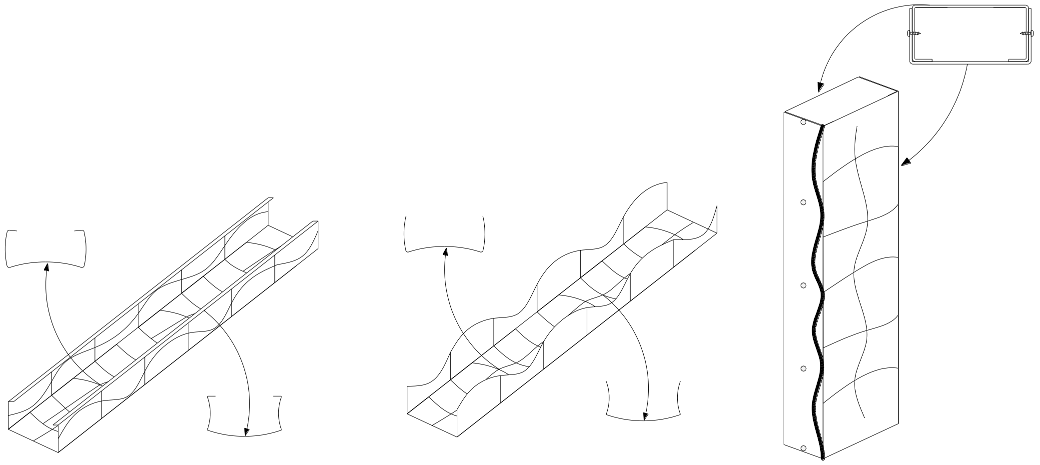

(a) Local buckling pattern in C-section

(b) Local buckling pattern in U-section

(c) Local buckling pattern of CFSBBS columns

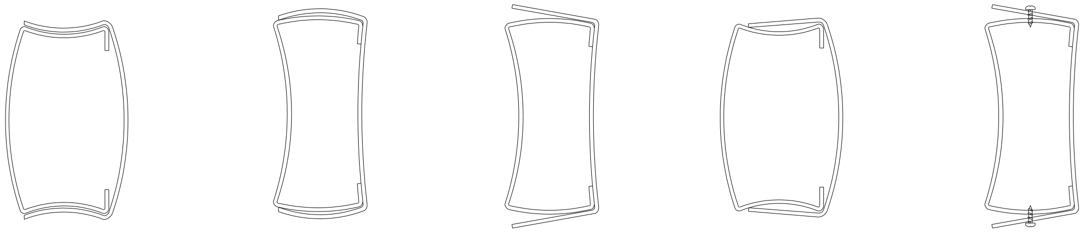

(d) Cross-section view of local buckling where there is no fasteners

(e) Cross-section view of local buckling where there is no fasteners

(f) Cross-section view of local buckling where there is close to fasteners

(g) Cross-section view of local buckling where there is away from fasteners

(h) Cross-section view of local buckling at fasteners connection locations

Fig. 10 Possible local buckling failure modes in CFSBBS columns

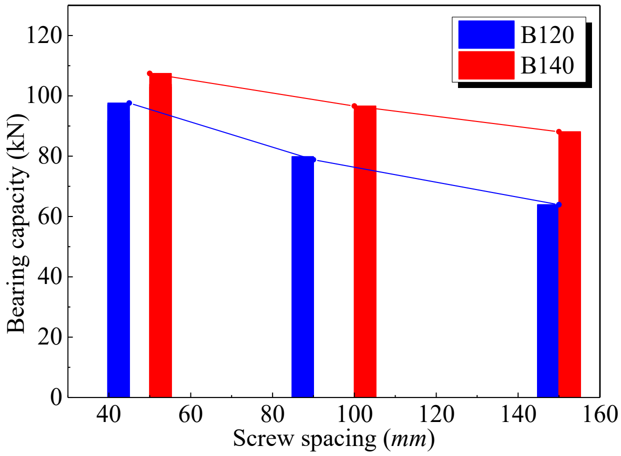

Fig. 11 Bearing capacity distribution of B120 and B140 members

2.4.4. Ultimate bearing capacity

The test results pertaining to the load-bearing capacity of the CFSBBS columns are presented in Table 2 and Fig. 11. The following key conclusions can be drawn from the analysis:

(1) The CBL and load-bearing capacity of CFSBBS are influenced by the spacing of the screws. Specifically, an increase in screw spacing correlates with a decrease in ultimate bearing capacity, suggesting that the effectiveness of the built-up section diminishes as screw spacing increases.

(2) For B120 series specimens, the variation in ultimate capacity due to different screw spacings ranges from 3% to 8%. Conversely, for the B140 series specimens, this variation is observed to be between 3% and 13%.

(3) The load-bearing capacity of specimens with a web height of 140 exceeds that of those with a web height of 120. Additionally, the B120 series specimens exhibit a greater sensitivity to changes in the screw spacing compared to the B140 series specimens.

3. Numerical simulation

The finite element (FE) software ABAQUS [38] was used to develop the linear and nonlinear numerical models of the CFSBBS columns, as illustrated in Fig.12. The geometric dimensions, initial imperfection, and material properties of FE models were all based on experimental data. The critical buckling load, elastic buckling state, failure characteristics, and the relationship between ultimate bearing capacity and axial displacement of the test specimens are obtained. The verified FE model also lays the foundation for the subsequent analysis of a large number of parameters.

3.1. Element and mesh

The finite element (FE) model utilized the S4R shell element, characterized as a four-node linear reduced integration element. Each node within this element possesses six degrees of freedom, encompassing translations along the x, y, and z axes, as well as rotations about these axes, as illustrated in Fig.12. For the modeling of the self-drilling screw ST4.8, an 8-node hexahedral linear reduced integration solid element, designated as C3D8R, was employed.

The mesh division of the FE model has two objectives: creating a sufficiently fine mesh to simulate the basic features of the deformation, and minimizing the number of elements to reduce the computational time. It is worth mentioning that the flange section of the built-up column is a perforated section with a hole in the middle, as provided in Fig.12. Therefore, the built-up flange section was divided into several regions. The 'Free Grid' command was applied to the screw area for fine meshing. A fine mesh was created near the screw hole to interpret the stress concentration. The maximum size of the shell element was 5 mm×5 mm. The mesh size of the self-drilling screw was about 0.68 mm×0.68 mm.

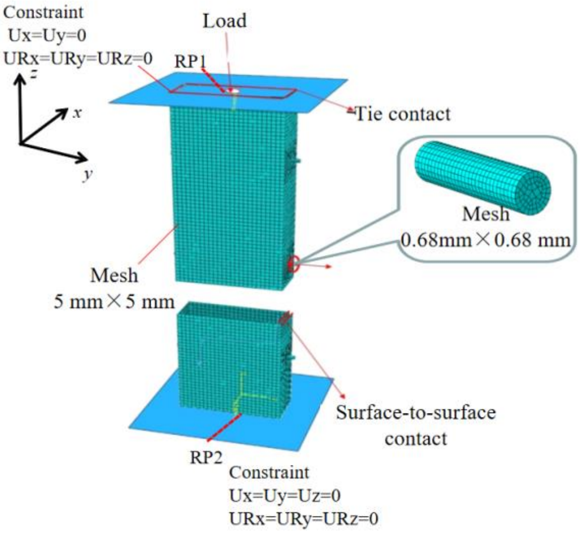

Fig. 12 Finite element model

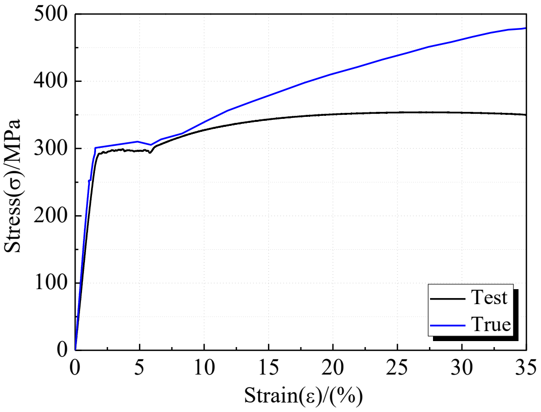

Fig. 13 Stress vs strain curve of the CFS

3.2. Material properties

The material properties of the FE models were entirely derived from the experimental results. It is important to note that there exists a discrepancy between the engineering stress-strain curve obtained from the tensile testing of the material and the actual stress-strain behavior of the material. Consequently, the measured engineering stress (σ) and strain (ε) curve was converted into the true stress ($\sigma_{\text{true}} = \sigma(1+\varepsilon)$) and strain ($\varepsilon_{\text{true}} = \text{In}(1+\varepsilon)\text{-}\sigma_{\text{ture}} / E$) curve of the steel in accordance with the specifications of ABAQUS software. The true stress-strain curve for the CFS, as obtained through this conversion, is illustrated in Fig. 13.

3.3. Initial imperfections

CFS inevitably has certain imperfections in processing and manufacturing as other types of metal materials. These imperfections mainly include geometric imperfections and material imperfections of members. Schafer [39] proposed several modeling methods when accurate data of geometric imperfection distribution cannot be obtained. The initial imperfections may be integrated into the numerical model through the superposition of various buckling modes, with their magnitudes regulated via Fourier transformation. Schafer [39] proposed the application of a maximum deviation, roughly equivalent to the thickness of the plate, as a straightforward heuristic. In the present study, the initial eigenvalue buckling analysis of the ideal member was conducted utilizing ABAQUS software to investigate the potential buckling modes. The initial eigenvalue buckling mode shape was appropriately scaled and subsequently incorporated into the ideal geometry, ensuring that the maximum imperfection remained below the section thickness. This approach effectively integrated the initial imperfections into the FE model. Following this, a geometric nonlinear load-displacement analysis was conducted on the member exhibiting imperfections to ascertain its failure characteristics and load-bearing capacity.

3.4. Boundary conditions, contact, and loading

The end of the specimen was connected with the steel end-plate of the analytical rigid body through a “Tie”, as shown in Fig.12. The reference points RP1 and RP2 were established on the end-plate along the axial direction at each extremity of the column. The boundary conditions of fixed connections at both ends are achieved by regulating the degrees of freedom of the reference points RP1 and RP2, as illustrated in Fig.12. The six degrees of freedom associated with RP2, comprising three translational and three rotational degrees of freedom, were restricted. In contrast, five degrees of freedom for RP1 were constrained, with the exception of the directional freedom (*U*z) along the length of the column, as illustrated in Fig. 12.

The interface between the screw and the screw hole is characterized by surface-to-surface contact, as illustrated in Fig.12. Furthermore, surface-to-surface contact was also established between the upper and lower flanges to prevent interpenetration of the contact surfaces of the two flanges, as depicted in Fig.12. Research findings presented in reference [40] suggest that the tangential friction force has a negligible effect on the assembled flanges; consequently, this frictional influence was disregarded in the contact settings. The FE analysis was conducted in two phases: eigenvalue analysis and nonlinear analysis. The eigenvalue analysis employed a concentrated load application method, while the nonlinear analysis utilized a displacement load application method. The loading was applied at the reference point RP1 in the axial direction along the column.

3.5. Numerical results and validation

3.5.1. Buckling and failure modes

The buckling modes, failure modes, and the failure location of the FE simulation were the same as those of the test results, as presented in Fig. 14. It showed that ripples were observed on the web of the C-section of the specimen before the local buckling failure of the flanges. And the peaks and troughs of the ripples were almost consistent with the position of the screw, as shown in Fig. 14. The verification results indicate that the FE model in this paper is accurate.

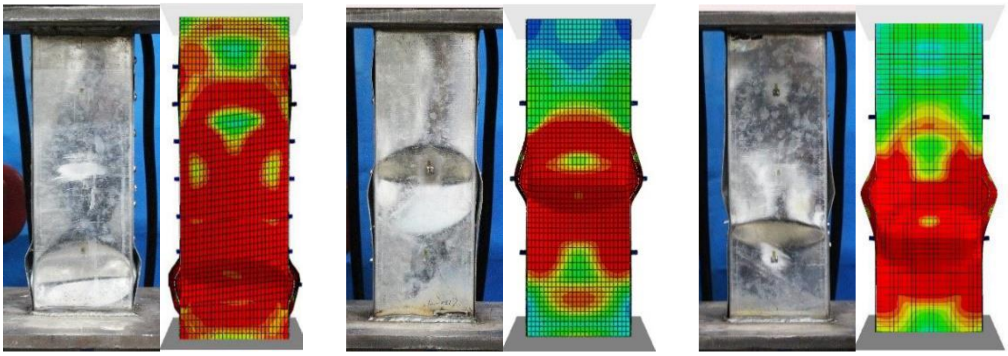

(a) B4-L120-45 (b) B4-L120-90 (c) B4-L120-150

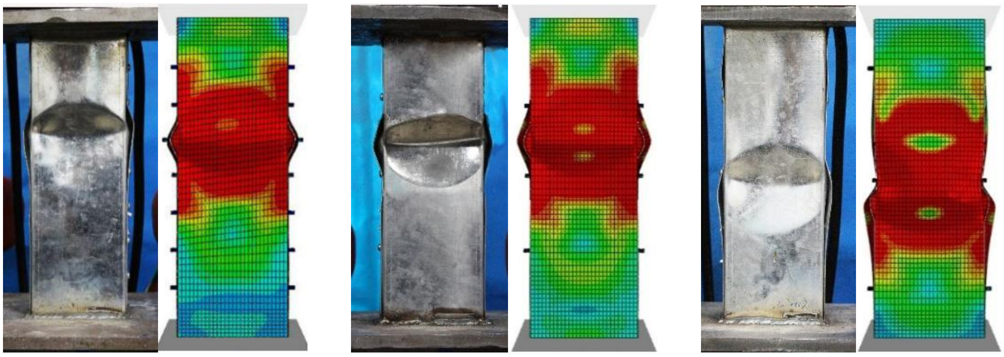

(d) B4-L140-50 (e) B4-L140-100 (f) B4-L140-150

Fig. 14 Comparison of the failure modes

Therefore, the stress distribution plots from the FE analysis are used to explain the mechanism of stress redistribution and the interaction effect. Take the 120 series columns as an example. The local buckling stress distribution plots of the single-limb C-section, U-section, and built-up section are presented in Fig. 15(a) - 15(c) respectively. The internal stress of the specimen is relatively evenly distributed according to the overall stress condition before local buckling. When the local buckling begins to occur, the stress state in the buckling region changes significantly, and the uniformly distributed stress will transfer to the surrounding region without buckling. The maximum stress occurs in the web for single C-section column, as presented in Fig. 15(a). The maximum stress mainly occurs on both sides of the flange for single U-section column, as shown in Fig. 15(b). However, the maximum stress and the buckling position of the CFS built-up box-section column assembled by C- and U-section mainly occur in the middle of the web, as plotted in Fig. 15(c).

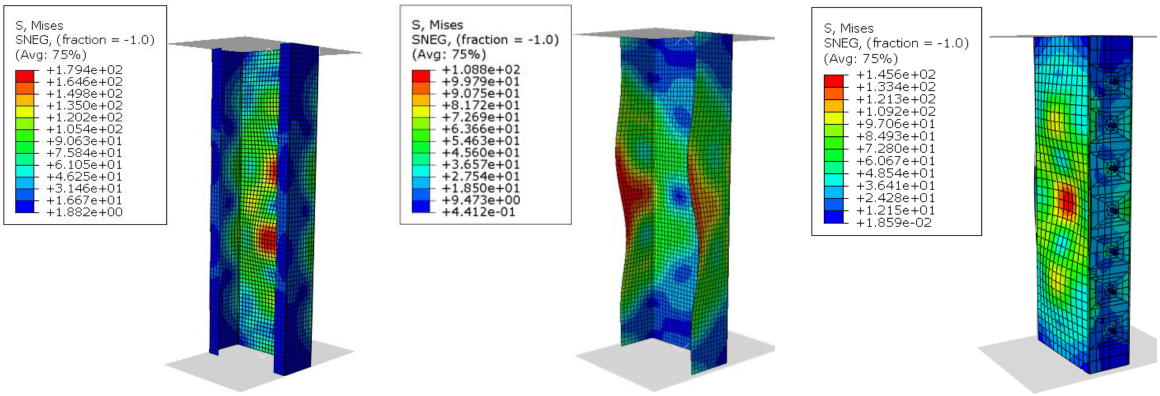

(a) C-section (b) U-section (c) Built-up section

Fig. 15 Stress distribution plots of the C-section, U-section, and Built-up section columns

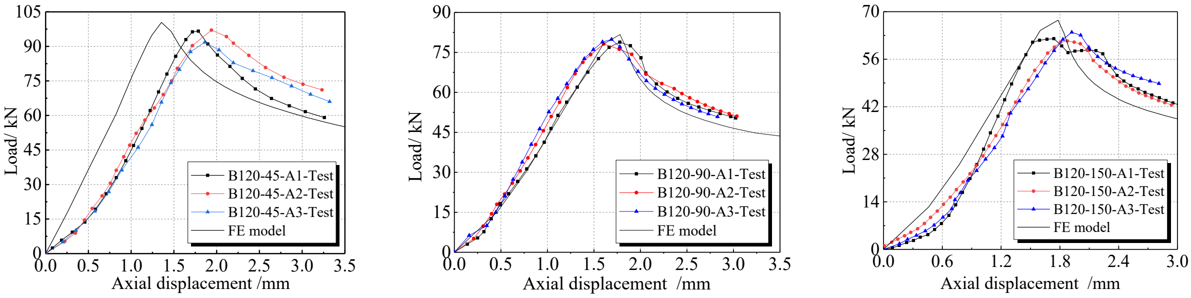

(a) B120-45 (b) B120-90 (c) B120-150

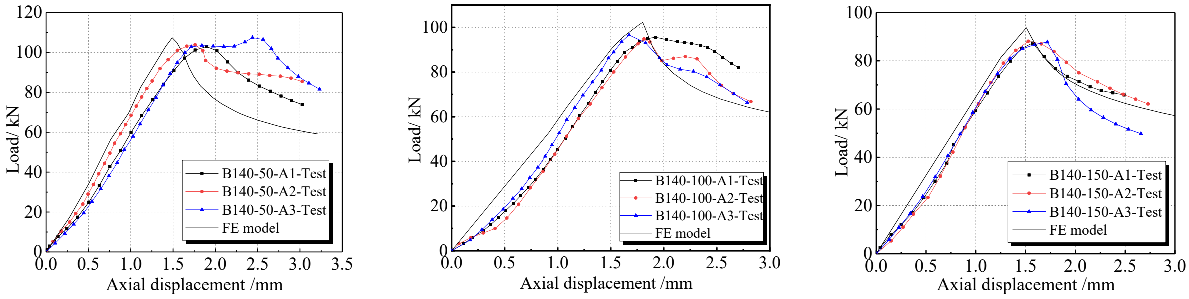

(d) B140-50 (e) B140-100 (f) B140-150

Fig. 16 Comparison of the axial load-displacement

3.5.2. Bearing capacity and load-axial displacement curve

The load-bearing capacities obtained from the FE (P_{FE}) and test (P_t) are listed in Table 2. The mean value of P_{FE}/P_t is 1.07, with a standard deviation of 0.03. The FE simulation results were close to the experimental values, and the discreteness was small. Fig. 16 shows the load-axial displacement curves of the FE results and the experimental results. The slope of the curve of the FE specimen was basically the same as that of the test specimen before the specimen reached the ultimate bearing capacity. However, the test curve was relatively flat at the beginning of the curve in comparison. This is principally because there was a gap between the specimen and the device before loading. The trend of the load-axial displacement curve of the FE was basically consistent with that of the experimental specimen when the specimen was compacted. The peak point was also basically close. It is indicated that the accuracy and reliability of the FE model in this paper.

4. Discussion on the buckling mechanism

4.1. Built-up interaction effect on buckling strength

The different cross-sectional dimensions are listed in Table 4. Four series specimens are designed based on the height of the web (90mm、120mm、150mm and 200mm). The height-width ratio of the parameters varies from 1 to 13. The critical buckling stresses of the C- and U-section are analyzed by GBTUL software [41]. The ratio of $\sigma_{crL\text{-}U}$ to $\sigma_{crL\text{-}C}$ is analyzed to study the influence of the coordination between the two single-limb members on the built-up effect of the built-up columns. This paper could provide suggestions for the design of specimens in practical engineering. In addition, the ultimate capacities of the built-up columns with different height-width ratios are listed in Table 5. Taking 150 series of specimens as an example, the failure mode of the built-up column is shown in Fig 17.

(1) From Table 4, it can be observed that the $\sigma_{crL\text{-}U}$ /$\sigma_{crL\text{-}C}$ ratios of all specimens are on the rise for the width-to-thickness ratio $b/h \leq 5$. Nevertheless, the $\sigma_{crL\text{-}U}$ /$\sigma_{crL\text{-}C}$ ratios of 90 series specimens are on the decline for the width-to-thickness ratio $b/h < 5$. The $\sigma_{crL\text{-}U}$ /$\sigma_{crL\text{-}C}$ ratios of 120 series specimens are on the decline for the width-to-thickness ratio $6 \leq b/h \leq 11$. However, the $\sigma_{crL\text{-}U}$ /$\sigma_{crL\text{-}C}$ ratio begins to show an upward trend for the width-to-thickness ratio $b/h \geq 12$. The $\sigma_{crL\text{-}U}$ /$\sigma_{crL\text{-}C}$ ratios of 150 series specimens are on the decline for the width-to-thickness ratio $6 \leq b/h \leq 10$. However, the $\sigma_{crL\text{-}U}$ /$\sigma_{crL\text{-}C}$ ratio begins to show an upward trend for the width-to-thickness ratio $b/h \geq 11$. The main reason may be that the flange width of the C-section is too narrow, and the lip length is much longer than the flange width, resulting in the C-section quickly reaching yield strength and buckling. Interestingly, the $\sigma_{crL\text{-}U}$ /$\sigma_{crL\text{-}C}$ ratio of the 200 series specimens is unique. Like the observed specimens, the $\sigma_{crL\text{-}U}$ /$\sigma_{crL\text{-}C}$ ratio is on the rise for $b/h \leq 5$. However, the ratio $\sigma_{crL\text{-}U}$ /$\sigma_{crL\text{-}C}$ changes irregularly with the increase of width-to-thickness ratio.

(2) From Table 5, the load-bearing capacity of the built-up column decreases by about 28.9% -37.1% for the column with a thickness of 1.0mm. While the load-bearing capacity of the built-up column decreases by about 31.9%~46.3% for the column with a thickness of 1.2mm. The ultimate capacity of each group of specimens decreases significantly with the increase of the height-width ratio. Except for individual specimens, the load-bearing capacity of the built-up column decreases by about 20% for every 2 times increase in the height-width ratio. Therefore, the height-width ratio of the cross-section is an important factor affecting the ultimate capacity of the CFS built-up box section column.

(3) The height-width ratio of the cross-section is also an important factor affecting the buckling mode of the CFS built-up column. In this study, local and distortional interactive buckling occurs in the CFSBBS columns with height-width ratios of 1 and 10, as presented in Fig. 17(a) and Fig. 17(d). The CFSBBS columns undergo local buckling with the height-width ratio of 2 and 5, as presented in Fig. 17(b) and Fig. 17(c).

Table 4
Critical local buckling stress of the C-section and U-section for CFSBBS columns

*h*b*d*t*	$\sigma_{crL\text{-}C}$	$\sigma_{crL\text{-}U}$	$\sigma_{crL\text{-}U}/\sigma_{crL\text{-}C}$		*h*b*d*t*	$\sigma_{crL\text{-}C}$	$\sigma_{crL\text{-}U}$	$\sigma_{crL\text{-}U}/\sigma_{crL\text{-}C}$	
90-90-15-1	41.6	5.16	0.12	Rise	150-150-15-1	22.17	3.11	0.14	Rise
90-45-15-1	70.58	11.11	0.16		150-75-15-1	40.72	6.72	0.17	
90-18-15-1	77.46	14.79	0.19		150-30-15-1	46.56	8.95	0.19	
90-15-15-1	79.34	13.68	0.17	Decline	150-25-15-1	47.91	8.37	0.17	Decline
90-12.9-15-1	81.36	12.89	0.16		150-21.4-15-1	49.45	7.90	0.16	
90-11.3-15-1	83.38	12.20	0.15		150-18.8-15-1	50.97	7.52	0.15	
90-10-15-1	85.47	11.58	0.14		150-16.7-15-1	52.45	7.18	0.14	
90-9-15-1	87.39	11.05	0.13		150-15-15-1	53.68	7.07	0.13	
90-8.2-15-1	89.13	10.58	0.12		150-13.6-15-1	12.88	6.66	0.52	
90-7.5-15-1	90.83	10.08	0.11		150-12.5-15-1	11.88	6.47	0.54	
90-6.9-15-1	92.40	9.36	0.10		150-11.5-15-1	10.99	6.28	0.57	
120-120-15-1	29.21	3.88	0.13	Rise	200-200-15-1	15.66	2.33	0.15	Rise
120-60-15-1	53.13	8.38	0.16		200-100-15-1	28.44	5.06	0.18	
120-24-15-1	60.98	11.15	0.18		200-40-15-1	31.62	6.73	0.21	
120-20-15-1	62.93	10.38	0.16	Decline	200-33.3-15-1	32.30	6.30	0.20	Decline
120-17.1-15-1	65.21	9.79	0.15		200-28.6-15-1	12.30	5.96	0.48	
120-15-15-1	67.11	9.29	0.14		200-25-15-1	34.00	5.67	0.17	
120-13.3-15-1	69.19	8.87	0.13		200-22.2-15-1	34.83	5.43	0.16	
120-12-15-1	70.96	8.51	0.12		200-20-15-1	35.46	5.32	0.15	
120-10.9-15-1	72.34	8.20	0.11		200-18.2-15-1	10.15	5.07	0.50	
120-10-15-1	13.77	7.93	0.58		200-16.7-15-1	10.15	4.93	0.49	
120-9.2-15-1	12.74	7.66	0.60		200-15.4-15-1	9.33	4.80	0.51	

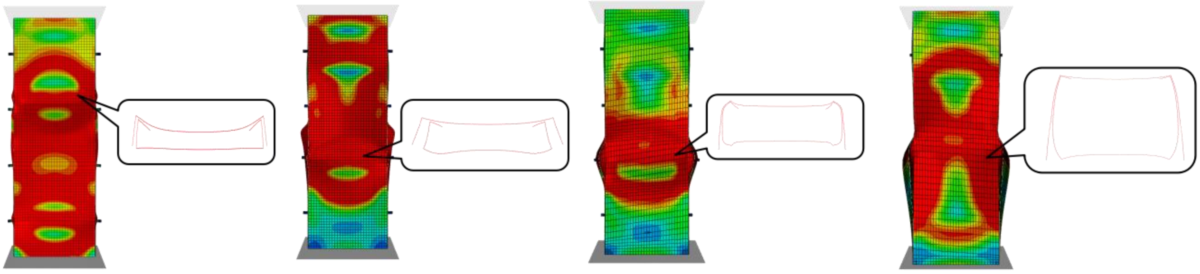

(a) B150-15-1.2 (b) B150-30-1.2 (c) B150-75-1.2 (d) B150-150-1.2

Fig. 17 Failure modes of the B150-1.2series specimens

Table 5

Ultimate capacity of different height-width ratio of CFSBBS columns

Specimens	*h/b*	P_A/kN	Specimens	*h/b*	P_A/kN
B90-90-1	1	75.8	B90-90-1.2	1	109.1
B90-45-1	2	70.5	B90-45-1.2	2	102.7
B90-18-1	5	57.5	B90-18-1.2	5	76.6
B90-9.0-1	10	47.7	B90-9.0-1.2	10	58
B120-120-1	1	79.9	B120-120-1.2	1	112.7
B120-60-1	2	75.3	B120-60-1.2	2	105.8
B120-24-1	5	63	B120-24-1.2	5	85
B120-12-1	10	52.9	B120-12-1.2	10	63.5
B150-150-1	1	82	B150-150-1.2	1	114.1
B150-75-1	2	78.4	B150-75-1.2	2	107.5
B150-30-1	5	68.3	B150-30-1.2	5	90.7
B150-15-1	10	56.9	B150-15-1.2	10	74.8
B200-200-1	1	85.2	B200-200-1.2	1	118.3
B200-100-1	2	81.3	B200-100-1.2	2	111.9
B200-40-1	5	74.8	B200-40-1.2	5	99.4
B200-20-1	10	60.6	B200-20-1.2	10	80.6

4.2. Influence of screw spacing on the ultimate capacity

The significant difference between the specimen composed of two or more single limbs and the whole specimen is the fastener. This has also become a key factor affecting their carrying capacity. Therefore, in this study, three kinds of FE models (see Fig. 18) are developed to study the influence of screw spacing on the local buckling bearing capacity of the CFSBBS column. The sectional dimension of the specimen is shown in Table 6. The comparison results of the local buckling ultimate capacity are shown in Table 6 and Fig. 19. The ultimate capacities of the B type model are mostly higher than the A type model and smaller than C type model. However, it is interesting that the ultimate capacity of the four series of specimens in Table 6 does not decrease with the increase of screw spacing, but fluctuates repeatedly. The reason for the fluctuation in the local buckling ultimate capacity may be attributed to the screw spacing being related to the buckling half-wavelength of the specimen.

Table 6 indicates that the mean value of the P_A/P_B ratio is 0.972, accompanied by a standard deviation (SD) of 0.079. In contrast, the mean value of the P_C/P_B ratio is 1.224, with a standard deviation of 0.067. The analysis reveals a minimal dispersion associated with the increase in screw spacing. Fig. 9 illustrates that the curve representing the B type model closely resembles that of model A while diverging from model C. This observation suggests that variations in screw spacing exert a negligible influence on the local buckling ultimate capacity of CFSBBS short columns, and the strengthening effect on the cross-section is not pronounced. When the screw spacing is less than the buckling half-wavelength, the screws effectively constrain the number of buckling half-waves along the specimen's length, thereby enhancing its ultimate capacity. However, this constraint effect diminishes as screw spacing increases. The ultimate capacity experiences a slight increase when the screw spacing equals the buckling half-wavelength. Moreover, when the screw spacing exceeds the buckling half-wavelength, the constraining effect of the screws on the specimen weakens progressively with further increases in spacing, leading to a gradual decline in the specimen's ultimate capacity.

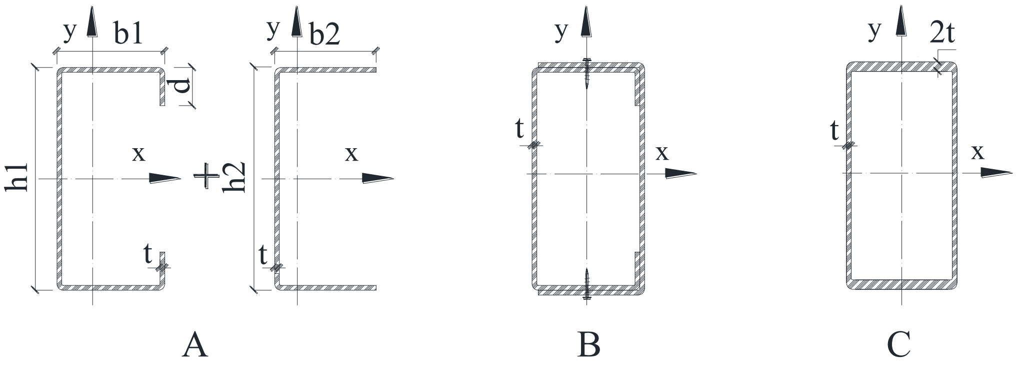

Fig. 18 Three calculation models

Table 6
Influence of screw spacing on the local buckling bearing capacity of CFS columns

Specimens	P_B/kN	P_A/kN	P_C/kN	P_A/P_B	P_C/P_B
B90-25-1	93.12	88.67	110.53	0.952	1.187
B90-50-2	92.37			0.960	1.197
B90-70-3	93.11			0.952	1.187
B90-100-4	91.88			0.965	1.203
B90-150-5	91.90			0.965	1.203
B120-25-6	110.97	102.68	141.16	0.925	1.272
B120-55-7	106.07			0.968	1.331
B120-91-8	109.68			0.936	1.287
B120-120-9	105.22			0.976	1.342
B120-150-10	105.51			0.973	1.338
B120-180-11	106.46			0.965	1.326
B150-25-12	111.77	105.21	126.23	0.941	1.129
B150-55-13	107.99			0.974	1.169
B150-85-14	105.53			0.997	1.196
B150-117-15	110.69			0.950	1.140
B150-150-16	106.87			0.984	1.181
B150-180-17	106.95			0.984	1.180
B150-210-18	107.65			0.977	1.173
B200-25-19	115.78	112.42	132.80	0.971	1.147
B200-75-20	114.30			0.984	1.162
B200-125-21	113.96			0.986	1.165
B200-156-22	114.68			0.980	1.158
B200-180-23	113.64			0.992	1.169
B200-210-23	113.54			0.990	1.170
B200-240-24	113.14			0.994	1.174
Mean				0.972	1.224
SD				0.079	0.067

Note：P_A、P_B、P_C represent the ultimate capacity of finite element for A, B and C models, respectively.

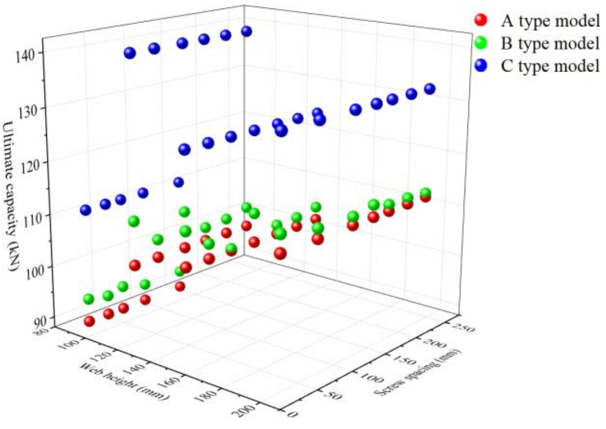

Fig. 19 Influence of screw spacing on the bearing capacity of CFS columns

5. Conclusion and discussion

This study examines the local buckling mechanism through both experimental and numerical simulations, focusing on various aspects such as buckling behavior, buckling modes, load-bearing capacity, post-buckling strength, and the interaction effects of the CFSBBS columns. The influence of screw spacing on the buckling mechanism was thoroughly analyzed through comprehensive parametric studies. The following significant conclusions have been drawn:

(1) The local buckling patterns of the CFSBBS column were clarified. There are 5 types of buckling modes (see Fig.11(d)-(h)) for the same specimen with different cross-sections. This deformation process reveals the mechanism of local buckling instability of the CFSBBS columns.

(2) The smaller the ratio $\sigma_{\mathrm{crL\text{-}U}}$ /$\sigma_{\mathrm{crL\text{-}C}}$, the greater the deformation coordination effect of the C-section on the U-section, and the more likely the built-up part of the CFSBBS column is to undergo coordinated deformation, and the more obvious the built-up effect is.

(3) Screw spacing can not make a large gap in the bearing capacity of the CFS built-up box section columns. However, the buckling mode of the CFS built-up column will change with the increase of the screw spacing. In addition, almost all of the built-up plates are coordinated buckling deformation, which also lays the foundation for the theoretical study of the CFSBBS column subjected to local buckling by the author's team. The author will carry out experimental and theoretical research on the buckling mechanism of different built-up sections.

(4) When the screw spacing is less than the half-wavelength (λ_c), the local buckling ultimate capacity of the CFS built-up box section column decreases with the increase of the screw spacing. When the screw spacing is equal to the λ_c, the ultimate capacity does not increase significantly. While the ultimate capacity shows a downward trend when the screw spacing is greater than the λ_c.

(5) Appropriate screw spacing can ensure that the connection between adjacent components can adapt to this buckling and avoid local stress concentration leading to failure. In the processing stage of CFS members, the use of high-precision equipment can ensure the dimensional accuracy and shape regularity of the steel and reduce the defects caused by the quality problems of the material itself. The research results are beneficial to the popularization and application of CFSBBS column in the field of residential and industrial buildings.

Declaration of competing interest

The authors declare that they have no known competing financial interests or personal relationships that could have appeared to influence the work reported in this paper.

Acknowledgments

The authors sincerely appreciate the financial support provided by the Key R&D and promotion projects in Henan Province (No.242102321151) and (No.242102321152), Key Scientific Research Projects of Colleges and Universities in Henan province (23A560011) and (22A560013), Water conservancy project innovative science and technology team cultivation plan (2023XK100100086).

References

[1] Selvaraj S, Madhavan M. Structural Behaviour of Cold-Formed Steel Built-Up Closed Cross-section Columns - Assessing the Influence of Parameters and Design Methods. Engineering Structures 2023; 294:116600.

[2] Nie SF, Eatherton MR, Han Y, et al. Investigation of built-up box columns composed of four cold-formed steel channels. Thin-Walled Struct 2022; 175:109258.

[3] Deepak MS, Ananthi GBG. Local buckling behaviour and capacities of Cold-Formed Steel Double-I-Box stub and short column sections. Structures 2021; 34:1761-1784.

[4] Huynh MT, Pham CH, Hancock GJ. Experimental behaviour and modelling of screwed connections of high strength sheet steels in shear. Thin-Walled Struct 2020; 146:106357.

[5] Kherbouche S, Megnounif A. Numerical study and design of thin walled cold formed steel built-up open and closed section columns. Engineering Structures 2019; 179:670-682.

[6] Wang LP, Young B. Behaviour and design of cold-formed steel built-up section beams with different screw arrangements. Thin-Walled Struct 2018;131:16–32.

[7] Li YQ, Li YL, Wang S, Shen ZY. Ultimate load-carrying capacity of cold-formed thin-walled columns with built-up box and I section under axial compression. Thin-Walled Structures, 2014, 79:202–217.

[8] Yang JJ, Xu L, Shi Y, Wang WY. Experimental and analytical study of flexural buckling of cold-formed steel quadruple-limb built-up box columns. Journal of Structural Engineering, 2022, 148(1):04021228.

[9] Zhang L, Zhou TH, Sang LR, Wang YZ, Wang SB. Experiments on local-distortional interaction buckling of cold-formed steel three-limbed built-up open-section columns. Thin-Walled Structures, 2023, 182:110239.

[10] Li YC, Zhou TH, Han AH, Li WH, Xu Y. Failure mechanism and reliability prediction of CFS built-up columns considering distortional buckling. Structures, 2024, 69:107337.

[11] Li YC, Li RB, Zhou TH, Han AH, Li WH. Mechanics of cold-formed steel built-up box section columns in local buckling modes. Structures, 2025, 71:107957.

[12] Timoshenko SP. Theory of Elastic Stability, 2nd ed., Mcgraw-Hill, New York. 1961.

[13] Bleich F. Buckling Strength of Metal Structures. Mcgraw-Hill, 1952.

[14] Szymczak C, Kujawa M. On local buckling of cold-formed channel members. Thin-Walled Structures, 2016, 106:93-101.

[15] Ragheb WF. Local buckling of welded steel I-beams considering flange–web interaction. Thin-Walled Structures, 2015, 97:241-249.

[16] Li YC, Li RB, Zhou TH, et al. Novel design method of screwed connections of cold-formed steel built-up plates. Structures, 2023, 55:2433–2444.

[17] Roy K, Ting TCH, et al. Effect of thickness on the behaviour of axially loaded backto-back cold-formed steel built-up channel sections-Experimental and numerical investigation. Structures, 2018, 16:327–46.

[18] Pham DK, Pham CH, Pham SH, et al. Experimental investigation of high strength cold-formed channel sections in shear with rectangular and slotted web openings. J Constr Steel Res, 2020;165:105889.

[19] Li YC, Zhou TH, Zhang L, et al. Distortional buckling behavior of cold-formed steel built-up closed section columns. Thin-Walled Struc, 2021;166:108069.

[20] Zhou TH, Li YC, Ren LJ, et al. Research on the elastic buckling of composite webs in cold-formed steel back-to-back built-up columns - Part I: Experimental and numerical investigation. Structures, 2021;30:115–133.

[21] Fratamico DC, Torabian S, Zhao Xi, Rasmussen KJR, Schafer BW. Experimental study on the composite action in sheathed and bare built-up cold-formed steel columns. Thin-Walled Struct, 2018, 127:290-305.

[22] Chen B, Roy K, Uzzaman A, Raftery G, Lim JBP. Axial strength of back-to-back cold-formed steel channels with edge-stiffened holes, un-stiffened holes and plain webs. J Constr Steel Res, 2020, 174:106313.

[23] Ting TCH, Roy K, Lau HH, et al. Effect of screw spacing on behavior of axially loaded back-to-back cold-formed steel built-up channel sections. Adv Struct Eng 2018, 21(3):474–87.

[24] Roy K, Ting TCH, Lau HH, et al. Nonlinear behaviour of back-to-back gapped builtup cold-formed steel channel sections under compression. J Constr Steel Res, 2018, 147:257–76.

[25] Wang L, Young B. Behaviour and design of cold-formed steel built-up section beams with different screw arrangements. Thin-Walled Struct, 2018, 131:16–32.

[26] Roy K, Lau HH, Ting TCH, et al. Experiments and finite element modelling of screw pattern of self-drilling screw connections for high strength cold-formed steel. ThinWalled Struc, 2019, 145:106393.

[27] Lu Y, Zhou TH, Li WC, et al. Experimental investigation and a novel direct strength method for cold-formed built-up I-section columns. Thin-Walled Structures, 2017, 112:125–139.

[28] Zhou TH, Li YC, Wu HH, et al. Superposition method for bearing capacity of cold-formed thin-walled steel built-up box-section short columns. Journal of Hunan University, China, 2020, 47(11):46-55.

[29] Li YC, Zhou TH, Ding JH, et al. Investigation on distortion buckling behavior of cold-formed thin-walled steel built-up box-section columns. Journal of Hunan University, China, 2021, 48(11):91-100.

[30] Reyes W, Guzmán A. Evaluation of the slenderness ratio in built-up cold-formed box sections. Journal of Constructional Steel Research, 2011, 67(6): 929-935.

[31] Selvaraj S, Madhavan M. Design of cold-formed steel built-up closed section columns using direct strength method. Thin-Walled Struct, 2022, 171:108746.

[32] Abbasi M, Rasmussen KJR, Kheari M, et al. Experimental investigation of the sectional buckling of built-up cold-formed steel columns. J Constr Steel Res, 2023, 203:107803.

[33] Qiao WT, Wang YH, Li RF, et al. Research on axial bearing capacity of cold-formed thin-walled steel built-up column with 12-limb-section. Steel Compos. Struct, 2023, 47(3):437–450.

[34] Lu Y, Zhou TH, Li WC, et al. The critical local buckling load and ultimate strength of cold-formed thin-walled C-sections under axial compression. Journal of Harbin Institute of Technology, 2017, 49(6):72-76. (In Chinese)

[35] Schafer BW, CUFSM4.05—finite strip buckling analysis of thin-walled members. Department of Civil Engineering, Johns Hopkins University, Baltimore, U.S.A, 2012.

[36] AISI S100, North American Specification for the Design of Cold-Formed Steel Structural Members, American Iron and Steel Institute, Washington, DC, 2016.

[37] Ziemian RD. Guide to Stability Design Criteria for Metal Structures. Sixth edition, Hoboken: John Wiley & Sons, 2010.

[38] ABAQUS, ABAQUS Analysis user's Manual, Version 6.21, Dassault Syst`emes Simulia Corp, Providence, RI, USA, 2021.

[39] Schafer BW, Li Z, Moen CD. Computational modeling of cold-formed steel. Thin-Walled Structures, 2010, 48(10):752-762.

[40] Zhang JH, Young B. Numerical investigation and design of cold-formed steel built-up open section columns with longitudinal stiffeners. Thin-Walled Structures, 2015, 89(4):178-191.

[41] Bebiano R, Pina P, Silvestre N, et al. GBTUL — buckling and vibration analysis of thin-walled members. Lisbon, Technical University of Lisbon, 2008.

Advanced Steel Construction – Vol. 21 No. 3 (2025) 231–242
DOI:10.18057/IJASC.2025.21.3.5

A PROPOSAL OF SIMPLIFIED SEISMIC DESIGN METHOD FOR STEEL PIER WITH POTENTIAL FAILURE MODES OF LOCAL INSTABILITY AND ULTRA-LOW CYCLE FATIGUE

Cheng Cheng, Xu Xie * and Tian-Jia Wang

College of Civil Engineering and Architecture, Zhejiang University, Hangzhou, China
** (Corresponding author: E-mail: xiexu@zju.edu.cn)*

ABSTRACT

Local instability (LI) and ultralow-cycle fatigue (ULCF) are two potential failure modes of steel piers subjected to strong earthquakes. Steel bridges constructed in highly seismic regions must account for both failure modes in their seismic design calculations. While the issue of LI has largely been addressed, with preventive measures incorporated into various bridge design codes, the ULCF assessment remains challenging due to its high computational cost. Therefore, investigating the conditions under which the ULCF assessment can be avoided is of great significance for simplifying the seismic design of steel bridges. To this end, this study focuses on the damage occurrence priority of the two failure modes of steel piers. The proposed simplified seismic design method is the avoidance of ULCF check by constructing piers with the failure occurrence priority of LI. Taking the widely used box section single-column steel pier as an example, 90 piers with different structural parameters, representative of practical engineering applications, were designed in this paper. Based on a hypothetical cyclic loading protocol, the parameter ranges of steel piers with different damage priorities were determined. Discussion on the seismic performance of piers showed that the order of failure occurrence sequence is controlled by the mechanical properties of pier structure, rather than the load conditions it is subjected to. Additionally, the credibility of the derived damage occurrence sequence and the simplified seismic design method was verified through dynamic analyses using real seismic wave inputs. The work shown in this paper can serve as a reference to simplify the seismic design process of steel piers.

ARTICLE HISTORY

Received:	20 April 2024
Revised:	7 January 2025
Accepted:	8 January 2025

KEYWORDS

Local instability;
Ultralow-cycle fatigue;
Damage occurrence priority;
Seismic design;
Steel pier

1. Introduction

The local instability (LI) and the ultralow-cycle fatigue (ULCF) are two typical failure modes of steel piers exposed to strong earthquakes. The LI damage is characterized as the bending of steel plates accumulated in a local area of flange or web, which eventually results in the significant deterioration of the bearing capacity. While, the ULCF damage starts from the premature cracks aroused by several cycles of extremely large strain loops, followed by the stable growth of cracks and the sudden crack propagation under subsequent cyclic loads. The ULCF life of steel structures is within the range of very few cycles, that is, usually less than 20 loading cycles [1-2]. The plasticity of steel cannot be fully utilized until the final failure. Severe damage, including these two failure modes, was widely observed during the Northridge earthquake in 1994 and the Kobe earthquake in 1995 [3-5]. Since then, extensive experimental and analytical investigations on the seismic performance of steel piers have been conducted [4-12]. Up to now, researchers have reached the consensus of the coexistence of LI and ULCF and the fatality of the two failure modes.

During the past 30 years, scholars have conducted various studies on the LI failure of steel piers. For example, based on experimental findings, Ge et al. defined the point at which the bearing capacity of steel piers reaches its maximum value and subsequently decreases to 95% as the limit state to determine the initiation of LI damage in pier structures [13]. Goto et al. proposed a limit state criterion for steel piers from an energy prospect by testing pier specimens under different loading histories [14]. Based on the numerical investigation, Gao et al. established several empirical formulae of the limit state values for providing guidance of seismic design of steel piers [15]. At present, the LI failure of steel piers has been basically solved, and the relevant provisions can be found in bridge design codes of various countries [16-18].

Great efforts have been devoted to developing effective ULCF assessment methods, which can be divided into two categories according to their analytical dimension. One category involves the empirical methods modified from the Coffin-Manson law [19-20] applied in the low-cycle fatigue field (LCF). Examples of these methods include the Tateishi model [21], the Xue model [22], and the macro deformation history-based assessment method [23]. However, Tamura et al. have demonstrated that the triaxial stress states within the damage area has significant influence on the material ductility from the tensile-shear tests of structural steels [24-25], which is contrary to the practice of using plastic strain as the only calculation factor adopted in the empirical methods. Direct application of the empirical methods in engineering structures lacks sufficient credibility. Another category of ULCF assessment method includes the stress triaxiality-associated prediction formulae and micro-damage mechanisms-based damage models, such as the large-range stress triaxiality-adaptive ductile fracture prediction model [26], the continuous damage model (CDM) [27] based on the continuum damage mechanisms, and the cyclic void growth model (CVGM) [28] developed from the void growth theory. These methods can take into account the influence of stress triaxiality on the ductile damage of materials, which are logically clear and suitable for precise ULCF evaluation under complex loading conditions. Nevertheless, the computation of the stress triaxiality needs very refined numerical simulation with solid elements, wherein the mesh size should be set to be consistent with the material characteristic length (usually 0.2-0.4mm for commonly used steel [2, 29-30]). The great discrepancy between the structural dimensions and the mesh size of the refined solid elements imposes great computational burden. Thus, the ULCF assessment is difficult to be popularized in practical engineering.

Due to the fatality of LI and ULCF, steel bridges constructed in seismically active areas should take both failure modes into account in their seismic design calculations. However, as mentioned above, such a seismic design process is difficult to apply in practical engineering because of the high computational costs involved in ULCF assessment. Currently, there is no appropriate approach available to efficiently process the seismic design. To this end, this paper proposed a simplified seismic design method that can avoid the burdensome ULCF calculations. Focusing on the damage occurrence priority of the two failure modes, the proposed method assumes that the ULCF assessment can be exempted by constructing piers with the failure occurrence priority of LI. Taking the widely used box-section single column steel pier as an example, the implementation and the credibility of the proposed method were illustrated. First, 90 piers with different structural parameters, representative of practical engineering applications, were designed. Then, based on a series of numerical work, the empirical formulae for the limit states of the LI failure of piers, such as the critical displacement and critical load, were fitted. After that, the ULCF assessment of piers under a hypothetical cyclic loading protocol were conducted to determine the damage occurrence priority. The seismic behavior of steel piers was also discussed to explain the mechanisms of different failure occurrence orders. Finally, dynamic analyses with real seismic wave inputs were conducted to verify the credibility of the proposed seismic design method.

2. Failure assessment methods for LI and ULCF

2.1. LI

Fig. 1 shows a typical hysteretic curve of a single-column steel pier under a constant axial load P and lateral cyclic displacement δ. In this figure, H represents the horizontal bearing capacity and the solid line indicates the hysteresis envelope. (δ_m, H_m) represents the peak point of the bearing capacity, and (δ_{95}, H_{95}) signifies the critical state where the bearing capacity begins to drop sharply. The entire envelope can be divided into three stages according to the structural mechanical degradation: In stage I, the structure is in the elastic and strengthening stage when the top displacement is less than δ_m, and no stiffness deterioration occurs; in stage II, its bearing capacity and stiffness begin to deteriorate slightly when the top displacement is between δ_m and δ_{95}; in stage III, the bearing capacity and stiffness start to degrade significantly when the lateral displacement δ exceeds δ_{95}.

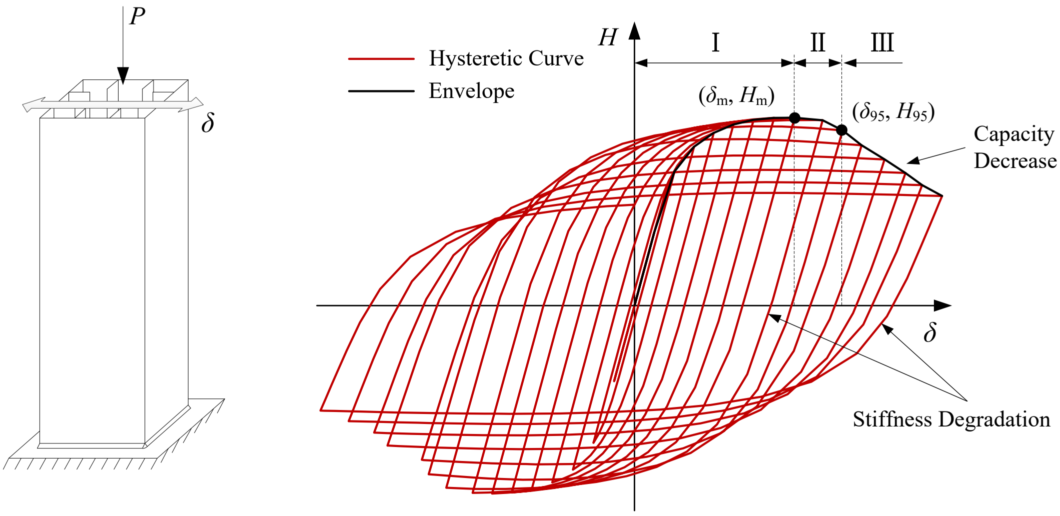

Fig. 1 Typical hysteretic curve of the single-column pier under cyclic lateral loads

Ge et al. summarized the experimental and theoretical results, and suggested the point (δ_{95}, H_{95}) that reduces to 95% of the peak bearing capacity as the critical state of LI [13]. Usami et al. conducted a series of tests and numerical analyses on the seismic performance of steel piers, and found that after reaching a certain critical state, the buckling instability of the structure initiates, and the bearing capacity begins to degrade rapidly, which leads to the final failure [31]. Generally, points (δ_m, H_m) and (δ_{95}, H_{95}) are always accepted as the vital limit state points for evaluating the seismic performance of steel piers, and the point (δ_{95}, H_{95}) is regarded as the LI damage initiation point [31-32].

2.2. ULCF

Under cyclic loading, complex and multidimensional stress states are involved in the vulnerable sites of piers. As mentioned above, among the two categories of assessment methods, the multi-dimensional methods that could take into account the effect of stress triaxiality can have a better interpretation for the ULCF fracture mechanism of the metal. Credible ULCF predictions can be obtained through precise material parameter calibration. The CVGM [28], which is developed from the micro-void growth mechanism, is a typical example. Applications of CVGM on different steel connections and steel piers for ductile fracture prediction have confirmed its feasibility and serviceability [33-37]. In this study, the CVGM was selected as a reference for initial cracking life assessment of steel piers.

The main content of this method includes a nonnegative cyclic void growth index VGI_{cyclic} and a cyclic void capacity index $VGI_{\text{cyclic}}^{\text{critical}}$, which are formulated as follows:

$$VGI_{\text{cyclic}} = \sum_{\text{tensile}} \int_{\varepsilon_1}^{\varepsilon_2} \exp\left(|1.5T|\right) \mathrm{d}\varepsilon_{\mathrm{p}} - \sum_{\text{compressive}} \int_{\varepsilon_1}^{\varepsilon_2} \exp\left(|1.5T|\right) \mathrm{d}\varepsilon_{\mathrm{p}} \geq 0 \tag{1}$$

$$VGI_{\text{cyclic}}^{\text{critical}} = \eta \cdot \exp\left(-\lambda \varepsilon_{\mathrm{p}}^{\text{accumulated}}\right) \tag{2}$$

where the upper and lower limits of Eq. (1), ε_1 and ε_2, are the equivalent plastic strains at the beginning and end of each tensile or compressive cycle, respectively; T is derived by the ratio of hydrostatic pressure σ_m and mises stress σ_{eq}, termed as stress triaxiality; $\mathrm{d}\varepsilon_{\mathrm{p}}=\sqrt{(2/3)\mathrm{d}\varepsilon_{ij}^{\mathrm{p}}\mathrm{d}\varepsilon_{ij}^{\mathrm{p}}}$ denotes the equivalent plastic strain; η and λ are two material constants governing the material toughness and damage degradation, respectively. It is assumed that ULCF fractures occurs when $VGI_{\text{cyclic}} \geq VGI_{\text{cyclic}}^{\text{critical}}$. According to our previous study [23], the two constants of Q345qC steel are taken as η=2.03 and λ=0.10, respectively.

3. Pier structure and FE model

3.1. Steel pier

The single-column steel pier with a stiffened box section was selected as the research object in this study. Its outline and sectional details are shown in Fig. 2. Piers are made of Q345qC steel, which is a commonly used material in Chinese steel bridges; full penetrating weld process is applied to connect the stiffening plates and the end plates, and the yellow part shown in Fig. 2 represents the welded area. The main structural parameters of steel piers include the slenderness ratio λ_B, width-to-thickness ratio R_R, axial compression ratio P/P_y and the relative stiffness of the stiffeners. The λ_B and R_R calculations are expressed as [38]:

$$\lambda_{\mathrm{B}} = \frac{2h}{r}\frac{1}{\pi}\sqrt{\frac{\sigma_{\mathrm{y}}}{E}} \tag{3}$$

$$R_{\mathrm{R}} = \frac{B}{t}\sqrt{\frac{12\left(1-v^2\right)}{4\pi^2 n_{\mathrm{r}}^2}}\sqrt{\frac{\sigma_{\mathrm{y}}}{E}} \tag{4}$$

where h is the height of the piers, r denotes the radius of gyration in the deformed direction, B is the width of the flange, t is the thickness of the stiffening plate, n_r is the number of regions divided by stiffeners in the stiffening plate, v = 0.3 is the Poisson's ratio. Stipulated by the codified standards [18], the relative stiffness of the stiffener is defined and limited as:

$$\begin{cases} \dfrac{\gamma}{\gamma^*} = \dfrac{EI_{\mathrm{l}}}{BD'\gamma^*} \geq 1 \\ \gamma_{\mathrm{t}} = \dfrac{EI_{\mathrm{t}}}{BD'} \geq \dfrac{1+n_{\mathrm{r}}\gamma}{4\left(a/B\right)^3} \end{cases} \tag{5}$$

$$\frac{b_{\mathrm{s}}}{t_{\mathrm{s}}} \leq 12\sqrt{\frac{345}{\sigma_{\mathrm{y}}}} \tag{6}$$

where γ and γ_t denote the relative stiffness of the longitudinal stiffeners and diaphragms, respectively; I_l and I_t are the bending moments of inertia of a single longitudinal stiffener and a single diaphragm, respectively; D' is the bending stiffness of the steel plates per unit width; a is the spacing of the transverse partitions; t_s and b_s are the thickness and width of the vertical stiffener, respectively; γ^* represents the optimal stiffness ratio of stiffeners, which is defined as:

$$\gamma^* = \begin{cases} \dfrac{1}{n_r}\left[4n_r^2\left(1+n_r\dfrac{b_s t_s}{Bt}\right)\alpha^2-\left(\alpha^2+1\right)^2\right] & \alpha \le \sqrt[4]{1+n_r\gamma} \\ \dfrac{1}{n_r}\left\{\left[2n_r^2\left(1+n_r\dfrac{b_s t_s}{Bt}\right)\alpha^2-1\right]^2-1\right\} & \alpha > \sqrt[4]{1+n_r\gamma} \end{cases} \quad (7)$$

where $\alpha = a/B$. According to the ranges of the structural parameter values in practical projects, $0.25 \le \lambda_B \le 0.50$, $0.30 \le R_R \le 0.50$ and $0.10 \le P/P_y \le 0.30$ were selected. Table 1 presents the geometric characteristics of the designed 90 piers, using the free combination of these three parameter ranges. Each row of data listed in this table represents three pier working conditions ($P/P_y = 0.1$, 0.2, and 0.3). Some constant variables, such as flange width B (0.45m), sectional aspect ratio W/B (1.0), diaphragm spacing a (0.45m), and optimal stiffness ratio γ/γ^* (1.5), are not included in Table 1.

Table 1
Geometric dimensions and structural parameters of piers

No.	h(m)	λ_B	R_R	t(m)	t_s(m)	b_s(m)
S25-30	1.61	0.250	0.298	0.0110	0.0110	0.083
S25-35	1.63	0.250	0.349	0.0094	0.0094	0.073
S25-40	1.64	0.250	0.395	0.0083	0.0083	0.066
S25-45	1.65	0.250	0.449	0.0073	0.0073	0.060
S25-50	1.66	0.250	0.504	0.0065	0.0065	0.055
S30-30	1.95	0.302	0.298	0.0110	0.0110	0.083
S30-35	1.96	0.301	0.349	0.0094	0.0094	0.073
S30-40	1.98	0.301	0.395	0.0083	0.0083	0.066
S30-45	2.00	0.302	0.449	0.0073	0.0073	0.060
S30-50	2.00	0.301	0.504	0.0065	0.0065	0.055
S35-30	2.26	0.350	0.298	0.0110	0.0110	0.083
S35-35	2.29	0.351	0.349	0.0094	0.0094	0.073
S35-40	2.30	0.350	0.395	0.0083	0.0083	0.066
S35-45	2.31	0.349	0.449	0.0073	0.0073	0.060
S35-50	2.31	0.348	0.504	0.0065	0.0065	0.055
S40-30	2.59	0.402	0.298	0.0110	0.0110	0.083
S40-35	2.62	0.402	0.349	0.0094	0.0094	0.073
S40-40	2.63	0.400	0.395	0.0083	0.0083	0.066
S40-45	2.65	0.401	0.449	0.0073	0.0073	0.060
S40-50	2.65	0.399	0.504	0.0065	0.0065	0.055
S45-30	2.91	0.451	0.298	0.0110	0.0110	0.083
S45-35	2.95	0.452	0.349	0.0094	0.0094	0.073
S45-40	2.97	0.452	0.395	0.0083	0.0083	0.066
S45-45	2.99	0.452	0.449	0.0073	0.0073	0.060
S45-50	3.00	0.451	0.504	0.0065	0.0065	0.055
S50-30	3.16	0.490	0.298	0.0110	0.0110	0.083
S50-35	3.19	0.490	0.349	0.0094	0.0094	0.073
S50-40	3.21	0.490	0.395	0.0083	0.0083	0.066
S50-45	3.25	0.491	0.449	0.0073	0.0073	0.060
S50-50	3.25	0.490	0.482	0.0065	0.0065	0.055

Note: Taking S25-30 as an example, S indicates steel pier; 25 means $\lambda_B = 0.25$ and 30 represents $R_R = 0.30$.

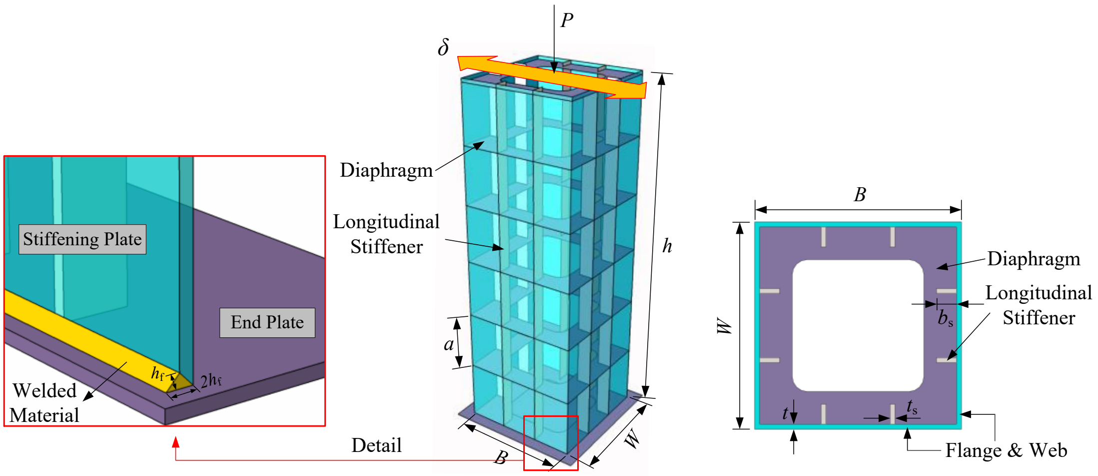

Fig. 2 Schematic diagram of steel pier

3.2. FE Model

The operation of CVGM requires the results of stress triaxiality, where local solid modelling is required, and the solid element size should be consistent with the characterized length L^* (0.2 mm) of Q345qC steel [28, 36]. Experimental investigations of steel piers have shown that the welded corners are the most vulnerable sites of ductile crack initiation [6, 10-12], which is the region where local refinement is imposed. Given the significant difference between the characteristic length L^* and the structural dimensions of piers, the two-level zooming sub-model strategy was adopted to pursue a cost-effective simulation process.

The FE simulation process is carried out on the ABAQUS 6.14-4 platform. As illustrated in Fig. 3, the first-level zooming consists of the global model and the sub1 model; the second-level zooming consists of the sub1 model and the sub2 model. In the global model, the pier bottom is completely fixed and the basic geometric content of the pier structure is included. The whole model is modelled by the 4-node reduced integral shell element S4R, except that a short range at the top is simulated by the 2-node linear beam element B31 to transfer the horizontal cyclic deformation δ and axial force P. The multi-point coupling (MPC) is exerted between shell elements and beam elements for consolidating their boundary. The followed sub1 model, representing a part of the bottom of the pier, is entirely modelled by the 8-node reduced integral brick element C3D8R, in which the geometry of the weld joints is reflected. Owing to the restriction of element characteristics, at least four layers of solid elements is divided along the thickness direction of the plates to cater to the change in bending stress [39], as depicted in Fig.3(b). The final sub2 model only contains a weld corner of the sub1 model, which is also modelled by solid element C3D8R. The mesh size of the solid element in the vulnerable sites corresponds to the material characteristic length L^*, controlled at 0.2 mm [30]. These three models present a progressive relationship towards the refined simulation of weld toe. For each sub-model, the displacement solution generated from the previous-level model is converted to the enforced displacement acted on its exposed surfaces as the driven load. Weld details are ignored in the global model because that it has no effect on the nodal displacement of the driven surface between the global model and the sub1 model. To ensure the reliability of the stress and strain results, the exposed surfaces of each sub-model are kept at least 1.5 times the width or thickness away from the areas of concern, such as 1.5B or 1.5t shown in Fig. 3(b, c). The Chaboche hybrid hardening constitutive model is applied for the accurate expression of cyclic metal plasticity. The constitutive parameters of Q345qC steel have been calibrated in the previous study [30] and are listed in Table 2.

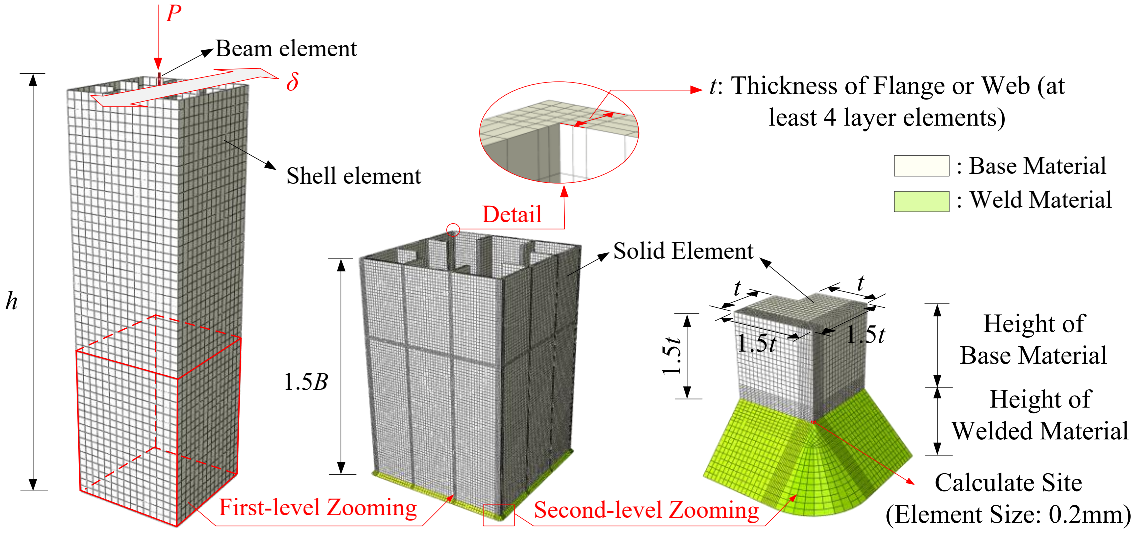

(a) Global model (b) Sub1 model (c) Sub2 model

Fig. 3 Schematic diagram of FE model

Table 2
Parameters of the Chaboche constitutive model of Q345qC steel [30]

Material	$\sigma\|_0$(MPa)	Q_∞(MPa)	b_{iso}	C_1(MPa)	γ_1	C_2(MPa)	γ_2	C_3(MPa)	γ_3
Base Material	354.10	13.2	0.6	44373.7	523.8	9346.6	120.2	946.1	18.7
Weld Material	428.45	17.4	0.4	12752.3	160.0	1111.2	160.0	630.5	26.0

Note: $\sigma|_0$ is initial yield stress; Q_∞ is the maximum variation of yield surface; b_{iso} is the change ratio of the yield surface with the plastic strain; C_1, C_2 and C_3 are initial kinematic moduli of the three back stress components; γ_1, γ_2 and γ_3 are kinematic moduli of the three back stress components.

3.3. Experimental verification

Three cyclic loading tests that were conducted in our previous experimental investigation [10, 40] are applied here to examine the validity of the above analytical system. Geometrics of these three piers are listed in Table 3. Cyclic displacement was set along the 45 ° direction of the main sectional axis, with the loading protocol of displacement amplitude increasing by 0.5 times of δ_y (the yield displacement) per cycle. The weld corner at pier bottom was repeatedly pulled and compressed under this loading condition, making it the vulnerable site to fracture. The damage phenomena of these three piers were basically the same: micro cracks were firstly observed at the weld corner and propagated stably under the subsequent cyclic loads, followed by the sudden fracture and accompanied with the slight curvature of steel plates, as shown in Fig. 5(b). See references [10, 40] for more experimental details.

Table 3
Geometric dimensions and structural parameters of pier specimens [10, 40]

No.	H(m)	B(m)	W/B	λ_B	R_R	P/P_y	a(m)	t(m)	t_s(m)	b_s(m)
SP-1	2.00	0.45	1.00	0.32	0.467	0.2	0.45	0.008	0.008	0.049
SP-2	1.25	0.32	1.00	0.31	0.332	0.2	0.16	0.0074	0.0074	0.039
SP-3	0.65	0.20	1.00	0.29	0.311	0.2	0.10	0.0074	0.0074	0.034

The purpose of using the two-level zooming analytical system in this paper is to judge the damage occurrence sequence of the two failure modes of steel bridge piers. Thus, the experimental verification of the analytical system starts from these two parts. Comparations were made between the numerical and experimental hysteretic curves of pier specimens to verify the reliability of LI assessment, as shown in Fig. 4. The maximum relative errors between the experimental and numerical results are 7.6%, 10.9%, and 22.6% for SP-1, SP-2 and SP-3, respectively. The larger error shown in specimen SP-3 may be caused by the sliding between the fixture and pier base, as illustrated in the previous research [10]. Other key properties, such as the structural stiffness revolution and skeleton curve shape, are in good agreement with the test, which supports the reliability of the analytical system for LI assessment. Besides, the experimental ULCF fracture initiation results N_e and the cracking life N_p predicted by CVGM are presented in Table 4, in which only slight errors exist. The contour plot of the equivalent plastic strain of the sub2 model shown in Fig. 5 reveals that the calculated element has the highest plastic concentration, corresponding to the first occurrence position of ULCF cracks, which indicates the acceptable convincement of applying the two-level zooming strategy for ULCF assessment.

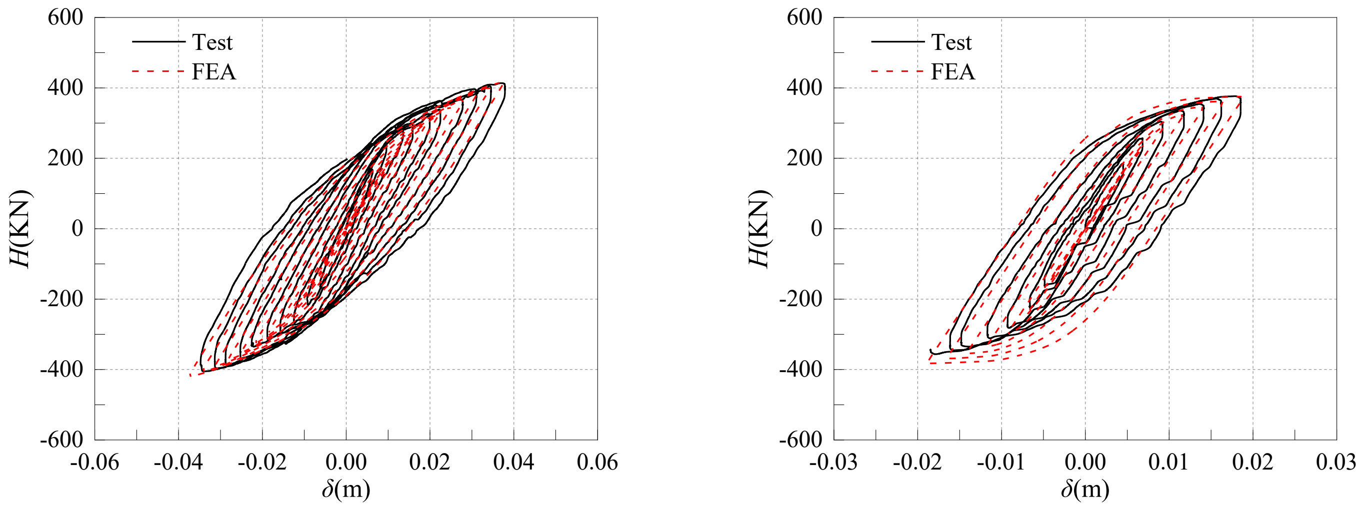

(a) SP-1

(b) SP-2

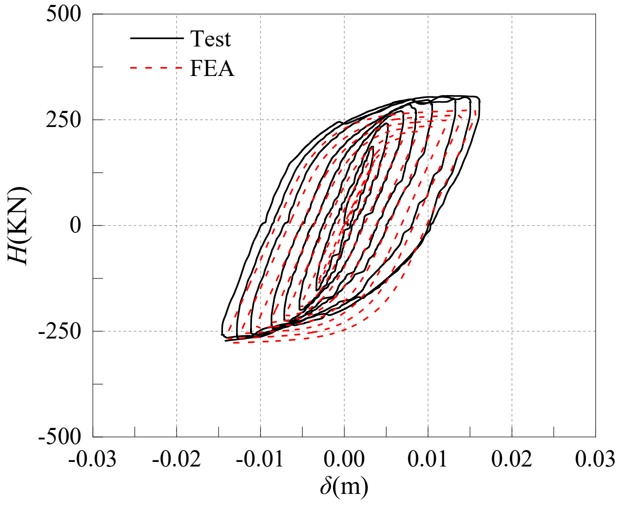

(c) SP-3

Fig. 4 Comparison of hysteretic curves obtained from tests and numerical analyses

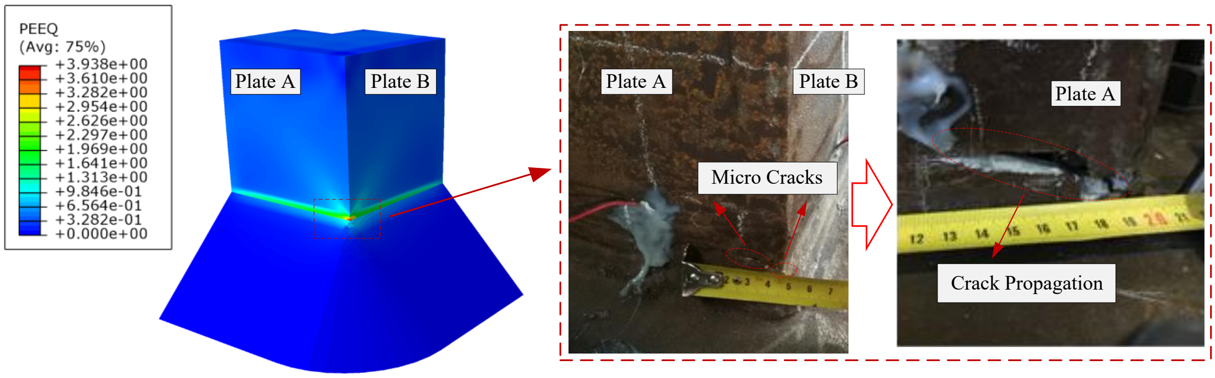

(a) Contour plot of equivalent plastic strain

(b) ULCF initiation observed in tests

Fig. 5 Plastic strain accumulation and ULCF initiation at the weld corner

Table 4
Comparation of experimental and numerical ULCF life

Specimen	N_e (Cycle)	N_p (Cycle)	Relative Error
SP-1	8	7	12.5%
SP-2	7	8	14.3%
SP-3	7	7	0.0%

4. Quasi-static analysis

4.1. Limit states

As illustrated earlier in Section 2.1, H_m, δ_m, and δ_{95} are the vital limit state points for evaluating the LI failure of steel piers, which also serve as the intermediate variables for the subsequent failure sequence judgment in this study. Elastoplastic analyses were carried out for the designed 90 piers with the load protocol shown in Fig. 6(a) [41-42] to acquire these limit states. Results are shown in Tables 5-7.

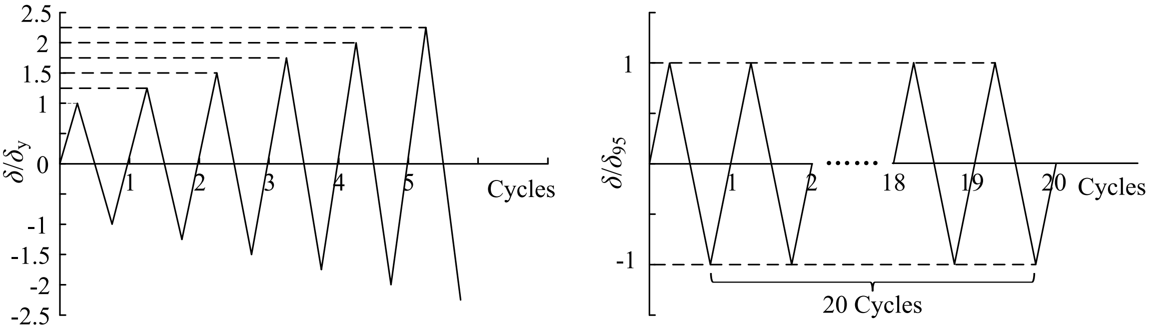

(a) Used for limit state analyses (b) Used for damage priority determination

Fig. 6 Loading protocols

Table 5
Limit states of box section steel piers (P/P_y=0.10)

No.	λ=0.25			No.	λ=0.30			No.	λ=0.35		
	H_m/H_y	δ_m/δ_y	δ_{95}/δ_y		H_m/H_y	δ_m/δ_y	δ_{95}/δ_y		H_m/H_y	δ_m/δ_y	δ_{95}/δ_y
S25-30	2.03	4.74	5.88	S30-30	2.02	4.95	5.87	S35-30	2.00	4.78	5.62
S25-35	1.93	4.26	5.15	S30-35	1.91	4.12	4.86	S35-35	1.89	3.96	4.58
S25-40	1.87	3.87	4.47	S30-40	1.85	3.71	4.26	S35-40	1.83	3.48	4.08
S25-45	1.80	3.14	3.61	S30-45	1.79	2.97	3.48	S35-45	1.77	2.89	3.40
S25-50	1.74	3.06	3.43	S30-50	1.72	2.89	3.24	S35-50	1.71	2.80	3.13

No.	λ=0.40			No.	λ=0.45			No.	λ=0.50		
	H_m/H_y	δ_m/δ_y	δ_{95}/δ_y		H_m/H_y	δ_m/δ_y	δ_{95}/δ_y		H_m/H_y	δ_m/δ_y	δ_{95}/δ_y
S40-30	1.97	4.59	5.28	S45-30	1.95	4.42	5.17	S50-30	1.94	4.03	5.01
S40-35	1.87	3.71	4.43	S45-35	1.86	3.74	4.17	S50-35	1.83	3.57	4.18
S40-40	1.81	3.40	3.92	S45-40	1.79	3.21	3.79	S50-40	1.77	3.21	3.71
S40-45	1.75	2.80	3.30	S45-45	1.73	2.72	3.25	S50-45	2.68	3.18	1.71
S40-50	1.69	2.71	3.02	S45-50	1.67	2.66	2.99	S50-50	1.69	2.71	3.02

Table 6
Limit states of box section steel piers (P/P_y=0.20)

No.	λ=0.25			No.	λ=0.30			No.	λ=0.35		
	H_m/H_y	δ_m/δ_y	δ_{95}/δ_y		H_m/H_y	δ_m/δ_y	δ_{95}/δ_y		H_m/H_y	δ_m/δ_y	δ_{95}/δ_y
S25-30	2.18	4.80	5.66	S30-30	2.16	4.48	5.35	S35-30	2.14	4.40	5.39
S25-35	2.08	4.12	4.79	S30-35	2.06	3.93	4.54	S35-35	2.03	3.82	4.39
S25-40	2.01	3.71	4.28	S30-40	1.99	3.57	4.09	S35-40	1.96	3.50	3.96
S25-45	1.95	3.23	3.62	S30-45	1.93	3.15	3.49	S35-45	1.91	3.06	3.42
S25-50	1.87	3.15	3.44	S30-50	1.86	3.06	3.32	S35-50	1.83	2.97	3.24

No.	λ=0.40			No.	λ=0.45			No.	λ=0.50		
	H_m/H_y	δ_m/δ_y	δ_{95}/δ_y		H_m/H_y	δ_m/δ_y	δ_{95}/δ_y		H_m/H_y	δ_m/δ_y	δ_{95}/δ_y
S40-30	2.10	4.25	4.92	S45-30	2.07	4.12	4.79	S50-30	2.05	3.96	4.55
S40-35	2.00	3.63	4.27	S45-35	1.98	3.67	4.04	S50-35	1.94	3.46	4.03
S40-40	1.93	3.40	3.85	S45-40	1.90	3.30	3.74	S50-40	1.88	3.14	3.63
S40-45	1.88	2.97	3.35	S45-45	1.86	2.89	3.31	S50-45	1.83	2.80	3.27
S40-50	1.81	2.80	3.09	S45-50	1.78	2.71	3.01	S50-50	1.78	2.80	3.11

Table 7
Limit states of box section steel piers (P/P_y=0.30)

No.	λ=0.25			No.	λ=0.30			No.	λ=0.35		
	H_m/H_y	δ_m/δ_y	δ_{95}/δ_y		H_m/H_y	δ_m/δ_y	δ_{95}/δ_y		H_m/H_y	δ_m/δ_y	δ_{95}/δ_y
S25-30	2.36	4.56	5.42	S30-30	2.33	4.41	5.11	S35-30	1.96	2.97	3.21
S25-35	2.24	4.06	4.64	S30-35	2.22	3.86	4.42	S35-35	2.18	3.74	4.28
S25-40	2.17	3.74	4.19	S30-40	2.14	3.58	4.01	S35-40	2.11	3.50	3.90
S25-45	2.11	3.35	3.63	S30-45	2.08	3.15	3.50	S35-45	2.05	3.10	3.40
S25-50	2.02	3.17	3.43	S30-50	1.99	3.01	3.30	S35-50	1.96	2.97	3.21

No.	λ=0.40			No.	λ=0.45			No.	λ=0.50		
	H_m/H_y	δ_m/δ_y	δ_{95}/δ_y		H_m/H_y	δ_m/δ_y	δ_{95}/δ_y		H_m/H_y	δ_m/δ_y	δ_{95}/δ_y
S40-30	2.25	4.16	4.74	S45-30	2.20	3.96	4.60	S50-30	2.20	3.93	4.46
S40-35	2.14	3.65	4.15	S45-35	2.11	3.58	3.99	S50-35	2.06	3.48	3.94
S40-40	2.07	3.41	3.81	S45-40	2.02	3.32	3.69	S50-40	1.99	3.23	3.60
S40-45	2.01	2.97	3.34	S45-45	1.98	2.97	3.32	S50-45	1.94	2.93	3.27
S40-50	1.92	2.88	3.14	S45-50	1.88	2.79	3.04	S50-50	1.88	2.80	3.13

From Tables 5-6, it is obvious that higher piers with thinner plates are more prone to suffering LI failure. The statistical analysis software IBM SPSS Statistics [43] was used to perform the nonlinear multivariate regression of the empirical limit state formulae of piers. The fitted empirical formulae are expressed as Eq. (8):

$$\begin{cases} \dfrac{H_m}{H_y} = 1.163\left(1+\dfrac{N}{N_y}\right)^{0.819} R_R^{\,0.384}\lambda_B^{-0.1}\left(\lambda_s^{'}\right)^{-0.641}, & \left(R^2 = 0.991\right) \\ \dfrac{\delta_m}{\delta_y} = 1.267\left(1+\dfrac{N}{N_y}\right)^{-0.121} R_R^{-10.068}\lambda_B^{-0.231}\left(\lambda_s^{'}\right)^{8.768}, & \left(R^2 = 0.965\right) \\ \dfrac{\delta_{95}}{\delta_y} = 1.328\left(1+\dfrac{N}{N_y}\right)^{-0.347} R_R^{-7.92}\lambda_B^{-0.248}\left(\lambda_s^{'}\right)^{6.616}, & \left(R^2 = 0.979\right) \end{cases} \tag{8}$$

where, $\lambda_s^{'}$ is the modified slenderness ratio parameter of the stiffener defined by Ge et al. [38]; R^2 is the determinant coefficient. A value of R^2 closer to 1 indicates a better fit between the data and model. These formulae work for piers with stiffened box section within the parameter case $0.25 \le \lambda_B \le 0.50$, $0.30 \le R_R \le 0.50$, $0.10 \le P/P_y \le 0.30$ and $\gamma/\gamma^* = 1.5$, providing an empirical reference for quick evaluation of LI damage of piers. Fig. 7 depicts the empirical curves, wherein the discrete points are the FE results listed in Tables 5-7. The agreement between the numerical data and regression curve suggests the high credibility of the empirical formulae.

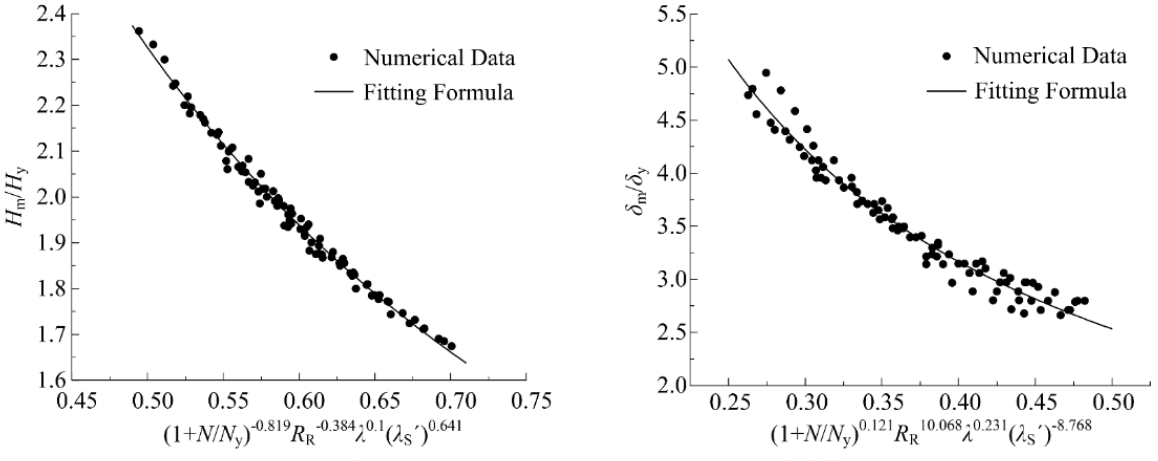

(a) H_m/H_y (b) δ_m/δ_y

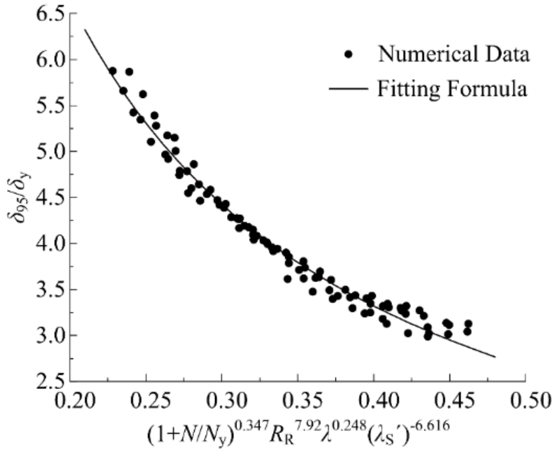

(c) δ_{95}/δ_y

Fig. 7 Fitting results of the regression formula for the limit state values

4.2. Damage occurrence priority

Given that the ULCF life is usually less than 20 loading cycles [1-2], the constant amplitude cyclic loading protocol shown in Fig. 6(b), which is characterized by the displacement amplitude of each pier's δ_{95} and the total loading cycle of 20, was adopted as the loading strategy for determining the failure occurrence priority of LI and ULCF. And there is a logical explanation for this selection. If a steel pier does not experience ULCF failure by the end of loading, that is, the structure is subjected to the LI failure for 20 times without undergoing the ULCF failure, it can be considered that the damage occurrence priority is LI. Otherwise, the damage occurrence priority is ULCF. Since the LI calculation is necessary whether LI or ULCF occurs first, this loading protocol is considered conservative to determine the damage priorities. Tables 8-10 list the estimated ULCF life of the 90 piers, in which "-" indicates that no ULCF fracture occurs until the end of the load. Furthermore, a dotted polyline is attached to each table to have a more intuitive distinguishment of different damage sequence.

Table 8

Predicted ULCF life versus structural parameters under P/P_y=0.10 (Unit: cycle)

λ R_R	0.25	0.30	0.35	0.40	0.45	0.50
0.50	-	-	-	-	-	-
0.45	-	-	-	-	-	-
0.40	5.78	-	-	-	-	-
0.35	0.77	0.73	1.76	1.77	2.79	2.81
0.30	0.65	0.65	0.65	0.69	0.73	0.71

Table 9

Predicted ULCF life versus structural parameters under P/P_y=0.20 (Unit: cycle)

λ R_R	0.25	0.30	0.35	0.40	0.45	0.50
0.50	-	-	-	-	-	-
0.45	-	-	-	-	-	-
0.40	-	-	-	-	-	-
0.35	2.76	2.81	0.71	4.80	-	-
0.30	0.75	1.67	1.69	1.81	2.76	3.77

Table 10

Predicted ULCF life versus structural parameters under P/P_y=0.30 (Unit: cycle)

λ R_R	0.25	0.30	0.35	0.40	0.45	0.50
0.50	-	-	-	-	-	-
0.45	-	-	-	-	-	-
0.40	-	-	-	-	-	-
0.35	-	-	-	-	-	-
0.30	2.79	2.77	-	-	-	-

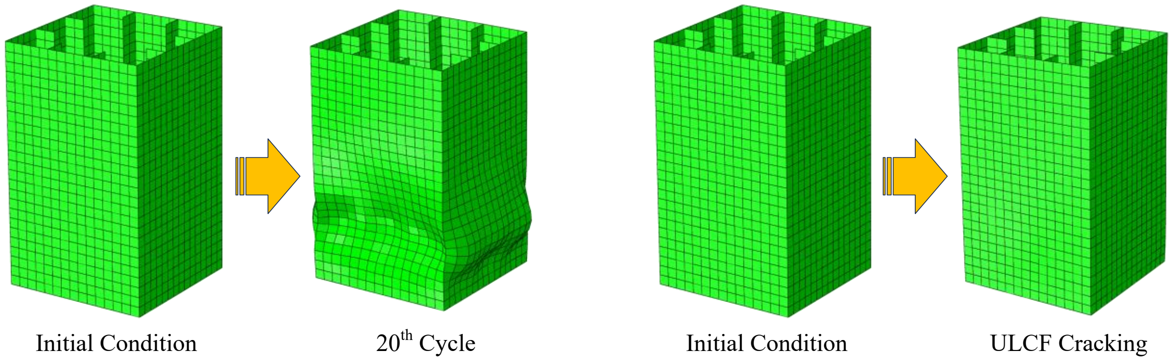

(a) S50-40P20 (thin-walled) (b) S25-35P20 (thick-walled)

Fig. 8 Deformation diagram

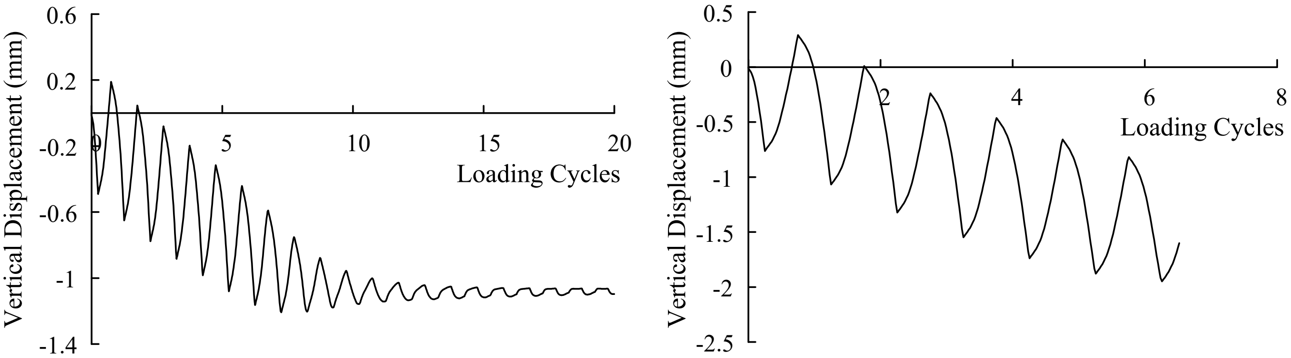

(a) S50-40P20 (thin-walled) (b) S25-35P20 (thick-walled)

Fig. 9 Plastic displacement history of weld corner

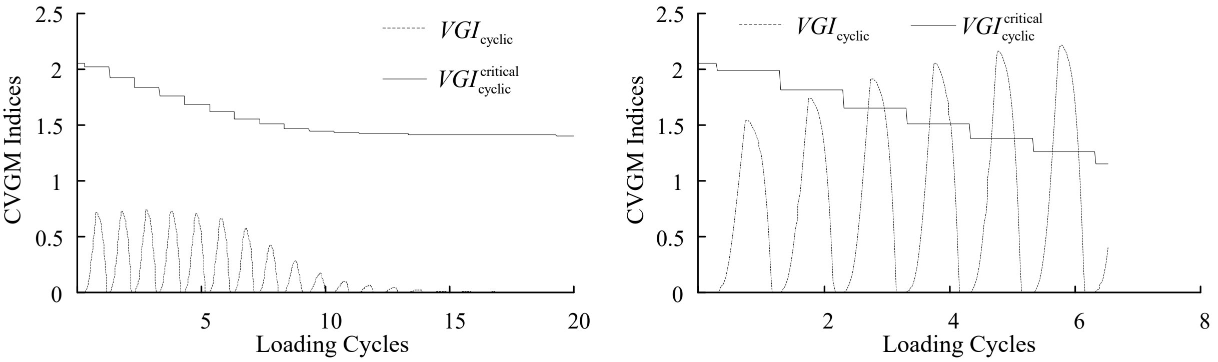

(a) S50-40P20 (thin-walled) (b) S25-35P20 (thick-walled)

Fig. 10 ULCF calculation process

It is obvious from the data presented in the tables that shorter piers with thicker plates are more inclined to ULCF damage, which is consistent with the qualitative relationship derived by Ge. et al. based on pier tests [11]. Also, it is found that with the increase of P/P_y, the damage occurrence priority tends to be the LI failure. An insight into the ULCF assessment process indicates that for piers with the ULCF life of "-", the absence of ULCF failure is not caused by the limited loading cycles (only 20 cycles) of the loading assumption. As shown in Fig. 10(a), the cyclic void growth index VGI_{cyclic} seems never exceeds the cyclic void capacity index $VGI_{\text{cyclic}}^{\text{critical}}$. In other words, the ULCF failure will never occur. To have a better explanation of the mechanism of this phenomenon, the ULCF damage evolution is discussed with the LI damage aggravation. Taking piers S50-40 with P/P_y=0.20 (abbreviated as S50-40P20) and S25-35 with P/P_y =0.20 (abbreviated as S25-35P20) as the representatives of the two different failure priorities, the deformation diagram of the overall structure at the instant of ULCF initiation or the end of the load, as well as the plastic displacement history of the weld corner are depicted in Fig. 8 and Fig. 9, respectively. Fig. 10 also depicts the evolution of the cyclic void growth index VGI_{cyclic} and the cyclic void capacity index $VGI_{\text{cyclic}}^{\text{critical}}$ of the two piers. It is found that for the typical thin-walled member (S50-40P20), the LI damage is particularly dominant, indicated by the steeply curved flange and web (Fig. 8(a)). Moreover, with the accumulation of LI damage, the amplitude of plastic displacement at the weld corner gradually decreases (Fig. 9(a)). Thus, it is of a rational deduction that the cyclic displacement transmitted from the superstructure is concentrated at a local area of the flange or web and is no longer transmitted downward. Correspondingly, the repeated expansion and compression of micro-voids within the metal of weld corner slows down, resulting in the prolonged ULCF life (Fig. 10(a)). In contrast, for the thick-walled member (S25-35P20), due to the absence of LI damage (Fig. 8(b)), the amplitude of plastic displacement at the weld corner remains constant until the final fracture (Fig. 9(b)), resulting in the continuous damage of ULCF (Fig. 10(b)). Apparently, it is the deformation characteristics of the structure, which is the comprehensive reflection of the relative thickness (width-to-thickness ratio), bending tolerance (slenderness ratio) and the degree of compression (axial compression ratio), that determine the different deformation patterns and further control the failure priorities.

In practical engineering, the structural parameters of steel pier can be set following the derived damage priorities, by which the designed pier will be prone to suffering LI damage. Thus, it is unnecessary to perform the burdensome ULCF assessment, and the seismic design calculations can be simplified.

5. Dynamic analysis

The derived damage occurrence priority is based on the quasi-static analyses under the assumed load protocol. To verify its reliability and applicability, nonlinear dynamic time-history analyses of steel piers with real earthquake wave inputs were performed.

5.1. Seismic excitation

To ensure the coexistence of LI and ULCF damage during time-history analyses, the selected seismic excitation should be destructive. In this study, the Northridge earthquake recorded at the LDM station in 1994, the Chi Chi earthquake recorded at the Caotun station in 1999 and the Lushan earthquake recorded at the 51BXD station in 2013 were used as ground motion inputs. The LDM station of the Northridge earthquake is located on the hanging wall of the fault; the Caotun station of the Chi Chi earthquake is located in the northwest of the source, which is near the rupture surface of the fault and is located on the footwall of the fault; the 51BXD station of the Lushan earthquake is located in the northwest of the source and on the hanging wall of the fault. These three seismic records are typical near-field motions. Among them, the seismic waves recorded at the LDM and Caotun stations have obvious pulse effects, and the ground motion in the long period range is dominant. While for the Lushan earthquake recorded at the 51BXD station, its pulse effect is not obvious and the ground motion in the short-period range is dominant. The acceleration time histories of these three records are presented in Fig. 11, where a_g represents the ground acceleration and t represents time.

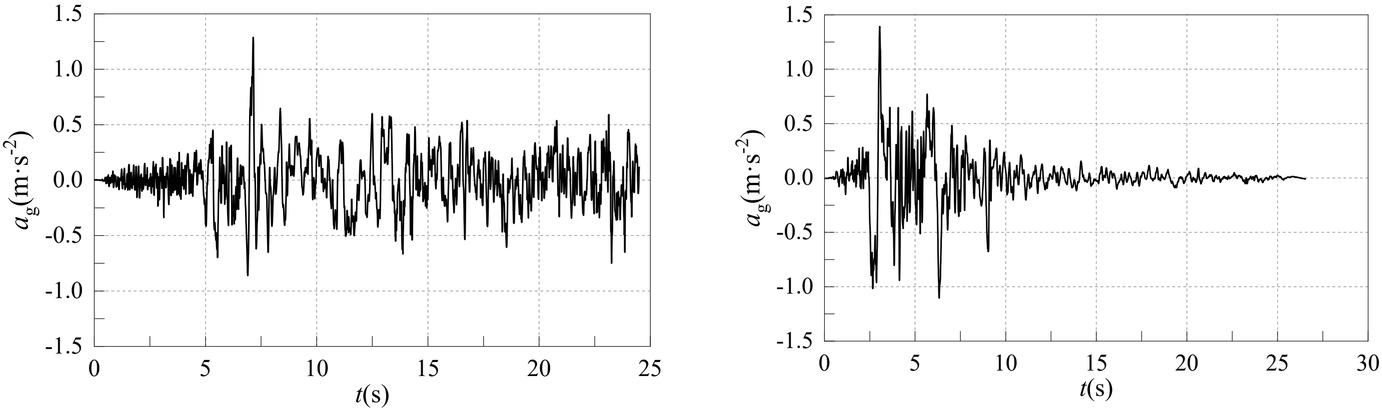

(a) the Chi Chi earthquake (b) the Northridge earthquake

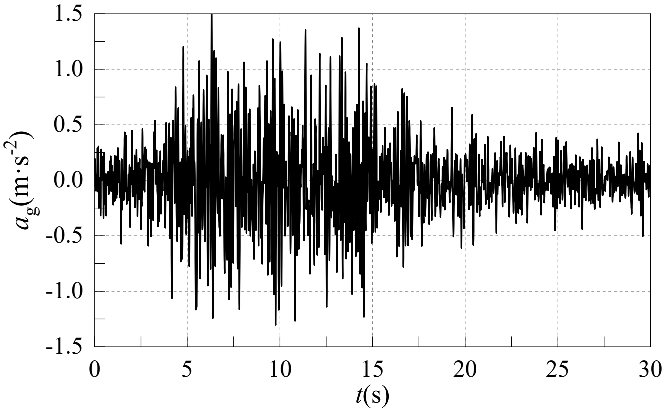

(c) the Lushan earthquake

Fig. 11 Seismic waves

5.2. Seismic performance of piers

Owing to the space limitation of the paper, only three piers, namely S40-45P20, S30-35P10, and S30-35P30, were applied as examples for validating the reliability of the derived damage occurrence priority. The structural parameters of these three piers are located near the dotted polylines attached in Tables 8-10 for the sake of effective verification. Results of the hysteresis curves and the CVGM indices evolution of these three piers under seismic excitations are presented in Figs. 12-14. Initiations of LI failure and ULCF failure are determined by the limit state point (δ_{95}, H_{95}) and CVGM criterion $VGI_{\text{cyclic}} \ge VGI_{\text{cyclic}}^{\text{critical}}$, respectively, which are marked in the figures. It is shown that the computed damage occurrence priorities are LI damage-dominant for piers S40-45P20 and S30-35P30, and ULCF damage-dominant for pier S30-35P10, indicating the good consistency with the damage occurrence listed in Tables. 8-10.

The dynamic analyses conducted in this paper were only examples to verify the reliability of the simplified seismic design method using the damage occurrence sequence. Due to the assumed loading protocol, the determination of whether ULCF checking is necessary, as discussed in this paper, is conservative. The piers prioritized for ULCF damage in this study may undergo LI damage before ULCF under actual seismic loading. However, piers designed using the simplified design method proposed in this paper are considered to be on the safer side under such a situation.

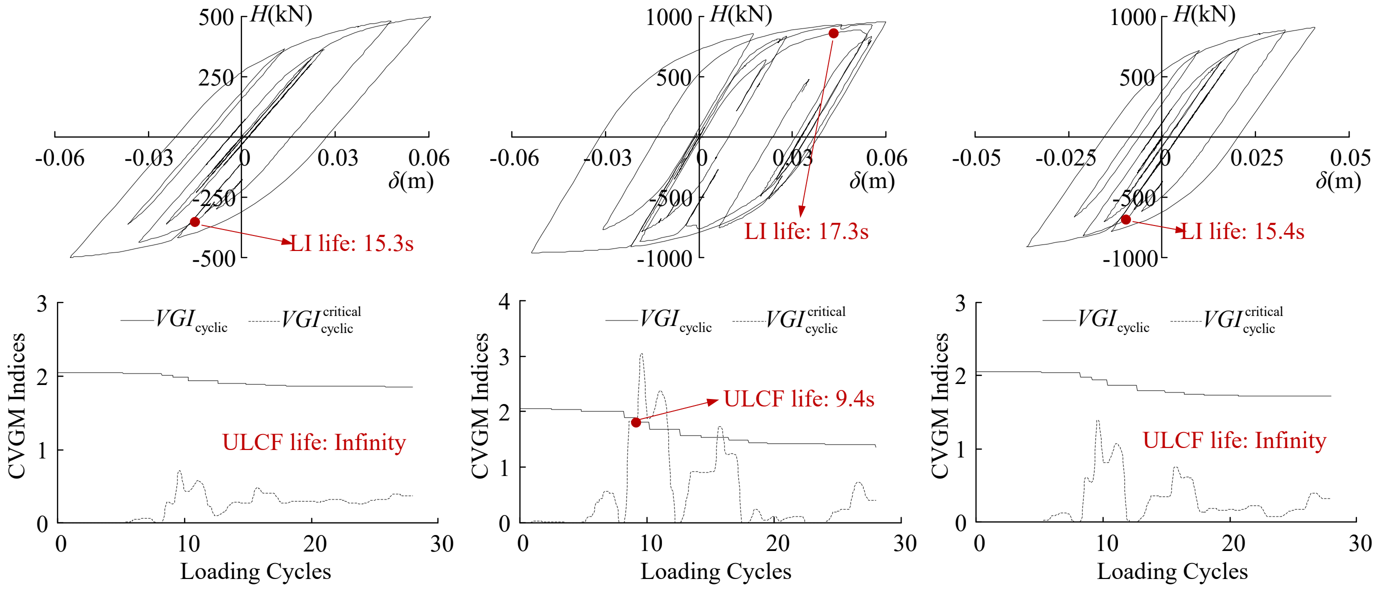

(a) S40-45P20 (b) S30-35P10 (c) S30-35P30

Fig. 12 Seismic performance of piers under Chi Chi earthquake

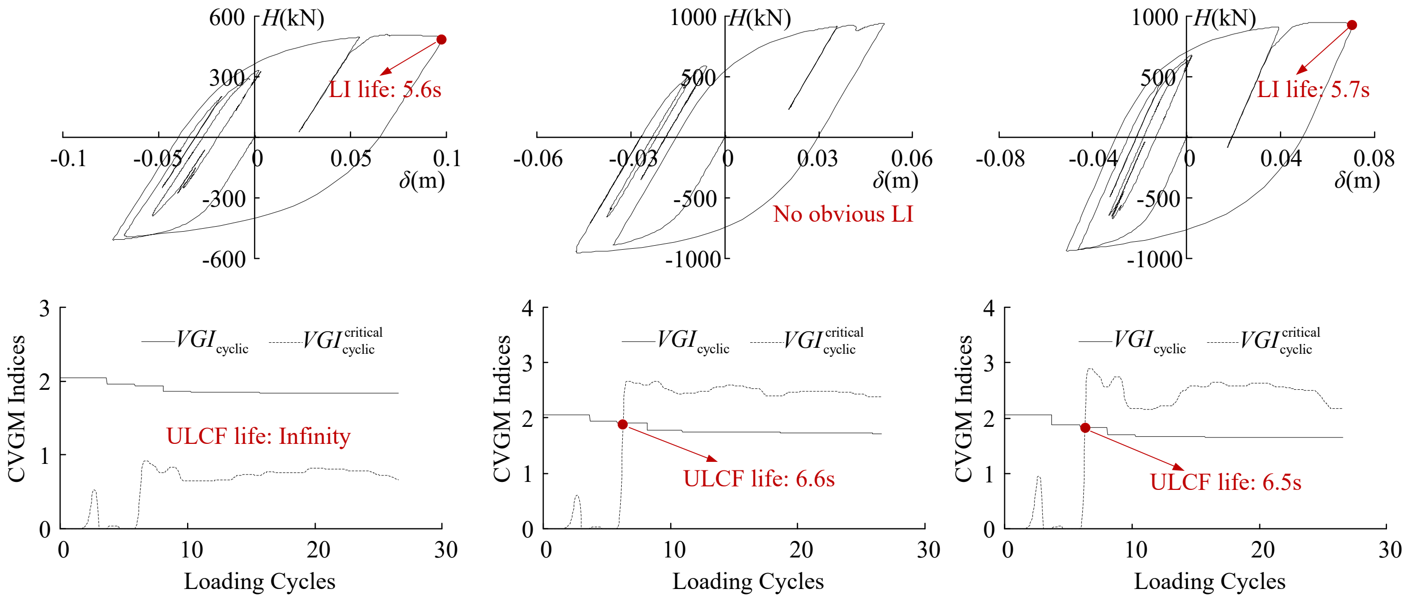

(a) S40-45P20 (b) S30-35P10 (c) S30-35P30

Fig. 13 Seismic performance of piers under Northridge earthquake

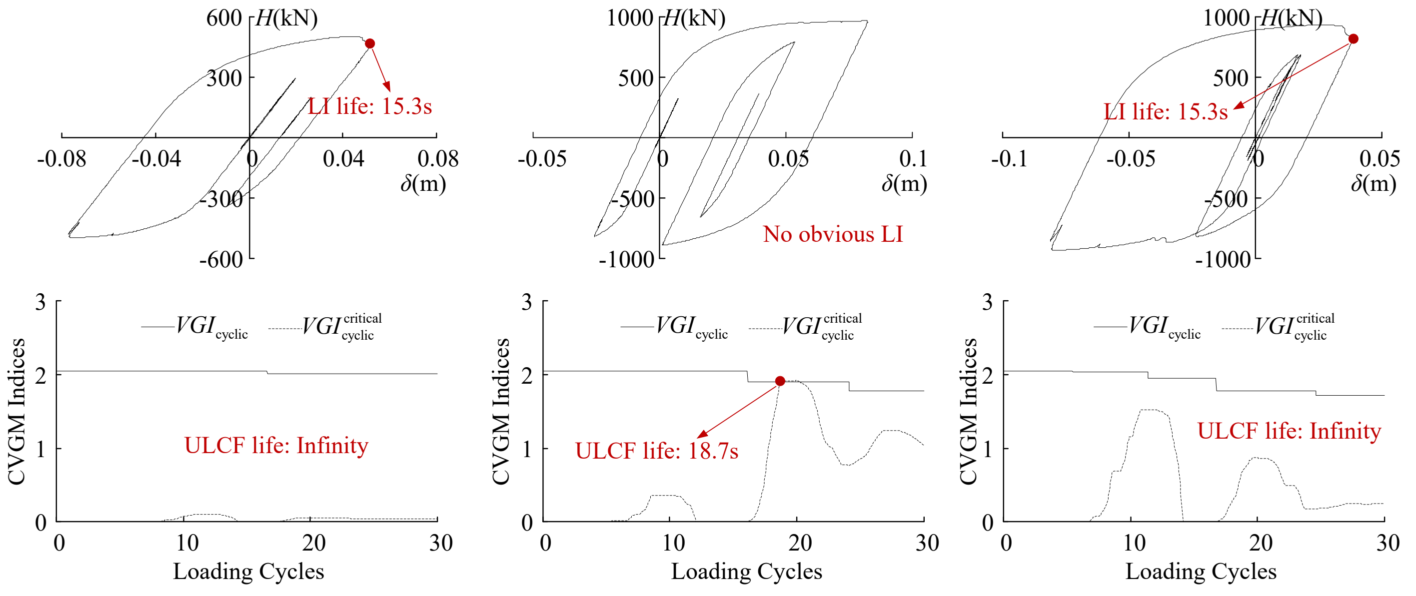

(a) S40-45P20 (b) S30-35P10 (c) S30-35P30

Fig. 14 Seismic performance of piers under Lushan earthquake

6. Conclusions

A simplified seismic design method of steel piers is presented in this study by investigating the failure occurrence priority of LI and ULCF, which are two main potential failure modes of steel piers under severe earthquake. Based on the derived failure occurrence sequence, it is possible to construct piers with the LI failure occurrence priority in the potential seismic area, avoiding the burdensome ULCF check. The main conclusions of this study which could be drawn are as follows:

- The constant amplitude cyclic loading protocol, with the displacement amplitude of each pier's critical displacement δ_{95} and the total loading cycle of 20, can serve as the loading assumption to determine the failure occurrence priority. The qualitative regulation of the failure occurrence priority derived in this paper is the same as that reported in the literature [11].
- The quantitative relationship between the structural parameters and the failure occurrence priority of box section single-column Q345qC steel constructed steel pier, within the structural parameter ranges of $0.25 \leq \lambda_B \leq 0.50$, $0.30 \leq R_R \leq 0.50$, $0.10 \leq P/P_y \leq 0.30$ and $\gamma/\gamma^* = 1.5$, was established.
- Discussions on the seismic performance of steel piers prove that the regulation of the failure occurrence sequence is determined by the mechanical properties of the pier structure, rather than the loading condition.
- Dynamic time-history analyses with real seismic wave inputs were conducted to verify the results of the failure occurrence priority derived by the quasi-static analyses. The damage sequences derived from the two kinds of analyses show good consistency, indicating the reliability of the simplified seismic design method proposed in this study.

Due to the assumed loading protocol applied in this paper, the judgment on the necessity of ULCF checking in this paper is conservative. Piers with the damage priority of ULCF in this study may experience the LI damage before the ULCF under real seismic motion. Although the piers designed using the proposed method are considered to be on the safer side under such a situation, the available structural parameter range is narrowed. In future research, further refinement of the assumed quasi-static loading protocol can be performed to pursue a more accurate relationship between damage priorities and structural parameters according to the seismic motion characteristics of different seismic regions, such as the magnitude, fault parameters and seismic propagation paths.

Acknowledgement

The research in this paper has been conducted as part of the research projects granted by the National Natural Science Foundations of China (51878606 and 52178174). Data for this study are provided by Institute of Engineering Mechanics, China Earthquake Administration. Besides, further appreciation is given to Dassault Systèmes Simulia Corporation for the FE simulation of the powerful commercial FE software ABAQUS-6.14.

References

[1] Kuwamura H., "Transition between fatigue and ductile fracture in steel", Journal of Structural Engineering, 123(7), 864-870, 1997.

[2] Kanvinde A.M., Micromechanical simulation of earthquake-induced fracture in steel structures, Dissertation, Stanford University, 2004.

[3] Nakashima K., Inoue K., and. Tada M., "Classification of damage to steel buildings observed in the 1995 Hyogoken-Nanbu earthquake", Engineering Structures, 20(4), 271-281, 1998.

[4] Subcommittee on Investigation of Seismic Damage of Steel Structure, "Investigation of causes of damage to steel structure on Hanshin-Awaji earthquake disaster", Doboku Gakkai Ronbunshu, 64, 17-30, 2000. (In Japanese)

[5] Miller D.K., "Lessons learned from the Northridge earthquake", Engineering Structures, 20(4), 249-260, 1998.

[6] Ge H.B. and Kang L., "Ductile crack initiation and propagation in steel bridge piers subjected to random cyclic loading", Engineering Structures, 59, 809-820, 2006.

[7] Goto Y., Jiang K.S. and Obata M., "Stability and ductility of thin-walled circular steel columns under cyclic bidirectional loading". Journal of Structural Engineering. 132(10), 1621-1631, 2006.

[8] Goto Y., Ebisawa T., Lu X.L., Lu W.S., "Ultimate state of thin-walled circular steel columns subjected to biaxial horizontal forces and biaxial bending moments caused by bidirectional seismic accelerations", Journal of Structural Engineering, 141(4), 04014122, 2015.

[9] Zhuge H.Q., Xie X. and Tang Z.Z., "Lengths of damaged zones of steel piers under bidirectional horizontal earthquake components", China Journal of Highway and Transport, 32(8), 79-91, 2019. (In Chinese)

[10] Li S.L, Lin J.H., Zhuge H.Q., Xie X. and Cheng C., "Ultra-low cycle fatigue fracture initiation life evaluation of thick-walled steel bridge piers with microscopic damage index under bidirectional cyclic loading", Structures, 43, 669-681, 2022.

[11] Ge H.B., Kang L. and Tsumura Y., "Extremely low-cycle fatigue tests of thick-walled steel bridge piers", Journal of Bridge Engineering, 18(9), 858-870, 2013.

[12] Jenothan M., Jayasinghe J. A. S. C. and Bandara C. S., "Lateral behaviour and performance evaluation of steel piers under cyclic lateral loading", Journal of Constructional Steel Research, 201, 107764, 2023.

[13] Ge H.B. and Usami T., "Cyclic tests of concrete-filled steel box columns", Journal of Structural Engineering, 122(10), 1169-1177, 1996.

[14] Goto Y., Muraki M. and Ebisawa T., "Ultimate state and design of thin-walled circular steel columns under bi-directional seismic excitations", Kozo Kogaku Ronbunshu, 629-642, 2009.

[15] Gao S.B., Usami T. and Ge H.B., "Ductility evaluation of steel bridge piers with pipe sections. Journal of Engineering Mechanics", 124(3), 260-267, 1998.

[16] Specifications for Highway Bridges, Part II: Steel Bridges 2017., Japanese Road Association, Tokyo, Japan, 2017.

[17] Guide Specifications for LRFD Seismic Bridge Design 2011., American Association of State Highway and Transportation Officials, Washington, America, 2017.

[18] Specifications for Design of Highway Steel Bridge 2017., Ministry of Transport of the People's Republic of China, Beijing, China, 2017.

[19] Coffin L.F., "A study of the effects of cyclic thermal stresses on a ductile metal", Trans. ASME, 76, 931-50, 1954.

[20] Manson S.S., "Fatigue: a complex subject – some simple approximations", Experimental Mechanics, 5, 193-226, 1965.

[21] Tateishi K., Hanji T. and Minami K., "A prediction model for extremely low cycle fatigue strength of structural steel", International Journal of Fatigue, 29(5), 887-896, 2007.

[22] Xue L., "A unified expression for low cycle fatigue and extremely low cycle fatigue and its implication for monotonic loading", International Journal of Fatigue, 30(10), 1691-1698, 2008.

[23] Xie X., Cheng C. and Li S. L., "A deformation history-based approach for ultra-low cycle fatigue damage evaluation of steel structures", International Journal of Steel Structures, 20(4), 1378-1392, 2020.

[24] Tamura H., Sasaki E., Yamada H. and Katsuchi H., "Analytical study focusing on stress triaxiality on factor of brittle fracture during earthqakes in steel bridge bents", Structural Engineering & Earthquake Engineering, 66(3), 420-434, 2010. (In Japanese)

[25] Tamura H. and Sasaki E., "A study on modified weibull stress based evaluation of brittle fracture occurrence during earthquakes in steel members", Structural Engineering & Earthquake Engineering, 71(2), 173-185, 2015. (In Japanese)

[26] Liu Y., Kang L. and Ge H.B., "Experimental and numerical study on ductile fracture of structural steels under different stress states", Journal of Constructional Steel Research, 158, 381-404, 2019.

[27] Tong L.W., Huang X.W., Zhou F. and Chen Y.Y., "Experimental and numerical investigations on extremely-low-cycle fatigue fracture behavior of steel welded joints", Journal of Constructional Steel Research, 119(1), 98-112, 2016.

[28] Kanvinde A. M., Deierlein G. G., Kanvinde A. M. and Deierlein G. G., "Cyclic void growth model to assess ductile fracture initiation in structural steels due to ultra low cycle fatigue", Journal of Engineering Mechanics, 133(6), 701-712, 2007.

[29] Liao F.F., Micromechanical simulation of earthquake-induced fracture in steel structures, Dissertation, Tongji University, 2012. (In Chinese)

[30] Liao Y.H., Research on ultra low cycle fatigue properties and fracture mechanism of steel bridge welded joint, Dissertation, Zhejiang University, 2018. (In Chinese)

[31] Usami T., Gao S.B. and Ge H.B., "Elastoplastic analysis of steel members and frames subjected to cyclic loading", Engineering Structures, 22(2), 135-145, 2000.

[32] Liu N.F., Gao S.B., "Ductility prediction of stiffened steel pipe-section bridge piers", Journal of Harbin Institute of Technology, 49(3), 138-143, 2017. (In Chinese)

[33] Xie X., Zhuge H.Q., Tang Z.Z., Wang T. and Liao Y-H., "Damage characteristics of thin-walled steel arch bridges subjected to in-plane earthquake action", Journal of Constructional Steel Research, 151, 70-82, 2018.

[34] Tsai C.Y., Tsai K.C., Li C.H., Wu C.C., Lin K.C. and Jhuang S.J., "Seismic fracture evaluation of diaphragm joints in welded beam-to-box column moment connections", Earthquake Engineering & Structural Dynamics, 49(13), 1344-1362, 2020.

[35] Wang Y.M., Zhang H.D., Ju J.S. and Fu Y.D., "Influence of welding residual stress on ultra-low cycle fatigue properties of beam-column joints in steel frame", Strength of Materials, 54(4), 734-746, 2022.

[36] Noferesti H., Razmkhah M.H. and Gerami M., "Laboratory and ultra-low cycle fatigue evaluation of the seismic performance of BFP connection with different amounts of pre-tension in bolts", Journal of Constructional Steel Research, 212, 108295, 2023.

[37] Zhang Y.L., Wang W., Huo H.W., Wang Y. and Fang C., "Cyclic void growth model to assess ductile fracture initiation in structural steels due to ultra low cycle fatigue", Journal of Constructional Steel Research, 215, 108561, 2024.

[38] Ge H.B., Gao S.B. and Usami T., "Stiffened steel box columns. Part 1: Cyclic behaviour", Earthquake Engineering & Structural Dynamics, 29(11), 1691-1706, 2000.

[39] Shi Y.P. and Zhou Y.R., Detailed explanation of ABAQUS finite element analysis examples, Mechanical Industry Press, Beijing, 2006.

[40] Zhuge H.Q., Xie X., Li S-L., Wang J.D., "Seismic performance test and practical calculation method of thin-walled square-section steel piers under horizontal bi-directional seismic excitations", China Civil Engineering Journal, 53(12), 74-85, 2020. (In Chinese)

[41] Tang Z.Z., Xie X., Wang T. and Wang J.Z., "Study on FE models in elasto-plastic seismic performance evaluation of steel arch bridge", Journal of Constructional Steel Research, 113, 209-220, 2015.

[42] Chen S.X., Xie X., Zhuge H.Q., "Hysteretic model for steel piers considering the local buckling of steel plates", Engineering Structures, 183, 303-318, 2019.

[43] Pallant J., SPSS survival manual: a step by step guide to data analysis using SPSS for windows version 15, Open University Press, London, 2007.

Advanced Steel Construction – Vol. 21 No. 3 (2025) 243–252
DOI:10.18057/IJASC.2025.21.3.6

SEISMIC BEHAVIOR AND RESIDUAL SEISMIC CAPACITY OF CORRODED DOUBLE-STEEL-PLATE COMPOSITE SHEAR WALL

Jian Li [1, *], Bo-Kai Chen [1], Zhe Zhao [1], Gang Gao [2] and Yan Wang [1]

[1] *School of Civil Engineering, Qingdao University of Technology, Qingdao, 266033, China*
[2] *Yantai Jinjian Engineering Design Co, Ltd, Yantai, Shandong 264000, China*
* *(Corresponding author: E-mail: 1_li@qut.edu.cn)*

ABSTRACT

In long-term aggressive corrosion environments, steel structures are susceptible to corrosion, which can significantly impair their mechanical performance. The seismic behavior of the corroded double-steel-plate composite shear wall (DSCW) is investigated in this paper. The parameters investigated include the corrosion rate, steel plate thickness, axial compression ratio, and concrete strength. The corroded DSCW model was established using ABAQUS's secondary development function. The research results show that: local corrosion under cyclic loading may cause the steel plate to buckle prematurely, resulting in early concrete crushing and failure of the binding bars; The hysteresis curve of the corroded specimen shows a distinct "pinching" effect; With the increase of corrosion rate, the bearing capacity and ductility of DSCW decrease obviously. The optimal steel plate thickness for seismic performance is identified as 9 mm, while higher concrete strength correlates with enhanced bearing capacity; Increasing the axial compression ratio leads to a gradual decrease in bearing capacity. A shear capacity formula that accounts for corrosion rates is proposed, and the relationship between the residual seismic capacity and drift, in terms of energy dissipation, is also analyzed. Finally, the study calculates the reinforceable residual drift limits for DSCW damaged by earthquakes.

ARTICLE HISTORY

Received:	27 August 2024
Revised:	6 January 2025
Accepted:	8 January 2025

KEYWORDS

Double-steel-plate composite shear wall;
Seismic performance;
Local corrosion;
Finite element simulation;
Residual seismic capacity

1. Introduction

The double-steel-plate composite shear wall (DSCW) comprises of exterior steel plates, in-filled concrete, and mechanical connectors. Recently, DSCW has become widespread use as lateral force-resisting elements in high-rise buildings and nuclear power plants [1-2]. However, when exposed to corrosive environments, the exterior steel plates become susceptible to corrosion, which causes damage to the surface and makes the DSCW less able to handle earthquakes. Therefore, we need to explore how DSCW behaves during earthquakes after it has corroded.

The performance of the DSCW is largely determined by the bond between the steel plates and the concrete. Insufficient confinement between these materials may cause premature buckling of the steel plates [3]. Various connectors have been proposed to enhance the bond, including connectors with different shapes [4-10]. Zhang and Chen [11,12] proposed DSCW with shear bolts, stiffeners, and L-shaped connectors. It should be noted that these connectors require extensive welding, which may induce deformation and residual stresses. The DSCW connector selected in this study uses a binding bar, which is a bolt-based connection method. The constraint rod can be installed quickly and conveniently, without the need for welding. Zhu et al. [10] proposed the DSCW with binding bars and found that reducing the spacing between the binding bars effectively enhances the seismic performance of the DSCW. Although the seismic performance of DSCW has attracted significant attention, research on their seismic performance after corrosion remains limited.

Corrosion seriously affects the strength of steel, leading to significant degradation. A lot of research has been done to understand how corrosion affects steel. Imperatore et al. [13] studied how even corrosion affects the constitutive relationships of steel rebars. Sun et al. [14] found that in addition to uniform corrosion, random pitting corrosion also occurred in steel rebars. Pitting damage caused stress concentrations in steel bars, leading to varying degrees of degradation in their mechanical properties. Qin and Jin [15,16] conducted both experimental investigations and numerical simulations to assess the impact of corrosion on steel. Their results indicated that the decrease in the mechanical properties of the steel was linked to the loss of cross-sectional area in the steel, leading to substantial changes in the yield plateau, which ultimately resulted in decreased strength and ductility. Ren et al. [17] highlighted that the presence of pitting, particularly under conditions of nonuniform corrosion, caused localized stress concentrations, which expedited the failure of the steel. These studies, employing both experimental and numerical approaches, offer valuable insights into the degradation patterns of corroded steel. Although most of these studies have focused on the corrosion of individual steel members, they provide a solid foundation for understanding the mechanical behavior of composite structures exposed to corrosion.

Recent years have seen a surge in research examining the performance of corroded composite structures, particularly targeting Concrete-Filled Steel Tubes (CFST). Yang et al. [18] investigated the mechanical properties of CFST subjected to both uniform and local corrosion. Local corrosion is a common occurrence in practical engineering, prompting numerous studies on the mechanical behavior of CFST under such conditions [19-23]. Scholars have simulated local corrosion by introducing surface defects in steel tubes to assess their impact. Huang et al. [24] found that artificial notches, whether vertical or slanted, significantly reduced the peak resistance and ductility of the steel tubes. However, horizontal notches had a lesser impact on peak resistance and ductility, primarily causing global flexural buckling. Zhong et al. [25] observed that local defects in the steel tubes causing a shift in the specimen's centroid and a subsequent decrease in the bearing capacity of CFST. While simulating local defects effectively replicated the mechanical properties after local corrosion, it differed significantly from the damage observed in CFST under real corrosion environments. To bridge this gap, Xue et al. [26] designed CFST specimens subjected to NaCl solution and atmospheric corrosion. An accurate finite element (FE) model was developed based on 3D scanning profile data, revealing that corrosion exhibited fractal characteristics and significantly reduced the specimen's ductility. Corrosion-induced circumferential expansion often led to steel pipe fractures, further diminishing ductility. Zhang et al. [27] found that corrosion of the outer steel pipe significantly reduced the axial bearing capacity and plastic deformation capacity of CFST. As the corrosion ratio increased, the mechanical properties further decreased. Significant progress has been made in the aforementioned literature, which is critical for improving the design of CFST. However, few studies have been conducted on corroded DSCW in steel-concrete structures. Therefore, investigating the seismic performance of corroded DSCW is essential for evaluating its service life. Current codes also lack design methods for corroded DSCW. Therefore, studying the seismic performance of corroded DSCW is of significant meaning for assessment the service life of corroded DSCW.

DSCW are critical components in resisting lateral forces and are subjected to cyclic loading, necessitating a thorough investigation into their seismic performance after corrosion. This paper mainly studies the seismic performance of corroded DSCW with binding bars. Corrosion patterns were categorized into uniform corrosion and random pitting, based on relevant standards and corrosion tests on steel plates. Consequently, the model considers local uniform corrosion and random pitting on the exterior steel plates. A detailed parameter analysis is subsequently conducted to examine the mechanical characteristics of the corroded DSCW. Based on finite element calculations, a formula for calculating corroded DSCW bearing capacity is proposed. Considering the risk of seismic events affecting already damaged members, the study proposes a seismic damage evaluation method for DSCW, based on residual drift and residual seismic capacity post-earthquake. Furthermore, the study proposes limit values for evaluation indices to ensure the reinforced capacity of these structural members post-earthquake.

2. FE model establishment and verification

2.1. Design of local corrosion specimen model

Research on DSCW has primarily focused on their seismic performance with various connectors. However, a gap remains in understanding the mechanical behavior and failure modes of these shear walls under cyclic loading in corrosive environments. This study investigates the seismic performance of DSCWs with binding bars under cyclic loading after corrosion. Nonlinear static analysis methods were employed to comprehensively explore and elucidate the seismic behavior of these shear walls under varying corrosion levels. Under typical atmospheric conditions, steel plates corrode initially, forming areas with specific maximum residual thicknesses that later develop local pitting corrosion. According to the studies by Wang et al. [28] and using formulas derived from the mean values of corrosion pits, equations were fitted to estimate the uniform corrosion thickness and the diameter of pitting pits as the corrosion rate varies, shown in Fig. 1 and Eq. (1). Using these formulas, the uniform corrosion thickness and mean values of pitting pits for steel plates with corrosion rates of 10%, 15%, and 25% were determined. To realistically simulate the seismic performance of DSCWs under local corrosion, random functions in Python software were used to generate random corrosion pits on steel plates, as shown in Fig. 2. This approach ensures that the corrosion simulation captures the varied and unpredictable nature of pitting corrosion's effects on structural performance.

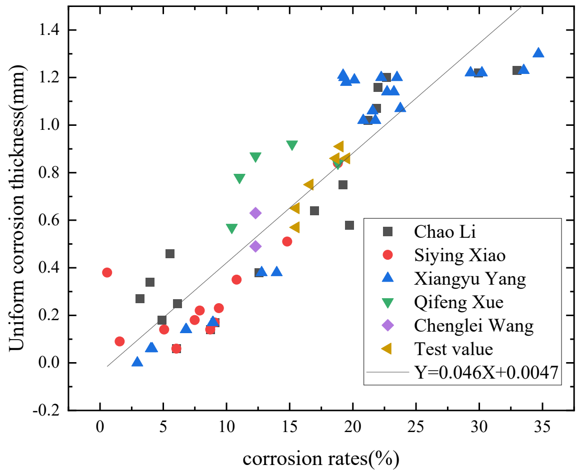

Fig. 1 The uniform corrosion thickness changes with the corrosion rates to fit the formula

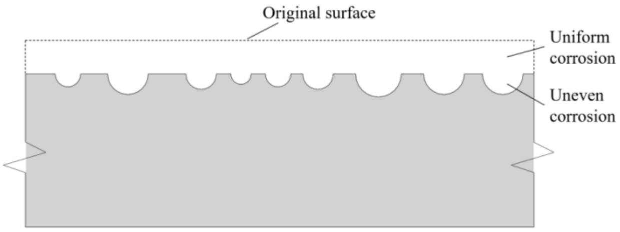

Fig. 2 The Python software's random function generates random rust pits on the steel plate

$$\mu_D = 0.729 + 0.041\rho_V \quad R^2=0.713 \tag{1a}$$

$$\sigma_D = 0.526 + 0.034\rho_V \quad R^2=0,789 \tag{1b}$$

where μ_D is the average diameter of the corrosion pits, σ_D is the standard deviation of the diameter of the pit, ρ_V is the local volume loss rate.

We focus on the numerical simulation of pitting randomness during the construction of the geometric model. Geometric modeling serves as the core of the simulation methodology. Previous studies have shown that the shape of corrosion pit has little effect on the mechanical properties of the structure. [29,30], so we chose a circular pit to simulate pitting. The locations of these pits were determined using Python's Random function, which defined the distribution of pitting. A Boolean operation was subsequently applied to generate the final geometric model, based on the relationship between the generated array of storage forms and the corresponding position vector array. The flowchart is shown in Fig. 3.

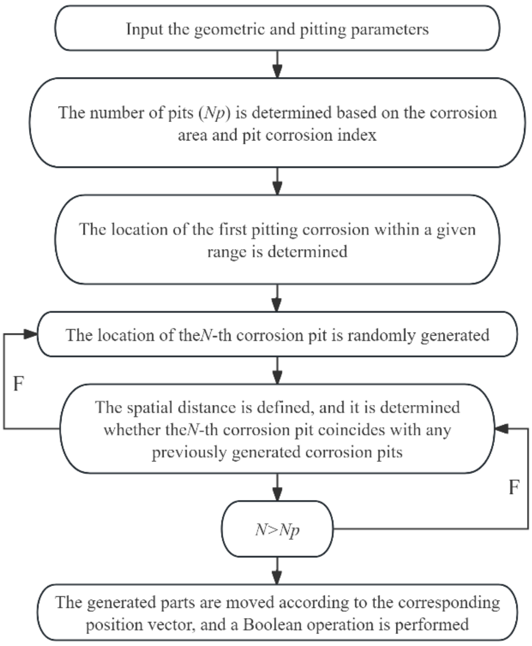

Fig. 3 The flow chart of modeling process

2.2. Material properties

2.2.1. Steel

In this study, steel was modeled using the isotropic elastic-plastic model in ABAQUS software. This model effectively describes the metal's plastic characteristics and satisfies the Von-Mises stress yield criterion. The stress-strain relationship follows the five-fold line model detailed in "Steel Pipe Concrete Structures" [31] by Zhong.

2.2.2. Concrete

In order to simulate the mechanical behavior of concrete, the concrete damage plasticity model in ABAQUA is adopted. This model was chosen based on yield surfaces proposed by Lubliner [32] and Lee [33], with an additional cracking energy criterion defined by Hillerborg et al. [34]. Han's [35] stress-strain relationship for concrete tension was adopted. The tensile cracking and compressive failure of concrete can be well simulated by using the corresponding stress-strain relationship in ABAQUS.

2.2.3. Element type and interaction

During the meshing process, the end plates, binding bars, and concrete were meshed using hexahedral elements. Due to pitting corrosion on the steel plate's surface, hexahedral meshing was applied to the non-corroded areas, while tetrahedral meshing was used for the corroded regions of the steel plates. The meshing of each part is shown in Fig. 4.

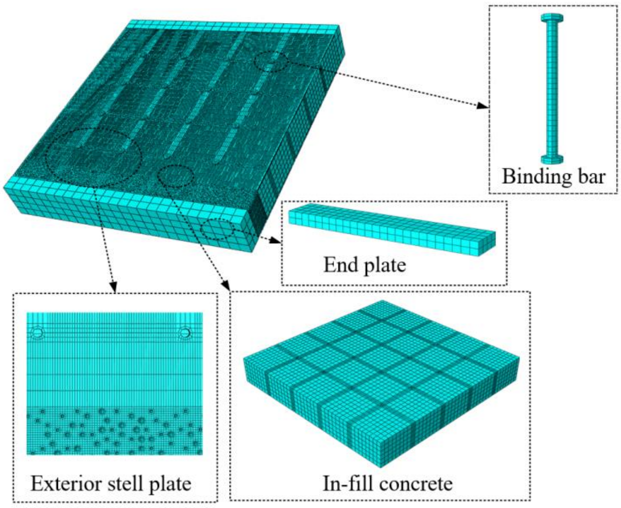

Fig. 4 FE model

The following interaction relationships were defined: “Tie” constraints were applied between the end plates and the concrete, still between the end plates and the steel plate. Frictional constraints were applied between the steel plate and concrete, with the coefficient of friction set to 0.6. The same contact setting was applied between the binding bars and the concrete. Frictional contact was defined between steel plates and binding bars, with the coefficient of friction is set to 0.3.

2.3. Boundary conditions

The loading process takes place in two stages. In the first stage, axial pressure is applied, followed by the application of horizontal load in the second stage. The lower end plate of the shear wall is fully fixed to prevent any movement. The upper end plate is coupled to the reference point. To prevent out-of-plane instability of the DSCW, a displacement constraint of out-of-plane is applied at the reference point.

2.4. Model verification

Based on the above Settings, SCSW4 specimens in reference [36] were selected for modeling to ensure correctness of parameters of the FE model. The size and loading mode of the FE model are same with test.

The failure mode and steel plate buckling position of the finite element analysis results are very similar to those of the test (Fig. 5). Both FE model and experimental test showed steel plate local buckling at the end of the specimen. This confirms the accuracy and reliability of the finite element simulation in predicting the failure mode of the DSCW. From the comparative analyses of the hysteresis curves and skeleton curves, it is evident that they all have very similar trends and the error in the curves is very small. However, during the specimen’s failure stage, the model predicts a slightly higher bearing capacity compared to the actual test value. This is caused by defects in the welding of steel plates and concrete placement during the production of samples.

(a)Test destructive mode

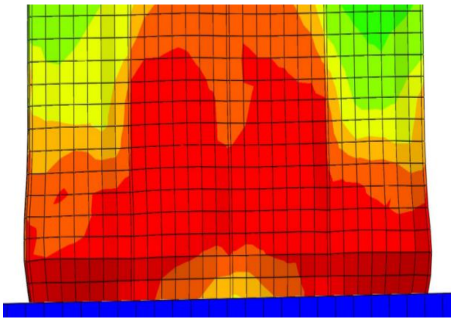

(b) Finite element destruction model

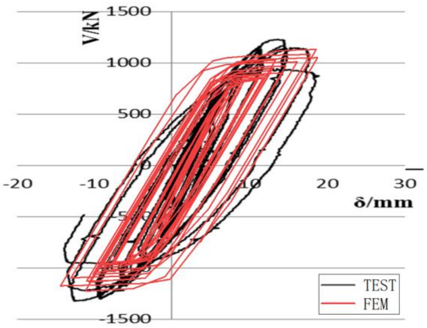

(c) Comparison of experimental and FE model hysteresis curves

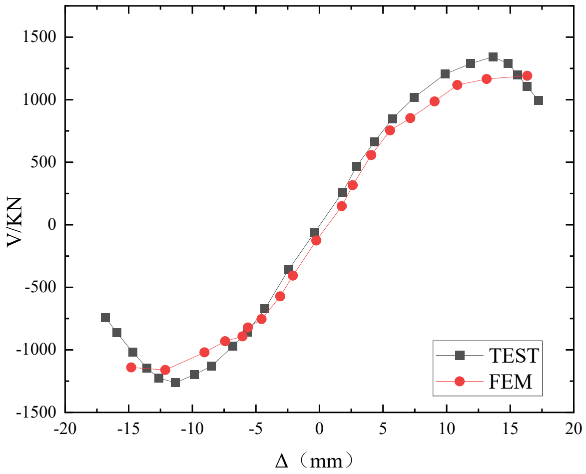

(d) Comparison of experimental and FE model skeleton curves

Fig. 5 Model validation

3. Parametric study

After verifying the test results using ABAQUS software, the study proceeded to investigate the seismic performance of DSCW with varying parameters. he effects of different parameters such as corrosion rate, plate thickness, concrete strength grade, and axial compression ratio, is examined in the parametric study. These variables significantly influence the mechanical properties of DSCW, highlighting the need to quantify their effects accurately. To realistically simulate the random corrosion scenarios encountered in practical engineering, corrosion models are generated using the random function in Python. These models simulate local corrosion rates on steel plates, ranging from 0% to 25%. This approach allows for a comprehensive evaluation of how varying corrosion levels affect the structural integrity and seismic behavior of DSCW.

3.1. Influence of the steel plate thickness

In this section, the influence of steel plate thickness on corroded DSCW bearing capacity is discussed (Table 1). DSCW specimens with steel plate thicknesses of 5 mm to 9 mm, and corrosion rates of 0% to 25%, are designed. The shear walls have a height-to-width ratio of 1.0, a concrete strength grade of C30, restraining tie bars with diameters of 10 mm, and steel plates made of Q235 material. FE-C1 to FE-C3 represent specimens with varying steel plate thicknesses, while FE-C1-0 to FE-C1-2-25 represent specimens with different corrosion rates.

Table 1
Design parameters of specimens

Test specimen	Steel plate thickness （mm）	Concrete strength grade	Axial compression ratio	Corrosion rates （%）
FE-C1-0	5	C30	0.2	0
FE-C1-10	5	C30	0.2	10
FE-C1-15	5	C30	0.2	15
FE-C1-25	5	C30	0.2	25
FE-C2-0	7	C30	0.2	0
FE-C2-10	7	C30	0.2	10
FE-C2-15	7	C30	0.2	15
FE-C2-25	7	C30	0.2	25
FE-C3-0	9	C30	0.2	0
FE-C3-10	9	C30	0.2	10
FE-C3-15	9	C30	0.2	15
FE-C3-25	9	C30	0.2	25

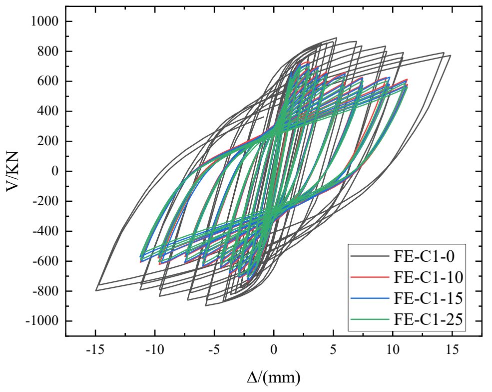

(a)FE-C1

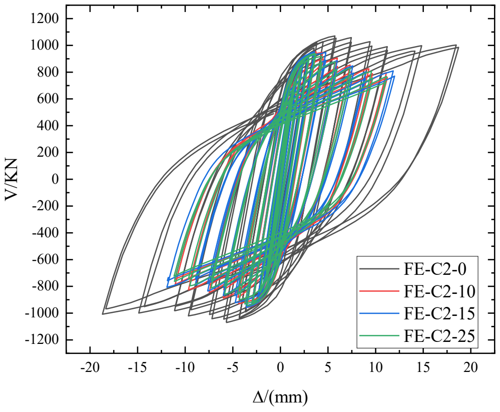

(b)FE-C2

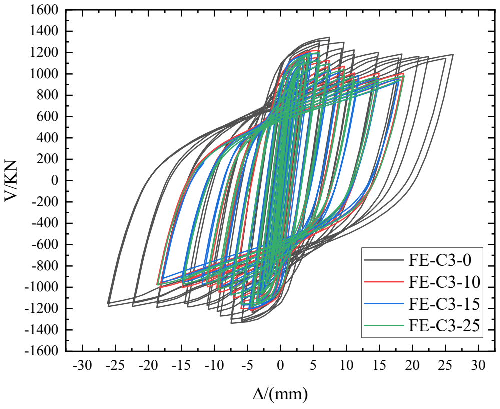

(c)FE-C3

Fig. 6 The hysteresis curves of different thicknesses of steel plate

Table 2
Peak load

Specimen number	Peak load
FE-C1-0	890.80
FE-C1-10	733.45
FE-C1-15	722.42
FE-C1-25	703.17
FE-C2-0	1177.03
FE-C2-10	1050.43
FE-C2-15	1046.11
FE-C2-25	1036.97
FE-C3-0	1343.01
FE-C3-10	1218.33
FE-C3-15	1200.75
FE-C3-25	1189.10

3.1.1. Hysteresis curve analysis

The hysteresis curve of FE-C3 is fuller than that of FE-C2 (Fig. 6), it shows that an increase in steel plate thickness may provide greater confinement to the concrete, thereby reducing concrete cracking. However, the hysteresis curves of specimens FE-C3-10, FE-C3-15, and FE-C3-25 gradually exhibit reduced fullness, indicating a weakening of energy dissipation capacity in corroded specimens. This trend highlights the significant detrimental effect of local corrosion on DSCW.

Among the specimens listed in Table 2, FE-C3-0 exhibits the highest peak load of 1343.01 kN. This value is 14.1% higher than that of FE-C2-0. With a constant corrosion rate, the peak load increases gradually with increasing steel plate thickness, indicating that a thicker steel plate enhances the shear wall's bearing capacity. Specifically, the peak load of FE-C3-0 is 10.2% higher than that of FE-C3-10. Conversely, with a constant steel plate thickness, the peak load decreases as the corrosion rate increases, show a reduced bearing capacity due to increased corrosion. Furthermore, the increase in peak load is more pronounced for specimens with 9 mm steel plate thickness compared to those with 7 mm at the same local corrosion rates. This observation underscores that thicker steel plates contribute to improved seismic performance and energy dissipation capacity, making them more resilient to corrosion.

3.1.2. Skeleton curve analysis

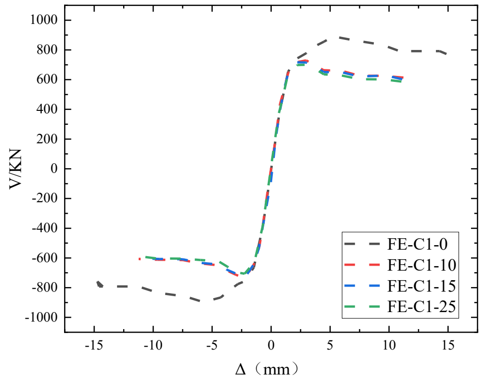

(a)FE-C1

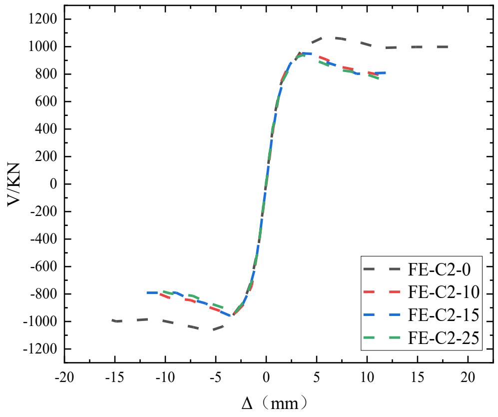

(b)FE-C2

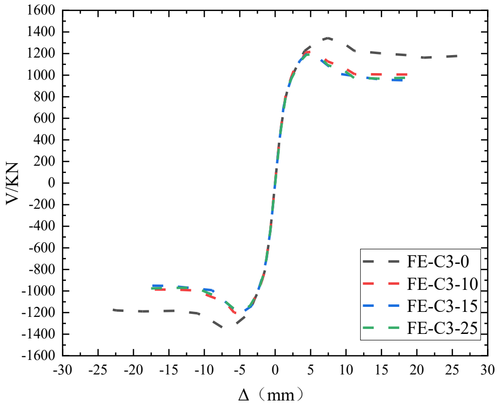

(c)FE-C3

Fig. 7 The skeleton curve of different thicknesses of steel plate

By processing the hysteresis curves, the skeleton curves are derived and shown in Fig. 7. Each specimen's skeleton curve exhibits three distinct stages. The following observations can be made from Fig. 7 (a-c): In the elastic stage, the curvature remains consistent, suggesting that corrosion has minimal effect on the initial stiffness of the DSCW. In the plastic stage, the curvature the curve diminishes significantly, and all specimens exhibited inflection points. The inflection points of specimens with corrosion rates of 10%–25% occurred significantly earlier than those of the uncorroded specimens. This is due to corrosion reducing the stiffness of the steel plate, causing it to yield prematurely. The inflection points of the FE-C3 series specimens occurred later than that of the FE-C2 and FE-C1 series specimens. This is primarily due to the increased thickness of the steel plate, which significantly enhances the lateral stiffness of the DSCW. During the failure stage, the curve shows a progressively steeper decline with increasing corrosion rates. The strength of the FE-C1-25 specimens decreased significantly, while the FE-C3-0 and FE-C2-0 specimens performed the best throughout the failure stage. The results show that increased steel plate corrosion diminishes the DSCW 's peak load, ductility, and deformation capacity. Increasing the thickness of steel plate can significantly improves the seismic performance of corroded DSCWs, but it reduces ductility. In practice, the thickness of steel plate can be appropriately increased to mitigate the negative impact of corrosion and enhance seismic performance of DSCW.

3.2. Influence of the concrete strength grade

In this section, the influence of concrete strength on corroded DSCW bearing capacity is discussed. DSCW specimens are designed using FE-C1 as the base model, with local corrosion rates of 0%, 10%, 15%, and 25%, and concrete strength grades of C30 to C50. The parameters for each model are shown in Table 3.

Table 3
Design parameters of specimens

Test specimen	Steel plate thickness （mm）	Concrete strength grade	Axial compression ratio	Corrosion rates （%）
FE-C1-0	5	C30	0.2	0
FE-C1-10	5	C30	0.2	10
FE-C1-15	5	C30	0.2	15
FE-C1-25	5	C30	0.2	25
FE-E1-0	5	C40	0.4	0
FE-E1-10	5	C40	0.4	10
FE-E1-15	5	C40	0.4	15
FE-E1-25	5	C40	0.4	25
FE-E2-0	5	C50	0.2	0
FE-C3-10	9	C30	0.2	10
FE-C3-15	9	C30	0.2	15
FE-C3-25	9	C30	0.2	25

Table 4
Peak load

Specimen number	Peak load
FE-C1-0	890.80
FE-C1-10	733.45
FE-C1-15	722.42
FE-C1-25	703.17
FE-E1-0	990.38
FE-E1-10	817.73
FE-E1-15	827.90
FE-E1-25	824.51
FE-E2-0	1005.5
FE-E2-10	880.37
FE-E2-15	871.23
FE-E2-25	858.40

3.2.1. Hysteresis curve analysis

An increase in the concrete strength grade from C30 (FE-C1-0) to C40 (FE-E1-0) resulted in a rise in the overall stiffness of the specimens, as well as a significant increase in the peak load, which increased by 11.18% (Fig. 8, Table 4). However, when the concrete strength was further elevated from C40 (FE-E1-0) to C50 (FE-E2-0), the peak load showed only a modest increase of 1.53%. With the increase of concrete strength, the effect on the peak load of DSCW decreases gradually. In the case of corroded DSCWs, when the corrosion rate increased from 0% to 10%, the peak horizontal bearing capacity of specimens with concrete strengths ranging from C30 to C50 decreased by 17.66%, 17.43%, and 12.44%, respectively. The reduction in peak load of corroded DSCW was effectively mitigated with the concrete strength grade added.

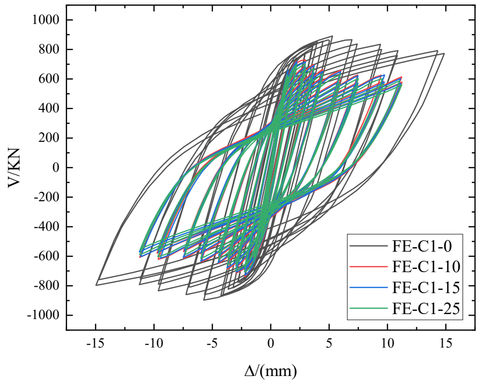

(a)FE-C1

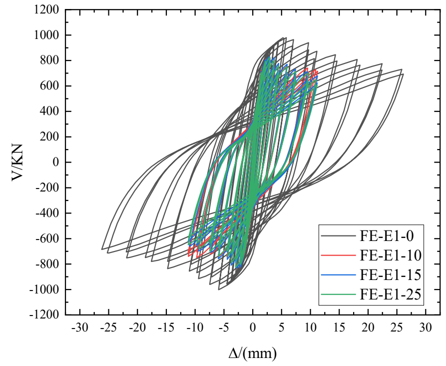

(b)FE-E1

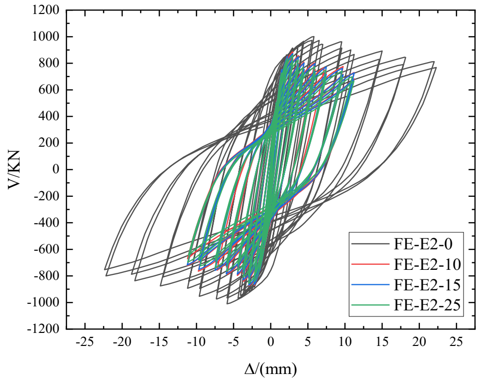

(c)FE-E2

Fig. 8 The hysteresis curves of different concrete strength grades

3.2.2. Skeleton curve analysis

The elastic and plastic stages of the skeleton curve are similar (Fig. 9). The peak load of the FE-E1 series specimens exceeds that of the FE-C1 series, but is lower than that of the FE-E2 series specimens. This suggests that, for the same corrosion rates, an increase in concrete strength grade gradually improves the peak load of the DSCW. Under non-corrosive conditions, the elastic and plastic stages of the skeleton curve exhibit similar characteristics, with a gradual decline observed in the failure stage. However, at corrosion rates of 10%, 15%, and 25%, the disparity in the skeleton curves increases as the concrete strength grade increases. This indicates that higher concrete strength, combined with increased corrosion rates, leads to greater variations in the shear wall's bearing capacity.

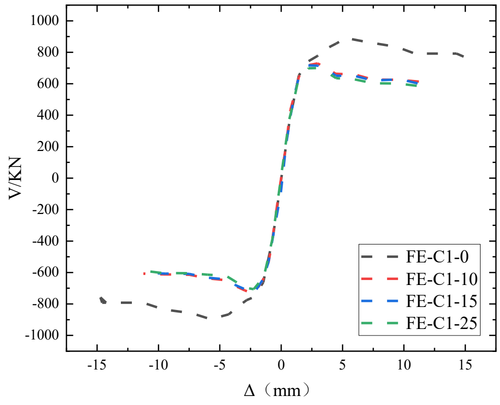

(a)FE-C1

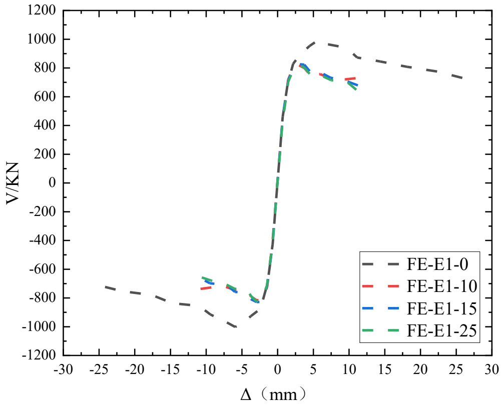

(b)FE-E1

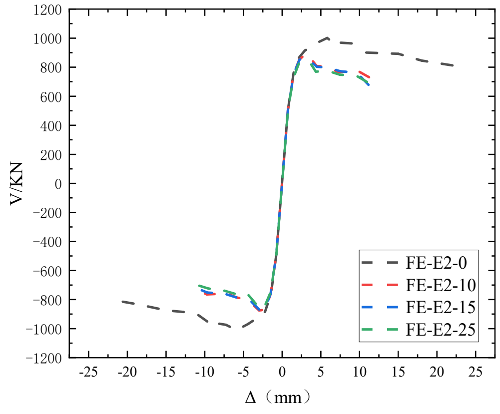

(c)FE-E2

Fig. 9 The skeleton curve of different concrete strength grades

3.3. *Influence of the axial compression ratio*

In this section, the axial compression ratio is the primary research parameter, while other parameters remain constant. DSCW specimens are designed with local corrosion rates of 0%, 10%, 15%, and 25%, and axial compression ratios from 0.2 to 0.6. The parameters for each model are provided in Table 5.

3.3.1. *Hysteresis curve analysis*

As shown in Fig. 10, In the case of no corrosion, the hysteresis loop pinching phenomenon more serious with the increase of axial compression ratio. This suggests that the energy dissipation capacity of DSCW decreases with the increase of axial compression ratio. Upon examining the hysteresis curve of FE-F1-0, an upward phase is observed after the initial decline. This phenomenon is caused by the buckling of the steel plate and the crushing of concrete in the DSCW. However, the binding bars continue to restrain the steel plate after buckling, preventing excessive deformation and extensive concrete crushing. Therefore, the bearing capacity has an upward trend when the shear wall continues to load.

Table 5
Design parameters of specimens

Test specimen	Steel plate thickness （mm）	Concrete strength grade	Axial compres-sion ratio	Corrosion rates （%）
FE-C1-0	5	C30	0.2	0
FE-C1-10	5	C30	0.2	10
FE-C1-15	5	C30	0.2	15
FE-C1-25	5	C30	0.2	25
FE-F1-0	5	C30	0.4	0
FE-F1-10	5	C30	0.4	10
FE-F1-15	5	C30	0.4	15
FE-F1-25	5	C30	0.4	25
FE-F2-0	5	C30	0.6	0
FE-F2-10	5	C30	0.6	15
FE-F2-15	5	C30	0.6	15
FE-F2-25	5	C30	0.6	25

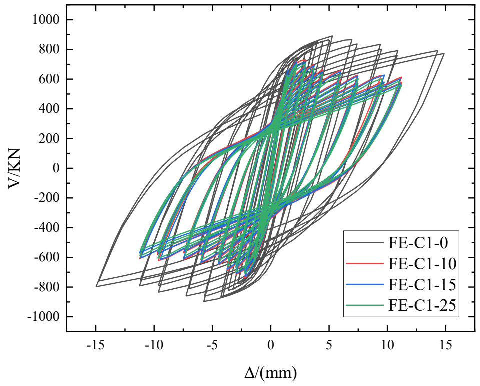

(a)FE-C1

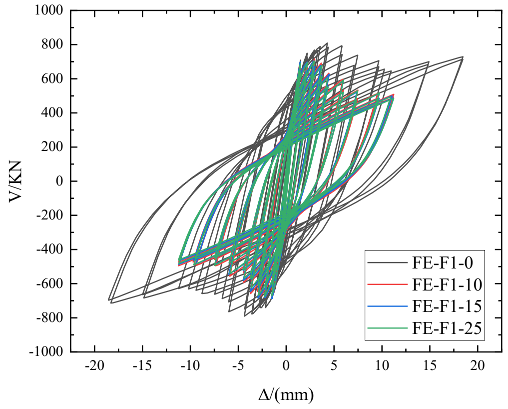

(b)FE-F1

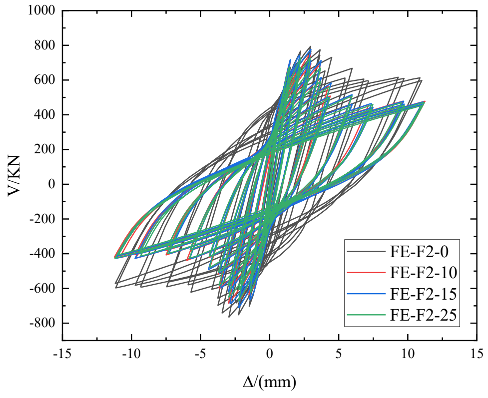

(c)FE-F2

Fig. 10 The hysteresis curves of different axial compression ratios

Table 6
Peak load

Specimen number	Peak load
FE-C1-0	890.80
FE-C1-10	733.45
FE-C1-15	722.42
FE-C1-25	703.17
FE-F1-0	799.91
FE-F1-10	698.94
FE-F1-15	693.97
FE-F1-25	689.18
FE-F2-0	779.59
FE-F2-10	719.64
FE-F2-15	743.38
FE-F2-25	700.07

At an axial compression ratio of 0.6, an increase in corrosion rates result in a marked reduction in the specimen's peak load, as indicated by the steeper descending section of the hysteresis curve. This trend indicates that higher axial compression ratios accelerate the decline in bearing capacity under seismic loading, potentially resulting in brittle failure. Consequently, in the practical engineering design of shear walls, it is advisable to regulate the axial compression ratio to mitigate substantial reductions in both bearing capacity and energy dissipation.

3.3.2. Skeleton curve analysis

The effect of the axial compression ratio on the seismic performance of the specimen is evident from the skeleton curve (Fig. 11). During cyclic loading, failure occurs in the corroded sections of the steel plate, resulting in buckling and reduced ductility of the DSCW. Comparing skeleton curves at different corrosion rates shows that corrosion significantly impacts the plastic phase. However, the trend in the failure phase shows minimal variation with increasing corrosion rates.

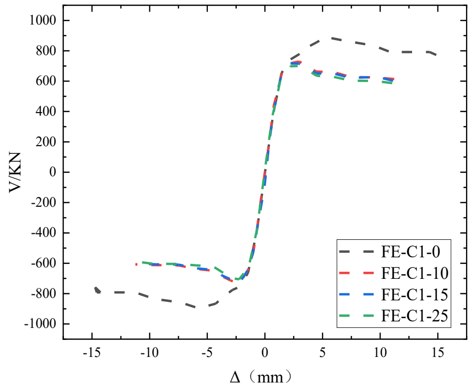

(a)FE-C1

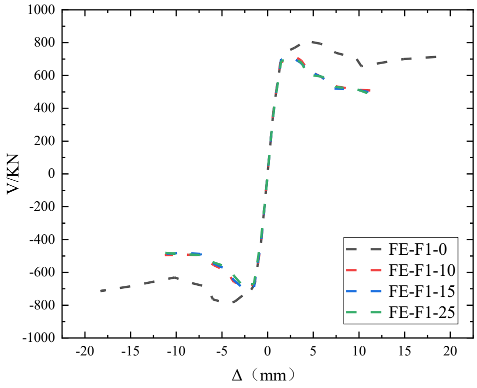

(b)FE-F1

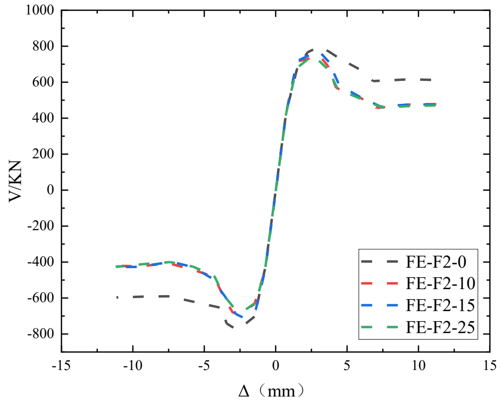

(c)FE-F2

Fig. 11 The skeleton curves different axial pressure ratios

4. Calculation of shear capacity of DSCW

Currently, the research on the shear capacity of DSCW has received widespread attention in both domestic and international academic circles. However, no existing specification specifically addresses the horizontal bearing capacity of corroded DSCW with binding bars. Therefore, a shear capacity formula specifically for DSCW with binding bars was proposed and assesses its effectiveness in predicting their shear capacity.

4.1. Calculation of shear capacity formula for DSCW

This paper studied the mechanical properties of DSCWs consisting of steel plates, concrete, and binding bars. These components work together to enhance the shear bearing capacity of the DSCW. While steel plates and concrete directly offer to the shear capacity, the binding bars provide indirect protection to the concrete by restricting steel plate buckling, a factor critical to maintaining shear capacity.

Finite element analysis shows that parameters significantly influence the seismic performance of these shear walls. To accurately quantify the shear bearing capacity, the formula from the specification [37] is modified to include the contribution of binding bars. This modification is based on least squares fitting of finite element simulation data using SPSS software, as detailed in Eq. (2) of this paper.

$$V \le \frac{1}{\gamma_{RE}}\left[\frac{0.12 f_t b_w h_w}{(\lambda-0.5)}+\frac{0.036 f_c b_w h_w}{(\lambda-0.5)}+\frac{0.2 f_y A_s h_w}{H}+0.16 f_{ys} A_{st}\right] R^2=0.95 \quad (2)$$

Where γ_{RE} is seismic adjustment factor for load capacity, f_t is design value of axial tensile strength of concrete, b_w is thickness of DSCW, h_w width of DSCW, λ is shear span ratio, f_c is design value of axial compressive strength of concrete, A_s is full cross-sectional area of steel plate in section, H is height of DSCW, f_{ys} is design value of tensile strength of binding bars, A_{st} is cross sectional area of binding bars.

The calculation of the above specimens was performed using Eq. (1), and the calculating results were compared with the FE values (Table 7).

The comparison reveals that the average ratio between finite element calculated values and the theoretical formula results is 0.930. The calculated value from the finite element method good agreement with the value obtained from the formula. Therefore, Eq. (2) for shear capacity is highly applicable, accurately estimating the shear capacity of the DSCW.

Table 7
Comparison of the finite element calculated values and calculated values of the formula

Specimen number	Finite element calculated value V_t/(kN)	Formula value V_c/(kN)	V_t/V_c
FE-C1-0	812.37	890.80	0.91
FE-F1-0	812.37	799.91	1.02
FE-C2-0	1021.35	1170.03	0.88
FE-E1-0	899.46	990.38	0.91

4.2. Calculation of shear capacity formula of DSCW after partial corrosion

An extension of Eq. (2) for the shear capacity of DSCW has been developed to account for corrosion. This extension involves fitting a formula to express the horizontal bearing capacity of corroded DSCW. To quantify the influence of corrosion on shear capacity, the average ratio of the shear capacity of each corroded model relative to the uncorroded model has been determined. Subsequently, an equation has been derived to describe how this average ratio varies with the corrosion rate (Eq. (3)).

$$\frac{N'}{N}=1-2.02x^2+1.521x-0.899\sqrt{x} \qquad R^2=0.92 \tag{3}$$

Where N' is the corrosion of the DSCW combination of shear capacity, N is the shear capacity of the uncorroded DSCW combination. x is the corrosion rate.

Eq. (2) and (3) have been combined to derive Eq. (4), which describes shear capacity of the corroded DSCW. The specific parameters of 16 specimens were substituted into Eq. (4) to calculate the horizontal bearing capacity of the DSCW, shown in Table 8.

$$\begin{aligned} N' \le & \left(1-2.02x^2+1.521x-0.899\sqrt{x}\right) \\ & \times \frac{1}{\gamma_{RE}}\left[\frac{0.12 f_t b_w h_w}{(\lambda-0.5)}+\frac{0.036 f_c b_w h_w}{(\lambda-0.5)}+\frac{0.2 f_y A_s h_w}{H}+0.16 f_{ys} A_{st}\right] \end{aligned} \tag{4}$$

Table 8

Comparison the finite element calculated values and theoretical formula results

Specimen number	Finite element calculated value V_t/(kN)	Formula value V_c/(kN)	V_t/V_c
FE-C1-0	812.37	890.8	0.91
FE-C1-10	688.58	733.45	0.94
FE-C1-15	677.94	722.42	0.94
FE-C1-25	653.55	703.17	0.93
FE-C2-0	1021.35	1063.66	0.96
FE-C2-10	865.71	954.94	0.91
FE-C2-15	852.34	951.01	0.90
FE-C2-25	821.68	942.70	0.87
FE-E1-0	899.46	990.38	0.91
FE-E1-10	762.39	817.73	0.93
FE-E1-15	750.61	827.9	0.91
FE-E1-25	723.61	824.51	0.88
FE-F1-0	812.37	799.91	1.02
FE-F1-10	688.58	698.94	0.99
FE-F1-15	677.94	693.97	0.98
FE-F1-25	653.55	689.18	0.95

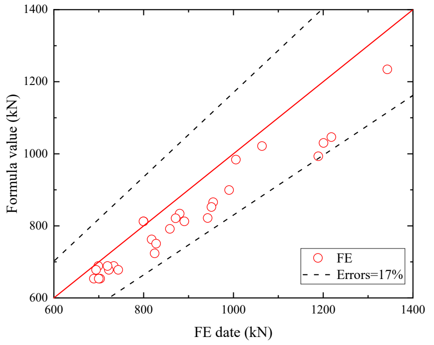

Fig. 12 Verification of calculation model

Table 8 compares the calculated values from the formula with those obtained through finite element analysis. The average ratio of the finite element calculation values to the theoretical formula results is 0.93. The finite element analysis data and formula calculation data are utilized to assess the accuracy of Eq. (4). The proposed formula clearly and accurately calculates the shear capacity of corroded DSCW, with a deviation of less than 17% (Fig. 12). In general, the theoretical formula can effectively calculate the shear capacity of DSCW. This formula provides a reliable basis for future engineering applications. It should be noted that the shear capacity formula for corroded DSCW proposed in this paper is specifically applicable to DSCW with local corrosion.

5. Residual seismic capacity

The seismic performance of buildings is reduced due to earthquakes, initial defects, and durability concerns. Assessing the residual seismic capacity of damaged structures is essential for preparing them for future earthquakes. Currently, the assessment of residual seismic capacity mainly involves assessing cracks and the post-earthquake behavior of structural components. This approach is subjective and requires extensive field investigations. Therefore, this study based on the energy dissipation capacity of DSCW to analyze their residual seismic capacity at each loading stage. The aim is to develop a seismic performance evaluation method for earthquake-damaged shear walls, using residual drift as the primary evaluation criterion.

5.1. Relative residual side shift and relative side shift correspondence

In the investigation of the seismic capacity of DSCW, residual drift is a crucial indicator for evaluating their resilience. A normalization approach is employed to conduct a quantitative analysis of residual drift. This involves dividing the drift (δ_{dr}) and residual drift (δ_{re}) at each loading stage by their respective values at the failure state. This normalization results in the relative drift ($\delta_{dr}/\delta_{dr,failure}$) and relative residual drift ($\delta_{re}/\delta_{re,failure}$). A model (Eq. 5) was developed to assess the characteristics of residual drift in shear wall specimens subjected to cyclic loading, as shown in Fig. 13(a).

$$\frac{\delta_{re}}{\delta_{re,failure}}=0.84\left(\frac{\delta_{dr}}{\delta_{dr,failure}}\right)^2+0.16\frac{\delta_{dr}}{\delta_{dr,failure}} \tag{5}$$

The formula's coefficient of determination R^2 is 0.94, confirming the accuracy and applicability of predicting the residual drift of specimens at different drift states. To further validate the formula's applicability in predicting the relationship between relative residual drift and drift in DSCWs, test results from three specimens subjected to low cyclic loading, as reported in the literature [34], were selected for model validation (Fig. 13(b)). The computational analysis model shows a relatively small difference when compared to the relationship between relative residual drift and relative drift proposed in this paper, demonstrating that the model can be broadly applied to predict residual drift in various types of DSCW with ductile failure.

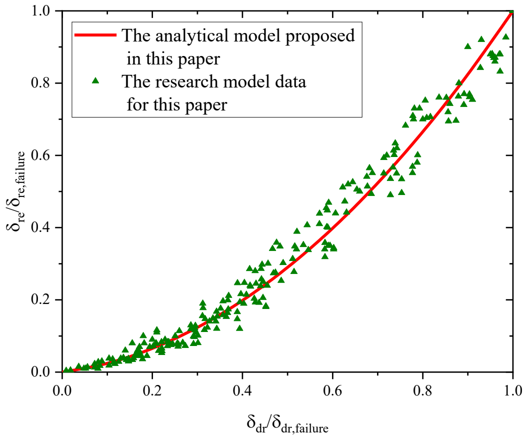

(a) Proposal of calculation model

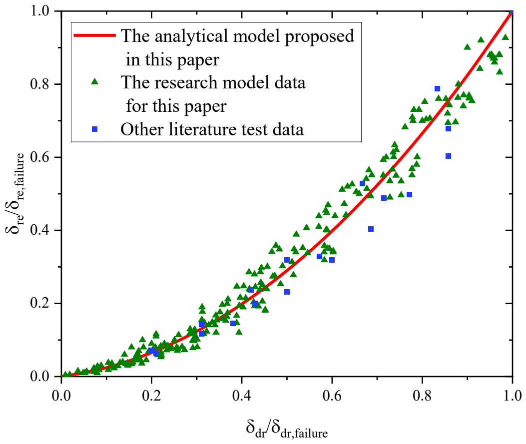

(b) Verification of calculation model

Fig. 13 The relationship of relative residual drift and relative drift for DSCW

5.2. Residual seismic capacity and reinforcement analysis

For assessment of the residual seismic capability of DSCW after earthquake damage, the residual seismic capacity discount factor R, put forward by JBDPA and Geng [38,39], is calculated based on Fig. 14, as shown in Eq. (6). The area under the skeleton curve from initial loading to the damaged state represents the total energy E_d. At any loading level, the area enclosed by the drift and residual drift on the skeleton curve represents the absorbed energy E_d. The residual absorbed energy E_r is then determined by subtracting the absorbed energy from the total energy.

$$R = \frac{E_r}{E_d + E_r} \tag{6}$$

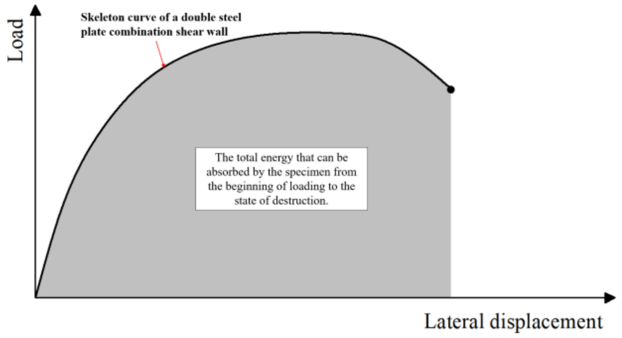

(a) Total absorbable energy

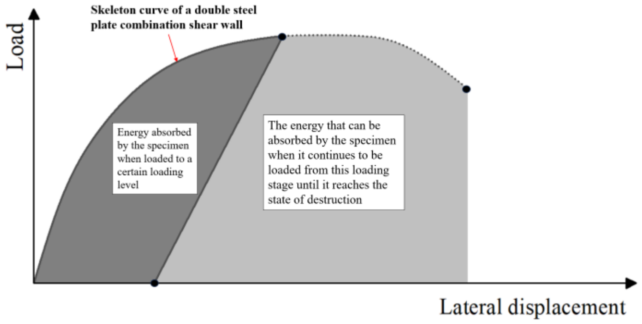

(b) Already absorbed energy

Fig. 14 Seismic capacity reduction factor for damaged DSCW

The residual seismic capacities of all shear wall specimens at different loading levels are combined (Fig. 15(a)). A fitting formula for the relative value of residual drift and residual seismic capacity is proposed, on the basis of the data degradation analysis method, as shown in Eq. (7). The coefficient of determination R^2 for this formula is 0.95, indicating that the results of DSCW calculated by this method's error is small.

To evaluate the accuracy and applicability of Eq. (7) in predicting the residual seismic capacity of earthquake-damaged shear walls using relative values of residual drift, shear wall specimens from the literature [37] are selected to validate the calculation model. The data points, shown in Fig. 15(b), are compared with the analytical model proposed in Eq. (7). This establishes the corresponding relationship between residual drift and residual seismic capacity in earthquake-damaged shear walls. Although the calculation model may slightly underestimate the average residual seismic capacity of earthquake-damaged shear walls approaching failure, it provides a more conservative and secure conclusion when assessing the safety of these shear walls.

$$R = 1 - 0.86\frac{\delta_{re}}{\delta_{re,failure}} \quad 0 \le \delta_{re}/\delta_{re,failure} \le 1 \tag{7}$$

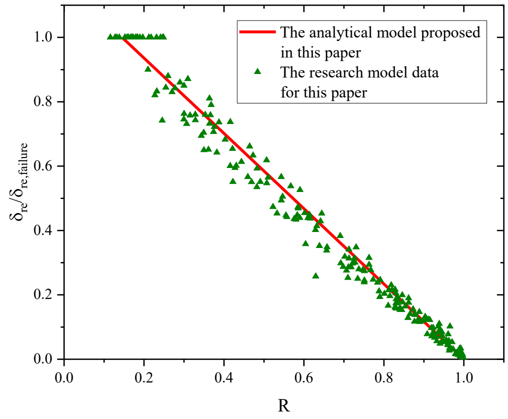

(a) Proposal of calculation model

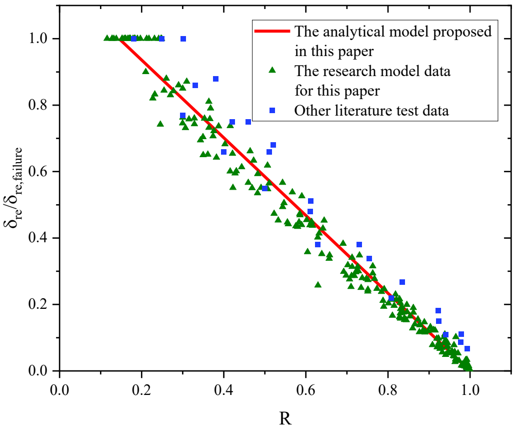

(b) Verification of calculation model

Fig. 15 Calculation model for the relationship of residual seismic capacity with relative residual drift for DSCW

Table 9
Evaluation index of damage evaluation for DSCW

Damage level	Residual seismic capacity	Relative Residual Side Shift
minimal	$R \geq 0.95$	$\delta_{re}/\delta_{re,failure} \leq 0.06$
general	$0.75 \leq R < 0.95$	$0.06 < \delta_{re}/\delta_{re,failure} \leq 0.30$
medium	$0.50 \leq R < 0.75$	$0.30 < \delta_{re}/\delta_{re,failure} \leq 0.60$
severity	$R < 0.50$	$\delta_{re}/\delta_{re,failure} > 0.60$

To further investigate the post-earthquake reinforcement of earthquake-damaged DSCW, residual drift is used as the control criterion. A proposed relationship between shear wall failure grades and residual seismic capacity is presented in Table 9. The medium failure grade of the shear wall is designated as the benchmark for reinforcement assessment, with an average value of 0.45 being the recommended threshold for determining reinforcement needs. Therefore, when the relative value of residual drift exceeds 0.45, it indicates that the earthquake-damaged shear wall may no longer significantly benefit from continued reinforcement. Fig. 16 shows the residual drift of the shear wall at different corrosion rates in relation to the reinforcement limit based on residual drift.

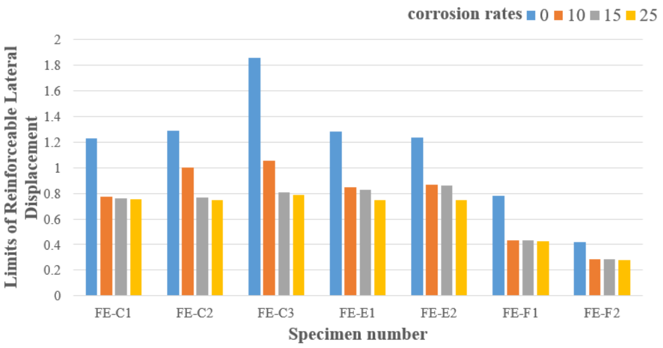

Fig. 16 The reinforcement limit based on residual drift

Compared to the uncorroded specimen, Corrosion of steel plate reduces its inhibition on internal concrete compared with non-corroded specimens. This results in less drift of the corroded specimen and less residual drift upon failure. The limit value of reinforced residual drift for the corroded specimen is also significantly reduced, with the reduction increasing as corrosion rates rise. At constant corrosion rates, both the thickness of the steel plate and the axial pressure ratio significantly affect the limit value of reinforced residual drift. Specifically, thicker steel plates gradually increase the limit value, although their impact diminishes as corrosion rates increase. Conversely, higher axial pressure ratios reduce the limit value. In practical applications, increasing the thickness of exterior steel plates in DSCW can enhance the limit value of reinforced drift. It is recommended to avoid components with high axial pressure ratios and to promptly assess reinforcement needs for corroded DSCWs in actual projects.

6. Conclusion

A detailed FE model of the corroded DSCW is developed in this paper. The model was validated through previous cyclic tests. On the basis of validation, different parameters were investigated. Based on the theoretical analysis, a formula for calculating corroded DSCW bearing capacity is proposed. The residual seismic capacity of the corroded DSCW is evaluated based on the energy dissipation, and the reinforced residual drift limit of the corroded DSCW after an earthquake is proposed. The main conclusions are drawn:

(1) The finite element analysis results demonstrate that corrosion significantly impacts the seismic performance of DSCW specimens, leading to consistent degradation in their bearing capacity. Corrosion diminishes energy dissipation, shear capacity, and ductility.

(2) The seismic performance of DSCW is primarily depends on variations in the constraint strength between the steel plate and concrete. The thickness of the steel plate is a crucial factor in determining the bearing capacity. As the thickness increases from 5 mm to 9 mm, shear capacity increases by 32.1% and 50.8%, respectively. Furthermore, the shear capacity of DSCW decreases linearly with increasing corrosion rates, regardless of other parameters.

(3) As corrosion levels rise, the bearing capacity of shear wall specimens decreases significantly, with a more pronounced reduction in displacement ductility compared to bearing capacity. Furthermore, increasing the axial compression ratio in corroded specimens leads to reductions in both bearing capacity and ductility. For DSCW subjected to significant corrosion, it is recommended that the axial pressure be controlled below 0.6 at the time of design.

(4) Considering both the effects of corrosion and the binging bars to bearing capacity, a shear capacity formula for DSCW incorporating both factors is proposed. Numerical simulation results validate the accuracy and applicability of this formula, with the maximum deviation remaining below 17%. Thus, the theoretical formulas can reliably predict the shear bearing capacity of DSCW.

(5) The residual seismic capacity at each loading stage for 28 specimens is evaluated using a modeling method based on the energy dissipation capacity of shear walls. The effectiveness of the proposed method is evaluated by calculating the relevant experiments. Additionally, a lateral displacement limit for DSCW after an earthquake is proposed, which can aid in the design of reinforcements for these structures.

References

[1] C.B. Wen, Y.L. Guo, H.J. Sun, et al. Experimental and numerical study on seismic performance of concrete-infilled double steel corrugated-plate walls[J]. Journal of Building Engineering, 2023, 68: 106171.
[2] Z.Q. Jiang, A.L. Zhang, L. Su, et al. Experimental study of axial compressive load capacity of internally stiffened double steel plate shear wall[J]. Journal of Constructional Steel Research, 2024, 216: 108566.
[3] Q. Luo, S. Zhao, W. Wang, et al. Research on interaction relationship and seismic performance efficiency of corrugated steel-plate composite shear wall[J]. Soil Dynamics and Earthquake Engineering, 2023, 172: 108046.
[4] Y. Qin, G.P. Shu, G.G. Zhou, et al. Compressive behavior of double skin composite wall with different plate thicknesses[J]. Journal of Constructional Steel Research, 2019, 157(JUN.):297-313.
[5] J. Li, F. Li, C. Liu, et al. Numerical and theoretical analysis of seismic behaviour of CFDSP composite shear walls. Journal of Building Engineering, 2020, 31: 101359.
[6] G.B. Lu, X.H. Zhou, Y.H. Wang, et al. Numerical investigation on circular concrete-filled double skin steel tube columns under torsion[C]. Structures. Elsevier, 2022, 37: 17-31.
[7] J.B. Yan, Z.X. Li, T. Wang. Seismic behaviour of double skin composite shear walls with overlapped headed studs[J]. Construction and Building Materials, 2018, 191: 590-607.
[8] L. Chen, S. Wang, Y. Lou, et al. Seismic behavior of double-skin composite wall with L-shaped and C-shaped connectors[J]. Journal of Constructional Steel Research, 2019, 160: 255-270.
[9] L. Chen, Q. Jin, J. Shi, et al. Seismic behavior of low shear-span ratio double-skin composite wall with L-shaped connectors[J]. Journal of Constructional Steel Research, 2022, 198: 107541.
[10] L. Zhu, D. Zhou, M. He, Experimental research on seismic behavior of composite concrete and steel plate shear walls with binding bars, [J]. Build. Struct. 2013, 6:93.
[11] W. Zhang, K. Wang, Y. Chen, et al. Experimental study on the seismic behaviour of composite shear walls with stiffened steel plates and infilled concrete[J]. Thin-Walled Structures, 2019, 144: 106279.
[12] L. Chen, C. Yin, C. Wang, et al. Experimental study on seismic behavior of double-skin composite wall with L-shaped connectors[J]. Journal of Constructional Steel Research,2020, 174:106312.
[13] S. Imperatore, Z. Rinaldi, C. Drago. Degradation relationships for the mechanical properties of corroded steel rebars[J]. Construction and Building Materials, 2017, 148: 219-230.
[14] X. Sun, H. Kong, H. Wang, et al. Evaluation of corrosion characteristics and corrosion effects on the mechanical properties of reinforcing steel bars based on three-dimensional scanning[J]. Corrosion Science, 2018, 142: 284-294.
[15] G. Qin, S. Xu, D. Yao, et al. Study on the degradation of mechanical properties of corroded steel plates based on surface topography[J]. Journal of Constructional Steel Research, 2016, 125: 205-217.
[16] L. Jin, X. Zhang, X. Liang, et al. Mechanical properties of corroded carbon steel based on random pit corrosion in marine environment[J]. Ocean Engineering, 2022, 260: 111759.
[17] R. Songbo, G. Song, K. Chao, et al. Fractal characteristic of corroded steel surface and application to the fracture analyses[J]. Construction and Building Materials, 2022, 340: 127759.
[18] Q. Yang, B. Zhao, B. Liu, et al. Influence of corrosion on loading capacity of circular concrete-filled steel tubular column[J]. Journal of Constructional Steel Research,2024,215108564-.
[19] Z. Zhao, T. Gao, X. Jian, et al. Eccentric compression capacity of circular CFST columns under random pitting corrosion[J]. Ocean Engineering, 2023, 288: 115975.
[20] S.S. Song, X. Liu, J. Chen, et al. Compressive behaviour of corroded thin-walled circular section steel stub columns[J]. Thin-Walled Structures, 2022, 180: 109794.
[21] Y. Wei, Z. Wu, X. Wang, et al. Mechanical behavior of locally corroded circular steel tube under compression[C]. Structures. Elsevier, 2021, 33: 776-791.
[22] F. Yuan, M. Chen, H. Huang, et al. Circular concrete filled steel tubular (CFST) columns under cyclic load and acid rain attack: Test simulation[J]. Thin-Walled Structures, 2018, 122: 90-101.
[23] S. Luo, M. Chen, H. Huang, et al. Eccentric compression test and ultimate load strength analysis of circular CFST long column with local corrosion[C]. Structures. Elsevier, 2023, 56: 104937.
[24] H. Huang, L. Guo, B. Qu, et al. Tests of circular concrete-filled steel tubular stub columns with artificial notches representing local corrosions[J]. Engineering Structures, 2021, 242: 112598.
[25] L. Zhong, L. Guo, C. Jia. Axial compression behavior of stub square concrete-filled steel tubes with regional defect[J]. Engineering Structures, 2023, 278: 115510.
[26] W. Xue, J. Chen, F. Xie, et al. Behavior of Corroded Thin-Walled Concrete-Filled Steel Tubular Stub Columns[J]. Buildings, 2022, 12(4): 481.
[27] F. Zhang, J. Xia, G. Li, et al. Degradation of axial ultimate load-bearing capacity of circular thin-walled concrete-filled steel tubular stub columns after corrosion[J]. Materials, 2020, 13(3): 795.
[28] C.L. Wang, Study on the monotonic and hysteretic constitutive relation of steel corrosion in general atmospheric environment, Xi'an University of Architecture and Technology, 2016.
[29] R. Wang, R. A. Shenoi. Experimental and numerical study on ultimate strength of steel tubular members with pitting corrosion damage[J]. Marine Structures, 2019, 64: 124-137.
[30] Y. Wang, X. Zhou, Z. Kong, et al. Effects of corrosion pits on the combined hardening behavior of low-carbon steel[J]. Construction and Building Materials, 2024, 447: 138058.
[31] S.T. Zhong, Concrete Filled Steel Tubular Structures, Tsinghua University Press, 2003.
[32] J. Lubliner, J. Oliver, S. Oller, et al. A plastic-damage model for concrete[J]. International Journal of solids and structures, 1989, 25(3): 299-326.
[33] J. Lee, G.L. Fenves. Plastic-damage model for cyclic loading of concrete structures[J]. Journal of engineering mechanics, 1998, 124(8): 892-900.
[34] A. Hillerborg, M. Modéer, P.E. Petersson. Analysis of crack formation and crack growth in concrete by means of fracture mechanics and finite elements[J]. Cement and concrete research, 1976, 6(6): 773-781.
[35] L.H. Han, G.H. Yao, Z. Tao. Performance of concrete-filled thin-walled steel tubes under pure torsion[J]. Thin-walled structures, 2007, 45(1): 24-36.
[36] Y.F. Luo, J. Li, X.N. Guo. Numerical analysis of hysteretic performance of double-steel-layer-concrete composite shear wall[J]. Journal of Hunan University, 2014, 41(6): 57-62.
[37] Harbin Institute of Technology. Steel Plate Shear Wall Technical Specification JGJ/T 380-2015[M]. China Architecture & Building Press,2016
[38] Guidelines for post-earthquake damage evaluation and rehabilitation[S]. Tokyo: Japan Building Disaster Prevention Association (JBDPA), 2001. (in Japanese)
[39] X.R. Geng. Evaluation procedures on post-earthquake residual drift and seismic capacity for RC columns. Harbin Institute of Technology, 2019

Advanced Steel Construction – Vol. 21 No. 3 (2025) 253–264
DOI:10.18057/IJASC.2025.21.3.7

STUDY ON FRACTURE BEHAVIOR OF CHS-X JOINTS WITH WELD DEFECTS

Jia-Xing Wang [1], Xiao-Gui Shi [1], Zheng-Lei Liu [1], Ting Ding [1], Qiu-Zhan Xiang [2] and Zheng-Hua Huang [1, *]

[1] *School of Civil Engineering, Guizhou University, Guiyang550025, China*

[2] *Experimental Center of the School of Civil Engineering, Guizhou University*

** (Corresponding author: E-mail: zhhuang@gzu.edu.cn)*

ABSTRACT

To study the fracture behavior of circular hollow section (CHS) X-joints with weld defects, an axial tensile static load test was performed on one penetration welding specimen and two non-penetration welding specimens. The VUSDFLD subroutine in the ABAQUS software is utilized to perform finite element analysis (FEA) of CHS-X joints with weld defects. The simulation is based on micromechanical fracture models (VGM model and SWDM model). The results demonstrate that both VGM and SWDM models can precisely forecast the fracture of CHS-X joints, regardless of the presence or absence of weld defects. The accuracy of the simplified weld defects model using the equivalent width method and equivalent area approach is confirmed by comparing it with the test findings. In the comparison of fracture displacement and ultimate load error between FEA and testing, it was shown that the error of the VGM model is within 21%, and the error of the SWDM model is within 17%. The numerical simulation of the SWDM model is closer to the test results than that of the VGM model, which can be well applied to the fracture prediction and fracture path simulation of CHS-X joint defective weld. This paper provides a new method and perspective for analyzing and evaluating the weld fracture behavior of CHS-X joints with weld defects, serving as an important reference for predicting the bearing capacity of CHS-X joints with non-penetration welding in actual engineering applications.

ARTICLE HISTORY

Received:	12 November 2024
Revised:	3 January 2025
Accepted:	8 January 2025

KEYWORDS

CHS-X joints;
Defective weld;
Fracture behavior;
Micromechanical fracture models;
Ultimate bearing capacity

1. Introduction

The possible defects in the welding process of the CHS-X joints seriously affect the quality and performance of the joints. In engineering practice, welding is a common method of metal connection for joining two or more metal parts together. Research has demonstrated that the quality of welding has a direct impact on both the quality and lifespan of the workpiece [1–4]. The presence of welding defects in the CHS-X joints will have a detrimental impact on the strength and stability of the welded components, perhaps resulting in their failure. Thus, it is crucial to possess thorough comprehension and efficient measures to prevent these weld defects. Insufficient tool current or excessive gun movement speed during welding might lead to incomplete penetration weld defects. Incomplete penetration defects are a type of weld defect that occurs when there is insufficient fusing of the weld metal, leading to an incomplete fusion area at the root of the welding section [5–7]. Hence, it is of great significance to comprehensively detect and analyze the welding defects of CHS-X joints to improve the overall welding quality.

Traditional fracture mechanics methods, including stress intensity factor, crack tip opening displacement (CTOD), and J-integral approach, have been extensively employed in the investigation of fracture issues in steel structures throughout the last few decades [8–10]. Currently, the predominant micromechanical fracture model used for predicting monotonic tensile fracture is the Void Growth Model (VGM) established by Rice et al. [11]. This model characterizes the stress state of materials by examining changes in stress triaxiality. The accuracy of the VGM model criterion is verified through a sequence of tests and FEA [12–18]. Yin et al. [19] performed monotonic tensile fracture tests on specimens with single-sided U-shaped and V-shaped notches. The VGM model and VGM-based continuous damage criterion were employed to simulate the ductile fracture of these specimens. The FEA accurately predicted the load-displacement curve, which was confirmed by the test data, thus validating the correctness of both fracture criteria. Kanvinde et al. [20] proposed a Cyclic Void Growth Model (CVGM) by studying the positive and negative changes of triaxial stress under cyclic loading. Han et al. [21] studied the influence of hysteresis characteristics of circular hollow section (CHS) X joints on the seismic performance of steel pipe structures by using the CVGM model. Through experiment and FEA, the hysteresis curve and crack propagation of the joints under cyclic load are evaluated. The results show that the experiment and FEA results are highly consistent, and the error of crack load is 10.8% and 5.7%. Recent research in fracture mechanics has demonstrated that, apart from stress triaxiality, the Lord's angle parameter is also a significant determinant of the plastic flow and toughness failure of metallic materials. Smith et al. [22] introduced the Lord's angle parameter based on the CVGM model and proposed the Stress Weighted Damage Model (SWDM). He et al. [23] designed five monotonic tensile specimens under different stress states, extracted the stress triaxiality, Lord's angle parameters, and equivalent plastic strain at the initial fracture point of each specimen, and calibrated the unknown parameters of the VGM model and SWDM model for Q355B steel base metal and weld metal.

While the study of micromechanical fracture models has reached a high level of development, research on steel structures with defects is limited. Steel structures are prone to various defects, which will affect their safety performance [24-28]. Aranđelović et al. [29] fabricated different combinations of defects and performed tests and numerical simulations. They found that the welded joints with misalignment and insufficient root penetration were the weakest and could be affected by internal defects. Zhu et al. [30] analyzed the effects of circumferential weld defects on the fracture behavior of X80 pipes under internal pressure and bending forces using ABAQUS. The findings indicate that the impact of defect depth on performance is more substantial than that of defect perimeter. Geng et al. [4] studied the linear elasticity of welded thin-walled steel tubes with circular arc weld defects under bending loads, modelling these defects as circular arc cracks. They calculated the energy release rate (J-integral) using finite element methods and found that the arc length influences the stress intensity factor. Mazurkiewicz et al. [31] examined how multiple defects—such as misalignments, undercuts, incomplete root penetration, and excess weld metal—affect the performance of welded joints, revealing that stress concentration from different defects significantly impacts yield stress and plasticity, especially in misaligned joints. Lai et al. [32] investigated butt fusion-welded MDPE tube joints with varying sizes of spherical and planar defects, addressing inadequate adhesion during welding in their tests and simulations. Research indicates that defects measuring 15% of the tube wall thickness do not affect pipeline strength. However, as defect sizes increase to 30% and 45% of the wall thickness, failure strain decreases significantly. Wang et al. [33] found that incomplete penetration weld defects reduce both the average tensile and impact strength in 316L welded joints. Yan et al. [34] showed that high-temperature defects in the weld zone cause stress concentration and decrease yield strength, leading to brittle fractures. Arandjelovic et al. [35] found that secondary defects combined with vertical misalignment are most likely to cause welding failures. Most studies on welding defects focus on their impact on mechanical properties, with little research on fracture behavior. Liao et al. [36] used J-integral, VGM, and SMCS models to predict fractures in Q460C beam-column joints with initial defects, while Xing et al. [37] assessed Q235 steel corrosion, finding a ductility reduction of about 36.811%, with SWDM and LOU models outperforming VGM in fracture predictions. While Liao and Xing studied initial defects and corrosion, they did not address fractures in CHS-X joints with weld non-penetration defects. Given the prevalence of incomplete penetration during welding and its tendency to cause cracks during cooling, further investigation into the fracture performance of CHS-X joints with incomplete weld penetration is necessary.

To study the fracture properties of CHS-X joints with initial defects, three joints were designed: one with a penetration weld and two with incomplete penetration welds, all for axial loading tests. All joints were made from Q355B steel. The simulation of these joints utilized the Void Growth Model (VGM) and Stress Weighted Damage Model (SWDM) within the VUSDFLD subroutine of ABAQUS software using Fortran. The study evaluated the accuracy of both models in predicting fractures by comparing simulation results with actual test specimens. This research provides valuable insights for the safety analysis of CHS-X joints with weld defects.

2. Micromechanical fracture model

2.1. VGM model

Rice [11] et al. pointed out that the cavity expansion rate is exponential with the triaxiality of the stress state and finally derived the VGM criterion, which is expressed as:

$$\eta = \frac{\ln\left(\frac{R}{R_0}\right)}{C} = \int \mathrm{e}^{AT}\mathrm{d}\bar{\varepsilon}_{\mathrm{p}} \tag{1}$$

where η is a material property constant, R is the instantaneous hole diameter, T is stress triaxiality, $T = \sigma_{\mathrm{m}}/\sigma_{\mathrm{e}}$, σ_m is average stress, σ_{e} is equivalent stress, C and A are parameters to be fitted, $d\bar{\varepsilon}_p$ is the equivalent plastic strain increment. Equation (1) can be expressed by the following damage variable:

$$D = \int Ce^{AT}d\bar{\varepsilon}_p \tag{2}$$

When damage variable D=1, the material can be considered to break.

2.2. SWDM model

Smith et al. [22], based on the CVGM model, considered the damage accumulation problem of members under low-stress triaxial degree, introduced the Lode angle parameter to describe the partial stress state, and used the hyperbolic sine function to replace the exponential function to adjust the fracture model, and proposed SWDM model, which is expressed as:

$$D = e^{\lambda\varepsilon_{\mathrm{p}}}\int_0^{\varepsilon_{\mathrm{p}}} C(\beta e^{A^+T} - e^{-A^-T})e^{\kappa\xi}d\varepsilon_{\mathrm{p}} \tag{3}$$

$$\xi = cos\ （3\theta） = \frac{3\sqrt{3}J_3}{2J_2^{3/2}} \tag{4}$$

where λ represents the cyclic degradation rate, while β denotes the relative rate of damage, with its value fixed at 1.0. The material parameters, A^+, A^-, and κ, can be determined through test calibration. The lode angle parameter ξ varies within the range of –1 to 1, where ξ=1 signifies the axisymmetric tensile state, and ξ=0 corresponds to the plane strain state. θ is the Lode angle, and J_2 and J_3 represent the second and third invariants of the deviator stress tensor, respectively.

Rewrite Eq. (3) into incremental form, and express SWDM fracture model in the form as:

$$dD = e^{\lambda\varepsilon_{\mathrm{p}}} \cdot C \cdot (e^{A^+T} - e^{-A^-T})e^{\kappa\xi}d\varepsilon_{\mathrm{p}} \tag{5}$$

Eq. (5) is simplified to the monotonic load form of the SWDM model, as presented in Eq. (6).

$$D = \int Ce^{AT}e^{k\xi}d\bar{\varepsilon}_p \tag{6}$$

When D=1, the material can be considered to start to break.

Reference [23] predicted the fracture behavior of both the base metal test piece and the weld metal using two models. The results showed that the VGM model is primarily applicable to test pieces under high-stress triaxial states and is not applicable to test pieces under low-stress triaxial states or shear states with complex stress distributions. In contrast, the SWDM model, which considers the effect of the Lord's angle parameter, can accurately simulate the damage extent of the joint under various stress triaxial states.

Under monotonic loading, a material point in an element reaches the critical ductile fracture state when it satisfies Eq. (2) and (6), initiating fracture. Notably, the joints maintain their bearing capacity even after cracking. Thus, post-cracking, a detailed analysis of the joint's mechanical properties is crucial for assessing its limit state. To replicate crack evolution, we undertake secondary development of the finite element (FE) software by integrating the VGM and SWDM models into the VUSDFLD subroutine using Fortran and embedding them in the ABAQUS interface. This setup allows the simulation of crack initiation and propagation within the joints.

The VUSDFLD subroutine mainly defines the state variables, and the state variables of the unit material points need to be updated during each calculation and analysis. In order to realize the crack propagation behavior of the joints after cracking, the method of birth and death element is adopted. When the state variables of the element material point meet the micromechanical fracture criterion, they will be deleted from the whole model and no longer participate in the subsequent calculation. The method of birth and death element first needs to define the deleted state variables in the VUSDFLD subroutine. It needs to be set in the property column of ABAQUS software before the formal analysis. Typically, a value of 1 for the deletion state variable indicates that the unit material point is active and actively participates in the model calculation. Conversely, a value of 0 for the deletion state variable signifies that the unit material point is in a failed state and does not contribute to the model calculation.

3. CHS-X joints fracture test

3.1. Design of joints specimens

Design three CHS-X joints, where specimen GX-1 is fillet weld without weld defects, specimen GX-2 is fillet weld with weld defects, and specimen GX-3 is butt weld with weld defects. The chord and brace of these joints consist of cylindrical steel tubes, and the steel tubes of specimens are Q355B steel tubes. Refer to Table 1 for the dimensions and geometric parameters of these test joints, and consult Fig. 1 for the geometric dimensions.

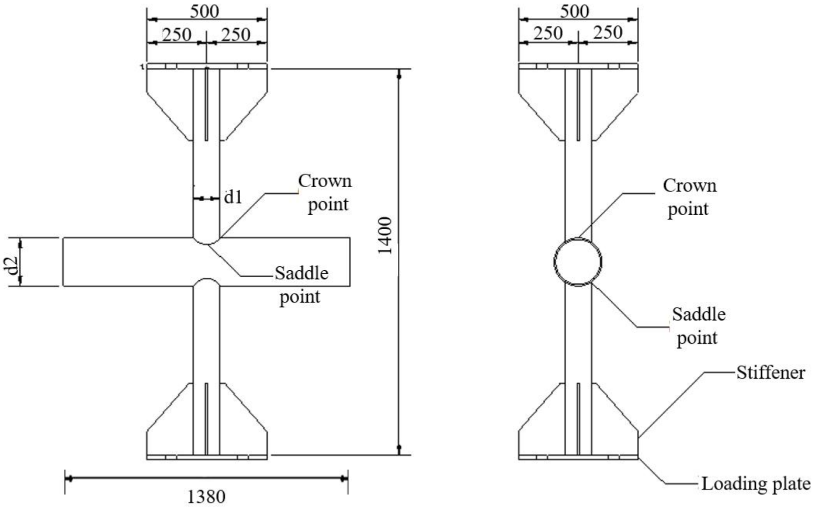

Fig. 1 Geometric dimension of specimen GX-1(unit: *mm*)

Table 1
Dimension and geometrical parameters of test joints

Specimen	Chord *d2×t1*	Brace *d1×t1*	h_f (*mm*)	β	γ	Weld form	Weld defects
GX-1	180×6	121×5	9	0.67	15	Fillet weld	No
GX-2	219×7	121×6	9	0.55	15.64	Fillet weld	Yes
GX-3	245×8	121×7	9	0.49	15.31	Butt weld	Yes

Where β is the ratio of brace diameter to chord diameter, γ is the chord radius-to-thickness ratio, and h_f is the weld size.

3.2. Material characteristics

As shown in Fig. 2, the micromechanical fracture parameters and true stress-plastic strain of Q355B steel calibrated by reference [22] are adopted. The elastic modulus of steel tube base material is 210392 MPa, yield strength is 355.49 MPa, the elastic modulus of weld metal is 206651.71 MPa, yield strength is 384.44 MPa, and Poisson's ratio is taken as 0.3. The fracture parameters of the VGM model and SWDM model are shown in Table 2 and Table 3.

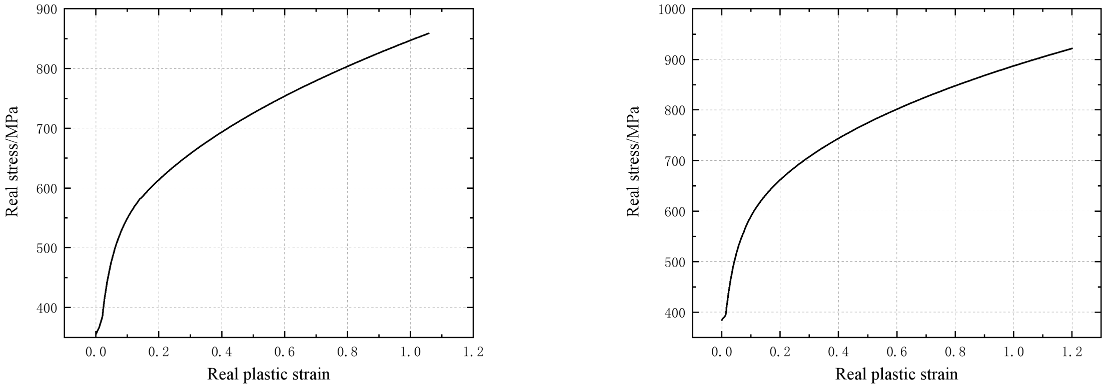

(a) base metal (b) weld metal

Fig. 2 Real stress- plastic strain curves

Table 2
Parameters of VGM model

Material	*C*	*A*	*K*
Base metal	0.466	1.232	--
Weld metal	0.255	1.537	--

Table 3
Parameters of SWDM model

Material	*C*	*A*	*K*
Base metal	0.844	0.635	0.081
Weld metal	0.802	0.771	-0.381

3.3. Loading mode

This test is carried out with the designed triangular reaction frame. The triangular reaction frame is securely fastened to the laboratory floor using ground anchor bolts. The brace of the test joint specimen is securely fastened to the triangle reaction frame at one end using bolts, while the other end is bolted to the MTS servo actuator. The actuator is attached to the laboratory reaction wall. The two ends of the chord are free and placed vertically. Fig.3 displays the test loading equipment.

The unidirectional axial tensile load is applied to the right brace, and displacement control is used. To ensure the smooth development of deformation and stress in the joints, as well as to monitor and obtain the real-time response of the structure under various load levels, the strain rate should be less than 0.00007 s^{-1}, the loading rate is set at 0.75 *mm/min*, according to the strain rate requirements specified in the Chinese and European tensile test specifications for metallic materials [38-39]. The test process is divided into two stages: preloading and formal loading. The purpose of preloading is to verify that the testing instrument can perform normally. During the formal loading stage, a loading speed of 0.75 *mm/min* is used to observe the deformation of the joint specimens and the process of crack propagation as the joints sustain damage. The load-displacement curve is monitored in real-time, with particular attention to the peak point of the curve until joint failure occurs.

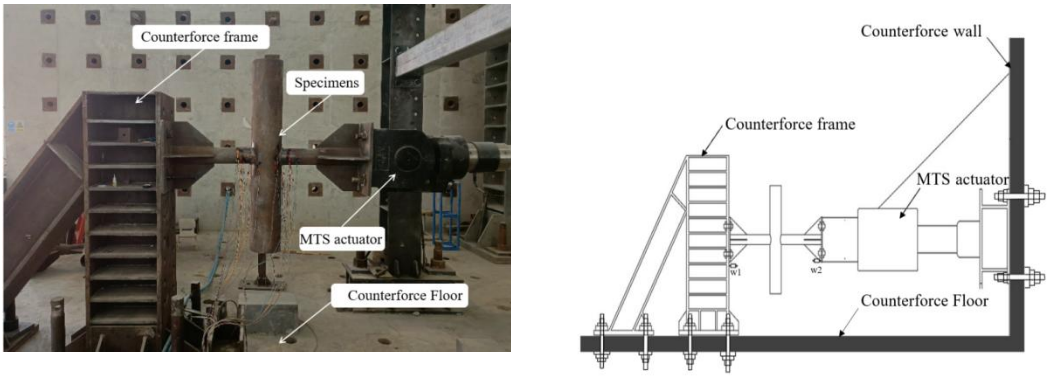

(a) Test field (b) Diagram of test loading device

Fig. 3 Test loading device

3.4. Test process and failure phenomenon of joints

Fig. 4 illustrates the fracture condition of specimen GX-1. A crack was observed at the saddle point of the weld where the brace and the chord intersected on the right side of the front side of the test piece. As the load increases, the crack propagates from the saddle point of the weld to the crown point on both sides. The crack propagation process is shown in Fig. 4. The gradual increase of load leads to large dent deformation of the chord wall and gradual flattening of the chord. At the same time, the crack on the right side of the brace in front of the joint also spreads from the saddle point to the crown point, the crack length gradually increases, and the crack width gradually increases along the axial direction of the brace. When the load reaches 421 *kN*, there is obvious dent deformation of the chord, the crack on the weld expands to the crown point, the crack width is significantly increased, and the joint loses the ability to continue bearing, that is, the maximum bearing capacity is reached, and the joint is damaged, which belongs to the weld failure form [32]. The destruction of the joint test piece is shown in Fig. 5.

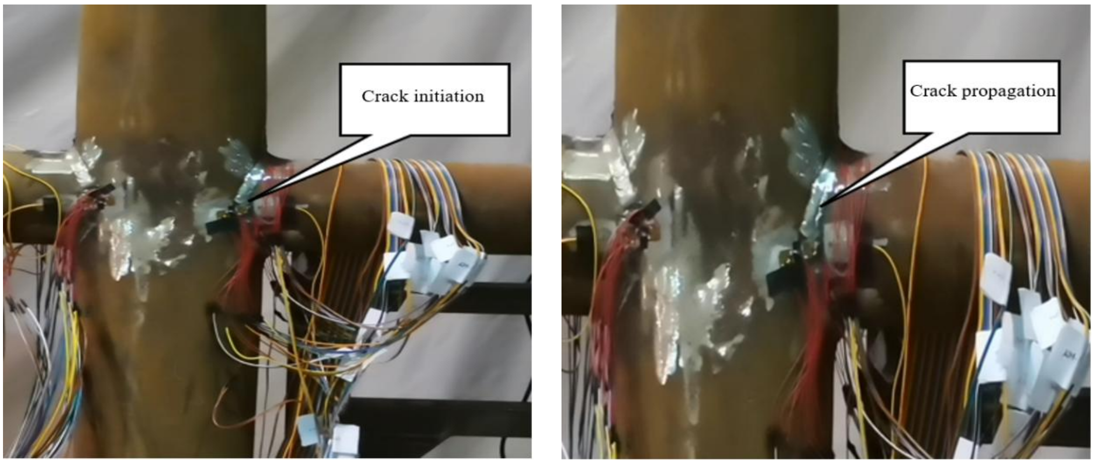

（a）Crack initiation (b) Crack propagation

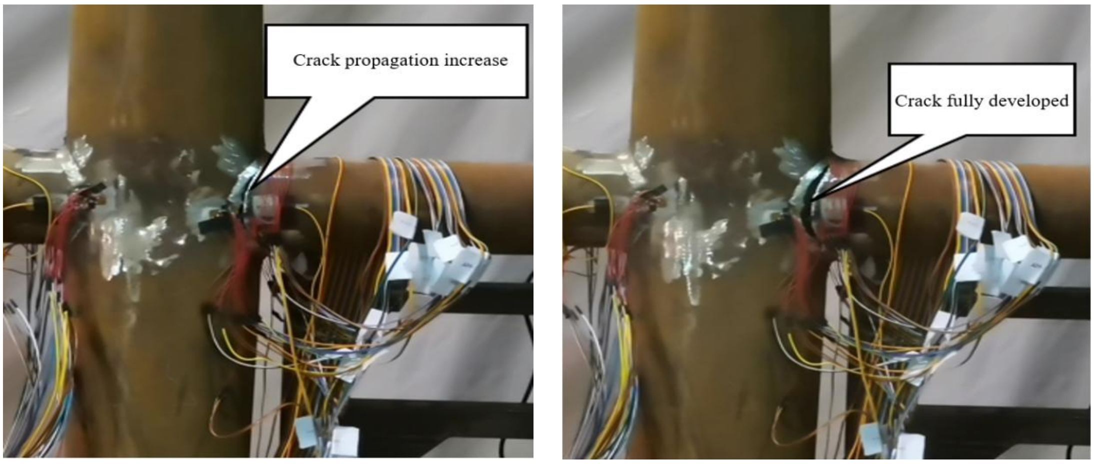

(c) Crack propagation increase (d) Crack fully developed

Fig. 4 GX-1 Crack propagation process

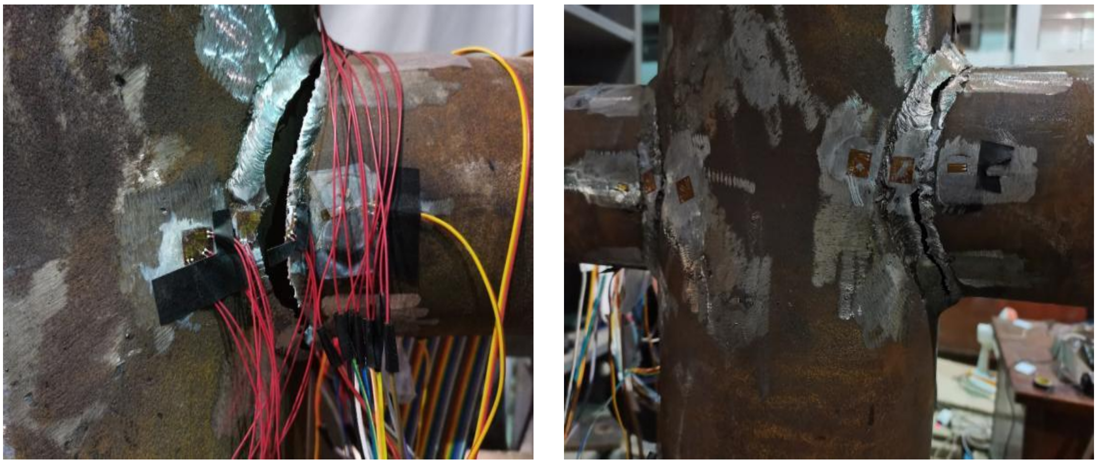

Fig. 5 Failure mode of joint specimen GX-1

Fig. 6 illustrates that as the load increases, specimen GX-2 has large dent deformation, resulting in the eventual flattening of the chord. At the moment the load hits 383.04 *kN*, an abrupt and distinct sound will be audible, indicating the sudden separation of the chord and brace. At this time, the brace of the joint is separated from the weld, and it is difficult to capture the picture of the weld crack from appearing to fracture during the failure process. Fig. 6 shows the final failure form of the joint, in which the failure mode is weld penetration zone fracture and incomplete penetration zone separation.

For joint specimen GX-3, no significant flattening of the chord occurred as the load applied to both ends of the specimen increased. When the load is loaded to 334.72 *kN*, a crisp sound is heard, the bearing capacity drops sharply, and the specimen is damaged. At the saddle of the weld in front of the specimen, the brace is separated from the weld, and there is no fracture crack at the weld behind the specimen. The failure mode of the weld joint of specimen GX-3 is fracture of the weld penetration zone, separation of the non-penetration zone, and short failure time. It is difficult to accurately record the crack growth in the process of weld crack from appearance to failure, and the final failure form of the joint is shown in Fig. 7.


(a) Damage pattern in front of the joint (b) Damage form behind the joint (c) The chord deformation morphology

Fig. 6 Failure mode of joint specimen GX-2


(a) Damage pattern in front of the joint (b) Damage form behind the joint (c) The chord deformation morphology

Fig. 7 Failure mode of joint specimen GX-3

3.5. Test results discussion

Due to the complete penetration of the weld seams in specimen GX-1, stress concentration was high at the joint saddle during the tensile process. Therefore, the cracking point first appeared at the joint saddle, and then the weld crack propagated along the intersecting line, ultimately causing the specimen to lose its bearing capacity and fail. In contrast, although specimen GX-2 has defective welds, its load-displacement curve show a plastic stage, and the chord undergoes significant deformation, with an ultimate bearing capacity of 383.04 *kN*. The time from cracking to fracture in the saddle weld of specimen GX-2 joint is short. Although the deformation of the chord can serve as a precursor to fracture, sudden fracture still poses a potential danger to the engineering structure. The reason for the failure of specimen GX-2 is that there is a small area of incomplete fusion between the weld and the brace. As for specimen GX-3, due to the small penetration area of the weld and the large non-penetration area, the weld defects were significant. The load-displacement curve did not show obvious plastic deformation, and the chord did not undergo dent deformation after fracture. Specimen GX-3 fractured at a load of 337.42 *kN*, with a rapid failure time and no signs of pre-fracture.

Fig.8 displays the load-displacement curves for the three specimens. From the load-displacement curve of specimen GX-2, it can be seen that it shows a plastic phase, while specimen GX-3 does not exhibit obvious plastic deformation. Observing the deformation of the chord, it is evident that the chord of specimen GX-3 undergoes no significant deformation. Regarding the form of fracture, the time from cracking to joint fracture in the weld of both specimens is very short, indicating sudden fracture. However, specimen GX-2 has a larger weld penetration area, and its chord exhibits concave deformation, which can serve as a precursor to joint fracture. In contrast, the joint fracture of specimen GX-3 is sudden, with no precursors before fracture. These differences are primarily attributed to the larger weld penetration area in GX-2 compared to the smaller area in GX-3, and they are quite similar to those observed by Lai [32], who studied butt fusion welded MDPE pipe joints with spherical and planar defects of various sizes through tensile tests and finite element analysis. That is, when the weld penetration area is large, the joint strength decreases slightly, whereas when the weld penetration area is small, the joint strength decreases significantly. In order to enhance the performance of joints and prevent similar issues, it is imperative to study CHS-X joints with weld defects, verify that the design satisfies the load-bearing criteria, and carry out comprehensive quality inspection and monitoring to guarantee the safety and stability of the structure.

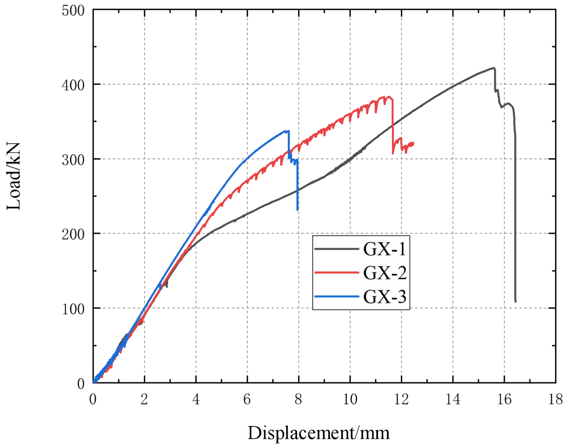

Fig. 8 Load-displacement curve of test specimens

4. Simplification of weld defects and finite element modelling

4.1. Weld defects analysis

The weld defects of specimen GX-2 are shown in Fig. 9, and the brace breaks at three positions, which indicates that the three welds are fused with the brace. The first weld penetration zone fracture occurs at the crown point, and the fracture point size is 36.8 *mm* long and 8.6 *mm* wide. The second weld penetration zone fracture occurs at the saddle point, and the fracture point size is 12.2 *mm* long and 4 *mm* wide. The third weld penetration zone fracture point is located at the crown on the other side, and the fracture point size is 19.4 *mm* long and 4 *mm* wide. Other weld penetration areas are the bright areas shown by the red curves in the figure. The weld penetration widths of these areas vary. The average width of the weld penetration area on the front side of the joint is 5.2 *mm*, while the average width of the weld penetration area on the behind side of the joint is 5.24 *mm*. In addition, the front of the joint has an 18 *mm* long weld penetration area at the saddle point.

(a) Brace and weld penetration breakpoints (b) Weld defects in the front side of joint (c) Weld defects in the behind side of joint

Fig. 9 Weld defects distribution of specimen GX-2

Fig. 10 Simplified weld defects finite element modelling of specimen GX-2

(a) Weld defects in the front side of joint (b) Weld defects in the behind side of joint (c) Simplification of weld defects

Fig. 11 Incomplete penetration weld zone of GX-3 and simplified finite element model

The weld defects of specimen GX-3 are shown in Fig. 11. The failure form is the separation between the weld and brace at the saddle point. The red curve light area in the figure is the part of weld and brace penetration. There was an area of about 23 *mm* in length at the saddle of the brace without any traces of light or fracture, suggesting that this part of the weld was not fully fused with the brace. There is no fracture crack on the rear weld of specimen GX-3, indicating that the rear weld of specimen GX-3 is fused with the brace. Therefore, during finite element modelling, only the defects of welds on the front side of the specimen are considered.

4.2. FEA and welds simplification

The FEA software [40] ABAQUS was used to create solid element models of the chords, braces, and welds. The test piece GX-1 is modeled by directly merging the weld, parent tube, and brace. The element type selected is C3D8R. 0.5 *mm* is taken as the root clearance between the chord and brace. In order to meet the requirement of feature-length L^*, local refinement is applied to the joints weld and its surroundings. The grid size is set at 0.3 *mm* away from the weld-seam area, and the grid size gradually increases to 6 *mm*. The joint constraint condition and load action mode are that the chord end is free, the symmetric axial monotonic load is applied to the section of the brace end, and the symmetric constraint condition is applied to the symmetric surface. Figs. 12 and 13 show the finite element modelling of fillet and butt welds, while the saddle and crown points of the weld model are illustrated in Figs. 14 and 15. The finite element model of the test specimens is shown in Fig. 16.

Due to the highly irregular welding defect areas in specimens GX-2 and GX-3, which include variations in weld penetration size and incomplete penetration areas, creating an accurate finite element model that simulates the actual shape of weld defects is very complex and difficult to realize. Drawing on the simplified methods for assessing weld defects found in the literature [41-44], this study proposes the equivalent width method and the equivalent area method. These approaches overlook the geometric characteristics of weld defects, focusing instead on the impact of their location and area on the specimens. The primary goal is to simplify the analysis of weld defects, reduce model complexity, and facilitate the construction of finite element models for analysis and calculations. Both methods operate under the assumption that the stress concentrations arising from the actual shape and the equivalent shape of a defect have an equal effect on the ultimate bearing capacity at fracture. However, this assumption overlooks variations in fracture-bearing capacity due to shape differences, which may potentially lead to certain errors. These discrepancies will be explored in relation to both test and FEA results. When employing the equivalent width and equivalent area methods, the shape of the weld defect is simplified to a regular form without detailed consideration of its specific geometric characteristics. For example, as illustrated in Fig. 10, the test specimen GX-2 depicts the weld defects simplified as weld seams with a width of 5.22 mm at the bottom of the brace, both in front of and behind the joint. In this region, these weld seams are entirely fused with the brace. During finite element modelling, the braces of the penetration part shall be bound with the welds, and the parts without penetration shall not be subject to any constraint treatment.

For specimen GX-3, a 23 *mm* long weld at the saddle is not penetrated. During modelling, this weld and brace at the corresponding position should not be subjected to any constraint treatment. The total length of the front weld fracture area of specimen GX-3 is 170.5 *mm*, and the sum of the areas of the front penetration areas is calculated to be 347.82 mm^2. The weld width of the weld penetration area is calculated to be 2.04 *mm* based on the area equivalent principle. As shown in Fig. 11, in the finite element modelling, the weld joint with a front length of 170.5 *mm* and a width of 2.04 *mm* is considered to be connected to the brace. The rest of the front weld of the joint is not subject to any constraint, and all welds at the back of the joint are fully penetrated and connected with the brace.

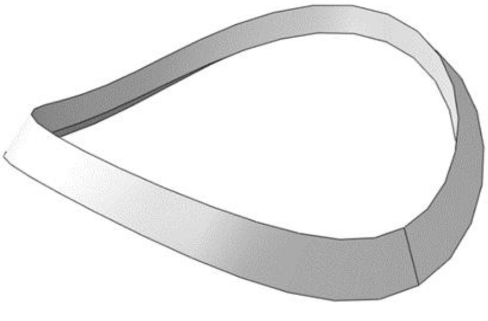

Fig. 12 Three-dimensional diagram of fillet weld

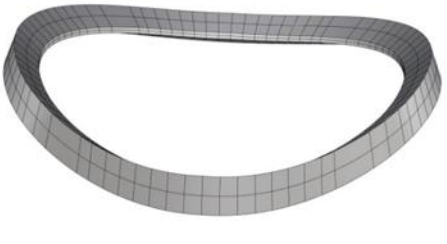

Fig. 13 Three-dimensional diagram of butt weld

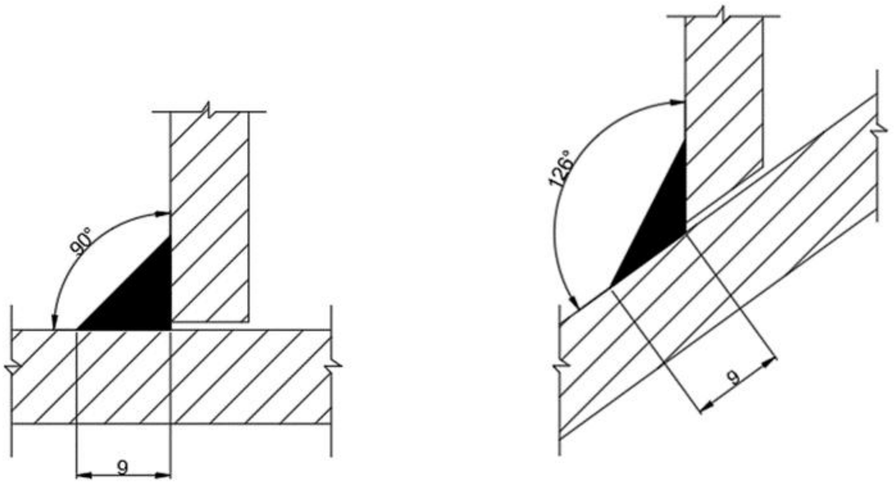

（a）Fillet weld at crown point

（b）Fillet weld at saddle point

Fig. 14 Geometric dimension of fillet weld

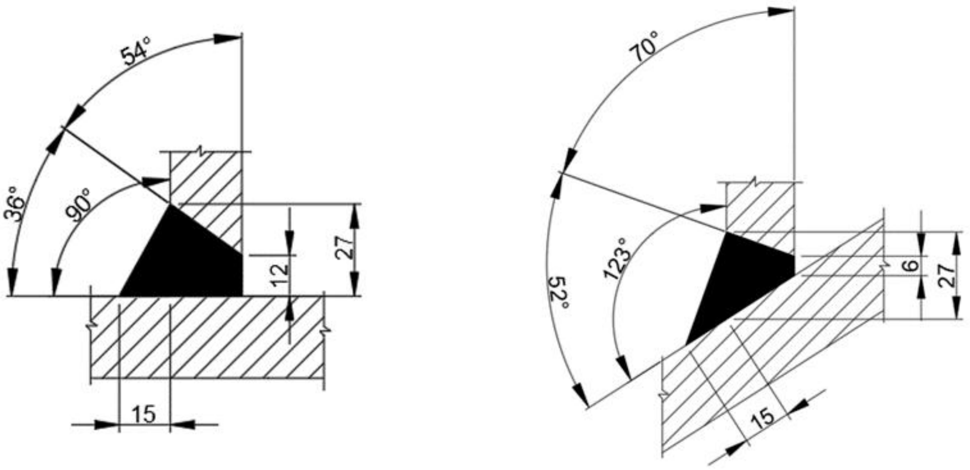

（a）Butt weld at crown point

（b）Butt weld at saddle point

Fig. 15 Geometric dimension of Butt solid welds

(a) GX-1 (b) GX-2 and GX-3

Fig. 16 FE model of specimens

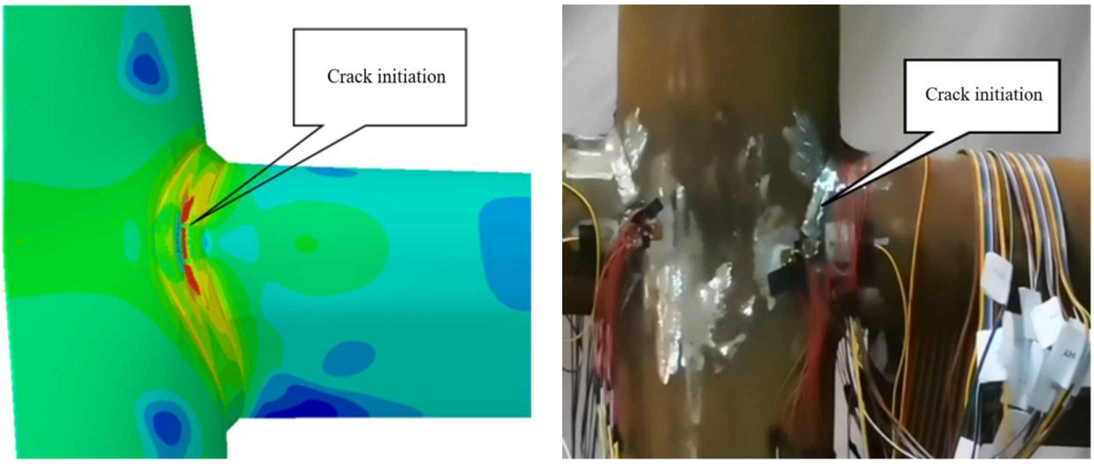

(a) Crack initiation (FEA) (b) Crack initiation (Test)

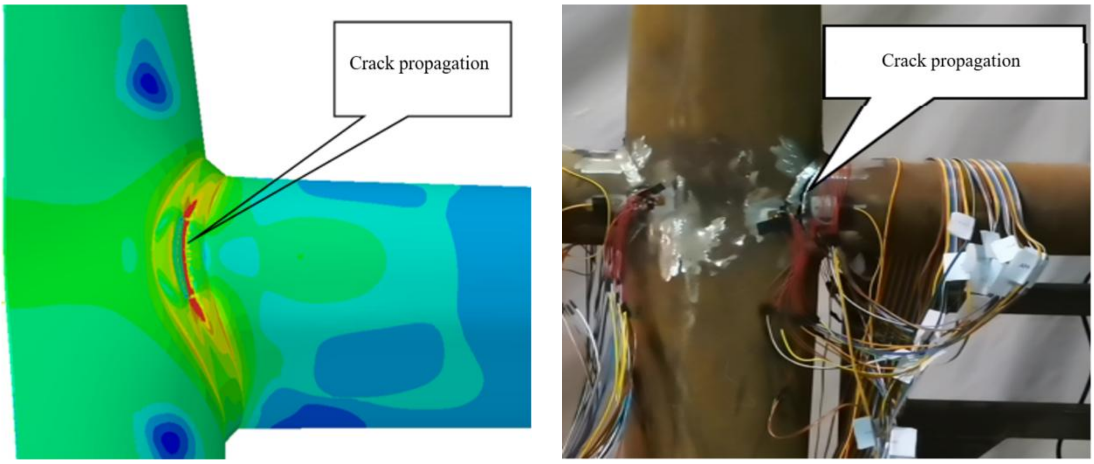

(c) Crack propagation (FEA) (d) Crack propagation (Test)

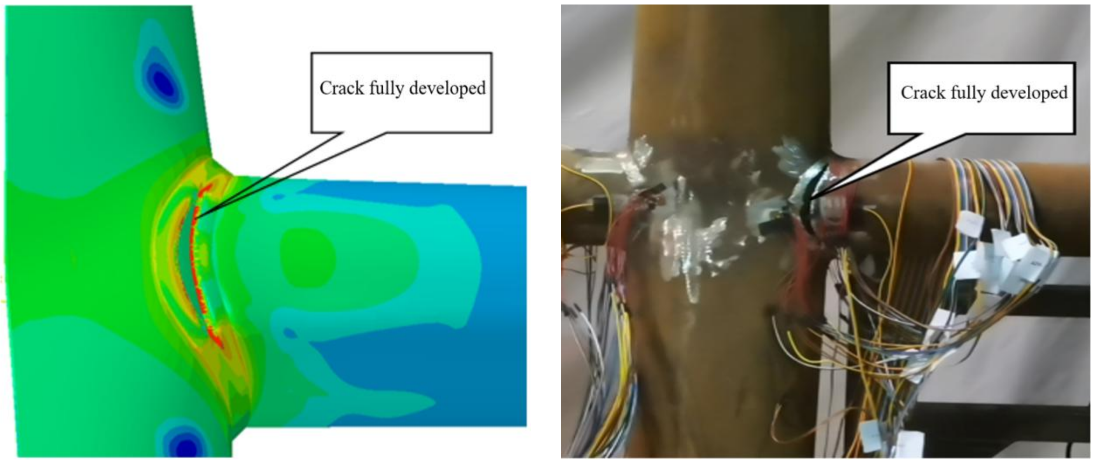

(e) Crack fully developed (FEA) (f) Crack fully developed (Test)

Fig. 17 Crack propagation comparison of GX-1

4.3. Comparison between numerical simulation results and test results

Based on the analysis of the crack point in the specimen GX-1 model, it is observed in Fig. 17 that the crack propagation path of the FEA results is consistent with the test results, and the failure of the joint is the failure of the weld. Since the stress concentration at the joint saddle point is relatively serious, the weld crack occurs at the joint saddle point. As the load continues to increase, cracks will propagate from the saddle point along the intersection line of the CHS-X joint to the crown point, and the length and width of the cracks will gradually increase, ultimately leading to fracture and failure of the joint and loss of bearing capacity. The crack propagation process and ultimate bearing capacity of the CHS-X joint, as predicted by the VGM and SWDM models, show a strong agreement with the test data. This finding aligns with the conclusion stated in reference [45], demonstrating the accuracy of FEA.

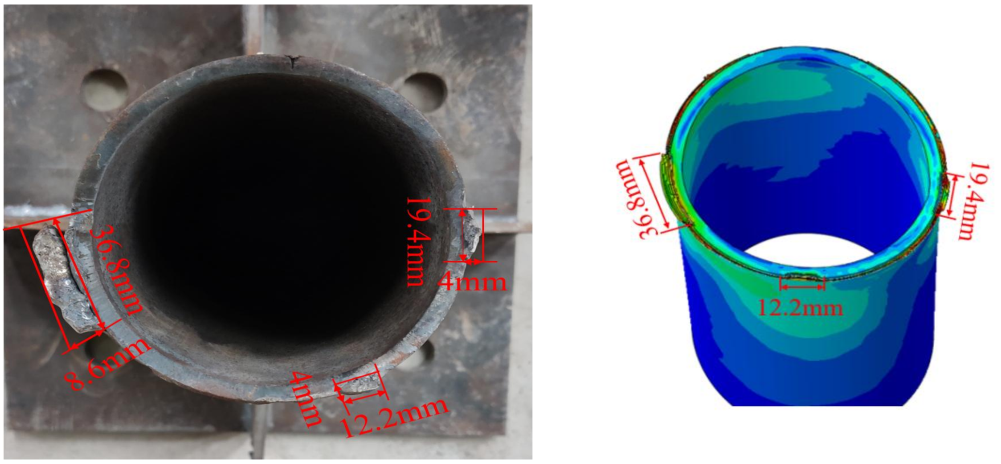

(a) Fracture point (Test) (b) Fracture point (FEA)

Fig. 18 Weld fracture comparison of GX-2

(a) Fractured in the front side (Test) (b) Fractured in the front side (FEA)

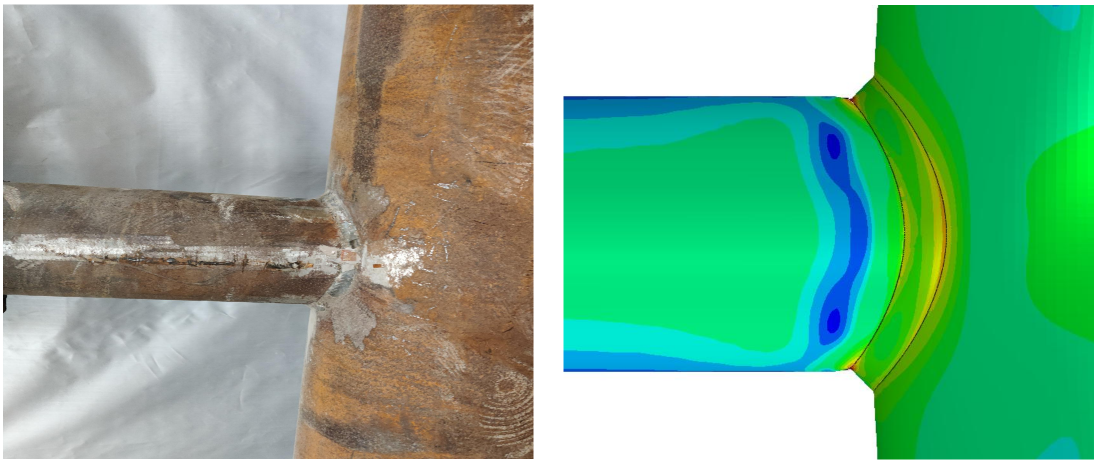

(c) Specimen in the behind side (Test) (d) Specimen in the behind side (FEA)

Fig. 19 Weld fracture comparison of GX-3

As shown in Figs. 18 and 19, the FEA results of specimens GX-2 and GX-3 are basically consistent with the fracture phenomenon of the test results. The stress concentration at the joint's saddle point is relatively severe, causing weld cracking at the CHS-X joint's saddle point. For specimen GX-2, the dimensions and positions of the chord deformation and brace fracture points simulated by FEA are basically the same as those of the test. The FEA and test of GX-3 indicate that the front side of the joint has experienced a fracture, while the rear of the joint does not show obvious failure characteristics except for large stress concentration. This proved that the simplified weld defects of the specimens GX-2 and GX-3 and the constraint imposed between the weld and the brace after the simplified weld defects were reasonable.

4.4. Load-displacement curves

The load-displacement curves for the FEA and test, as depicted in Figs.20, 21, and 22, exhibit similar trends and consistency. As shown in Table 4, the displacement error of the joints simulated by the VGM model without weld defects of GX-1 and with weld defects of GX-2 and GX-3 welds is 19.5%, 19.49%, and 19.97%, respectively, the load error is 19.48%, 20.45%, and 21% respectively, and the error is within 21%. The displacement error of the joints simulated by the SWDM model without weld defects of GX-1 and with weld defects of GX-2 and GX-3 welds is 5.77%, 8.67%, and 7.62%, respectively, and the load error is 11.92%, 16.93%, and 16.12% respectively, with the error within 17%. It can be seen that both the SWDM model and the VGM model can be used to predict the ultimate bearing capacity of CHS-X joints with weld defects. This is consistent with the conclusion that the micromechanical fracture models VGM and Stress Modified Critical Strain (SMCS) discussed in the literature [28] are applicable to the fracture prediction of beam-column joints with initial defects. SWDM model performs better than the VGM model in CHS-X joint fracture prediction.

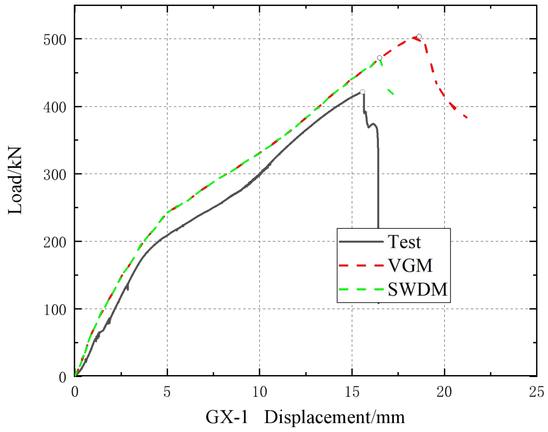

Fig. 20 FEA and test load-displacement curves for GX-1

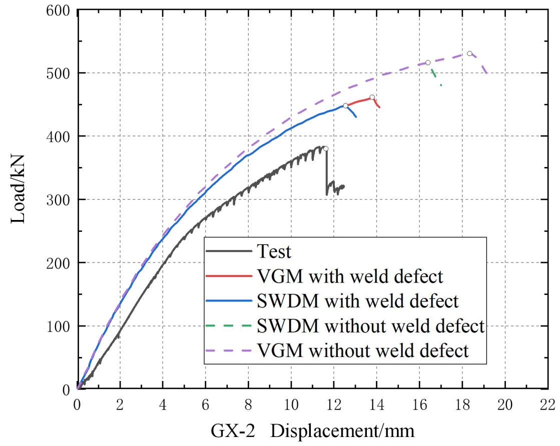

Fig. 21 FEA and test load-displacement curves for GX-2

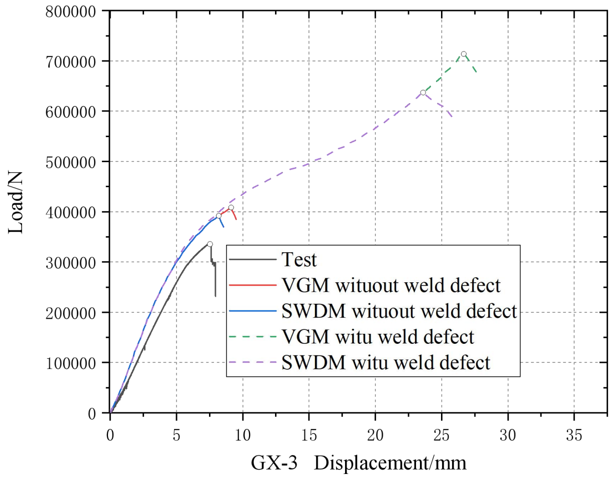

Fig. 22 FEA and test load-displacement curves for GX-3

Both SWDM and VGM can accurately predict the weld fracture of the CHS-X joint; However, considering the influence of the Lord's angle parameter, SWDM can accurately simulate the damage degree of the joint under different stress states, and its accuracy is higher than that of VGM, with good applicability [46]. At the same time, the equivalent area method and the equivalent width method are used to simplify the weld defect, and the influence of the weld defect shape on the joint is ignored. Only the influence of the weld defect position on the joint is considered, and the influence of the stress concentration and the local weld defect shear force is not considered. Therefore, the calculation results of the SWDM model and the VGM model are different, and the performance of the SWDM model is better than the VGM model.

This article employs the equivalent area method and the equivalent width method to simplify the analysis of weld penetration depth. The influence of weld defect shapes on the joint is primarily attributed to specific stress concentrations caused by irregular shapes, which have not been fully considered. Instead, the focus is on the impact of incomplete fusion locations and areas within the weld seam on the joint. Additionally, securing the end of the chord during load testing can be challenging. As the load increases, the fixed reaction frame tends to slide, introducing a certain degree of error into the test. Finite element modelling and simulation operate under ideal conditions, which contribute to discrepancies when compared to experimental results. Specifically, the finite element simulation results indicate that the VGM model has an error of nearly 20%, whereas the SWDM model exhibits an error of approximately 17%.

By comparing joint test and FEA results, VGM and SWDM models are used to predict the crack propagation process of joints and the ultimate bearing capacity of joints, which are in good agreement with the test results, proving the rationality of simplification of weld defects. FEA Comparison of Specimens with and without weld defects, the ultimate bearing capacity of GX-2 drops by 15%, the fracture displacement drops by 34.3%, the ultimate bearing capacity of GX-3 drops by 76.2%, and the fracture displacement drops by 189.7%. It can be seen that the existence of weld defects greatly influences the ultimate bearing capacity and fracture displacement of the CHS-X joints. Studying the impact of weld imperfections on the load-bearing capability of CHS-X joints can offer valuable insights for the safety assessment of CHS-X joints with weld defects.

Table 4
Load-displacement comparison between test and FEA results

Specimen	FEA (VGM)		Test		Displacement error	Load error
	Ultimate load (*kN*)	Δ_u/mm	Ultimate load (*kN*)	Δ_u/mm		
GX-1	503.67	18.63	421.55	15.59	19.5%	19.48%
GX-2 with weld defects	530.79	18.52	-	-	-	-
GX-2 without weld defects	461.37	13.79	383.04	11.54	19.49%	20.45%
GX-3 with weld defects	719.83	26.45	-	-	-	-
GX-3 without weld defects	408.39	9.13	337.42	7.61	19.97%	21%

Specimen	FEA (SWDM)		Test		Displacement error	Load error
	Ultimate load (*kN*)	Δ_u/*mm*	Ultimate load (*kN*)	Δ_u/*mm*		
GX-1	471.81	16.49	421.55	15.59	5.77%	11.92%
GX-2 with weld defects	515.95	16.30	-	-	-	-
GX-2 without weld defects	447.89	12.54	383.04	11.54	8.67%	16.93%
GX-3 with weld defects	641.05	23.45	-	-	-	-
GX-3 without weld defects	391.82	8.19	337.42	7.61	7.62%	16.12%

5. Conclusion

In order to study the fracture behavior of the CHS-X joints with initial defects, an axial test is designed for one weld penetration test piece and two test pieces without weld penetration. The Void Growth Model (VGM) and Stress Weighted Damage Model (SWDM) are programmed into the program of ABAQUS software VUSDFLD by Frotran language. The FEA of the CHS-X joints with initial defects was carried out, and the applicability of the two models in the fracture prediction of CHS-X joints with initial defects is discussed by comparing them with the test results. The following main conclusions are drawn from this study:

(1) The FEA of the GX-1 specimen with no weld defects is in good agreement with the test results, which indicates that the VGM and SWDM models can be used to predict the fracture of the joints effectively.

(2) Based on the irregularity of weld defects, finite element modelling is difficult. According to the actual welding condition of the weld, the equivalent width method and the equivalent area method are used to simplify the weld defects and establish the corresponding finite element model. VGM and SWDM models are used to predict the crack propagation process and the ultimate bearing capacity of the joints, which are in agreement with the test results, and the fracture phenomenon is basically the same. It is proved that the two models can effectively predict the fracture of the joints weld with defects and the rationality of simplifying the weld defects.

(3) By comparing the fracture displacement and ultimate load of the test and FEA, it can be found that the error of the VGM model is within 21%, and the error of the SWDM model is within 17%. The fracture prediction results of weld fracture of the CHS-X joints by the SWDM model are closer to the test results than those of the VGM model. This shows that the SWDM model can be well applied to the fracture prediction and fracture path simulation of the CHS-X joints defects weld.

Acknowledgements

The research presented in this paper was supported by the Natural Science Foundation of China (NSFC) through Grant No.51368009 and was also supported by the Natural Science Foundation of Guizhou province (CN) through Grant No. (2018) 1036.

Reference

[1] F.F. Liao, K.K. Li, W. Wang, Y.Y. Chen, G. Li, Experimental study and finite element analysis on fracture performance of ER55-G welds. *Journal of Constructional Steel Research*, 2020, 172: 106129.

[2] X. Chang, L. Fu, H.B. Zhao, Y. B. Zhang, Behaviors of axially loaded circular concrete-filled steel tube (CFT) stub columns with notch in steel tubes. *Thin-Walled Structures*, 2013, 73: 273-280.

[3] F.X. Ding, L. Fu, Z.W. Yu, Behaviors of axially loaded square concrete－filled steel tube (CFST) stub columns with notch in steel tube. *Thin － Walled Structures*, 2017, 115: 196-204.

[4] J.F. Geng, H.S. Cai, X. P. Liang, H. Wang, Y. J. Wang, Z.H. Wang, Welding Defect Analysis in Thin-Walled Steel Tube under Bending Moment. *Applied Mechanics and Materials*, 2011, 94: 1711-1714.

[5] M. Yan, Z. Guo, C. Li, Y. Liu, X. Wang, Effect of welding defects on mechanical properties of welded joints subjected to temperature. *Steel and Composite Structures, An International Journal*, 2021, 40(2): 193-202.

[6] S. Tang, X. Gao, K. Tian, Q. Zhang, X. Zhang, J. Peng, J Guo, Non-destructive evaluation of weld defect with coating using electromagnetic induction thermography, *Nondestructive Testing and Evaluation*, 2024, 39(2): 347-365.

[7] D. Shiraishi, R. Kato, H. Endoh, T. Hoshimiya, Destructive inspection of weld defect and its nondestructive evaluation by photoacoustic microscopy. *Japanese Journal of Applied Physics*, 2010, 49(7S): 07HB13.

[8] A. A. Griffith, VI. The phenomena of rupture and flow in solids. *Philosophical transactions of the royal society of london. Series A, containing papers of a mathematical or physical character*, 1921, 221(582-593): 163-198.

[9] G. R. Irwin, Analysis of stresses and strains near the end of a crack traversing a plate. (1957):361-364

[10] J.R. Rice, A path independent integral and the approximate analysis of strain concentration by notches and cracks. *Journal of Applied Mechanics*, 1967.

[11] J. R. Rice, D. M. Tracey, On the ductile enlargement of voids in triaxial stress fields∗. *Journal of the Mechanics and Physics of Solids*, 1969, 17(3): 201-217.

[12] Z.H. Huang, M. Ashraf, T. Zheng, Y. Yang, E.H. Bao, H. Han, Analysis of ultimate fracture bearing capacity of CHS XK-joints welds, *Sustainable Structures*. 2023, 3(2): 000031.

[13] A.M. Kanvinde, G.G. Deierlein, Finite-element simulation of ductile fracture in reduced section pull-plates using micromechanics-based fracture models. *Journal of Structural Engineering*, 2007, 133(5): 656-664.

[14] F.F. Liao, W. Wang, Y.Y. Chen, Parameter calibrations and application of micromechanical fracture models of structural steels, *Structural engineering and mechanics,* 2012, 42(2): 153-174.

[15] X. Qu, C. Qin, G. Sun, Y. Xie, Research on fracture of steel structure welded joint based on micro-mechanism. *Structures,* 2022, 43: 434-448.

[16] Y. Wang, H. Zhou, Y. Shi, J. Xiong, Fracture prediction of welded steel connections using traditional fracture mechanics and calibrated micromechanics based models. *International Journal of Steel Structures*, 2011, 11: 351-366.

[17] Y. Yin, X. Che, Z. Li, J. Li, & Q. Han, Ductile fracture analysis of welded hollow spherical joints subjecting axial forces with micromechanical fracture models. *International Journal of Steel Structures*, 2019, 19: 2010-2023.

[18] F.F. Liao, Y. Liu, W. Wang, Z. Lu, X. Li, Fracture performance study on Q460D steel and ER55-G welds after high temperature. *Journal of Constructional Steel Research*, 2023, 206: 107888.

[19] Y. Yin, X. Liu, Q. Han, Z. Liu, Simulation of ductile fracture of structural steels with void growth model and a continuum damage criterion based on it. *Theoretical and Applied Fracture Mechanics*, 2018, 98: 134-148.

[20] A. M. Kanvinde, G. G. Deierlein, Cyclic void growth model to assess ductile fracture initiation in structural steels due to ultra low cycle fatigue. *Journal of engineering mechanics*, 2007, 133(6): 701-712.

[21] J.Y. Han, J. Li, Y. Yang, Q. Xiang, Z. Huang, Numerical simulation of the crack propagation effect on the hysteretic behavior of CHS-X joints. *Engineering Failure Analysis*, 2024: 108549.

[22] C. M. Smith, A Stress-weighted Damage Model for Ductile Fracture Initiation in Structural Steel Under Cyclic Loading and Generalized Stress States, Stanford University, 2013.

[23] X. He, Q. Luo, Y. Yang, Z. Huang, Calibration of micromechanical fracture model parameters for Q355B steel and ER50–6 welds. *Journal of Constructional Steel Research*, 2024, 215: 108563.

[24] T. Lin, W. Huang, S.W. Liu, & R. Bai, AN INVESTIGATION ON THE EFFECT OF RANDOM PITTING CORROSION ON THE STRENGTH OF THE SUBSEA PIPELINE USING MONTE CARLO METHOD. *Advanced Steel Construction*, 2024, 20(1): 93–104.

[25] Q. Si, Y. Ding, L. Zong, & H.T. Zhao, MECHANICAL BEHAVIOUR OF CORRODED STRUCTURAL STEEL SUBJECTED TO MONOTONIC TENSION. *Advanced Steel Construction*, 2022, 18(3): 707-714.

[26] Z.Y. Jie, W.J. Wang, P. Zhuge, Y.D. Li, & X. Wei, FATIGUE PROPERTIES OF INCLINED CRUCIFORM WELDED JOINTS WITH ARTIFICIAL PITS. *Advanced Steel Construction,* 2021, 17(1): 20-27.

[27] Z.W. Zhang, H.J. Wang, H.L. Qian, X.F. Jin, Q. F, & F. Fan, RESIDUAL LIFE PREDICTION AND DESIGN CORRECTION METHOD OF CORRODED CIRCULAR STEEL TUBES BASED ON TIME-VARYING RELIABILITY. *Advanced Steel Construction,* 2024,20(1): 12-20.

[28] L.F. Xiao, J.X. Peng, J.R. Zhang, & C.S. Cai, MECHANICAL PROPERTIES OF CORRODED HIGH PERFORMANCE STEEL SPECIMENS BASED ON 3D SCANNING. *Advanced Steel Construction,* 2019, 15(2): 129-136.

[29] M. Aranđelović, S. Sedmak, R. Jovičić, S. Perković, Z. Burzić, D. Radu, Z. Radaković, Numerical and experimental investigations of fracture behaviour of welded joints with multiple defects. *Materials*, 2021, 14(17): 4832.

[30] L. Zhu, N. Li, B. Jia, Y. Zhang, Fracture response of X80 pipe girth welds under combined internal pressure and bending moment. *Materials*, 2023, 16(9): 3588.

[31] L. Mazurkiewicz, M. Tomaszewski, J. Malachowski, K. Sybilski, M. Chebakov, M. Witek, ... & R. Dmitrienko, Experimental and numerical study of steel pipe with part-wall defect reinforced with fibre glass sleeve. *International Journal of Pressure Vessels and Piping*, 2017, 149: 108-119.

[32] H.S. Lai, S.H. Kil, K.B. Yoon, Effects of defect size on failure of butt fusion welded MDPE pipe under tension. *Journal of Mechanical Science and Technology*, 2015, 29: 1973-1980.

[33] Y.B. Wang, Z.W. Guo, X.Q. Bai, C.Q. Yuan, Effect of weld defects on the mechanical properties of stainless-steel weldments on large cruise ship. *Ocean Engineering,* 2021, 235: 109385.

[34] M. Yan, Z. Guo, C. Li, Y. Liu, X. Wang, Effect of welding defects on mechanical properties of welded joints subjected to temperature. *Steel and Composite Structures, An International Journal,* 2021, 40(2): 193-202.

[35] M. Arandjelovic, B. Djordjevic, S. Sedmak, D. Radu, A. Petrovic, S. Dikic, A. Sedmak, Failure analysis of welded joint with multiple defects by extended Finite Element Method and Engineering Critical Analysis. *Engineering Failure Analysis,* 2024, 160: 108176.

[36] F.F. Liao, K. Zhang, W. Wang, Y. Chen, S. Tang, X. Xue, & C. Li, Fracture analysis of high-strength steel beam-column connections with initial defects. *Journal of Constructional Steel Research*, 2022, 194: 107301.

[37] J.H. Xing, D. Dilixiati, N. Yang, Q.S. Yang, Fracture properties of corroded steel under monotonic tension load. *Construction and Building Materials,* 2024, 437: 136918.

[38] GB / T 228.1-2021, Tensile testing of metallic materials--Part 1: Room temperature test method.

[39] EN ISO 6892-1: 2019, Metallic Materials - Tensile Testing - Part 1: Room Temperature Test Method.

[40] ABAQUS, Analysis User's Manual Version 6.14-4, Dassault Syst`emes Simulia Corp, Providence, RI, USA, 2010.

[41] B. Chen, Safety analysis of in-service pressure pipelines with incomplete penetration defects based on maximum load. Zhejiang University, 2010. (in Chinese)

[42] H.Y. Xiong, Research on the Ultimate Load Carrying Capacity of Steel Pipes with Ring Weld Defects. Southwest University of Science and Technology, 2023. (in Chinese)

[43] Q. Zhao, K. Tang, G.M. Huang, & Z.Z Lin, Effect of initial defect of butt weld on fatigue life. *Journal of Hefei University of Technology (Natural Science),* 2023, 46(04):473-480. (in Chinese)

[44] K. Yang, H. Feng, P. Wang, H.Y. Cheng, Q. Chi, Evaluation of Girth Weld Tensile Capaity of High Grade Pipeline Based on Full Size Test. *Petroleum Tubular Goods & Instruments,* 2022, 8(06):44-49. (in Chinese)

[45] Z.L. Liu, Ductility fracture test and finite element analysis of X-shaped circular steel tube intersecting nodes under static load. Guizhou University, 2023. (in Chinese)

[46] H. Han, T. Zheng, X.D. Wang, Z. H. Huang, Fracture prediction and bearing capacity analysis of weld of tubular circular hollow section X-joints. *Building Structures,* 2022, 52(13):99-105. (in Chinese)

Advanced Steel Construction – Vol. 21 No. 3 (2025) 265–276
DOI:10.18057/IJASC.2025.21.3.8

SEISMIC PERFORMANCE OF SQUARE CORE TUBE SQUARE STEEL TUBE COLUMN FULLY BOLTED CONNECTION JOINTS

Hai-Ling Bao [1], Pei-Bao Xu [2], Kai Li [2] and Zi-Qing Yuan [3, *]

[1] *Anhui Technical College of Water Resources and Hydroelectric Power, Hefei, Anhui 231603,China*
[2] *Department of Civil Engineering Anhui Jianzhu University, Hefei, Anhui 230601,China*
[3] *School of Civil Engineering, Hefei University of Technology, Hefei, Anhui 230009, China*
* *(Corresponding author: E-mail: yuanziqing@mail.hfut.edu.cn)*

ABSTRACT

Traditional steel structures often use full penetration welding for square steel tube column-to-column connections, which is labor-intensive and challenging to quality control. Prefabricated connections using high-strength bolts reduce welding but require drilling holes in the columns, potentially compromising stiffness and load-bearing capacity. To mitigate these issues, this paper introduces a novel fully bolted connection joint for square core tube square steel tube columns. This joint comprises outer extension end plates for both the column and the core tube, which are secured together using high-strength bolts. No holes needed in the steel tube wall, which ensures the stiffness and load-bearing capacity of the connection area, and allows for fully prefabrication. To reveal the working mechanism of proposed joint, finite element models were established using ABAQUS software. The entire stress process of the joint under low-cycle reciprocating loads was analyzed. The analysis examined how parameters like core tube strength, thickness, square steel tube column strength, axial compression ratio, and bolt pre-tension affected key mechanical performance indicators such as plastic deformation, failure modes, hysteresis, and energy dissipation. The results indicate that the core tube can increase the stiffness at the connection location, causing the plastic development region to be far from the connection area, achieving the seismic design goal of ‘strong joints, weak members’. Meanwhile, the joint’s hysteresis curves exhibit fullness without evident pinching, with ductility coefficients ranging from 2.66 to 3.79, inter-story displacement angles fall ranging from 1/98 to 1/71, which meets the GB50011-2010 specifications. Optimal design suggests a square steel tube to core tube strength ratio of 1.5-1.78, core tube to column strength ratio of 0.22-0.66, and axial compression ratio of 0.3-0.5. The core tube to column thickness ratio and bolt type should be selected based on structural needs. The research confirms the joint’s feasibility and provides design guidance.

ARTICLE HISTORY

Received:	28 September 2024
Revised:	6 January 2025
Accepted:	8 January 2025

KEYWORDS

Prefabrication;
Square steel tube column connection joint;
High-strength bolt connection;
Seismic performance;
Finite element analysis

1. Introduction

In prefabricated steel structures, the mechanical behavior of column base connections is vital for structural integrity. These joints bear vertical and lateral loads. Traditional connection methods usually involve equal-strength welding and high-strength bolts[1-3]. Equal strength welding, with its strong integrity, still risks stress concentration and pre-existing defects at the welds[4-7]. The adoption of high-strength bolts in connections enhances the structural safety margin and reduces on-site installation duration, facilitating full assembly on-site[8,9].

In the current landscape of prefabricated steel structure design, column-to-column connection joints are primarily classified into flange connection joints [10-14] and sleeve-type connection joints [15-18]. Wang et al [10, 11] studied steel tube flange connections through experiment and finite element methods. A practical design method for circular steel tube flange joints was developed using the virtual work principle and T-shaped end plate model. Couchaux et al[12] conducted experimental investigations on 6 flange column connection joints, resulting in the development of an analytical model for the compression deformation of flange connection joints. This model incorporates considerations of the flange’s bending-torsional behavior and the opening-closing actions of the joints. Huang et al[13] experimentally and numerically studied two types of specimens: one for upper column base joints and another for lower column top joints. The study’s outcomes revealed that both specimens exhibited bending failure in the concrete column sections. Furthermore, the high-strength bolt flange connection specimen demonstrated hysteresis performance comparable to that of the steel tube full-length specimen, categorizing it as an “equal strength connection.” Zhang et al[14] thoroughly investigated beam-column to column flange joints in prefabricated steel structures, proposing design parameter adjustments for effective damage control. The results demonstrate that the proposed design optimizations can safeguard structures during extreme scenarios such as earthquakes, mitigate component failure, and facilitate rapid functional recovery. Flange-type column connection joints are crucial in prefabricated steel structures, and their appropriate design and construction are vital for ensuring structural safety and stability. In conclusion, flange connection joints exhibit a range of desirable attributes, including broad applicability, convenient installation and maintenance, and high levels of reliability. Nonetheless, further comprehensive research is required to enhance the understanding of the systematic testing and theoretical aspects of both flexible and rigid flange connection joints.

In the context of sleeve-type connection joints, Qiu et al[15] have investigated a flange splicing joint designed for the connection of tubular fiber reinforced polymer (FRP) components. Their research findings suggest that an insertion depth of 100mm for square steel tubes into FRP tubes is optimal, guaranteeing adequate bonding strength and load-bearing capacity. Chu et al[16] have introduced a novel double-flange sleeve-type column-column-beam connection joint. Combining experiments and simulations, their research examines how factors like axial compression ratio, sleeve wall thickness, and height affect joint seismic performance. Furthermore, simplified formulae were proposed to determine the yield and ultimate load-bearing capacities of this innovative connection joint. Wu et al[17] created a fully bolted joint for planar modular steel structures. The joint features square steel tube columns with built-in sleeves, connected to H-shaped beams using angle steels and plates. The study shows that the joint displays semi-rigid behavior, and using high-strength bolts for vertical joints and thicker angle steels improves its seismic resistance. Xia Junwu et al[18] conducted comprehensive experimental investigations on a novel spliced outer sleeve joint. The findings highlight the exceptional rotational capability of this joint, with the beam-column angle surpassing 0.06 radians, signifying a high level of flexibility. In conclusion, the advantages of sleeve connection joints are their straightforward construction and cost-effectiveness, which enhance the construction efficiency of light steel structures, achieve superior fastening outcomes, and facilitate full bolt connections in closed cross-sections. Dai et al. [19] developed an innovative insertion-type self-locking connection joint and conducted thorough experimental research on its performance. Drawing from their experimental findings, a simplified mechanical model was proposed and design recommendations for the joint were offered, aiding in its effective implementation. Lancy et al. [20] have introduced a novel modular interlocking connection joint designed for modular steel building structures. This joint integrates bolts with interlocking components, thereby enhancing construction efficiency and significantly improving the joint’s resistance to slippage. Sendanayake et al[21] introduced two types of modular joints with extra steel plates and elastic layers, aiming at transferring the potential failure points of the structure from the columns to the modules, facilitating elastic deformation of the interconnection joints.

Building on current research, this paper introduces a novel design for a fully bolted connection joint in square core tube square steel tube columns, which facilitates full assembly while ensuring structural stiffness and load-bearing capacity. This design represents an improvement over previous flange and sleeve connection methods, as it maintains structural integrity and load-bearing capacity while prioritizing full prefabrication and enabling rapid post-earthquake repairs. The study utilizes ABAQUS software to develop 14 finite element models, investigating how key parameters such as core tube strength, thickness, square steel tube strength, bolt type, and axial compression ratio influence the seismic performance of the proposed joint. The findings are anticipated to provide new insights for the advancement of prefabricated steel structures.

2. Joint design and working principle

2.1. Joint design

The prefabricated joint is consist of upper and lower square steel tubes, a square core tube equipped with external end plates, and high-strength bolts. An external end plate connects the upper and lower columns by high-strength bolts. A core tube within the column strengthens the joint, improving its bending and shear resistance. The construction of this connection joint is illustrated in Fig. 1.

2.2. Stress analysis and force transmission path

Analyzing the stress distribution at a 4% inter-story displacement reveals the vertical stress S33 distribution of the component, depicted in Fig. 2, and the horizontal stress S11 distribution, illustrated in Fig. 3. The vertical stress S33 distribution within the square core tube joint indicates that the bending moment is effectively converted into a tension-compression couple, which is transmitted through the column walls on either side. The couple passes through the bolt holes to the square core tube, then via its flange to the lower section, and along the core tube's wall to the column foot.

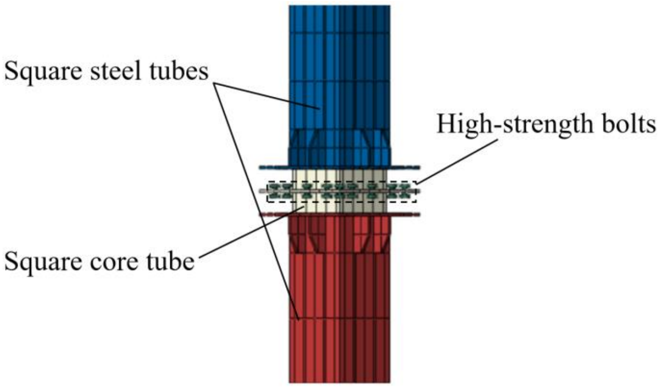

Fig. 1 Schematic of the square core tube square steel tube column fully bolted connection joint

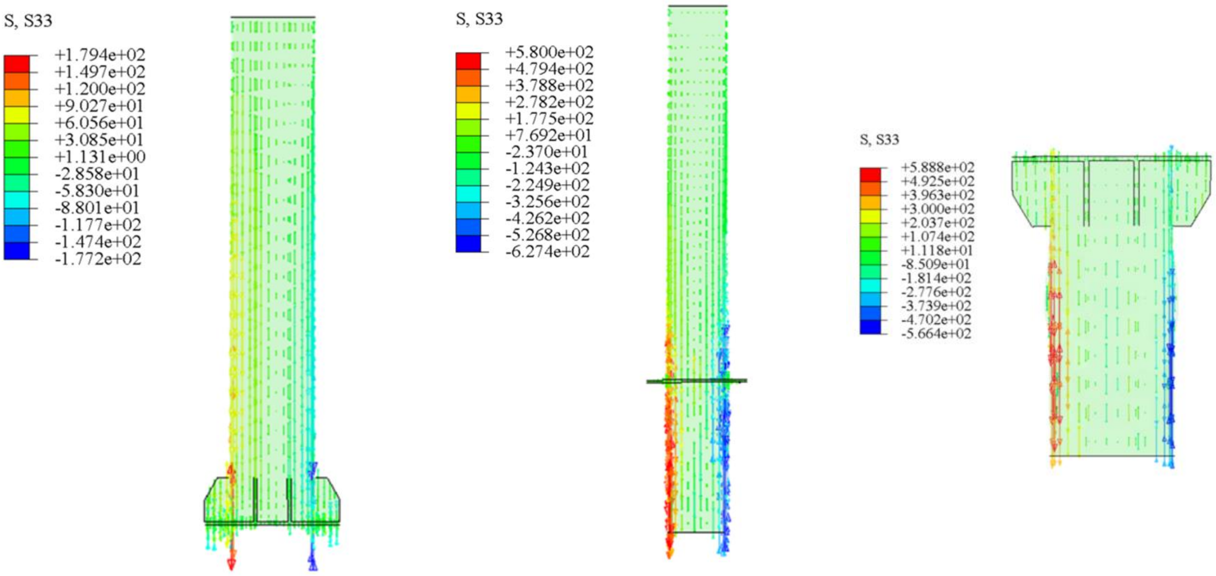

(a)S33 stress distribution of upper steel tube column (b)S33 Stress distribution of core (c)S33 stress distribution of lower steel tube column

Fig. 2 S33 Stress distribution of column

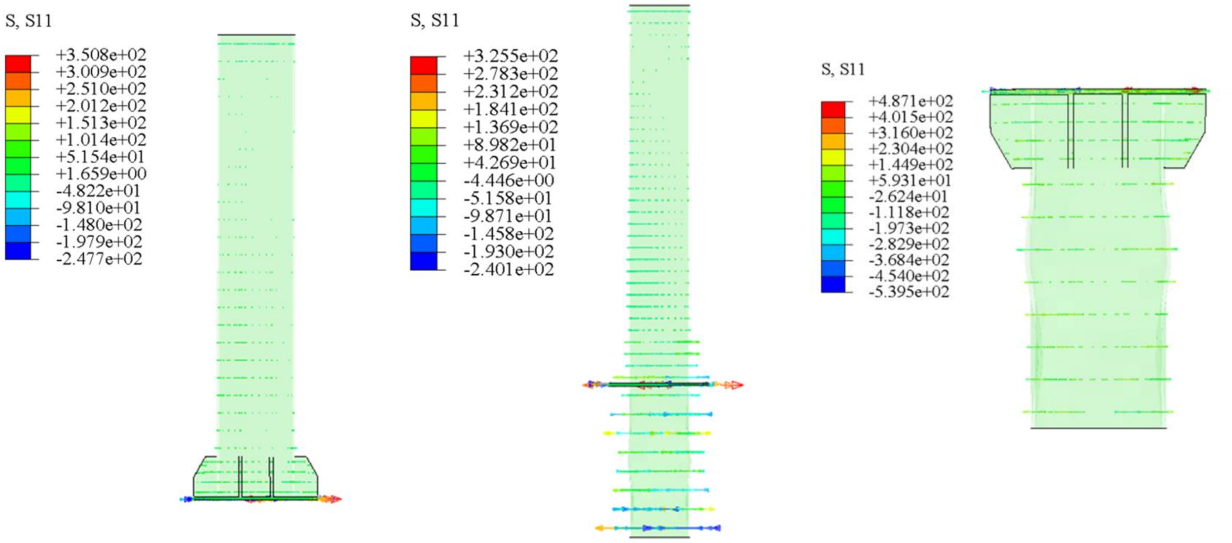

(a)S11 stress distribution of upper steel tube column (b)S11 Stress distribution of core (c)S11 stress distribution of lower steel tube column

Fig. 3 S11 Stress distribution of column

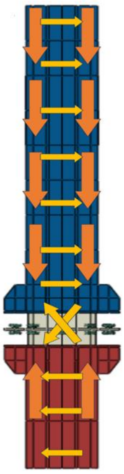

Fig. 4 Force transmission path

As shown in Fig. 3, the stress distribution at node S11 indicates that the horizontal shear force at the column top is transmitted through the upper steel tube to the bolt holes. This force is subsequently transmitted through the bolts to the square core tube wall, then to the lower steel tube wall, and continues its transmission along the column wall to the column base. Fig. 4 illustrates the force transmission path of the joint.

3. Model establishment

3.1. Model geometry

A total of 12 joint models have been designed across 4 groups, with comprehensive parameter details provided in Table 1. The first-floor column of the prototype structure, made from a 500mm×500mm×16mm square steel tube, stands at a height of 4200mm. Fig. 5 shows the detailed dimensions of the column base joint.

Additionally, the core tube inside the joint serves to increase the stiffness of the column's joint area. The core tube's dimensions must be chosen based on the balance between its bending strength and that of the outer steel tube to prevent joint interface damage.

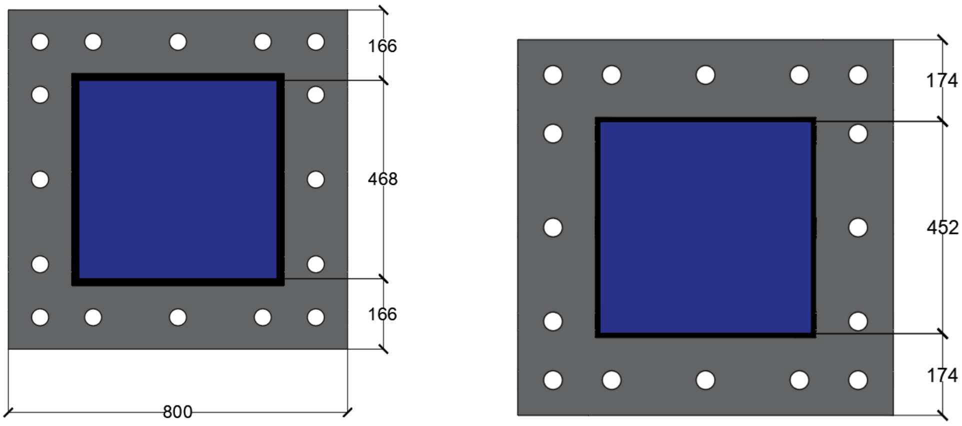

(a)Details of column dimensions (b)Details of core tube dimensions

Fig. 5 Section sizes of core tube components(mm)

Table 1
Details of joints parameters (mm)

Model No.	Steel tube size(mm)	Core tube size(mm)	Steel tube grade	Core tube frade	Axial compression ratio	Bolt type
JD-1	500×500×16	468×468×10	Q355	Q235	0.3	M24
JD-2	500×500×16	468×468×10	Q420	Q235	0.3	M24
JD-3	500×500×16	468×468×10	Q460	Q235	0.3	M24
JD-4	500×500×16	468×468×10	Q355	A6061	0.3	M24
JD-5	500×500×16	468×468×10	Q355	LY160	0.3	M24
JD-6	500×500×16	468×468×10	Q355	Q355	0.3	M24
JD-7	500×500×16	468×468×10	Q355	LY160	0.2	M24
JD-8	500×500×16	468×468×10	Q355	LY160	0.4	M24
JD-9	500×500×16	468×468×10	Q355	LY160	0.5	M24
JD-10	500×500×16	468×468×10	Q355	LY160	0.6	M24
JD-11	500×500×16	468×468×12	Q355	LY160	0.3	M24
JD-12	500×500×16	468×468×14	Q355	LY160	0.3	M24
JD-13	500×500×16	468×468×10	Q355	Q235	0.3	M27
JD-14	500×500×16	468×468×10	Q355	Q235	0.3	M30

The design choices for the strength ratios, axial compression, and thickness ratios of the column and core tube, as well as the selection of bolt sizes, are the result of a meticulous engineering process aimed at optimizing the joint's structural performance, safety, and cost-effectiveness. The strength ratio of the column to the core tube, ranging from 1 to 4.4, is carefully selected to ensure that the column can withstand the expected loads without excessive material use, while also providing a sufficient safety margin against failure. This range allows for a graduated response to varying load conditions, preventing over-strength columns that could be unnecessarily costly and heavy. The core tube's strength ratio to the column, varying between 0.22-1, is set to ensure that the core tube contributes adequately to the overall stiffness and load-bearing capacity of the joint, without being so strong as to be wasteful or so weak as to become a potential point of failure. The axial compression ratio, which spans from 0.2 to 0.6, is chosen to maintain a balance between the column's ability to resist compressive forces without experiencing buckling and its capacity to support the joint's weight and environmental loads. This range provides a buffer against both the risks of structural collapse and the potential for excessive deformation that could affect the joint's functionality. The column to core tube thickness ratio, established between 0.625 and 0.875, is a critical parameter that influences the joint's performance and the overall efficiency of the structure. This ratio ensures that the core tube is sufficiently thick to provide the necessary strength and stiffness while avoiding the use of excessive material, which could increase the structure's weight and cost. The selected range is a balance between structural requirements and economic considerations. Finally, the use of bolts sizes M24 to M30 for the connections between the column and core tube is a design choice that takes into account the mechanical properties of the fasteners, such as tensile strength and shear capacity. These bolt sizes are commonly used in structural applications and offer a range of options that can be tailored to the specific load requirements at each joint, ensuring that the connections are neither under-strength, which could compromise safety, nor over-strength, which could lead to unnecessary costs and complications during construction. The selection of bolt sizes is also influenced by the ease of installation, the availability of materials, and the potential for future maintenance or modifications to the joint.

3.2. Element type and meshing

The finite element model incorporates C3D8R solid elements for all components, with considerations for integration and hourglass effect[22]. To account for the complex forces present at the joint, the mesh in the flange area is densified to ensure the accuracy of the analysis data. Smaller mesh sizes are employed for high-strength bolts and core tubes during mesh generation, with the mesh size for high-strength bolts set at 10mm and that for core tubes at 20mm. The model components are shown in Fig. 6.

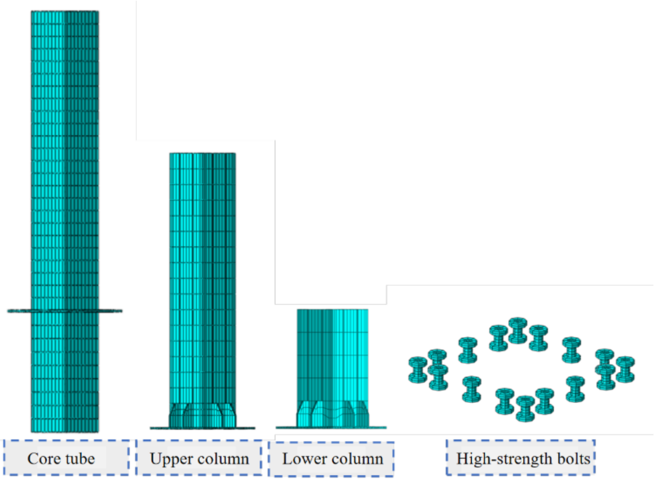

Fig. 6 Meshing

3.3. Constitutive models

The steel material's elastic modulus is taken as Es=2.06×105 N/mm^2, poison ratio is 0.3. The constitutive model of high-strength bolt adopts multi-linear isotropic strengthening model[23]. The nominal value of 10.9 grade high strength bolt is adopted as $f_y = 980\ MPa$、$f_u = 1100MPa$。The constitutive model for ordinary strength steel and low yield strength steel utilize the framework proposed in literature [24], which incorporates plateau and hardening segments. An initial 100kN pre-tightening force is applied to the bolt, then increased to 240kN for model convergence. Subsequently, the bolt rod dimensions are maintained at their current lengths throughout the analysis steps, ensuring that the bolt pre-tightening force adjusts dynamically with the model's displacement response.

3.4. Boundary conditions and loading approach

Fig. 7 illustrates the specific configurations for contact and boundary conditions of the model, the interaction between the bolt, nut, and the steel tube and core tube is characterized by "hard contact". Additionally, the tangential interaction among these components adopted coulomb friction model[2], with a specified coefficient of friction of 0.45. To ensure a fully rigid connection at the column foot, fixed boundary conditions are implemented at this location. The high-strength bolt connections are restrained to prevent lateral instability of the components. A coupled reference point is positioned at the column top, through which both horizontal and vertical loads are applied, with a compressive load of 0.3 times the column's axial compression ratio applied at the top.

Following AISC seismic specifications, a displacement-controlled variable amplitude loading method is used for horizontal loading. Each loading level encompasses two cycles, with the levels progressively increasing to 0.00375, 0.005, 0.0075, 0.01, 0.02, 0.03, and 0.04 rad. The loading protocol is outlined in Fig. 8 for clarity.

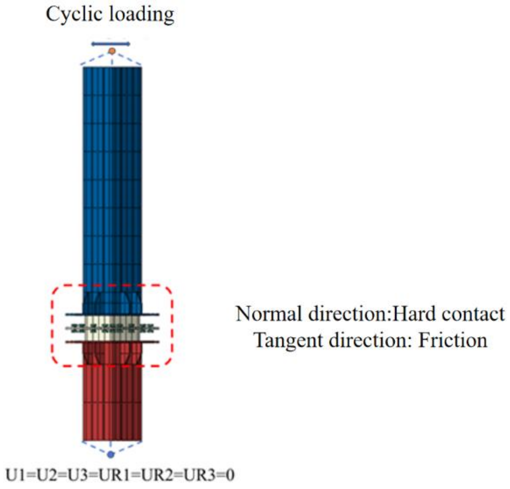

Fig. 7 Boundary conditions

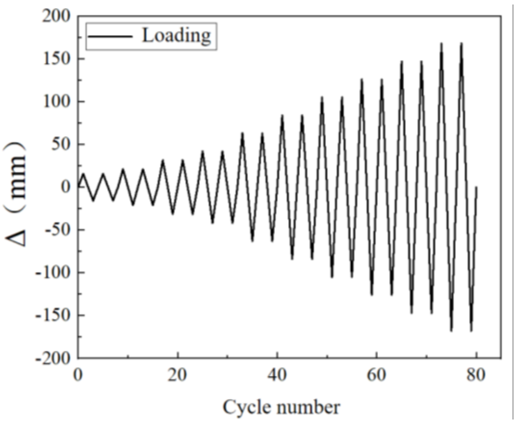

Fig. 8 Loading system

4. Model validation

4.1. Failure mode

To verify the finite element model's accuracy, a comparative simulation analysis was conducted using the test case from literature [25]. The test joint configuration in the referenced literature closely mirrors that of the joints in the present study, with the element selection and mesh division in the validation model aligning with those reported above. Fig. 9 compares the failure modes in the finite element simulation with the experimental results from the literature.

The joint underwent cyclic loading as described, reaching a 7% inter-story displacement. Fig. 9 shows a significant bulge in the eastern steel tube wall at the column base, which is in substantial agreement with the column wall bulging observed in the experimental setup.

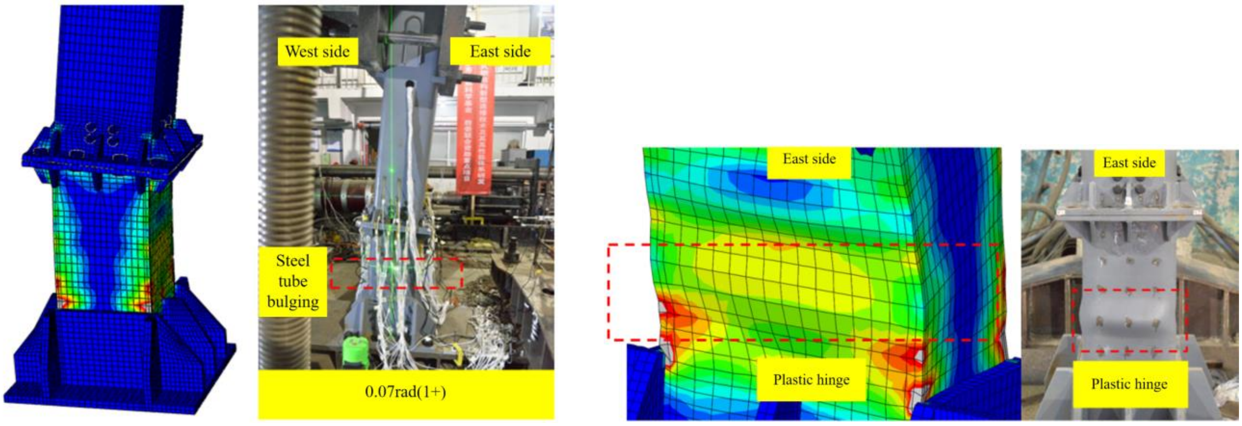

Fig. 9 Comparison of failure mode

4.2. Verification of hysteresis curves and skeleton curves

Fig. 10 provides a comparative analysis of the hysteresis and skeleton curves of experiment and simulation results. Fig. 10 illustrates that the hysteresis and skeleton curves from the finite element analysis closely align with the experimental results, particularly in the aspect of initial stiffness. The finite element analysis reveals that the positive and negative peak bearing capacities from the model are lower than the experimental results by approximately 7.1% and 9.8%, respectively, with both differences falling within a 10% margin. The results suggest that the finite element modeling approach employed is effective in simulating the mechanical properties of proposed joint under cyclic load conditions.

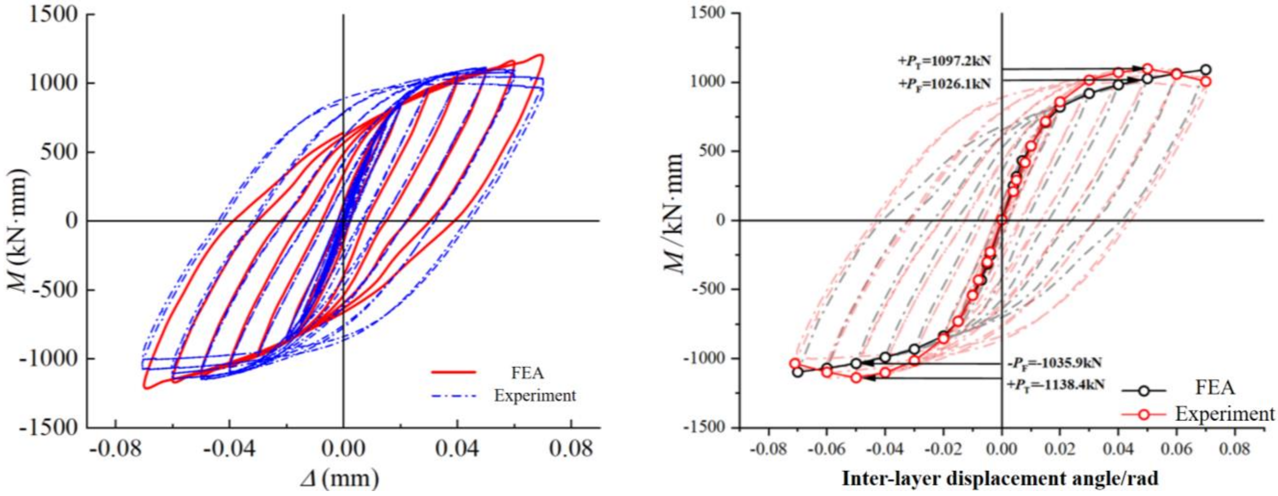

(a) Hysteresis curves

(b) Skeleton curves

Fig. 10 Comparison of calculation results

5. Mechanical performance of core tube

5.1. Failure mode

Fig. 11 displays the equivalent plastic stress contours for various parameters at a 4% inter-story displacement angle, revealing significant bulging in the steel tube column walls at the column foot. This observation indicates the potential for local deformation and failure under seismic loads, highlighting the need for robust design and construction practices to prevent such issues.

The relationship between the grade upgrade of the square steel tube and the corresponding increase in plastic stress levels at the column foot, as shown in Fig. 11(a), suggests that material selection is crucial. Higher-grade materials can withstand greater stresses but may also be more prone to brittle failure. Therefore, a balance must be struck between material strength and ductility to ensure the joint's performance under seismic events.

Fig. 11(b) demonstrates that with the increase in core tube strength, the plastic stress level at the column foot decreases. This finding implies that strengthening the core tube can enhance the joint's overall seismic performance. It suggests that optimizing the core tube's design, rather than simply increasing the strength of the square steel tube, may be a more effective strategy for improving joint performance.

The axial compression ratio's significant effect on the mechanical properties of the joints, as highlighted in Fig. 11(c), indicates that proper consideration of this parameter is essential. A higher axial compression ratio increases the vertical load on the column, which can lead to higher stress concentrations and potential failure modes. The axial compression ratio should be carefully evaluated in the designing process to ensure the joint can safely withstand expected loads.

Fig. 11(d) emphasizes the importance of the core tube thickness and bolt model in enhancing the joint's performance. Increasing the core tube thickness improves its contribution to the square steel tube column, while upgrading the bolt model increases the bolt pre-tension force, improving the stress level at the column base. However, the modest influence of the bolt model upgrade on seismic performance suggests that other factors, such as material selection and joint geometry, may have a more significant impact.

In summary, the strength ratio of the square steel tube column in relation to the core tube, as well as the thickness ratio of the core tube to the square steel tube, significantly affect the plastic stress levels at the column foot in column-to-column connection joints. The understanding of these relationships is crucial for designing joints that can withstand seismic loads and prevent failure modes such as local deformation, brittle failure, and stress concentrations. Considerations of these factors and ensure proper reinforcement and detailing to enhance the joint's overall performance and safety are needed in the practical designing.

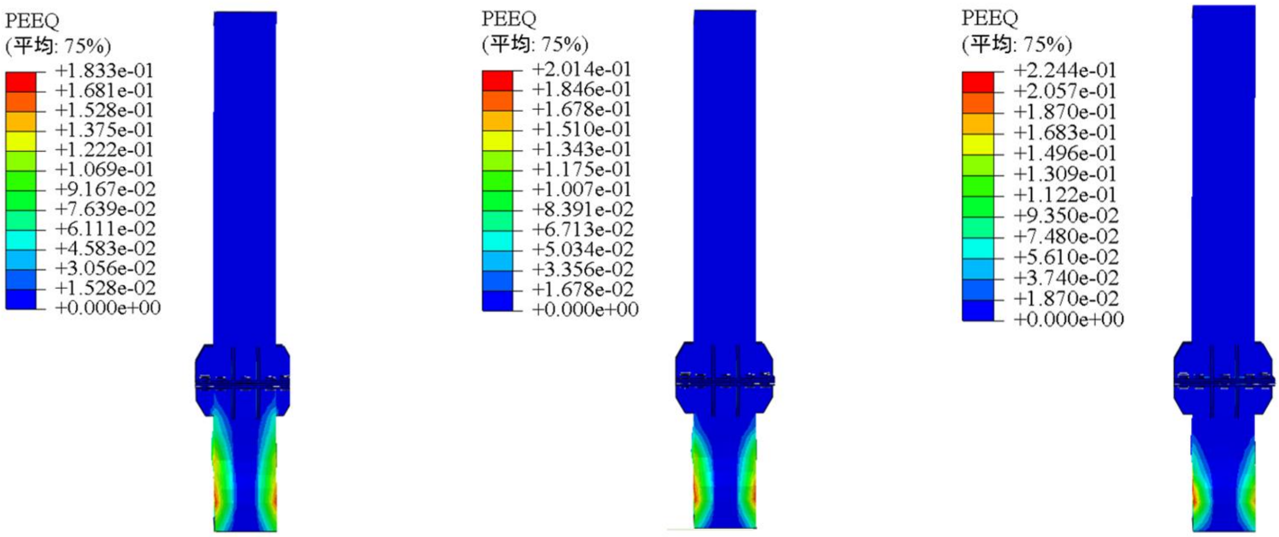

(a)Comparison of JD-1, JD-2, JD-3

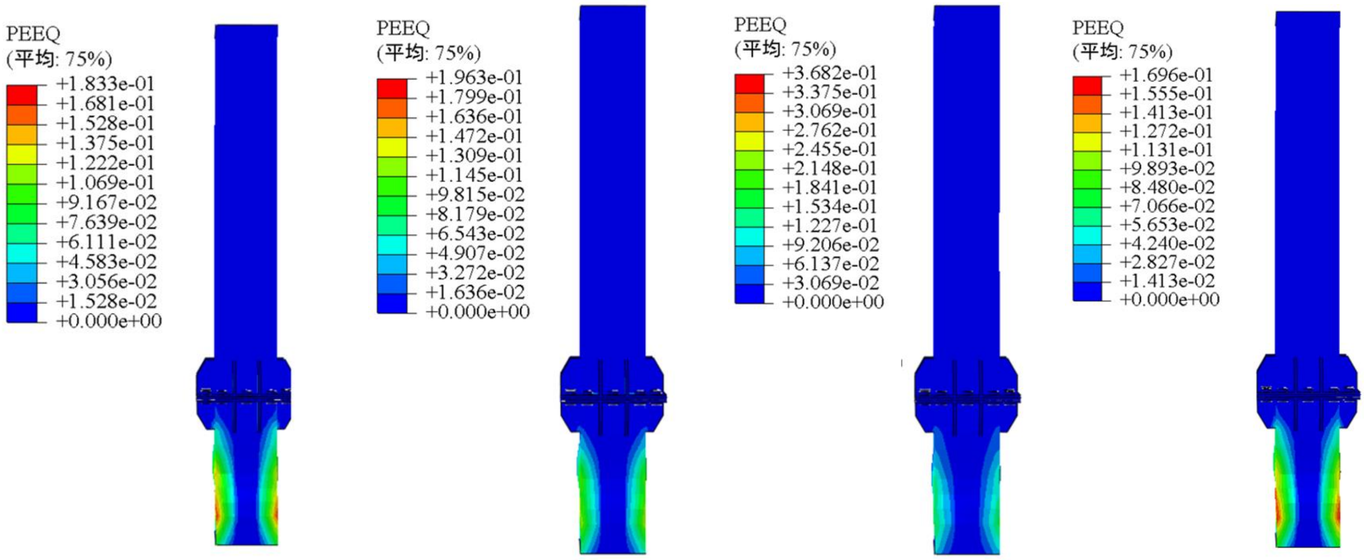

(b)Comparison of JD-1, JD-4, JD-5,JD-6

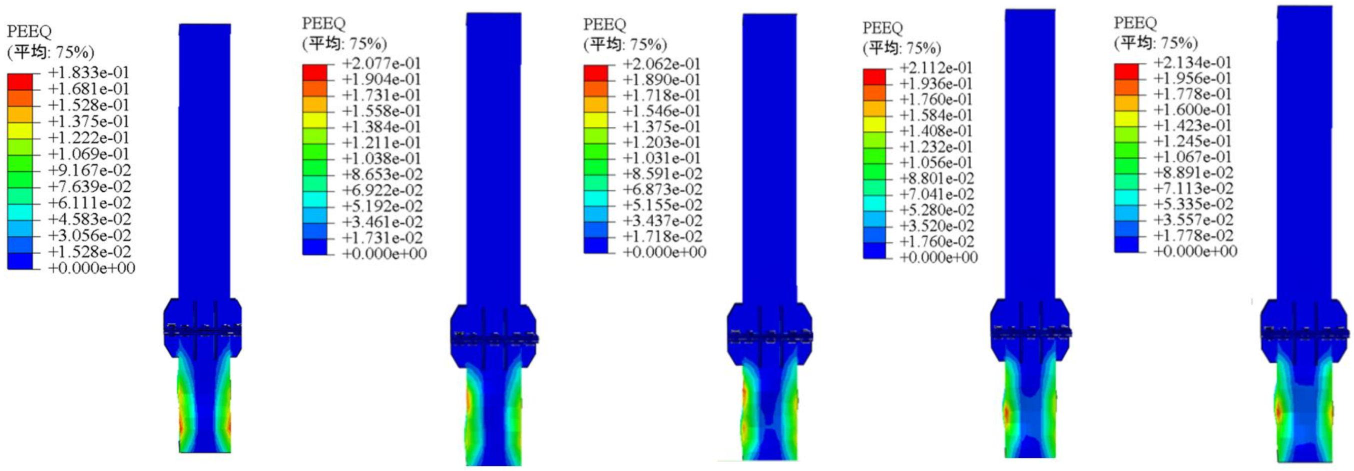

(c)Comparison of JD-1, JD-7, JD-8,JD-9, JD-10

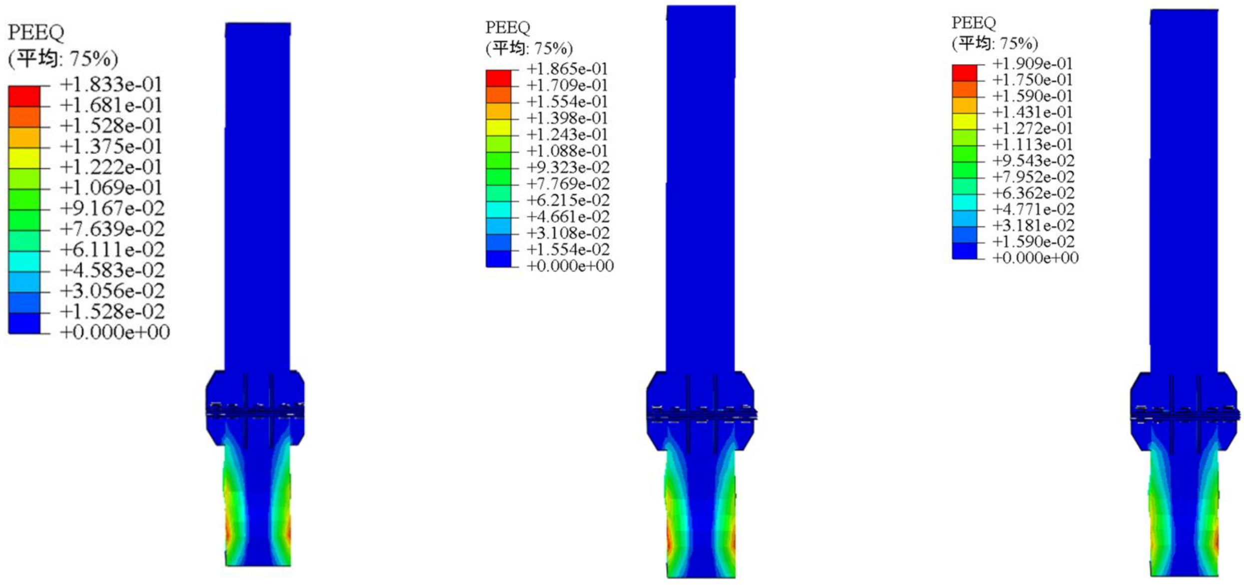

(d)Comparison of JD-1, JD-11, JD-12

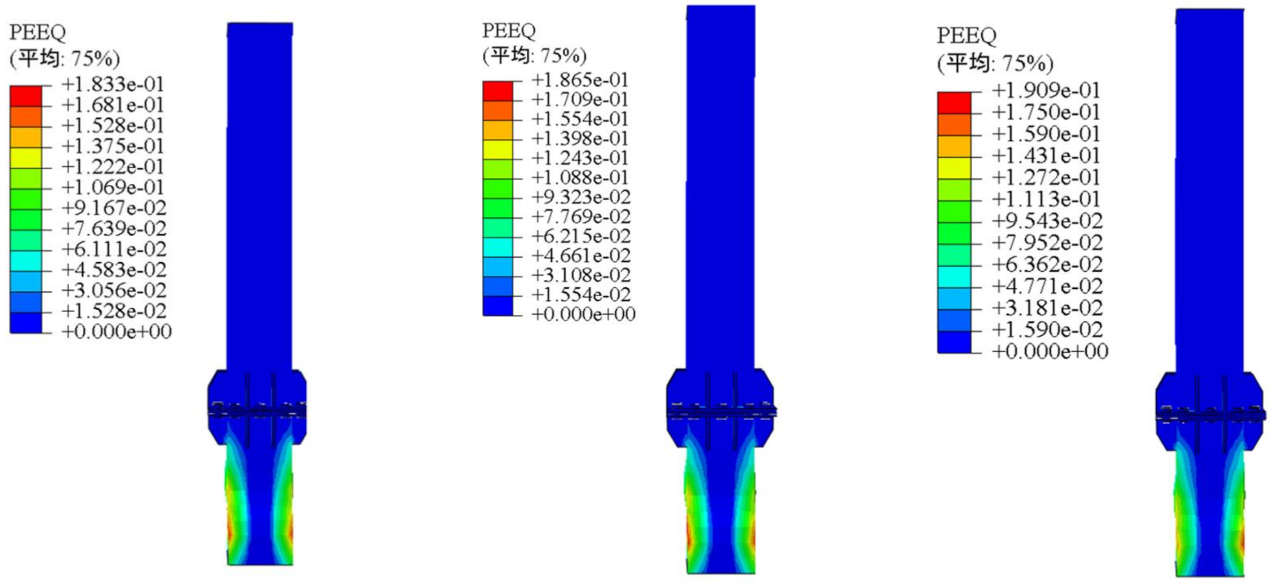

(e)Comparison of JD-1, JD-13, JD-14

Fig. 11 Comparison of equivalent plasticity

5.2. Stress analysis

Fig. 12 presents the stress diagram obtained from the lower column's S1 path. It is observed that the column base undergoes yielding with stresses above 355 MPa. As the strength ratio of the square steel tube relative to the core tube increases, there is a corresponding increase in stress at the column base, with the impact remaining within a 10% range. As illustrated in Fig. 12(c), the stress at the column base increases continuously with the axial compression ratio, with the increment ranging from 11% to 24%. Furthermore, Figs. 12(d) and 12(e) demonstrate that under a 4% inter-story drift, the thickness ratio between the column and core tube and the bolt model exert a relatively small effect on the stress at the column foot, within a 5% limit.

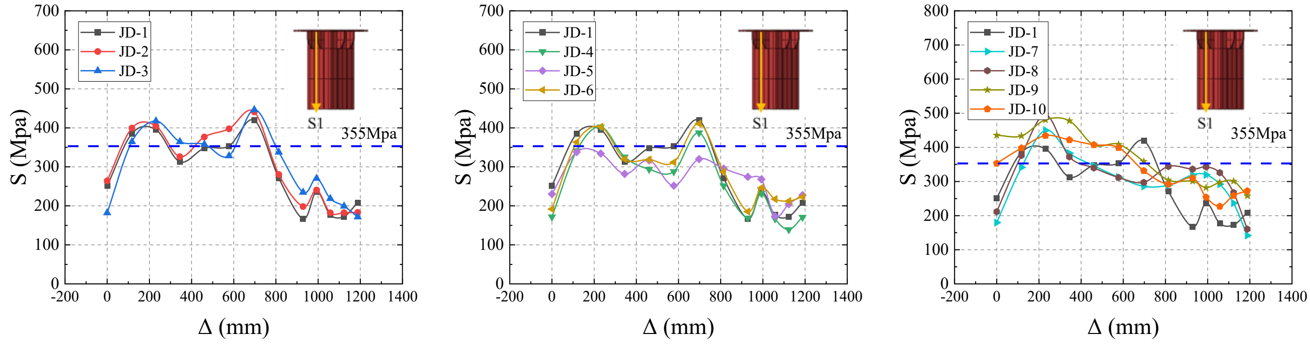

(a)

(b)

(c)

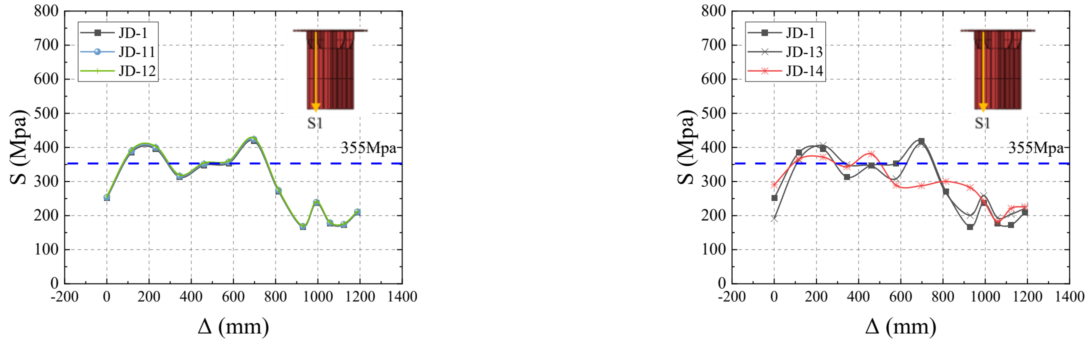

(d) (e)

Fig. 12 Stress analysis

5.3. Hysteresis performance

Fig. 13 displays the hysteresis curves for models JD1-JD14. It is apparent from the figure that these curves are robust and exhibit no significant pinching phenomena, indicating that the connection joints possess a high capacity for energy dissipation. The strength ratio of the column to the core tube, as shown in Fig. 13(a), directly effects the bearing capacity and the completeness of the hysteresis curves. This suggests that strengthening this ratio effectively improve the hysteresis performance of the joints. In Fig. 13(b), the models' ultimate bearing capacity increases with the core tube-to-column strength ratio, highest when strengths match. Fig. 13(c) shows joint capacity reduction with axial compression ratio, 21% less at 0.6 than 0.3, recommending a ratio between 0.3 and 0.5. Figs. 13(d) and 13(e) suggest minimal influence of thickness ratio and bolt preload force on joint properties.

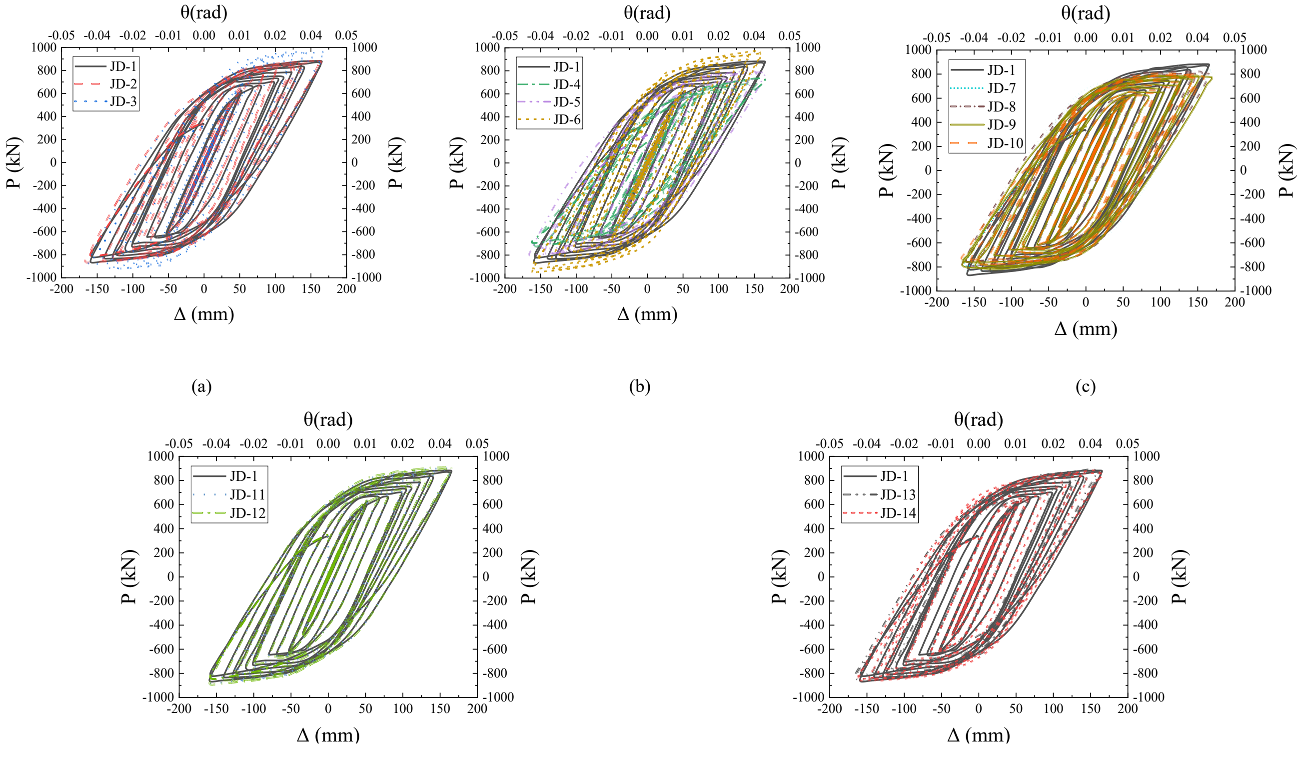

(a) (b) (c)

(d) (e)

Fig. 13 Comparison of hysteresis curves

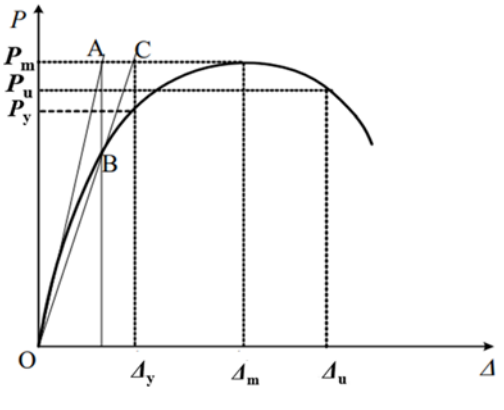

Fig. 14 Schematic of determining yield point by yield moment method

5.4. Skeleton curves

In accordance with the guidelines provided in the JGJ101-2015 code [26], it is essential to accurately determine the yield load, yield displacement, failure load, and failure displacement for the column-to-column connection joints. The yield load is ascertained through the application of the yield moment method. In Fig. 14, a tangent line, labeled OA, is drawn on the initial segment of the skeleton curve. Additionally, a horizontal line is constructed at the peak of the curve. The intersection of OA with the horizontal line occurs at point A. A perpendicular line is then drawn through point A, intersecting the skeleton curve at point B. By connecting points OB and extending this line to intersect the horizontal line at the peak, the x-coordinate at this intersection, point C, denotes the yield displacement(Δ_y), the y-coordinate of the skeleton curve indicates the yield load(P_y). The coordinates of the peak point denote the ultimate load(P_m) and ultimate displacement(Δ_m). The coordinate values corresponding to 0.85 times the P_m are designated as the failure load P_u and the failure displacement Δ_u. This facilitates the identification of the characteristic points on the $P-\Delta$

relationship curve.

Fig. 15 presents the skeleton curves for the various models studied. The initial stiffness remains stable despite variations in the column to core tube strength ratio, axial compression ratio, column thickness ratio, and bolt model. However, the strength ratio of the core tube to the column notably influences the initial stiffness of the specimens. A significant change in stiffness is observed at a 1% inter-story displacement angle, with stiffness decreasing progressively as the inter-story displacement angle increases. Following the peak load, there is a decreasing trend in the load as displacement continues to increase.

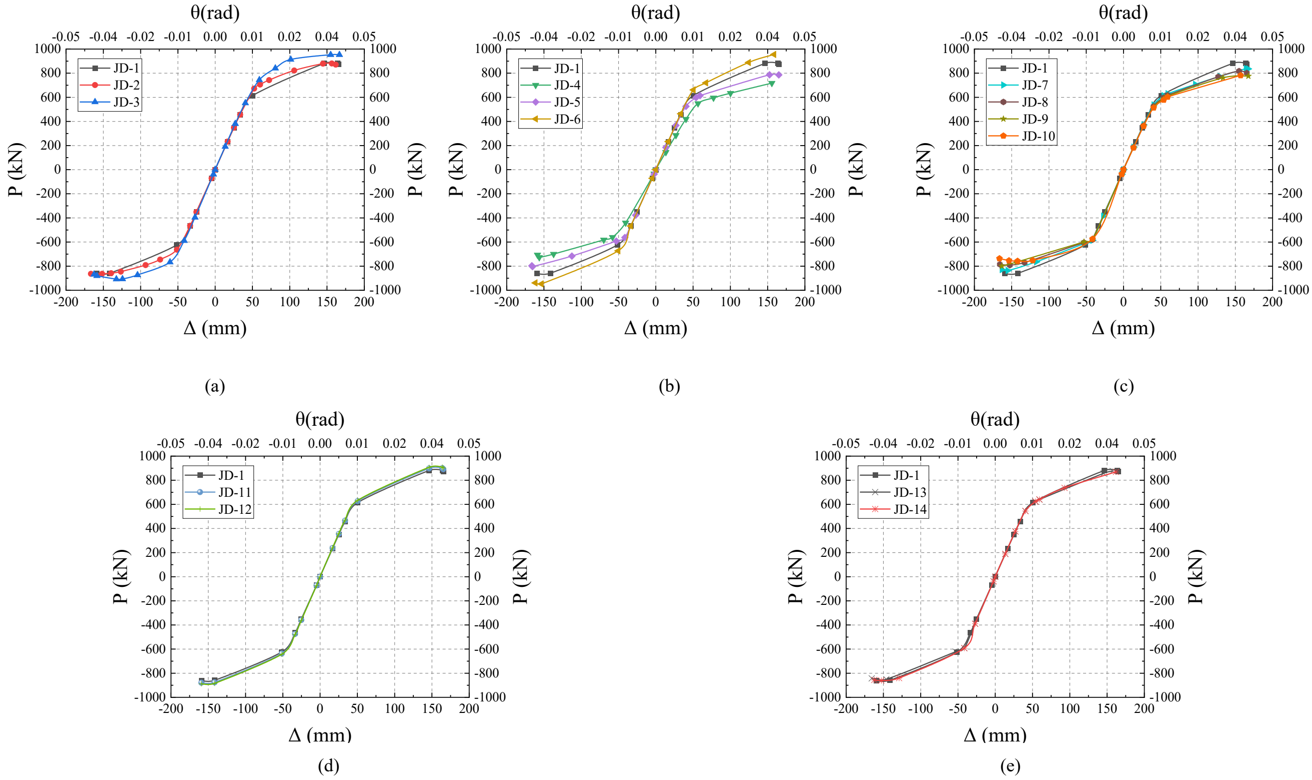

(a) (b) (c) (d) (e)

Fig. 15 Comparison of skeleton curves

5.4.1. Load capacity

A detailed comparison of the structural integrity of different models has been carried out, with a focus on parameters such as stiffness, ductility, and inter-story displacement angle. This analysis is based on the calculation results of key mechanical indicators from the skeleton curve, as detailed in Table 2. The data illustrates that as the ratio of column strength to core tube strength increases, there is a noted enhancement in the yield bearing capacity of the model by 6.71% and 9.05%, respectively. Conversely, the ultimate bearing capacity experiences a decrease of 1.14% and 1.17%. This trend indicates that an escalation in the column to core tube strength ratio is inversely proportional to the model's overall bearing capacity. As the column to core tube strength ratio increases, the model exhibits varying degrees of change in yield bearing capacity, including a decrease of 2.58%, an increase of 2.32%, and a substantial increase of 27.87%. Conversely, the ultimate bearing capacity shows a significant reduction, with decreases of 24.48%, 17.19%, and 0.51%. As the axial compression ratio of the model increases, the yield bearing capacity progressively enhances by 10.92%, 8.85%, 5.17%, and 4.48%. Conversely, the ultimate bearing capacity undergoes a significant reduction, with decreases of 11.87%, 13.98%, 18.33%, and 21.95%. To ensure optimal structural integrity, maintaining the axial compression ratio within the range of 0.3 to 0.5 is recommended. In addition, as the thickness ratio of the core tube to the columns increases, the model's yield bearing capacity is notably enhanced, with increases of 2.34% and 19.96% observed. Furthermore, an increase in the bolt pretension force leads to improvements in yield bearing capacity by 15.51% and 16.42%.

The analysis reveals intricate trends in the seismic performance of the joint, with the column to core tube strength ratio showing a significant influence on the yield bearing capacity, which enhances as the ratio increases. However, this comes at the expense of a decrease in the ultimate bearing capacity, indicating an inverse relationship. The axial compression ratio also plays a critical role, with an increase leading to enhanced yield bearing capacity but a notable reduction in ultimate bearing capacity, suggesting a balance is necessary for optimal structural integrity. Furthermore, the thickness ratio of the core tube to the columns emerges as a more influential factor than the bolt pretension force, with increases in this ratio resulting in substantial improvements in yield bearing capacity. Although the bolt pretension force has a moderate impact, it still contributes to enhancements in yield bearing capacity. The findings underscore the importance of carefully considering these design parameters to achieve the desired balance between yield and ultimate bearing capacities, ensuring the safety and integrity of the structure under seismic conditions.

Table 2
Key mechanical indicators

Model No.	Loading direction	Yield capacity Py （kN）	Ultimate capacity Pu （kN）	Yield displacement Δ_y (mm)	Displacement ductility coefficient μ	Yield displacement angle θ_y
JD-1	+	607.8	950.2	53.99	2.92	1/78
JD-2	+	648.6	939.4	55.68	2.87	1/75
JD-3	+	662.8	933.7	59.27	2.66	1/71
JD-4	+	592.1	717.6	51.92	3.04	1/81
JD-5	+	621.9	786.9	54.31	2.91	1/77
JD-6	+	777.2	955.0	56.71	2.79	1/74
JD-7	+	674.2	837.4	50.42	3.13	1/83
JD-8	+	661.6	817.4	48.99	3.23	1/86
JD-9	+	638.6	776.0	43.06	3.67	1/98
JD-10	+	635.0	741.6	41.74	3.79	1/80
JD-11	+	622.0	900.2	54.12	2.92	1/78
JD-12	+	729.1	909.0	54.28	2.91	1/77
JD-13	+	702.1	875.8	53.85	2.93	1/78
JD-14	+	707.6	869.5	52.70	3.00	1/80

5.4.2. Ductility and inter-story displacement angle

The ductility of a structure is commonly assessed using two key parameters: the displacement ductility coefficient and the rotation ductility coefficient. The displacement ductility coefficient μ can be calculated with Eq. (1), where Δ_u and Δ_y are displacements of the column ends when structure fails:

$$\mu = \Delta_u / \Delta_y \tag{1}$$

Utilizing the data for yield and failure displacements from Fig. 15, the coefficient is computed in accordance with Eq. (1), with the comprehensive results presented in Table 2. In compliance with GB50011-2010 code, the permissible elastic displacement angle for steel structures is 1/250. The results presented in Table 2 indicates that the positive yield displacement angles for the integrated square core tube joints fall within the range of 1/71 to 1/98, adhering to the code's requirements for elastic inter-story displacement angles.

The data presented in Table 2 indicates that the ductility coefficients for the models with various parameters span from 2.66 to 3.79. Notably, the strength ratio of the columns to the core tube has a significant influence on the model's ductility, with a range of variation from 2.66 to 2.92. It is recommended that the strength ratio of the columns to the core tube be maintained within the range of 1.5 to 1.78. The continuous increase in the core tube's strength leads to a decrease in the model's ductility and deformation capacity. Consequently, it is suggested that the strength ratio of the core tube to the columns be no greater than 0.66. The axial compression ratio's increase is observed to enhance the model's ductility coefficient, while factors such as the thickness ratio of the core tube to the columns and the bolt pretension force type exert a relatively minor impact on the mechanical properties of the joints.

5.5. Energy dissipation capacity

The column base joint, when subjected to seismic forces, must exhibit a high capacity for energy dissipation, primarily through the plastic deformation of its components. This research employs the cumulative energy dissipation of hysteresis loops to conduct a quantitative analysis of the joint, as depicted in Fig. 16 and detailed in Eq. (2):

$$E = \frac{S_{(\mathrm{ABC+CDA})}}{S_{(\mathrm{OBE+ODF})}} \tag{2}$$

In which：

$S_{(ABC+CDA)}$ - area encompassed by the hysteresis loop at each load level, corresponding to the energy dissipation value at the joint.

$S_{(\mathrm{OBE+ODF})}$ -the area encompassed by the triangles OBE and ODF during one loading cycle.

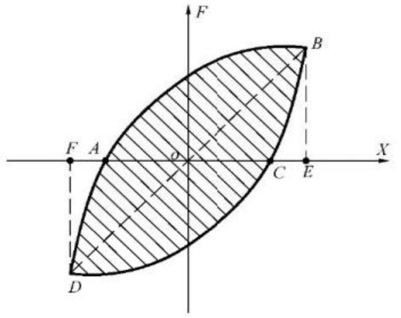

Fig. 16 Energy dissipation coefficient calculation diagram

Fig. 17 depicts the cumulative energy dissipation for the various models examined. It is evident that as the strength ratio of the columns to the core tube increases, there is a corresponding decrease in the model's cumulative energy dissipation. Compared to the JD-1 model, the cumulative energy dissipation for JD-2 and JD-3 is reduced by 4.2% and 6.8%, respectively. Contrarily, the analysis reveals that an increase in the strength ratio between the core tube and the column results in a significant enhancement of the joint's cumulative energy dissipation, with increases of 21.6%, 3.1%, and 2.2% observed relative to JD-1. This emphasizes the critical role of the core tube in energy dissipation within column-to-column connections and underscores the importance of the core tube's strength as a key parameter affecting the seismic resilience of proposed joints. Therefore, it is recommended to maintain the strength ratio of the core tube to the columns no less than 0.22. The analysis further reveals that the energy consumption ratio of the models initially increases and then decreases with the rising axial compression ratio. Consequently, it is advisable to maintain the axial compression ratio within the range of 0.3 to 0.5 for optimal performance. Additionally, the analysis indicates that the thickness ratio of the core tube to the columns has a negligible effect on the cumulative energy dissipation, with variations within a 3% range. Hence, this ratio can be determined based on specific structural design requirements. Furthermore, the models exhibit a decrease in cumulative energy dissipation during early loading stages as bolt strength increases. However, at a displacement angle of 4%, the cumulative energy dissipation among all models remains consistent, suggesting that while the bolt type significantly influences the initial energy dissipation, its effect on the model's behavior during the plastic-elastic phase is relatively minor.

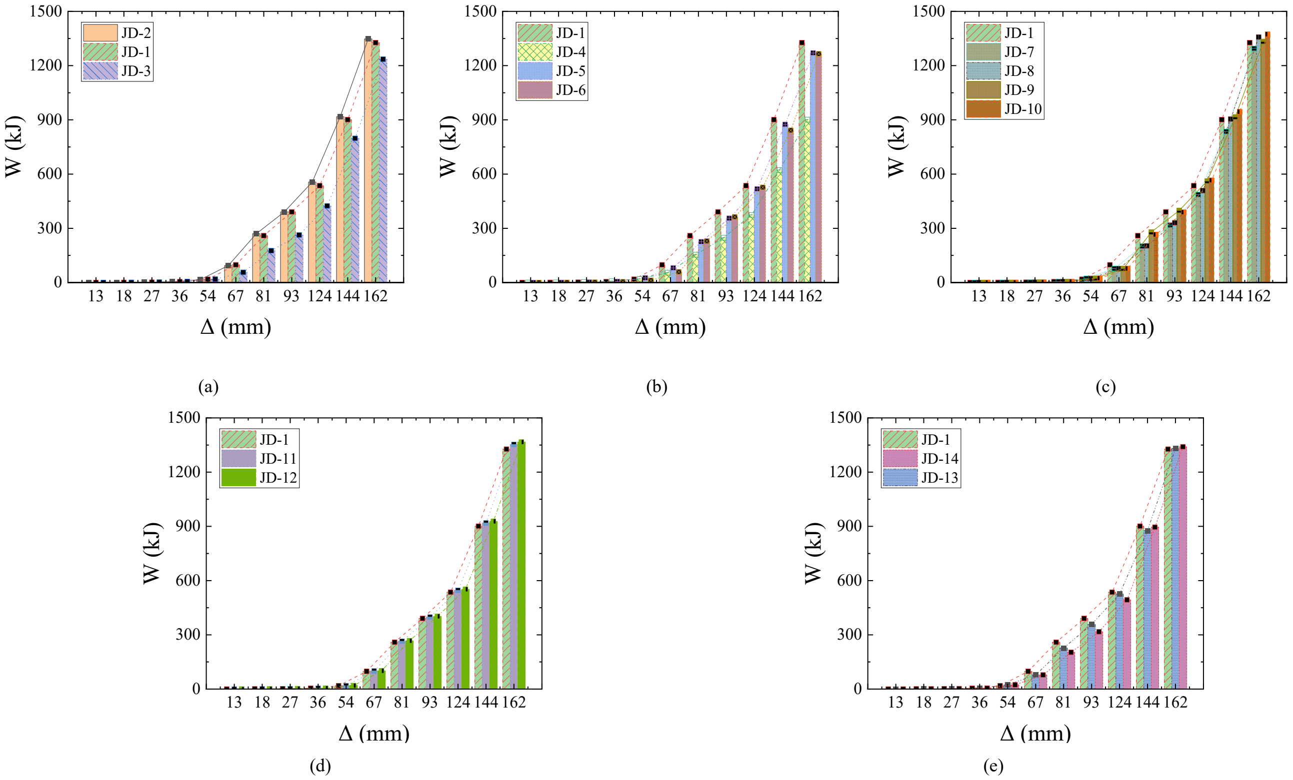

(a) (b) (c) (d) (e)

Fig. 17 Cumulative energy dissipation

5.6. Stiffness degradation

Upon the occurrence of damage within a structure or component, the $P-\Delta$ curve transitions from linear growth to a pattern of diminishing bearing capacity increments. Concurrently, the structural or component stiffness exhibits signs of degradation. The reduction in stiffness serves as a reflection of the cumulative damage progression within a structure, prompting the utilization of the stiffness degradation curve in this study to assess the seismic performance of column-to-column joints. The present work employs the secant stiffnessK_i, as recommended by the standard, to quantify the stiffness degradation of the joints with an integrated square core tube. This secant stiffness is defined as the slope of the line joining the peak load points under the same level of cyclic loading, with the calculation formula detailed in Eq. (3).

$$K_i = \frac{|+F_i|+|-F_i|}{|+\Delta_i|+|-\Delta_i|} \tag{3}$$

In which：

F_i-The peak load during the ith cycle of loading

Δ_i-The displacement value associated with the peak load during the ith cycle of loading

K_i-The secant stiffness for the ith cycle

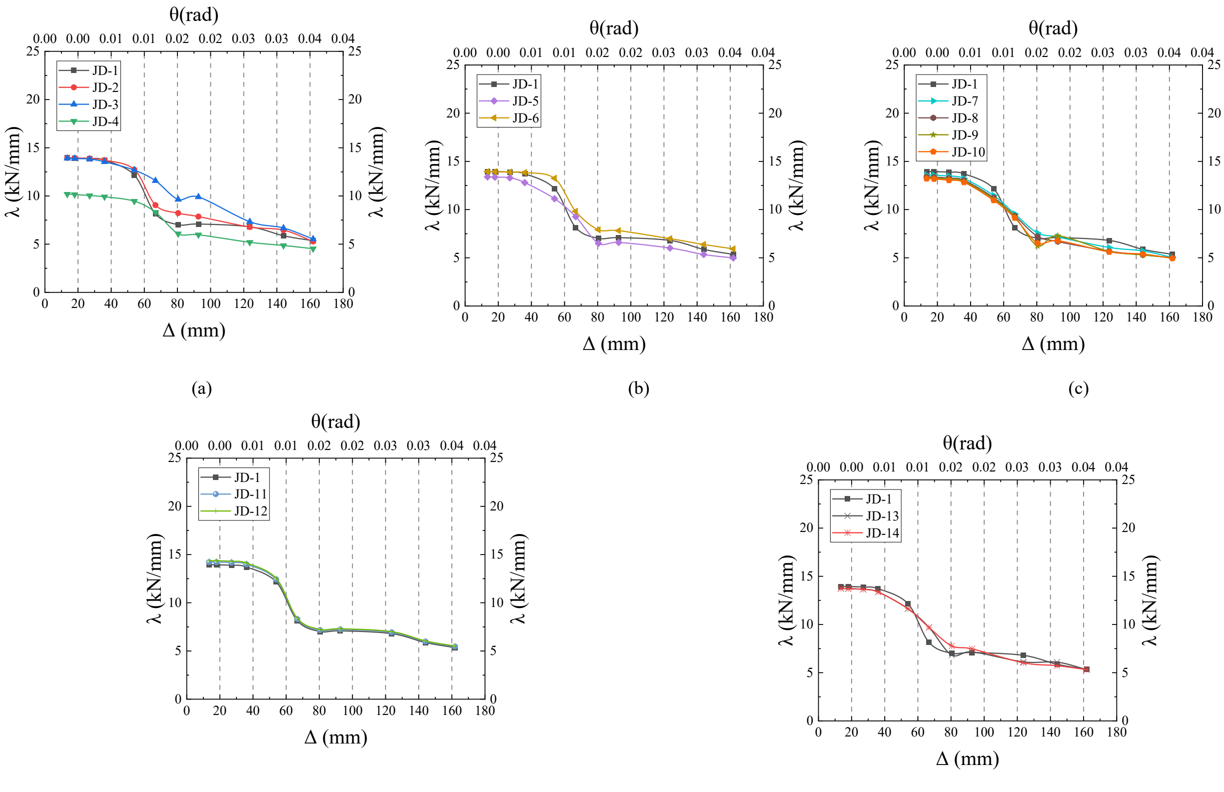

(a) (b) (c)

(d) (e)

Fig. 18 Stiffness degradation comparison

Fig. 18 illustrates the stiffness degradation of each joint. It is obvious that prior to the 1% displacement angle, the stiffness of the models remains largely unchanged, indicating no significant degradation. However, beyond this threshold, a notable decline in stiffness is observed, with a reduction of 27% to 43%. The main factors influencing stiffness degradation include the strength ratio between the core tube and the column, the axial compression ratio, and the bolt pre-tension force. Conversely, the thickness ratio of the core tube to the columns has a lesser effect.

6. Conclusions

The study introduces a square core tube square steel tube column fully bolted connection joint, elaborating on the design principles and assembly process. Through ABAQUS software, finite element analysis models of the joint were created. The models facilitated the analysis of stress distribution within the joint under cyclic loading, elucidating the joint's failure mechanism and load transfer path. Subsequently, a parametric analysis was conducted to evaluate how key design parameters influence the joint's seismic performance.These parameters included the strength ratio of the column to the core tube, the axial compression ratio, the thickness ratio of the core tube to the column, and the bolt pre-tension force. The specific conclusions drawn from the study are as follows:

(1) A comprehensive finite element model of the joint was meticulously constructed. The accuracy of the finite element simulation was validated through a comparative analysis of the simulated hysteresis curves, skeleton curves, and failure modes against experimental data from pertinent studies.

(2) Detailed analysis was conducted to examine the plastic evolution and ultimate failure modes of the square core tube throughout the entire loading phase. The vertical and horizontal load transfer mechanisms of the column-to-column joint were identified. Throughout the loading process, the joint connections remained elastic, with plastic deformation confined to the bottoms of the core tube and the column, which adhered to the seismic design principle of "strong joints, weak members".

(3)The proposed joints have successfully realized the seismic design objective, conforming to the specified requirements for elastic and elastic-plastic inter-story displacement angles. The ductility coefficients across the models range from 2.66 to 3.79, with the elastic inter-story displacement angle varying between 1/98 and 1/71.

(4) The seismic performance of the joint is primarily influenced by three factors: the strength ratio of the column to the core tube, the strength ratio of the core tube to the column, and the axial compression ratio. Additionally, the bolt pre-tension force significantly affects the initial stiffness and energy dissipation capacity of the column, although the cumulative energy dissipation capacity remains consistent in the later stages. The recommended ranges for these parameters are as follows: the strength ratio of the column to the core tube should be between 1.5 and 1.78, the strength ratio of the core tube to the column should range from 0.22 to 0.66, and the axial compression ratio should be within the range of 0.3 to 0.5. Furthermore, the ratio between the core tube and the column thickness and the bolt type should both be selected based on the specific structural design requirements.

Funding

The research was funded by the Anhui Provincial Natural Science Foundation, Youth Project(2008085QA50).

References

[1] Wang Y Q, Liu, XY, Lin Y. Experimental study on fracture toughness of high-strength structural steel and its butt weld[J]. Advanced Steel Construction.2015,11(4):440-451.

[2] Jiao J F, Fan L X, Liu Y, et al. Investigating fatigue mechanisms and crack growth in 20mntib steel high-strength bolts: an experimental and simulation study[J]. Advanced Steel Construction.2023,19(4):329-340.

[3] Zhu Y P, Chen X Q, Zhong Y,et al.Seismic fragility analysis of steel frames with fully-bolted core tube joints[J]. Advanced Steel Construction.2024,20(3):208-221.

[4] Xue P, Gao M. Stress magnification effect of initial deformation on the notch stress field and fatigue strength of thin plate welded joints[J]. International Journal of Pressure Vessels and Piping, 2023(206): 253-262.

[5] Yan R Z, Zhang C L, Wang S, el al. Distribution of residual steel in the sphere-pipe connection welds of welded hollow spherical joints[J]. Advanced Steel Construction.2023,19(3):262-272.

[6] Wu C, Liu J L, Wang R H.A study on the dynamic response of welded hollow spherical joints under impact loading[J].Progress in Steel Building Structures,2021,23(11):82-93.(in Chinese)

[7] Feng J, Jin J, Xia j, et al. Experimental study on seismic performance of pec composite column-steel beam beam frame with welded T-stub strengthened connections[J]. Advanced Steel Construction.2021,17(3):264-272.

[8] Vucetic V, Kostic M, Karadzic D. Reliability assessment of connections with slip-critical bolts and fillet welds in combination[J]. Journal of Constructional Steel Research, 2019(159): 289-299.

[9] Sha L, Tu F, Kang C Y. Study on seismic performance of cantilever beam-column connection with Z-shaped full-bolted joint with double friction surfaces at the flange[J]. Progress in Steel Building Structures,1-8[2024-12-29].(in Chinese)

[10] Zhang T, Wang Y, Li H. Cyclic behavior of column-to-column connections in novel prefabricated H-shaped steel beam to CFST column joint[J]. Journal of Constructional Steel Research, 2021(178): 106489.

[11] Wang Y Q, Zong L, Shi Y J. Bending behavior and design model of bolted flange-plate connection[J]. Journal of Constructional Steel Research, 2013, 84: 1-16.

[12] Couchaux M, Hjiaj M, Ryan I, et al. Bolted circular flange connections under static bending moment and axial force[J]. Journal of Constructional Steel Research, 2019, 157: 314-336.

[13] Zhang S, He X, Liu X. Bending-shear performance of column-to-column bolted-flange connections in prefabricated multi-high-rise steel structures[J]. Journal of Constructional Steel Research, 2021(178): 106488.

[14] Bao Y, Uy B. Connection design in modular steel construction: A review[J]. Journal of Constructional Steel Research, 2019(154): 193-209.

[15] Qiu C, Ding C, He X, et al. Axial performance of steel splice connection for tubular FRP column members[J]. Composite Structures, 2018, 189: 498-509.

[16] Chu Y, Zhong Y, Luo P, et al. Experimental study on the seismic performance of the new fully-bolted beam-column joint[J]. Journal of Constructional Steel Research, 2022, 199: 107619.

[17] Wang H, Zhao X, Ma G. Experimental study on seismic performance of column-column-beam joint in panelised steel-modular structure[J]. Journal of Constructional Steel Research, 2022, 192: 107240.

[18] Wu X, Hu Q, Zhang Z, et al. Analysis of bolted connection for H-section beam and square steel tube column[J]. Journal of Constructional Steel Research, 2018(148): 277-286.

[19] Dai X M, Zong L, Ding Y, et al. Experimental study on seismic behavior of a novel plug-in self-lock joint for modular steel construction[J]. Engineering Structures, 2019, 181: 143-164.

[20] Lacey A W, Chen W, Hao H, et al. New interlocking inter-module connection for modular steel buildings: Experimental and numerical studies[J]. Engineering Structures, 2019, 198: 109465.

[21] Sendanayake S V, Thambiratnam D P, Perera N, et al. Seismic mitigation of steel modular building structures through innovative inter-modular connections[J]. Heliyon, 2019, 5(11): e02751.

[22] D'Aniello M, Cassiano D, Landolfo R. Simplified criteria for finite element modelling of European preloadable bolts[J]. Steel and Composite Structures, 2017, 24(6): 643-658.

[23] Liu X C, He X N, Wang H X, et al. Bending-shear performance of column-to-column bolted-flange connections in prefabricated multi-high-rise steel structures[J]. Journal of Constructional Steel Research, 2018, 145(JUN.): 28-48.

[24] Han LH. Concrete-filled steel tubular structures [M]. Beijing: Science Press, 2004: 477. (in Chinese)

[25] Zhang Yanxia, Li Hongwei, Huang Zhewen, et al. Finite element analysis of the seismic performance of self-tapping bolt-core sleeve flange column connection nodes in prefabricated steel structures [J]. Journal of Beijing University of Civil Engineering and Architecture, 2023, 39(02): 98-104. (in Chinese)

[26] Ministry of Housing and Urban-Rural Development of the People's Republic of China. Code for seismic test of buildings: JGJ/T101-2015 [M]. Beijing: China Architecture & Building Press, 2015. (in Chinese)